NASA Contractor Report 4623

Aeroelastic Simulation of Higher Harmonic Control

Lawson H. Robinson and Peretz P. Friedmann

Mechanical, Aerospace and Nuclear Engineering Department
School of Engineering and Applied Science
University of California, Los Angeles
Los Angeles, California

Prepared for
Ames Research Center
CONTRACT NAG-477
August 1994

National Aeronautics and
Space Administration

Ames Research Center
Moffett Field, California 94035-1000

PREFACE

This research was conducted at the Mechanical, Aerospace and Nuclear Engineering Department, School of Engineering and Applied Science, University of California, Los Angeles. This research was sponsored jointly by the McDonnell Douglas Helicopter Company, Mesa, Arizona and NASA Ames Research Center, Moffett Field, California, under NASA Grant NAG-477.

The research was monitored by Dr. F. Straub from McDonnell Douglas Helicopter Co. and Dr. S. Jacklin from NASA Ames Research Center. The authors wish to express their appreciation to the grant monitors for their useful comments and suggestions.

The principal investigator for this sponsored research activity was Professor Peretz P. Friedmann. This document constitutes essentially the first author's Ph.D. dissertation; however, some changes were made to the dissertation before turning it into a report.

CONTENTS

List of Figures . . . . . .

List of Tables . . . . . .

Notation . . . . . .

Summary . . . . . .

Chapter page

I. Introduction 1
Background 1
Reduction of Helicopter Vibrations 2
Objectives of the Research 5
The Aeroelastic Model 8

II. Geometric Coordinates and Transformations 10
Coordinate Systems 10
Nonrotating, Hub-fixed Coordinate System 10
Rotating, Hub-fixed Coordinate System 11
Preconed, Undeformed Blade Coordinate System 11
Deformed Blade Coordinate System 12
Rotated, Deformed Blade Coordinate System 12
Coordinate Transformations 12
Rotating to Nonrotating Transformation 12
Coned to Unconed Transformation 13
Deformed to Undeformed Transformation 13
Deformed and Rotated to Deformed Transformation . 14
Undeformed to Deformed and Rotated Transformation 14

III. Method of Solution of Equations of Motion 15
Free Vibration Solution and Modal Transformation 15
Solution Method for Hover 17
Trim Procedure 20
Introduction 20
Flap Trim 21
Full Propulsive Trim 22
Assumptions 22
Trim Variables and Equilibrium Equations 22
Aeroelastic Model for Trim 24

Introduction 20
Flap Trim 21
Full Propulsive Trim 22
Assumptions 22
Trim Variables and Equilibrium Equations 22
Aeroelastic Model for Trim 24
Method for Determining the Trim State 25
Solution Method for Forward Flight 27
Quasilinearization 27
Convergence 30

IV. Incorporation of Unsteady Aerodynamics in Equations of Motion 34
Equations of Motion 34
Derivation of Unsteady Aerodynamic Loads 37
Introduction 37
General Arbitrary-Motion Lift and Moment Expressions 38
Lift and Moment in Terms of Local Blade Velocities . 39
A Previous Formulation for the Circulatory Lift 42
General Expressions for Aerodynamic Forces and Moments 44
Numerical Implementation of Aerodynamic Loads 46
Introduction 46
Implicit Implementation 47
Explicit Implementation 51
Solving Numerically for the Augmented States 56

V. Calculation of Hub Forces and Moments 60
Introduction 60
Calculation of Local Loads 61
Local Aerodynamic Loads 61
Local Inertia Loads 62
Calculation of Root Loads 68
Summation of Local Aerodynamic and Inertia Loads . 68
Expressions for Local Contributions to Root Loads . . 69
Integration of Loads Over the Blade 71
Calculation of Total Hub Forces and Moments 71
Transformation to the Nonrotating Hub Coordinate System 71
Summation Over the Blades 72
Harmonic Analysis of the Hub Loads 73
Performance Coefficients and Normalization 74

VI. HHC for Vibration Reduction 76
Previous Work 76
The HHC Models 84
Linearity of HHC 84

Global Model 85
Local Model 86
Identification 86
Assumptions 86
Kalman Filter Identification 87
General Kalman Filter 87
Kalman Filter for Case 1 90
Kalman Filter for Case 2 91
Kalman Filter for Case 3 91
Kalman Filter for Case 4 92
Least Mean Squares (LMS) Identification 94
Control Algorithms 96
Minimum Varaince Control Algorithms 96
Deterministic Controller 98
Cautious Controller 100
Dual Controller 102
General Minimum Variance Controller 104
LMS Direct Inverse Control 106
HHC Implementation 107
HHC Input Formulation 107
Minimization Objectives 110

VII. Results Showing Effects of Unsteady Aerodynamics 111
Baseline Blade Configurations 111
Comparison With Previous Unsteady Results 112
Comparison of Quasisteady and Unsteady Results 114
Response and Stability 114
Hub Vibratory Loads 116
Comparison of Old and New Trim Results 117

VIII. Open Loop Results 121
Introduction 121
Hub Load Variation With HHC Phase 121
Linearity of Response to HHC 123
Transfer Matrix Calculation 124

IX. Closed-Loop Control Results 127
Introduction 127
Fixed Gain Control 128
Adaptive Control at Design Flight Condition 129
Control With Step Change in Flight Condition 133

X. HHC for Articulated Versus Hingeless Rotors 135
Introduction 135
Reduction of Hub Shears 136
Reduction of Shears and Moments 139

Rotating Blade Root Loads 142
Power Requirements and Stability 144

XI. Modeling the OH6A Helicopter 147
Introduction 147
Simplified OH6A Blade 150
Open-Loop HHC for the OH6A 151
Closed-Loop HHC for the OH6A 153
Power Requirements and Stability 154

XII. Concluding Remarks 156

References 163

Figures 170

LIST OF FIGURES

Figure		page
2. 1	Geometry of the Nonrotating Coordinate System and Hub Shears and Moments.	170
2. 2	Geometry of the Undeformed Blade in the Rotating System.	170
2. 3	Geometry of the Elastic Axis of the Deformed Blade.	170
2. 4	Deformed Blade Cross Sectional Geometry.	170
3. 1	Forces and moments on the helicopter in straight and level flight.	170
3. 2	Flow chart showing procedure used to solve the full trim equations.	170
4. 1	Geometry of motion of a typical airfoil.	170
4. 2	Various components of the unsteady loads acting on the airfoil.	170
5. 1	Flow chart showing procedure for hub force and moment calculation.	170
6. 1	Schematic of helicopter plant model.	171
6. 2	Block chart showing generation of the adaptive error vector for the extended LMS identification algorithm.	171
7. 1	Flap and lag response, advance ratio $\mu = 0.4$, results of Ref. 13, torsionally stiff blade, and baseline soft-in-plane blade.	171
7. 2	Stability eigenvalues for flap and lag for the torsionally stiff blade and the baseline soft-in-plane blade, and their comparison to the results of Ref. 13.	171
7. 3	Flap, lag, and torsional response, soft-in-plane blade, advance ratio $\mu = 0.4$, previous and current unsteady aerodynamics.	171

7. 4 Stability eigenvalues for flap and lag, soft-in-plane blade, previous and current unsteady aerodynamics. 171

7. 5 Flap, lag, and torsional response, soft-in-plane blade, advance ratio $\mu = 0.2$, quasisteady and unsteady aerodynamics. 171

7. 6 Flap, lag, and torsional response, soft-in-plane blade, advance ratio $\mu = 0.4$, quasisteady and unsteady aerodynamics. 171

7. 7 Flap, lag, and torsional response, stiff-in-plane blade, advance ratio $\mu = 0.2$, quasisteady and unsteady aerodynamics. 171

7. 8 Flap, lag, and torsional response, stiff-in-plane blade, advance ratio $\mu = 0.4$, quasisteady and unsteady aerodynamics. 172

7. 9 Flap response, soft-in-plane blade, advance ratio $\mu = 0.4$, quasisteady, quasisteady with apparent mass, and unsteady aerodynamics. 172

7.10 Lag and torsional response, soft-in-plane blade, advance ratio $\mu = 0.4$, quasisteady, quasisteady with apparent mass, and unsteady aerodynamics. 172

7.11 Stability eigenvalues for the first lag, first flap, and third flap modes, soft-in-plane blade, quasisteady and unsteady aerodynamics. 172

7.12 Stability eigenvalues for the second lag, second flap, and first torsion modes, soft-in-plane blade, quasisteady and unsteady aerodynamics. 172

7.13 Stability eigenvalues for the second lag, first flap, and second flap modes, stiff-in-plane blade, quasisteady and unsteady aerodynamics. 172

7.14 Stability eigenvalues for the first lag, third flap, and first torsion modes, stiff-in-plane blade, quasisteady and unsteady aerodynamics. 172

7.15 Variation of 4/rev. vertical and lateral hub shears with advance ratio, soft-in-plane blade, quasisteady aerodynamics, calculated from converged and unconverged response solutions. 172

7.16 Variation of 4/rev. vertical shear and yawing moment with advance ratio, soft-in-plane blade, quasisteady and unsteady aerodynamics. 173

7.17 Variation of 4/rev. lateral shear and pitching moment with advance ratio, soft-in-plane blade, quasisteady and unsteady aerodynamics. 173

7.18 Variation of 4/rev. longitudinal shear and rolling moment with advance ratio, soft-in-plane blade, quasisteady and unsteady aerodynamics. 173

7.19 Variation of 4/rev. vertical shear and yawing moment with advance ratio, stiff-in-plane blade, quasisteady and unsteady aerodynamics. 173

7.20 Variation of 4/rev. lateral shear and pitching moment with advance ratio, stiff-in-plane blade, quasisteady and unsteady aerodynamics. 173

7.21 Variation of 4/rev. longitudinal shear and rolling moment with advance ratio, stiff-in-plane blade, quasisteady and unsteady aerodynamics. 173

7.22 Trim values for collective pitch, inflow ratio, and rotor angle of attack, soft-in-plane blade, flap trim and full trim values. . . . 173

7.23 Trim values for cosine cyclic pitch and sine cyclic pitch, soft-in-plane blade, flap trim and full trim values. 173

7.24 Flap, lag, and torsional response, soft-in-plane blade, advance ratio $\mu = 0.3$, unsteady aerodynamics, flap trim and full trim. 174

7.25 Variation of 4/rev. vertical shear and yawing moment with advance ratio, soft-in-plane blade, unsteady aerodynamics, flap trim and full trim. 174

7.26 Variation of 4/rev. lateral shear and pitching moment with advance ratio, soft-in-plane blade, unsteady aerodynamics, flap trim and full trim. 174

7.27 Variation of 4/rev. longitudinal shear and rolling moment with advance ratio, soft-in-plane blade, unsteady aerodynamics, flap trim and full trim. 174

8. 1 Variation of 4/rev. vertical shear and yawing moment with HHC phase, collective input, soft-in-plane blade, quasisteady and unsteady aerodynamics, $\mu = 0.3$. 174

8. 2 Variation of 4/rev. lateral shear and pitching moment with HHC phase, collective input, soft-in-plane blade, quasisteady and unsteady aerodynamics, $\mu = 0.3$. 174

8. 3 Variation of 4/rev. longitudinal shear and rolling moment with HHC phase, collective input, soft-in-plane blade, quasisteady and unsteady aerodynamics, $\mu = 0.3$. 174

8. 4 Variation of 4/rev. vertical shear and yawing moment with HHC phase, longitudinal input, soft-in-plane blade, quasisteady and unsteady aerodynamics, $\mu = 0.3$. 174

8. 5 Variation of 4/rev. lateral shear and pitching moment with HHC phase, longitudinal input, soft-in-plane blade, quasisteady and unsteady aerodynamics, $\mu = 0.3$. 175

8. 6 Variation of 4/rev. longitudinal shear and rolling moment with HHC phase, longitudinal input, soft-in-plane blade, quasisteady and unsteady aerodynamics, $\mu = 0.3$. 175

8. 7 Variation of 4/rev. vertical shear and yawing moment with HHC phase, lateral input, soft-in-plane blade, quasisteady and unsteady aerodynamics, $\mu = 0.3$. 175

8. 8 Variation of 4/rev. lateral shear and pitching moment with HHC phase, lateral input, soft-in-plane blade, quasisteady and unsteady aerodynamics, $\mu = 0.3$. 175

8. 9 Variation of 4/rev. longitudinal shear and rolling moment with HHC phase, lateral input, soft-in-plane blade, quasisteady and unsteady aerodynamics, $\mu = 0.3$. 175

8.10 Variation of hub shear harmonics with HHC amplitude, quasisteady and unsteady aerodynamics, longitudinal cosine HHC applied, $\mu = .0.3$. 175

8.11 Variation of hub shear harmonics with HHC amplitude, quasisteady and unsteady aerodynamics, longitudinal cosine HHC applied, $\mu = 0.3$. 175

8.12 Variation of peak-to-peak hub shears with HHC amplitude, quasisteady and unsteady aerodynamics, longitudinal cosine HHC applied, $\mu = 0.3$. 176

8.13 Proportional change in hub shears with different 1/3° HHC incrementations, quasisteady and unsteady aerodynamics, soft-in-plane blade, advance ratio $\mu = 0.3$. 176

9. 1 Iteration history of HHC input angles for fixed gain control, quasisteady aerodynamics, $\mu = 0.3$. 176

9. 2 Iteration history of vertical, lateral, and longitudinal shears for fixed gain control, quasisteady aerodynamics, $\mu = 0.3$. 176

9. 3 Iteration history of HHC input angles for fixed gain control, unsteady aerodynamics, $\mu = 0.3$. 176

9. 4 Iteration history of vertical, lateral, and longitudinal shears for fixed gain control, unsteady aerodynamics, $\mu = 0.3$. 176

9. 5 Iteration history of vertical shears, four different deterministic controllers, quasisteady aerodynamics, $\mu = 0.3$. 176

9. 6 Iteration history of lateral shears, four different deterministic controllers, quasisteady aerodynamics, $\mu = 0.3$. 176

9. 7 Iteration history of longitudinal shears, four different deterministic controllers, quasisteady aerodynamics, $\mu = 0.3$. 176

9. 8 Iteration history of HHC input angles for deterministic versus cautious local control, quasisteady aerodynamics, $\mu = 0.3$. . . . 177

9. 9 Iteration history of vertical and lateral hub shears for deterministic versus cautious local control, quasisteady aerodynamics, $\mu = 0.3$. 177

9.10 Iteration history of longitudinal hub shear for deterministic versus cautious local control, quasisteady aerodynamics, $\mu = 0.3$. . . . 177

9.11 Iteration history of HHC input angles for deterministic versus cautious global control, quasisteady aerodynamics, $\mu = 0.3$. . . 177

9.12 Iteration history of vertical and lateral hub shears for deterministic versus cautious global control, quasisteady aerodynamics, $\mu = 0.3$. 177

9.13 Iteration history of longitudinal hub shear for deterministic versus cautious global control, quasisteady aerodynamics, $\mu = 0.3$. . . 177

9.14 Iteration history of HHC input angles for deterministic versus cautious local control, unsteady aerodynamics, $\mu = 0.3$. 177

9.15 Iteration history of vertical and lateral hub shears for deterministic versus cautious local control, unsteady aerodynamics, $\mu = 0.3$. 177

9.16 Iteration history of longitudinal hub shear for deterministic versus cautious local control, unsteady aerodynamics, $\mu = 0.3$. 178

9.17 Iteration history of HHC input angles for deterministic versus cautious global control, unsteady aerodynamics, $\mu = 0.3$. 178

9.18 Iteration history of vertical and lateral hub shears for deterministic versus cautious global control, unsteady aerodynamics, $\mu = 0.3$. 178

9.19 Iteration history of longitudinal hub shears for deterministic versus cautious global control, unsteady aerodynamics, $\mu = 0.3$. 178

9.20 Optimal shears for deterministic and cautious versions of local and global controllers using quasisteady aerodynamics, $\mu = 0.3$. . . 178

9.21 Optimal shears for deterministic and cautious versions of local and global controllers using unsteady aerodynamics, $\mu = 0.3$. 178

9.22 Comparison of optimal HHC inputs for the cautious version of the local controller using quasisteady versus unsteady aerodynamics, $\mu = 0.3$. 178

9.23 Flap, lag, and torsional elastic tip response, baseline response and optimal response due to cautious global HHC, unsteady aerodynamics, soft-in-plane blade, $\mu = 0.3$. 178

9.24 Total torsional geometric and elastic tip displacement, baseline response and optimal response due to cautious global HHC, unsteady aerodynamics, soft-in-plane blade, $\mu = 0.3$. 179

9.25 Iteration history of HHC input angles for deterministic versus cautious local control, unsteady aerodynamics, step change from $\mu = 0.3$ to $\mu = .35$. 179

9.26 Iteration history of hub shears for deterministic versus cautious local control, unsteady aerodynamics, step change from $\mu = 0.3$ to $\mu = 0.35$. 179

9.27 Iteration history of HHC input angles for deterministic versus cautious global control, unsteady aerodynamics, step change from $\mu = 0.3$ to $\mu = .35$. 179

9.28 Iteration history of hub shears for deterministic versus cautious global control, unsteady aerodynamics, step change from $\mu = 0.3$ to $\mu = 0.35$. 179

9.29 Baseline shears for $\mu = 0.35$, and shears five iterations after a step change from $\mu = 0.3$ to $\mu = 0.35$, local and global controllers, unsteady aerodynamics. 179

10. 1 Iteration history of HHC input angles for hingeless blade, 5% blade root offset, cautious global control, $\mu = 0.3$. 179

10. 2 Iteration history of vertical, lateral and longitudinal peak-to-peak hub shears, hingeless blade, 5% blade root offset, cautious global control, $\mu = 0.3$. 179

10. 3 Iteration history of pitching, rolling and yawing peak-to-peak hub moments, hingeless blade, 5% blade root offset, cautious global control, $\mu = 0.3$. 180

10. 4 Iteration history of HHC input angles for articulated blade, 5% blade root offset, cautious global control, $\mu = 0.3$. 180

10. 5 Iteration history of vertical, lateral and longitudinal peak-to-peak hub shears, articulated blade, 5% blade root offset, cautious global control, $\mu = 0.3$. 180

10. 6 Iteration history of pitching, rolling and yawing peak-to-peak hub moments, articulated blade, 5% blade root offset, cautious global control, $\mu = 0.3$. 180

10. 7 Iteration history of HHC input angles for hingeless blade, 5% blade root offset, 6×12 cautious global control, $\mu = 0.3$. 180

10. 8 Iteration history of vertical, lateral and longitudinal peak-to-peak hub shears, hingeless blade, 5% blade root offset, 6×12 cautious global control, $\mu = 0.3$. 180

10. 9 Iteration history of pitching, rolling and yawing peak-to-peak hub moments, hingeless blade, 5% blade root offset, 6×12 cautious global control, $\mu = 0.3$. 180

10.10 Comparison of peak-to-peak hub loads for baseline, 6×6 optimum, and 6×12 optimum, hingeless blade, 5% blade root offset, cautious global control, $\mu = 0.3$. 180

10.11 Iteration history of HHC input angles for articulated blade, 5% blade root offset, 6×12 cautious global control, $\mu = 0.3$. 181

10.12 Iteration history of vertical, lateral and longitudinal peak-to-peak hub shears, articulated blade, 5% blade root offset, 6×12 cautious global control, $\mu = 0.3$. 181

10.13 Iteration history of pitching, rolling and yawing peak-to-peak hub moments, articulated blade, 5% blade root offset, 6×12 cautious global control, $\mu = 0.3$. 181

10.14 Comparison of peak-to-peak hub loads for baseline, 6×6 optimum, and 6×12 optimum, articulated blade, 5% blade root offset, cautious global control, $\mu = 0.3$. 181

10.15 Iteration history of axial, cordwise, and vertical peak-to-peak rotating blade root shears, hingeless blade, 5% blade root offset, cautious global control, $\mu = 0.3$. 181

10.16 Iteration history of feathering, flapping, and lagging peak-to-peak rotating blade root moments, hingeless blade, 5% blade root offset, cautious global control, $\mu = 0.3$. 181

10.17 Iteration history of maximum values of feathering, flapping, and lagging rotating blade root moments, hingeless blade, 5% blade root offset, cautious global control, $\mu = 0.3$. 181

11. 1 OH6A main rotor hub. 181

11. 2 Variation of 4/rev. vertical and lateral pilot seat vibrations with phase of 1/3° lateral HHC input, flight test results of Ref. 67 for the OH6A helicopter, 100 knots. 182

11. 3 Variation of 4/rev. vertical, lateral, and longitudinal hub shears with HHC phase, 1/3° collective HHC input, OH6A rotor, unsteady aerodynamics, $\mu = 0.253$. 182

11. 4 Variation of 4/rev. vertical, lateral, and longitudinal hub shears with HHC phase, 1/3° lateral HHC input, OH6A rotor, unsteady aerodynamics, $\mu = 0.253$. 182

11. 5 Variation of 4/rev. vertical, lateral, and longitudinal hub shears with HHC phase, 1/3° longitudinal HHC input, OH6A rotor, unsteady aerodynamics, $\mu = 0.253$. 182

11. 6 Iteration history of HHC input angles for OH6A rotor, cautious, global control, $\mu = 0.253$, unsteady aerodynamics. 182

11. 7 Iteration history of vertical, lateral, and longitudinal 4/rev. hub shears for OH6A rotor, cautious global controller, $\mu = 0.253$, unsteady aerodynamics. 182

11. 8 Iteration history of pitching, rolling, and yawing 4/rev. hub moments for OH6A rotor, cautious global controller, $\mu = 0.253$, unsteady aerodynamics. 182

LIST OF TABLES

Table		page
6. 1	Kalman Filter Inputs	94
8. 1	Quasisteady HHC Transfer Matrix	125
8. 2	Unsteady HHC Transfer Matrix	125
11. 1	OH6A Basic Data	148
11. 2	OH6A Rotating Natural Frequencies	151

NOTATION

$\mathbf{a}$	acceleration of a point in the blade
A	rotor area
A_x	blade cross sectional area
$\{A(\vec{y}, \dot{\vec{y}})\}$	assembled blade aerodynamic load vector
$\{a^e\}$	vector of nodal displacements abd rotations for finite elements
a_i	lift-curve slope
A_{21} , A_{22}	coefficients in equations for augmented states
$\bar{a}\bar{b}R$	cross-sectional elastic center offset from midchord $\bar{a} = \frac{a}{b}$
B	blade chord, $\bar{b} = \frac{b}{R}$
b_e	an equivalent semi-chord over the blade, typically an average value
B_1 , B_2, B_3	coefficients in expressions for Fourier coefficients of H
$[B(\psi)]^k$	matrix of coefficients of the linearized system at the kth iteration of quasilinearization
$[B_1^e]$	linear element stiffness matrix
$[C(\vec{y}, \dot{\vec{y}})]$	assembled blade damping matrix
C_T , C_W, C_H	thrust, weight, and in-plane force coefficients

C_P	power coefficient
E	blade bending elastic modulus
e_1	blade root offset from center of rotation
$\hat{e}_x$, $\hat{e}_y$, $\hat{e}_z$	unit vectors in the undeformed blade coordinate system
$\hat{e}'_x$, $\hat{e}'_x$, $\hat{e}'_x$	the triad $\hat{e}_x$, $\hat{e}_y$, $\hat{e}_z$ after the deformation
$\hat{e}''_x$, $\hat{e}''_x$, $\hat{e}''_x$	the triad $\hat{e}'_x$, $\hat{e}'_x$, $\hat{e}'_x$ after rotation by ϕ
F	time-domain lift deficiency function
f	parasite drag area of fuselage
$\{F\}$	assembled blade nonhomogeneous load vector
$\left\{F_{NL}\left(\{q\},\{\dot{q}\};\psi\right)\right\}$	right hand side of blade equations of motion written in first order state variable form, Eqn. (3.24)
FT	vector of trim equations
G	blade torsional elastic modulus
$\bar{h}$	offset of fuselage center of drag or center of mass from rotor hub
$\Delta h(t)$	vertical displacement of elastic center of airfoil
H , H_0 , H_{sn} , H_{cn}	a function incorporating unsteady aerodynamic effects and its Fourier coefficients
$[I]$	identity matrix
$[I_1^e]$	linear element matrix, acceleration dependent inertia terms
I_b	flapping mass moment of inertia, $\bar{I}_b = \dfrac{I_b}{m_0 \ell^3}$
$\hat{i}$, $\hat{j}$, $\hat{k}$	unit vectors in the unconed rotating

	coordinate system
$\hat{i}_{nr}$, $\hat{j}_{nr}$, $\hat{k}_{nr}$	unit vectors in the nonrotating coordinate system
I_2 , I_3	blade cross-sectional chordwise and flapwise area moments
I_{m2} , I_{m3}	blade cross-sectional mass moments of inertia about the $\hat{e}'_z$ and $\hat{e}'_y$ axes
J	blade cross-section torsional area moment
$[K(\vec{y},\vec{y})]$	assembled blade stiffness matrix
$[K^e_1]$	linear element matrix, displacement dependent inertia terms
k_{m2} , k_{m3}	equivalent radii of gyration for I_{m2} and I_{m3} about the $\hat{e}'_z$ and $\hat{e}'_y$ axes
ℓ	length of elastic portion of blade
L_{nc} , L_c	noncirculatory and circulatory components of lift
$[L(\psi)]$	matrix containing the coefficients of the linear terms in the blade equations of motion
m_0	reference mass per unit length of the blade
m	mass per unit length of the blade, $\overline{m} = \frac{m}{m_0}$
m	number of vibration measurements
M_{nc} , M_c	noncirculatory and circulatory components of moment
M_{pt} , M_{rl} , M_{yw} , M_{dr}	nondimensional hub moments in pitch, roll, yaw, and in pitch due to fuselage drag only
$[M(\vec{y},\vec{y})]$	assembled blade mass matrix

n	number of control inputs
$\left\{N\left(\{q\}, \{\dot{q}\}; \psi\right)\right\}$	vector containing nonlinear terms in the blade equations of motion
P	covariance matrix
$\mathbf{P}_i$	vector of local inertia forces
$\overline{P}_x$, $\overline{P}_y$, $\overline{P}_z$	nondimensional local forces, subscript a for aerodynamic, subscript i for inertia
$\mathbf{q}_i$	vector of local inertia moments
$Q(t)$, $\overline{Q}_0$, $\overline{Q}_{sn}$, $\overline{Q}_{cn}$	three quarter chord downwash velocity and its Fourier coefficients
$\overline{q}_x$, $\overline{q}_y$, $\overline{q}_z$	nondimensional local moments, subscript a for aerodynamic, subscript i for inertia
$\{q\}$	first order state variable vector of generalized coordinates
q_{SL}, q_{SF}	blade structural damping in lag and flap equations of generalized coordinates
$[Q^e]$	matrix containing normal mode information for a finite element
R	rotor radius
$\mathbf{R}_p$	position vector from the elastic axis to a point in the blade cross section
$\mathbf{R}_{EA}$	position vector to a point on the blade elastic axis from the center of rotation
$\overline{S}_{vt}$, $\overline{S}_{lt}$, $\overline{S}_{\ln}$	nondimensional hub shears in vertical,

	lateral, and longitudinal directions
$[S]$	dynamic stability matrix for case of hover
$[T_1^e]$	linear element matrix, centrifugal tension loads
T	$n \times m$ HHC transfer matrix
T	tension force in blade equations
$\bar{T}$	vector of trim variables
u, v, w	components of displacement of a point on the elastic axis of the blade in the $\hat{e}_x$, $\hat{e}_y$, and $\hat{e}_z$ directions
$U_T(t)$, $U_P(t)$	freestream velocities in the horizantal and vertical directions in figure 4.1
$\overline{U}_{T0}$	constant portion of $\overline{U}_T$
U'_x , U'_y , U'_z	velocity vector components in the $\hat{e}'_x$, $\hat{e}'_x$, $\hat{e}'_x$ system
U''_x , U''_y , U''_z	velocity vector components in the $\hat{e}''_x$, $\hat{e}''_x$, $\hat{e}''_x$ system
$\overline{U}''_{y0}$	constant portion of $\overline{U}''_y$
V	velocity of the helicopter
$\mathbf{V}_A$	velocity of air due to inflow
$\mathbf{V}_{EA}$	velocity of the blade elastic axis
W_z	diagonal weighting matrix on vibrations
W_θ	diagonal weighting matrix on control amplitudes
$W_{\Delta\theta}$	diagonal weighting on control rate of change

x_0 , y_0 , z_0	coordinates of a point in the blade in the $\hat{e}'_x$, $\hat{e}'_x$, $\hat{e}'_x$ coordinate system
x , y , z	coordinates of a point in the rotating hub coordinate system
x_{nr} , y_{nr} , z_{nr}	coordinates of a point in the nonrotating hub coordinate system
x_A	aerodynamic center offset from elastic axis
x_I	center of mass offset from elastic axis
$X_1(t)$, $X_2(t)$	augmented aerodynamic state variables
$\overline{X}_{TS1}(t)$, $\overline{X}_{TS2}(t)$	nondimensional augmented aerodynamic state variables for a typical section
y	$n \times 1$ vector of vibration measurements
$\{y\}$	vector of generalized coordinates
$\{Z(\psi)\}$	vector containing nonhomogeneous terms in the blade equations of motion
Z	$n \times 1$ vector of vibration amplitudes
Z_0	$n \times 1$ vector of baseline vibrations
$\alpha(t)$, α_0 , $\Delta\alpha(t)$	angle of incidence of the airfoil at the elastic axis $\alpha(t) = \alpha_0 + \Delta\alpha(t)$
α_R	rotor angle of attack
β	factor to implement cautious control
β_p	blade precone angle
γ	blade Lock number $= \dfrac{2a_i\rho_a b_e R^4}{I_b}$

Γ	proportional factor between inertia and aerodynamic loads
ε	symbolic term quantifying the order of magnitude of blade slopes
θ	$m \times 1$ vector of HHC inputs
$\Delta\theta(i)$	$\theta(i) - \theta(i-1)$
θ_G	total geometric pitch angle
θ_{HH}	HHC control angle
θ_0 , θ_{1s} , θ_{1c}	collective and cyclic pitch control inputs
θ_0 , θ_c , θ_s	amplitudes of HHC input in collective, longitudinal, and lateral control degrees of freedom
θ_{0s} , θ_{cs} , θ_{ss}	amplitudes of HHC sine input in collective, longitudinal, and lateral control degrees of freedom
θ_{0c} , θ_{cc} , θ_{sc}	amplitudes of HHC cosine input in collective, longitudinal, and lateral control degrees of freedom
λ	inflow ratio $= \dfrac{V \sin \alpha_R + v}{\Omega R}$
λ_j	stability eigenvalue in hover
λ_{cj}	characteristic exponent of transition matrix in forward flight
μ	advance ratio $= \dfrac{V \cos \alpha_R}{\Omega R}$
v	rotor induced velocity
ρ	mass density of the blade
ρ_A	density of air
ϕ	torsional elastic deformation of the blade

ϕ_{HH}	general HHC phase angle
ϕ_0 , ϕ_c , ϕ_s	phases of HHC input in collective, longitudinal, and lateral control degrees of freedom
$[\Phi(2\pi)]^k$	Floquet transition matrix at the end of one period
ψ	blade azimuth
ω_{HH}	HHC frequency
Ω	rotor angular speed
Ω	rotor angular velocity vector
ω_{HH}	HHC frequency
ω_j	imaginary part of hover stability eigenvalue
ω_{cj}	imaginary part of characteristic exponent in forward flight
ζ_j	real part of hover stability eigenvalue
ζ_{cj}	real part of characteristic exponent in forward flight
$(\ )_{,x}$	$\frac{\partial}{\partial x}$
$(\dot{\ }), (\ddot{\ })$	$\frac{\partial}{\partial t}, \frac{\partial^2}{\partial t^2}$
$(\overset{*}{\ }), (\overset{**}{\ })$	$\frac{\partial}{\partial \psi}, \frac{\partial^2}{\partial \psi^2}$
$\overline{(\ )}$	indicates nondimensional quantity
$\overline{\overline{(\ )}}$	indicates normalized, nondimensioal hub loads
$(\ )^R$	indicates incremental load at blade root
$(\ )^B$	indicates integrated load at blade root
$E\{\ \}$	indicates expected value, accounting for uncertainty in the system

SUMMARY

This report describes the development of an aeroelastic analysis of a helicopter rotor and its application to the simulation of helicopter vibration reduction through higher harmonic control (HHC). An improved implementation of a finite-state, time-domain model of unsteady aerodynamics is developed to capture high frequency aerodynamic effects. Helicopter trim parameters are determined using an improved trim procedure accounting for flap, lag, and torsional deformations of the blade. A procedure for calculating 4/rev rotor hub loads is developed and control algorithms are incorporated into the analysis to determine the optimal HHC inputs necessary to minimize these rotor hub loads.

Using this analysis, the effect of unsteady aerodynamics on the aeroelastic response and stability of a hingeless rotor blade is studied in detail. The effect of time domain unsteady aerodynamics on blade aeroelastic stability and low frequency response is found to be small. On the other hand, the influence of unsteady aerodynamics on high frequency response, especially in the presence of high frequency pitch excitations, is found to be significant. Furthermore, the two aerodynamic formulations lead to significantly different response levels in rotor hub vibrations as a result of phasing changes introduced in open-loop HHC inputs.

Several different HHC algoritms are implemented on a hingeless rotor using both quasisteady and unsteady aerodynamic models, and their effectiveness in reducing rotor hub vibratory shears is compared. A number of closed loop adaptive controllers are studied. All the controllers are found to be quite effective in reducing vibrations, but very differing HHC inputs are required depending on the aerodynamic model used. Effects of HHC on rotor stability and power requirements are found to be quite small. Simulations of roughly equivalent articulated and hingeless rotors are carried out, and it is found that hingeless rotors can require considerably larger HHC inputs to reduce rotor vibratory shears. Additionally, hub moments for the hingeless rotor may increase significantly while shears are being minimized. This implies that the practical implementation of HHC on hingeless rotors might be considerably more difficult than its implementation on articulated rotors. Finally, this analysis is used to compare with some flight test results obtained on an OH6A light helicopter.

Chapter I

INTRODUCTION

1.1 BACKGROUND

A major goal of current helicopter research is to reduce the vibration levels experienced by crew, passengers or equipment during flight. This research has been driven by both commercial and military requirements. Commercial passenger acceptance would benefit greatly from the perception of the helicopter as having a "jet smooth ride." Furthermore high vibration levels lead directly to higher maintenance costs. High vibration levels frequently cause problems during high speed flight and also during transition flight at 60-80 mph. Decreasing vibration levels and allowing higher cruise speeds would increase the load utilization of helicopters and so decrease relative capital costs. From a military point of view, increased speed leads to benefits in survivability and deployment response times. The same maintenance and comfort benefits as for civil operations apply. Reduction in vibration levels allows more accurate weapons deployment and more effective intelligence gathering, therefore current Army requirements specify vibration levels below 0.05 g.

The traditional approach to vibration reduction in helicopters has depended on the use of passive means such as vibration absorbers or isolation devices. A comprehensive review of helicopter vibration control by Reichert[55] describes many of these methods. The development of such methods has lead to

large decreases in vibration levels over the last thirty years and can now keep them below 0.10 g. However in the last ten years the trend has been to reduce acceptable vibration levels from 0.10 g to 0.05 g. This objective can be only rarely accomplished using a passive vibration control approach.

1.2 REDUCTION OF HELICOPTER VIBRATIONS

The desire to find methods to drastically reduce vibrations below the levels reached by these traditional means has lead to research in new areas. One promising approach is to design rotor blades which inherently have low levels of vibration. This may be done by applying optimum structural design to the aeroelastic tailoring of the blade. Geometry, mass, and stiffness distributions may be optimized to give minimum vibration levels at the rotor hub or somewhere in the fuselage. The fuselage itself may also be tailored to reduce vibrations at various points of interest such as the pilot seat, passenger compartment or the tail boom. Surveys of the application of structural optimization to helicopter vibration problems have been presented by Friedmann[20] and Miura[44]. Another approach is to optimize the use of conventional devices, such as vibration absorbers or isolators, via conformal mapping in order to reduce vibrations at critical points in the fuselage[1].

A different approach to vibration reduction, which is the subject matter of this research, is to use active controllers to reduce vibrations by eliminating them at their source, namely the aerodynamic excitation of the rotor. This concept, referred to as Higher Harmonic Control (HHC), relies on the appli-

cation of higher harmonic (i.e. above the 1/rev. pitch changes used for directional control and trim) pitch changes to modify the blade airloads so as to minimize harmonic blade loading. For an N bladed rotor the predominant vibrations in the fuselage are at N/rev. These are normally alleviated by applying N/rev. pitch excitations superimposed on the collective (i.e. average), lateral (i.e. 1/rev. sine), and longitudinal (i.e. 1/rev. cosine) pitch inputs used to control the helicopter attitude and velocity. This may be done by applying N/rev. harmonics to a standard helicopter swashplate through the use of hydraulic servo-actuators. Aircraft flight tests[67,68,43,53], wind tunnel tests[45,28,59, 37], and analytical simulations[62,46,10,34,41]. have shown that HHC is capable of substantial reduction in helicopter vibration levels encountered in forward flight.

The majority of all HHC studies, either analytical or experimental, have been based on linear, quasi-static, frequency domain representations of the helicopter response to control. Least-squares or Kalman filter type identification of the helicopter control parameters has been used along with a minimum variance or quadratic performance function type controller to determine optimal control harmonics for vibration alleviation. An extensive review of previous work in this area is given in Ch. 6. The purpose of this research is not to present advances in the area of control theory, but rather to investigate its interaction with an aeroelastic model of the helicopter.

Previous analytical studies have generally relied on simple analog[41] or frequency domain[10] models of the helicopter response. The helicopter aeroelastic problem is inherently non-linear, with design parameters interacting

in a complex manner. Thus simplistic models of the helicopter response can be unreliable. Other studies[62,46] were based on using a fairly old aeroelastic response code, the G400 code[2,3], for simulation purposes. The aeroelastic model in the G400 code does not have a consistent representation of the geometrical nonlinearities due to moderate blade deflections. Other shortcomings of this simulation capability consist of the lack of time domain aerodynamics needed for capturing high frequency unsteady aerodynamic effects combined with a step by step time integration solution technique which does not enable one to obtain direct information on blade stability, which is usually obtained by more recent methods such as numerical implementation of Floquet theory.

Most previous studies involving HHC have been limited to conventional rotors consisting of articulated blades. In recent years the desire to decrease mechanical complexity and weight and minimize maintenance costs has lead to the development of hingeless and bearingless rotor hubs. In hingeless rotors the mechanical hinges in flap and lag present in articulated blades are replaced by a flexible cantilevered blade, where blade flexibility provides for virtual hinges. In such blades the mechanical pitch bearing is retained. Bearingless rotor blades are similar to hingeless blades except that the pitch bearing is eliminated and the pitch input is introduced through a torsionally flexible structural element. The mechanical simplicity and weight savings in hingeless and bearingless rotors is generally accompanied by increased vibration levels. The literature contains no aeroelastic simulation capability which is based on a hingeless or bearingless blade model and includes the effects of HHC.

1.3 OBJECTIVES OF THE RESEARCH

This study has a number of objectives. The first group of objectives encompass the modification of an existing aeroelastic analysis, and associated computer code, to enable one to model HHC control effects with time domain unsteady aerodynamics. This is a major extension of an existing analysis and code because it requires the introduction of several new ingredients which are listed below:

1. Adaptation of the aeroelastic analysis of Ref. 8 to allow modeling of rotor response to HHC. Coding must be provided for the application of HHC root pitch changes in the inertia and aerodynamic portions of the program. The Galerkin finite element portion of the program must be modified to allow the modeling of articulated rotors. An improved procedure for calculating the N/rev. harmonics of the six hub forces and moments to be used as objects of minimization must be developed.
2. Development of an improvement on the unsteady aerodynamic theory of Ref. 13 overcoming its deficiencies. Algebraic manipulation software is used to develop implicit expressions for the aerodynamic loads which include previously neglected higher order terms including some apparent mass terms which can be important in calculating accurate helicopter response data. Methods for implementing these aerodynamics in an implicit manner on the aeroelastic model of this study must also be developed.
3. Development of an improved trim procedure accounting for flap, lag, and torsional deformations of the blade and allowing modeling of real-

istic blade cross sectional property distributions. This procedure will provide for full equilibrium of the helicopter in forward flight.

4. Provision of appropriate means to implement closed-loop HHC on the aeroelastic model. This involves the coding of routines to calculate several types of control and to implement filters for identification of problem parameters.

These four objectives, which constitute the development of a significantly improved aeroelastic model for the analytic study of the application of HHC for helicopter vibration reduction, are covered in detail in Chs. 4 through 6 of this research.

With the aeroelastic model developed, a second group of objectives was undertaken. These objectives, consisting of various comparative studies which are the ultimate aim of this research, are listed below:

1. Determination of the importance of unsteady aerodynamic modeling on the response and stability of hingeless rotor blades in forward flight. Quasisteady aerodynamics, the unsteady aerodynamics of Ref. 13, and the improved unsteady aerodynamics of this study are evaluated. This will include an investigation of the importance of unsteady modeling when simulating application of HHC to rotors. In this simulation differences in high frequency response become important.
2. Implementation of several HHC algorithms and identification approaches in order to determine the effectiveness of different algorithms in reducing hub vibrations in steady flight and when step changes are

made in the flight condition. Differences in simulation results using quasisteady and unsteady aerodynamics will again be evaluated.

3. Investigation of the effects of HHC on rotor stability. This has not been previously done because of a lack of appropriate simulation capacity. The solution procedure of this investigation is ideally suited to this since the Floquet theory used provides direct stability information in forward flight.
4. Studying the effect of HHC on power requirements of the rotor. This is particularly relevant since small decreases in rotor torque or power requirement were observed in the first flight tests of an HHC system[67]. Such a decrease in rotor power requirements could make up for the power required for actuators to implement HHC. This small decrease has not been investigated and may in fact be an anomaly unrelated to HHC.
5. Simulation of the application of HHC to roughly equivalent articulated and hingeless rotors. Previous investigations have shown HHC to be very effective when applied to articulated rotors but comparisons with hingeless rotors have not been made. Hingeless rotors generally have somewhat higher vibration levels than articulated rotors and if larger HHC angles are needed to counter them this could decrease the attractiveness of HHC for vibration reduction.
6. Use of the aeroelastic model developed to simulate the application of HHC to an actual rotor, that of the OH6-A light helicopter. These results will be compared with actual flight test data. Because of the limi-

tations of the model, particularly the lack of modeling of fuselage degrees of freedom, comparison will be limited to general trends in rotor response.

Results of investigations toward these six objectives are given in Chs. 7 through 11 of this research.

1.4 THE AEROELASTIC MODEL

The research conducted in this study is carried out using an analytical model which improves on some restrictions which were present in previous models. A brief description of the aeroelastic model follows. A detailed description is presented in Ch. 4.

The coupled flap-lag-torsional equations of motion which serve as the basis of this analysis are similar to those derived in Ref. 57 and are based on a structural model developed in Ref. 56. They contain geometrically nonlinear terms due to moderate blade deflections as illustrated in Figs. 2.2-2.4. These equations form the basis of an implicit flap-lag-torsional analysis[7,8] of a flexible, isotropic blade, modeled as an Euler-Bernoulli beam undergoing small strains and moderate deflections. Thus the equations contain geometrically nonlinear terms in the structural, inertia, and aerodynamic operators associated with this aeroelastic problem. The spatial dependence in the equations is eliminated by using a Galerkin finite element analysis developed by Straub and Friedmann[61]. A modal coordinate transformation, using six rotating coupled modes, is performed to reduce the number of degrees of freedom.

These modes are calculated at a fixed value of collective pitch which depends only on advance ratio. For the configurations considered, the six lowest modes are usually the first three flap, two lead-lag, and one torsional modes. The ordinary differential equations are solved using quasilinearization in an iterative manner to obtain the periodic equilibrium position in forward flight, for a propulsive trim type flight condition.

The inertia loads are determined by using D'Alembert's principle. An implicit formulation for the aerodynamic loads is used. At each iteration an approximation to the blade response is produced. This response is then used to generate numerical values of the modeling quantities needed in expressions for the aerodynamic loads to be used in the next iteration. Derivatives of the aerodynamic loads with respect to the generalized coordinates, required for stability analysis, are computed using finite difference approximations[7]. The equations are linearized by writing perturbation equations about the nonlinear equilibrium position. Stability is determined by using Floquet theory.

Use of this model for the research of this study requires major modifications and additions to the analysis of Ref. 8. The derivations required to make these changes are described in Chs. 3 through 6.

Chapter II

GEOMETRIC COORDINATES AND TRANSFORMATIONS

This chapter presents the coordinate systems and transformations used in deriving the equations of motion for the blade and in determining the expressions for various forces and moments used in calculating the rotor hub loads.

2.1 COORDINATE SYSTEMS

2.1.1 *Nonrotating, Hub-fixed Coordinate System*

This coordinate system, shown in Fig. 2.1, has its origin at the center of rotation of the rotor. The axes are x_{nr} pointing toward the helicopter tail, y_{nr} pointing to starboard, and z_{nr} coinciding with the vector of rotor rotation. The corresponding unit vectors are $\hat{i}_{nr}$, $\hat{j}_{nr}$, and $\hat{k}_{nr}$. Hub shears and moments are defined in this coordinate system and are oriented along the coordinate axes as shown in Fig. 2.1.

2.1.2 *Rotating, Hub-fixed Coordinate System*

This coordinate system, shown in Fig. 2.2, has its origin at the center of rotation of the rotor. The axes are x and y, which rotate in the x_{nr}, y_{nr} plane, and z which is coincident with the z_{nr} axis. The corresponding unit vectors are $\hat{i}$, $\hat{j}$, and $\hat{k}$. The coordinate system rotates at constant angular velocity $\Omega\hat{k}$ around the z axis.

2.1.3 *Preconed, Undeformed Blade Coordinate System*

This coordinate system, shown in Fig. 2.2, has its origin at the blade root, offset from the center of rotation by a distance e_1 . The axes are x_0 and z_0, in the x, z plane, and y_0 which is coincident with the y axis. The unit vectors $\hat{e}_x$, $\hat{e}_y$, and $\hat{e}_z$ are obtained by rotating the $\hat{i}$, $\hat{j}$, $\hat{k}$ system by a precone angle β_p about the y axis. This is the global structural coordinate system used for the finite element model. The x_0 axis represents the undeformed elastic axis of the blade, where the elastic axis is defined as the line connecting the shear centers of the blade cross-sections. A shear force applied at a point on the elastic axis will not cause torsional deformations.

2.1.4 *Deformed Blade Coordinate System*

This coordinate system, shown in Figs. 2.3 and 2.4, represents the orientation of the local blade geometry after deformation. The unit vectors $\hat{e}'_x$, $\hat{e}'_y$, and $\hat{e}'_x$ are obtained by rotating the $\hat{e}_x$, $\hat{e}_y$, $\hat{e}_z$ system around all three axes in accordance with the deformation of the blade. The $\hat{e}'_x$ unit vector is always parallel to the local deformed elastic axis.

2.1.5 *Rotated, Deformed Blade Coordinate System*

This coordinate system is the deformed blade coordinate system with the torsional deformation removed. The unit vectors $\hat{e}''_x$, $\hat{e}''_y$, and $\hat{e}''_z$ are obtained by rotating the $\hat{e}'_x$, $\hat{e}'_y$, $\hat{e}'_z$ system by an angle of $-\phi\hat{e}'_x$. This coordinate system is used in deriving the aerodynamic loads.

2.2 COORDINATE TRANSFORMATIONS

2.2.1 *Rotating to Nonrotating Transformation*

$$\begin{Bmatrix} \hat{i} \\ \hat{j} \\ \hat{k} \end{Bmatrix} = \begin{bmatrix} \cos\psi & \sin\psi & 0 \\ -\sin\psi & \cos\psi & 0 \\ 0 & 0 & 1 \end{bmatrix} \begin{Bmatrix} \hat{i}_{nr} \\ \hat{j}_{nr} \\ \hat{k}_{nr} \end{Bmatrix} \tag{2.1}$$

2.2.2 *Coned to Unconed Transformation*

$$\begin{Bmatrix} \hat{e}_x \\ \hat{e}_y \\ \hat{e}_z \end{Bmatrix} = \begin{bmatrix} \cos\beta_p & 0 & \sin\beta_p \\ 0 & 1 & 0 \\ -\sin\beta_p & 0 & \cos\beta_p \end{bmatrix} \begin{Bmatrix} \hat{i} \\ \hat{j} \\ \hat{k} \end{Bmatrix} \tag{2.2}$$

and its inverse:

$$\begin{Bmatrix} \hat{i} \\ \hat{j} \\ \hat{k} \end{Bmatrix} = \begin{bmatrix} \cos\beta_p & 0 & -\sin\beta_p \\ 0 & 1 & 0 \\ \sin\beta_p & 0 & \cos\beta_p \end{bmatrix} \begin{Bmatrix} \hat{e}_x \\ \hat{e}_y \\ \hat{e}_z \end{Bmatrix} \tag{2.3}$$

2.2.3 *Deformed to Undeformed Transformation*

From Ref. 56:

$$\begin{Bmatrix} \hat{e}'_x \\ \hat{e}'_y \\ \hat{e}'_z \end{Bmatrix} = \begin{bmatrix} 1 & v_{,x} & w_{,x} \\ -(w_{,x}\phi + v_{,x}) & 1 & \phi \\ -(w_{,x} - \phi v_{,x}) & -(v_{,x}w_{,x} + \phi) & 1 \end{bmatrix} \begin{Bmatrix} \hat{e}_x \\ \hat{e}_y \\ \hat{e}_z \end{Bmatrix} \tag{2.4}$$

and its inverse:

$$\begin{Bmatrix} \hat{e}_x \\ \hat{e}_y \\ \hat{e}_z \end{Bmatrix} = \begin{bmatrix} 1 & -(v_{,x} + \phi w_{,x}) & -(w_{,x} - \phi v_{,x}) \\ v_{,x} & 1 & -(\phi + v_{,x}w_{,x}) \\ w_{,x} & \phi & 1 \end{bmatrix} \begin{Bmatrix} \hat{e}'_x \\ \hat{e}'_y \\ \hat{e}'_z \end{Bmatrix} \tag{2.5}$$

2.2.4 *Deformed and Rotated to Deformed Transformation*

$$\begin{Bmatrix} \hat{e}''_x \\ \hat{e}''_y \\ \hat{e}''_z \end{Bmatrix} = \begin{bmatrix} 1 & 0 & 0 \\ 0 & \cos\phi & -\sin\phi \\ 0 & \sin\phi & \cos\phi \end{bmatrix} \begin{Bmatrix} \hat{e}'_x \\ \hat{e}'_y \\ \hat{e}'_z \end{Bmatrix} \tag{2.6}$$

2.2.5 *Undeformed to Deformed and Rotated Transformation*

By setting ϕ equal to zero in Eqn. 2.5 we obtain:

$$\begin{Bmatrix} \hat{e}_x \\ \hat{e}_y \\ \hat{e}_z \end{Bmatrix} = \begin{bmatrix} 1 & -v_{,x} & -w_{,x} \\ v_{,x} & 1 & -v_{,x}w_{,x} \\ w_{,x} & 0 & 1 \end{bmatrix} \begin{Bmatrix} \hat{e}''_x \\ \hat{e}''_y \\ \hat{e}''_z \end{Bmatrix} \tag{2.7}$$

Chapter III

METHOD OF SOLUTION OF EQUATIONS OF MOTION

3.1 FREE VIBRATION SOLUTION AND MODAL TRANSFORMATION

The natural frequencies and mode shapes of the blade are calculated using a local Galerkin Method of Weighted Residuals. The method, as presented in Ref. 8, has been modified to allow for modeling of articulated rotor blades. The following description uses the notation of Ref. 8. The finite element used has 11 degrees of freedom: displacement and rotation in lag at the end nodes (4), displacement and rotation in flap at the end nodes (4), and torsional rotation at the end nodes and a mid-element node (3). Displacements inside the element are in terms of cubic Hermitian interpolation polynomials for flap and lag, and quadratic Hermitian interpolation polynomials for torsion. The axial displacements are eliminated by making the assumption that the blade is inextensional. The Galerkin method requires that the sum of the weighted residuals of both the differential equations and the natural boundary conditions be equal to zero. These calculations are based on the linear, homogeneous, undamped equations of motion of the blade in a vacuum, which are obtained from the nonlinear partial differential equations of motion given in Eqns. 4.3 through 4.6. The equations of motion for the elements used in modeling the blade, where superscript e indicates the element number and subscript 1 indicates that these are linear matrices, are:

$$[I_1^e]\{\ddot{a}^e\} + ([B_1^e] + [K_1^e] + [T_1^e])\{a^e\} = 0 \qquad e = 1,2,\ldots,E \tag{3.1}$$

The E equations 3.1 are assembled and root boundary conditions are imposed by dropping the rows and columns of the system mass and stiffness matrices corresponding to the degrees of freedom restrained at the root. These degrees of freedom will vary depending on whether an articulated or hingeless blade is being modeled.

In forward flight the blade root pitch varies periodically with azimuth. This causes coupling between the modes and periodicity in the mode shapes. For this study the modes do not vary with azimuth and are calculated for a constant root pitch angle equal to the collective pitch. The coupled mode shapes of the blade are normalized by dividing each mode shape by its maximum tip displacement in either flap, lag, or torsion.

A modal coordinate transformation is introduced to reduce the number of unknowns in the problem and to assemble the various element matrices into the system matrices and load vectors. The modal transformation has the form:

$$\{a^e\} = [Q^e]\{y\} \tag{3.2}$$

The vector {y} of generalized coordinates become the new problem unknowns. If m modes are used to perform the modal coordinate transformation, then {y} is of length m. The matrix $[Q^e]$ is of size 11 by m. The columns of this matrix contain the portions of the normal mode eigenvectors corresponding to the modal degrees of freedom for the given blade element.

The stiffness matrix $[K(\vec{y},\vec{y})]$ of the complete blade is assembled by summing the stiffness matrices of the individual blade elements, each of which has had the modal coordinate transformation applied to it:

$$[K(\vec{y},\vec{y})] = \sum_{e=1}^{E} [Q^e]^T [K^e(\vec{y},\vec{y})][Q^e] \tag{3.3}$$

where $[K^e(\vec{y},\vec{y})]$ is the stiffness matrix of the e-th finite element in the local coordinate system. The blade mass matrix $[M(\vec{y},\vec{y})]$, damping matrix $[C(\vec{y},\vec{y})]$, aerodynamic load vector $\{A(\vec{y},\vec{y})\}$, and nonhomogeneous load vector $\{F\}$, which contains forcing terms independent of the generalized coordinates, are assembled similarly. This assembly results in the following set of nonlinear, coupled, ordinary differential equations which, for the case of forward flight, have periodic coefficients:

$$[M(\vec{y},\vec{y})]\{\ddot{y}\} + [C(\vec{y},\vec{y})]\{\dot{y}\} + [K(\vec{y},\vec{y})]\{y\} + \{A(\vec{y},\vec{y})\} + \{F\} = 0 \tag{3.4}$$

3.2 SOLUTION METHOD FOR HOVER

The solution method for the case of hover is similar to that of Ref. 8 but has been modified so that the aeroelastic response and the rotor trim condition are calculated simultaneously. For hover the nonlinear equations of motion have constant coefficients. The generalized coordinate vector $\{y\}$ is written as the sum of a constant vector $\{y_0\}$ and a perturbation vector $\{\Delta y(t)\}$:

$$\{y\} = \{y_0\} + \{\Delta y(t)\} \tag{3.5}$$

Substituting Eqn. 3.5 into Eqn. 3.4 results in a system of nonlinear algebraic equations:

$$[K(\vec{y}_0, \vec{0})]\{y_0\} + \{A(\vec{y}_0, \vec{0})\} + \{F\} = \vec{0} \tag{3.6}$$

and a system of small perturbation linear ordinary differential equations:

$$[M(\vec{y}_0, \vec{0})]\{\Delta\ddot{y}(t)\} + [\bar{C}(\vec{y}_0, \vec{0})]\{\Delta\dot{y}(t)\} + [\bar{K}(\vec{y}_0, \vec{0})]\{\Delta y(t)\} = \vec{0} \tag{3.7}$$

where:

$$[\bar{C}(\vec{y}_0, \vec{0})] = [C(\vec{y}_0, \vec{0})] + \left[\frac{\partial\{A\}}{\partial\{\dot{y}\}}\right]_{\vec{y} = \vec{y}_0, \vec{\dot{y}} = \vec{0}} \tag{3.8}$$

$$[\bar{K}(\vec{y}_0, \vec{0})] = [K(\vec{y}_0, \vec{0})] + \sum_{i=1}^{m} y_{0i}\left[\frac{\partial[K(\vec{y}, \vec{\dot{y}})]}{\partial y_i}\right]_{\vec{y} = \vec{y}_0, \vec{\dot{y}} = \vec{0}}$$

$$+ \left[\frac{\partial\{A\}}{\partial\{y\}}\right]_{\vec{y} = \vec{y}_0, \vec{\dot{y}} = \vec{0}} \tag{3.9}$$

Since the aerodynamic load vector $\{A(\vec{y}, \vec{\dot{y}})\}$ is calculated numerically, the aerodynamic stiffness and damping matrices $\left[\frac{\partial\{A\}}{\partial\{y\}}\right]$ and $\left[\frac{\partial\{A\}}{\partial\{\dot{y}\}}\right]$ must be computed using a numerical finite difference approximation[8].

In this study an additional equation is appended to Eqn. 3.6 requiring that the rotor be trimmed in the collective so that the rotor thrust equals the given helicopter weight. The modified equation becomes:

$$[K'(\vec{y}_0', \vec{0})]\{y_0'\} + \{A'(\vec{y}_0', \vec{0})\} + \{F'\} = 0 \tag{3.10}$$

where:

$$\{y'_0\} = \begin{Bmatrix} \vec{y}_0 \\ \theta_0 \end{Bmatrix} \tag{3.11}$$

$$[K'(\vec{y}_0', \vec{0})] = \begin{bmatrix} K(\vec{y}_0, \vec{0}) \\ 0 \end{bmatrix} \tag{3.12}$$

$$\{A'(\vec{y}_0, \vec{0})\} = \begin{Bmatrix} A(\vec{y}_0', \vec{0}) \\ C_T(\vec{y}_0, \vec{0}) \end{Bmatrix} \tag{3.13}$$

$$\{F'\} = \begin{Bmatrix} F \\ -C_W \end{Bmatrix} \tag{3.14}$$

Equation 3.10 is solved for $\{y'_0\}$, the static nonlinear blade equilibrium position, using a Newton-Raphson iterative procedure. The linearized stability is determined by solving the standard eigenvalue problem defined by the first-order, state variable form of Eqn. 3.7:

$$\{\Delta\dot{y}_1\} = \begin{bmatrix} [0] & [I] \\ -[M(\vec{y}_0, \vec{0})]^{-1}[\bar{C}(\vec{y}_0, \vec{0})] & -[M(\vec{y}_0, \vec{0})]^{-1}[\bar{K}(\vec{y}_0, \vec{0})] \end{bmatrix} \{\Delta y_1\}$$

$$= [S(\vec{y}_0, \vec{0})]\{\Delta y_1\} \tag{3.15}$$

where:

$$\{\Delta y_1\} = \begin{Bmatrix} \Delta y(t) \\ \Delta\dot{y}(t) \end{Bmatrix} \tag{3.16}$$

Blade stability is determined by the eigenvalues of $[S(\vec{y}_0, \vec{0})]$. The eigenvalues occur in complex congugate pairs. For m modes used in the modal coordinate transformation:

$$\lambda_j = \zeta_j \pm i\omega_j \qquad j = 1,2,\ldots,m \tag{3.17}$$

The blade is stable if all $\zeta_j < 0$.

3.3 TRIM PROCEDURE

3.3.1 *Introduction*

A helicopter in straight and level flight, flying at a constant velocity, must satisfy force and moment equilibrium. Determining the control inputs necessary for this equilibrium condition is referred to as trim analysis. In this study two trim procedures are used. The first is a flap trim procedure where the blade flexibility included in the trim analysis is limited to the first flap mode and all other blade deformations are neglected. This trim procedure is used principally to compare with results of Ref. 8 which also used this procedure. The second trim procedure was developed specifically for this study and includes the blade flap, lag, and torsional flexibility in the trim analysis and thus enables one to have a much more general model for the blade. The results from both these trim procedures are used subsequently as trim inputs to the full aeroelastic model. The full model produces stability and response information on the blade motions, including higher modes and higher harmonics of the solution which were neglected in the trim procedure.

3.3.2 *Flap Trim*

The flap trim analysis used in this study was developed in Ref. 19 and it was used in generating all the results of Ref. 8. This flap trim is a propulsive trim procedure based on the following assumptions:

1. Blade flexibility is modeled with a linear flapping equation of motion for the first flap mode.
2. The blade can have a precone angle β_p, a constant offset between the elastic axis and aerodynamic center x_A, and built-in twist with linear spanwise variation θ_B.
3. Quasisteady aerodynamics including reverse flow are used. Stall and compressibility effects are neglected.
4. Rotor shaft dynamics are neglected. Tail rotor and rotor speed variation effects are neglected and so yawing moment equilibrium and lateral force equilibrium are not enforced.
5. Vertical force equilibrium, longitudinal inplane force equilibrium, rotor pitch and roll moment equilibrium, and an inflow equation are enforced by with appropriate settings of the collective pitch θ_0, cyclic pitch components θ_{1s} and θ_{1c}, the inflow ratio λ, and the rotor angle of attack α_R.

3.3.3 *Full Propulsive Trim*

3.3.3.1 Assumptions

A helicopter in free flight has six degrees of translational and rotational freedom. Consequently equilibrium is guaranteed if three force and three moment equilibrium equations are satisfied. In this trim procedure yawing moment equilibrium and lateral inplane force equilibrium are not enforced and consequently the tail rotor pitch setting and the main rotor shaft angle in the lateral plane are not considered as trim variables. The helicopter is assumed to be in straight, steady flight at constant speed. Dynamics of the rotor shaft are neglected. Details of the blade modeling are given after the next section.

3.3.3.2 Trim Variables and Equilibrium Equations

The five trim variables are the inflow ratio λ, collective pitch angle θ_0, cyclic sine component θ_{1s} , cyclic cosine component θ_{1c}, and the rotor angle of attack α_R.

The five trim equilibrium equations are:

1. The inflow equation. This is a momentum theory relationship between the inflow ratio λ, advance ratio μ, rotor angle of attack α_R, and thrust coefficient C_T.

$$\mathbf{FT}(1) = 0 = C_T + 2\sqrt{\mu^2 + \lambda^2}\,(\mu \tan \alpha_R - \lambda) \tag{3.18}$$

2. The rolling moment equation. Since the tail rotor and the rotor angle in the lateral plane are not modeled, the rotor rolling moment is just set to zero.

$$\mathbf{FT}(2) = 0 = \overline{M}_{rl} \tag{3.19}$$

3. The pitching moment equation. The rotor pitching moment is countered by moments due to fuselage drag and the weight of the helicopter. All moments are taken about the rotor hub. The drag of the fuselage is given by:

$$D = \tfrac{1}{2}\rho_A V^2 f$$

where f is a parasite drag area. In nondimensional form this is:

$$C_{Df} = \tfrac{1}{2}\mu^2 \frac{f}{A}$$

where A is the rotor area. Typically $\frac{f}{A} \simeq 0.1$. If the fuselage drag is assumed to act a nondimensional distance $\bar{h}$ from the rotor hub, then the drag causes a nose down moment of:

$$\overline{M}_{dr} = -\tfrac{1}{2}\mu^2 \frac{f}{A}\bar{h}\cos\alpha_R$$

The weight of the helicopter, also assumed to act a distance $\bar{h}$ below the hub, produces a nose up moment due to its horizantal offset from the hub by a distance $\bar{h}\sin\alpha_R$. The sum of these two moments and the rotor moment, as shown in Fig. 3.1, must be zero.

$$\mathbf{FT}(3) = 0 = \overline{M}_{pt} - \tfrac{1}{2}\mu^2 \frac{f}{A}\bar{h}\cos\alpha_R + \bar{h}C_W \sin\alpha_R \qquad (3.20)$$

4. The vertical force equation. The weight of the helicopter is in equilibrium with the components of the rotor thrust and rotor longitudinal inplane force vectors as shown in Fig. 3.1.

$$\mathbf{FT}(4) = 0 = C_T \cos\alpha_R + C_H \sin\alpha_R - C_W \qquad (3.21)$$

5. The longitudinal force equation. The drag of the fuselage is countered by components of the rotor thrust and rotor longitudinal inplane force vectors as shown in Fig. 3.1.

$$\mathbf{FT}(5) = 0 = C_T \sin\alpha_R - C_H \cos\alpha_R - \tfrac{1}{2}\mu^2 \frac{f}{A} \qquad (3.22)$$

3.3.3.3 Aeroelastic Model for Trim

The aeroelastic model used in the trim procedure is a simplified version of the model used in the actual aeroelastic model of this study. This simplified model retains all the geometric, stiffness, mass, and aerodynamic modeling capabilities of the main analysis however the number of modes used in the analysis is reduced to four and furthermore only the constant and first and second harmonics in the Fourier series representations of the generalized coordinates are retained. In addition the mode shapes are calculated using only two finite elements. This reduces the cost of a response calculation using quasilinearization by more than an order of magnitude but retains the accuracy of the constant and one per rev portions of the solution which are re-

quired for determining the trim state of the rotor. Harmonics of the solution beyond the second are not modeled and so this simplified model is not suitable for calculation of the vibratory loads.

3.3.3.4 Method for Determining the Trim State

In order to trim the rotor, values for the trim variables λ, θ_0, θ_{1s}, θ_{1c}, and α_R must be found such that the five trim equations are simultaneously satisfied. The problem then is to solve the set of nonlinear algebraic equations

$$\mathbf{FT}(\lambda, \theta_0, \theta_{1s}, \theta_{1c}, \alpha_R) = 0 \tag{3.23}$$

where **FT** is the vector of trim equations of length 5 each of the elements of which is implicitly dependent on the trim variables. Equation 3.23 is solved by a packaged IMSL procedure called ZSPOW using a modification of the Powell Hybrid Method. This involves calculating the residual values of the components of the vector **FT** due to an initial estimate of the response, and the Jacobian of the system at this point, then using this information to make subsequent moves toward a minimum of the residuals in the five trim equations.

The procedure ZSPOW calls an external subroutine written for this study which, given the five trim variables, calculates the residuals in the five trim equations. The computation of these five trim equations is described next.

1. ZSPOW provides a vector $\vec{T}$ containing the trim variables, either with one element incremented when calculating the Jacobian (i.e. the matrix of first derivatives of the vector **FT** with respect to the five trim vari-

ables), or with all five elements changed when moving to a new solution estimate.

2. The coupled mode shapes of the blade are dependent on the collective angle θ_0, so if this angle has changed, the subroutine recalculates the mode shapes.
3. The mode shapes and the trim settings are used to determine a converged response for the blade using quasilinearization.
4. The new response is used to calculate the constant portion of the rotor hub shears and moments as described in Ch. 5.
5. The shears and moments are used in the trim equations to determine the trim equation residuals for this trim condition.
6. The trim equation residuals are returned to the algebraic equation solver which attempts to drive them all to zero.

A flow chart showing this procedure is given in Fig. 3.2.

Typically the algebraic equation solver calculates six responses to determine the starting condition and the Jacobian of the system. Subsequently 5-10 additional iterations are needed to obtain a trim solution which is accurate within three significant figures in terms of each of the trim variables.

3.4 SOLUTION METHOD FOR FORWARD FLIGHT

3.4.1 *Quasilinearization*

The quasilinearization procedure presented in Ref. 8 is used to determine periodic response and stability in forward flight. The equations of motion are written in first order form:

$$\begin{aligned}\{\overset{*}{q}\} &= [L(\psi)]\{q\} + \left\{N\left(\{q\}, \{\overset{*}{q}\}; \psi\right)\right\} + \{Z(\psi)\} + \left\{A\left(\{q\},\{\overset{*}{q}\}; \psi\right)\right\} \\ &= \left\{F_{NL}\left(\{q\},\{\overset{*}{q}\}; \psi\right)\right\}\end{aligned} \tag{3.24}$$

The state vector $\{q(\psi)\}$ is defined by:

$$\{q(\psi)\} = \begin{Bmatrix} \{y(\psi)\} \\ \{\overset{*}{y}(\psi)\} \end{Bmatrix} \tag{3.25}$$

and is of length $n = 2m$ where m is the number of modes used in the modal coordinate transformation. The generalized coordinates $\{y(\psi)\}$ represent the time varying contributions of each of the n modes to the periodic motion solution. The matrix L contains the linear portions of the blade model, N contains the nonlinear terms and Z contains the nonhomogeneous terms. All aerodynamic contributions are contained in the vector A which is calculated numerically.

Quasilinearization is based on a first-order Taylor series expansion of Eqn. 3.24 about an approximate solution $\{q(\psi)\}^k$:

$$\{\overset{*}{q}\}^{k+1} = \{\overset{*}{q}\}^k + \left[\frac{\partial\{F_{NL}\}}{\partial\{q\}}\right]^k (\{q\}^{k+1} - \{q\}^k)$$

$$+\left[\frac{\partial\{F_{NL}\}}{\partial\{\overset{*}{q}\}}\right]^k(\{\overset{*}{q}\}^{k+1}-\{\overset{*}{q}\}^k) \tag{3.26}$$

where:

$$\left[\frac{\partial\{F_{NL}\}}{\partial\{q\}}\right]^k=[L(\psi)]+\left[\frac{\partial\{N\}}{\partial\{q\}}\right]^k+\left[\frac{\partial\{A\}}{\partial\{q\}}\right]^k \tag{3.27}$$

$$\left[\frac{\partial\{F_{NL}\}}{\partial\{\overset{*}{q}\}}\right]^k=\left[\frac{\partial\{N\}}{\partial\{\overset{*}{q}\}}\right]^k+\left[\frac{\partial\{A\}}{\partial\{\overset{*}{q}\}}\right]^k \tag{3.28}$$

Equation 3.26 can be written as:

$$\{\overset{*}{q}\}^{k+1}=[B(\psi)]^k\{q\}^{k+1}+\{f(\psi)\}^k \tag{3.29}$$

where:

$$[B(\psi)]^k=\left([I]-\left[\frac{\partial\{N\}}{\partial\{\overset{*}{q}\}}\right]^k-\left[\frac{\partial\{A\}}{\partial\{\overset{*}{q}\}}\right]^k\right)^{-1}$$

$$\times\left(\left[\frac{\partial\{N\}}{\partial\{q\}}\right]^k+\left[\frac{\partial\{A\}}{\partial\{q\}}\right]^k+[L(\psi)]\right) \tag{3.30}$$

and:

$$\{f(\psi)]^k=\left([I]-\left[\frac{\partial\{N\}}{\partial\{\overset{*}{q}\}}\right]^k-\left[\frac{\partial\{A\}}{\partial\{\overset{*}{q}\}}\right]^k\right)^{-1}\Big\{\{Z\}+\{N\}^k+\{A\}^k$$

$$-\left(\left[\frac{\partial\{N\}}{\partial\{q\}}\right]^k+\left[\frac{\partial\{A\}}{\partial\{q\}}\right]^k\right)\{q\}^k-\left(\left[\frac{\partial\{N\}}{\partial\{\overset{*}{q}\}}\right]^k+\left[\frac{\partial\{A\}}{\partial\{\overset{*}{q}\}}\right]^k\right)\{\overset{*}{q}\}^k\Big\} \tag{3.31}$$

Equation 3.29 gives an iterative procedure, the sequence of solutions of which converge to the solution of Eqn. 3.24. Again, since the aerodynamic load vector $\left\{A\left(\{q\},\{\dot{q}\};\psi\right)\right\}$ is calculated numerically, the derivatives $\left[\frac{\partial\{A\}}{\partial\{q\}}\right]^k$ and $\left[\frac{\partial\{A\}}{\partial\{\dot{q}\}}\right]^k$ must be computed using a numerical finite difference approximation[8].

The response solution determined by this quasilinearization procedure is stored in the form of a constant and five sine and five cosine Fourier coefficients for each of the six generalized coordinates in the vector $\{y\}$. Wherever in the program values of the components of $\{y\}$ or $\{q\}$ are needed, these are calculated for the given azimuth ψ from this Fourier series.

In order to solve Eqn. 3.29, the state transition matrix $[\Phi(2\pi)]^k$ of the homogeneous system:

$$\{\dot{q}\}^{k+1} = [B(\psi)]^k\{q\}^{k+1} \tag{3.32}$$

at the end of one period is needed. The matrix $[\Phi(2\pi)]^k$ is computed using a single pass version[8] of the n-pass algorithm[51] in which the columns of $[\Phi(2\pi)]^k$ are obtained by solving Eqn. 3.32 n times, with initial condition vectors $\{q(0)\}^{k+1}$ $k = 1,2,\ldots,n$, which have all their elements equal to zero, except for the i-th, which is equal to one.

The initial vector $\{q(0)\}^{k+1}$ for Eqn. 3.29 is determined by requiring that the solution be periodic with period 2π. The vector $\{q(0)\}^{k+1}$ is shown[8] to be the solution of the linear algebraic system:

$$([I] - [\Phi(2\pi)]^k)\{q(0)\}^{k+1} = \{\bar{q}(2\pi)\}^k \tag{3.33}$$

where [I] is the identity matrix and $\{\bar{q}(2\pi)\}^k$ is the solution vector of Eqn. 3.29 integrated from $\psi = 0$ to $\psi = 2\pi$ with initial conditions $\{q(0)\}^k = \{0\}$.

System stability, linearized about the time dependent equilibrium position $\{q(\psi)\}^k$, is determined from Floquet theory[19]. The stability of the system is governed by the characteristic exponents obtained from the transition matrix $[\Phi(2\pi)]^k$. For the characteristic exponents

$$\lambda_{cj} = \zeta_{cj} \pm i\omega_{cj} \quad j = 1,2,\ldots,m \tag{3.34}$$

the linearized system is stable if all $\zeta_{cj} < 0$.

3.4.2 *Convergence*

A convergence criterion must be established to determine when the response solution from one iteration of quasilinearization is sufficiently close to the solution obtained in the previous iteration so that the procedure can be terminated. The response solution at the end of an iteration is saved in the form of a Fourier series for each of the six generalized coordinates in the vector $\{y\}$. The magnitude of the harmonic, i.e. the square root of the sum of the squares of the sine and cosine conponents of that harmonic, can be calculated for each harmonic. A 6×6 matrix, ${}^1M$ can then be constructed having as its six columns the magnitudes of the constant portion and first five harmonics for each of the six generalized coordinates.

In Ref. 8 a convergence criterion is used which is based on a sum of the absolute values of all the harmonics. From the response matrices ${}^1M$ and ${}^2M$

obtained for two consecutive response iterations, the following sums are calculated:

$$S_1 = \sum_{i=1}^{6} \sum_{j=1}^{6} |\,{}^1M_{ij}|\ ; \qquad S_2 = \sum_{i=1}^{6} \sum_{j=1}^{6} |\,{}^2M_{ij}| \tag{3.35}$$

If S_2 is not zero, convergence is assumed to have occured when:

$$\left| \frac{S_2 - S_1}{S_2} \right| * 100 < DELTA \tag{3.36}$$

If S_2 is equal to zero, convergence is assumed to have occured when:

$$|S_2 - S_1| * 100 < DELTA \tag{3.37}$$

In Ref. 8 the convergence control error parameter *DELTA* was set to 0.5. This required that the change in the sum of the absolute value of the harmonics from one iteration to the next be less than ½%.

The higher harmonics in an equilibrium solution have much smaller magnitudes than the constant and lower harmonics. Therefore the convergence criterion given above weighs more heavily the importance of the lower harmonics. When convergence has been achieved by this criterion, there can in fact still be large differences in higher harmonics of the solution. Another problem with this criterion is that occasionally, purely by chance, the sum of the harmonics from one iteration can be very near to that obtained from the previous iteration, without true convergence being achieved. This can lead to erroneous values for higher frequency phenomena such as vibratory hub shears

and moments. Results illustrating these problems and their solution are described in Ch. 7.

In this study a more stringent convergence criterion was developed based on a norm of the absolute differences in harmonics between two successive iterations. The matrices ${}^1M$ and ${}^2M$ are calculated as before and a norm is defined as:

$$NORM = \left[\sum_{i=1}^{6} \sum_{i=j}^{6} ({}^2M_{ij} - {}^1M_{ij})^2 \right]^{1/2} \tag{3.38}$$

This norm moves smoothly to its optimal value and has the additional advantage that it cannot produce a small number by chance, but only when two solutions are actually close in each harmonic. Convergence has occurred when $NORM < N_c$, where N_c can be varied to give different levels of accuracy in the harmonics.

It is not sufficient just to have a valid convergence criterion if progress is not being made toward convergence. If sufficiently tight error bounds are not used to solve the differential equation in quasilinearization, the higher harmonics of the solution will not converge and will instead vary from one iteration to the next in an apparently random fashion. If a loose convergence criterion is being used this can create the appearance of a spurious converged solution.

In this study, tighter local error bounds were used than in Ref. 8 and in addition bounds were always tightened systematically as the iterative process

continued. This led to more consistent values for the hub shears and moments used in the study.

Chapter IV

INCORPORATION OF UNSTEADY AERODYNAMICS IN EQUATIONS OF MOTION

4.1 EQUATIONS OF MOTION

In this study finite-state arbitrary-motion aerodynamics are incorporated in the coupled flap-lag-torsional equations of motion which are presented in Ref. 57 and are also given in this section for the sake of completeness. The geometry of the problem is shown in Figs. 2.2, 2.3, and 2.4. The assumptions used in deriving these equations are concisely summarized below.

The blade, in its undeformed state, is straight and has no angle of sweep or droop and no torque offset. The blade is cantilevered or hinged at the hub and has a blade root offset of e_1 from the axis of rotation. The feathering axis, which coincides with the blade elastic axis, is preconed by an angle β_p which is assumed to be small. The blade has an angle of built in twist of $\theta_b(\bar{x})$ which is assumed to occur about the undeformed elastic axis. Collective, cyclic, and higher harmonic pitch controls also contribute to the total geometric pitch angle which is given by:

$$\theta_G(\psi) = \theta_0 + \theta_{1c}\cos\psi + \theta_{1s}\sin\psi + \theta_{HHC}(\psi) + \theta_b(\bar{x}) \tag{4.1}$$

The cross section of the blade is symmetrical with respect to its major principal axis and the tension center and the elastic center are coincident. The

cross sectional center of gravity, aerodynamic center, and elastic axis need not be coincident, and values of these parameters can change over the blade span.

The blade is made of a homogeneous, isotropic, linearly elastic material. The Euler-Bernoulli assumption, that cross sections remain plane and normal to the deformed elastic axis during deformation, is made. This neglects the effects of shear deformation. The blade can bend in two mutually perpendicular directions. Elastic torsional deformations occur about the deformed elastic axis while additional deformations due to the flexibility of the control system occur about the feathering axis.

The blade is assumed to have moderate deflections, which implies small strains and finite rotations or slopes. The elastic rotations are assumed to be of the order ε where $\varepsilon \leq 0.20$. Terms containing the squares of the slopes are neglected when compared to terms of order one, i.e.

$$O(1) + O(\varepsilon^2) \cong O(1) \tag{4.2}$$

Structural damping forces are assumed to be of a viscous type. This is a reasonable assumption since modern rotor hubs are equipped with elastomeric dampers. No coupling exists between the blade dynamics and a fuselage. The rotor is rotating at a constant angular speed Ω and the helicopter is in steady trimmed level flight.

The final nonlinear partial differential equations of motion, including inertia loads but with aerodynamic loads left in symbolic form, are given by Eqns. 53, 54, 55, and 56 of Ref. 57. These, with several typographical corrections, are given below:

Axial Equation

$$T_{,x}+\tilde{p}_{XI}=0 \tag{4.3}$$

Lag Equation

$$[E(I_2\cos^2\theta_G+I_3\sin^2\theta_G)v_{,xx}+E(I_2-I_3)\sin\theta_G\cos\theta_G(w_{,xx}-2v_{,xx}\phi)$$

$$+E(I_2-I_3)\phi w_{,xx}cos2\theta_G]_{,xx}+(GJ\phi_{,x}w_{,xx})_{,x}-(v_{,x}T)_{,x}$$

$$+[2\Omega^2\overset{*}{\theta}_G(I_{m2}-I_{m3})\sin\theta_G\cos\theta_G]_{,x}-[m\Omega^2x_I(x_0+e_1)\cos\theta_G]_{,x}$$

$$+m\ddot{v}+2m\Omega\dot{u}-2m\Omega\beta_p\dot{w}-mx_I\Omega^2\overset{**}{\theta}_G\sin\theta_G-m\Omega^2v-m\Omega^2x_I\cos\theta_G$$

$$+q_{SL}\dot{v}-\tilde{p}_{YA}=0 \tag{4.4}$$

Flap Equation

$$[E(I_2-I_3)\sin\theta_G\cos\theta_G(v_{,xx}+2\phi w_{,xx})+E(I_2-I_3)\phi v_{,xx}cos2\theta_G$$

$$+E(I_2\sin^2\theta_G+I_3\cos^2\theta_G)w_{,xx}]_{,xx}-(GJ\phi_{,x}v_{,xx})_{,x}-(w_{,x}T)_{,x}$$

$$-[mx_I\Omega^2(x_0+e_1)\sin\theta_G]_{,x}+[2\Omega^2\overset{*}{\theta}_G(I_{m2}\sin^2\theta_G+I_{m3}\cos^2\theta_G)]_{,x}$$

$$+mx_I\Omega^2\overset{**}{\theta}_G\cos\theta_G+m\dot{w}+2m\Omega\beta_p\dot{v}+m\Omega^2\beta_p(x_0+e_1)$$

$$+q_{SF}\dot{w}-\tilde{p}_{ZA}=0 \tag{4.5}$$

Torsion Equation

$$[GJ(\phi_{,x} + v_{,xx}w_{,x})]_{,x} + E(I_2 - I_3)[\sin\theta_G \cos\theta_G(v_{,xx}^2 - w_{,xx}^2)$$

$$- v_{,xx}w_{,xx}\cos 2\theta_G] - q_{ST}\Omega\dot{\phi} - \Omega^2\{(I_{m2} + I_{m3})(\ddot{\theta} + \ddot{\phi})$$

$$+ mx_I \cos\theta_G[w_{,x}(x_0 + e_1) - (x_0 + e_1)v_{,x}\phi - \phi\ddot{v} + v\phi + \ddot{w}$$

$$+ \beta_p(x_0 + e_1) + 2\dot{v}(w_{,x} + \beta_p)] + mx_I \sin\theta_G[-v_{,x}(x_0 + e_1) - \ddot{v} + v]$$

$$+ I_{m2}[(1 + 2\dot{v}_{,x})\sin\theta_G \cos\theta_G + (-\beta_p v_{,x} + 2\dot{v}_{,x}\phi + \phi + w_{,x}\ddot{v}_{,x})\cos^2\theta_G$$

$$+ (2\dot{w}_{,x} - \phi)\sin^2\theta_G] + I_{m3}[-(1 + 2v_{,x})\sin\theta_G \cos\theta_G + \phi \sin^2\theta_G$$

$$+ (2\dot{v}_{,x}\dot{w}_{,x} + \ddot{v}_{,x}w_{,x} + 2\dot{w}_{,x} - 2\phi\dot{v}_{,x} - \phi + \beta_p v_{,x})\cos^2\theta_G]\} + \tilde{q}_{XA} = 0 \qquad (4.6)$$

4.2 DERIVATION OF UNSTEADY AERODYNAMIC LOADS

4.2.1 *Introduction*

The finite-state arbitrary-motion aerodynamics used in this study were developed originally in Ref. 13. In that work a generalized version of Greenberg's unsteady aerodynamic theory[24] was developed for the unsteady lift and moment on an airfoil undergoing arbitrary pitch and plunge motion about a steady pitch angle in the presence of time-varing oncoming velocity and variable inflow. Non-circulatory lift and moment were determined from the unsteady linearized Bernoulli's equation for the pressure on the surface of

the airfoil. A circulatory flow is calculated to enforce the Kutta condition at the trailing edge. After enforcing the Kutta condition, the circulatory lift is calculated in the Laplace domain.

A generalized Theodorsen lift deficiency function is found which acts as a Laplace domain operator between the ¾ chord downwash velocity and the circulatory loads divided by the time-varing oncoming velocity. A second order rational approximation for the generalized Theodorsen lift deficiency function is used to obtain a finite-state time-domain representation of the circulatory loads. The time-domain circulatory loads are finally expressed in terms of the airfoil degrees of freedom and two additional state variables denoted augmented states. The two state variables are governed by a system of ordinary differential equations driven by the ¾ chord downwash velocity.

4.2.2 *General Arbitrary-Motion Lift and Moment Expressions*

From Ref. 12, the general noncirculatory and circulatory arbitrary-motion airloads on an airfoil, such as that shown in Fig. 4.1, are given by:

$$L_{nc}(t) = \frac{1}{2}\rho_A a_t(\bar{b}R)^2\{\Delta\ddot{h}(t) + U_T(t)\Delta\dot{\alpha}(t) + \dot{U}_T(t)[\alpha_0 + \Delta\alpha(t)]$$

$$- \dot{U}_p(t) - (\bar{a}\bar{b}R)\Delta\ddot{\alpha}(t)\} \tag{4.7}$$

$$M_{nc}(t) = \underline{\frac{1}{2}\rho_A a_t(\bar{b}R)^2 U_T(t)Q(t)} + \frac{1}{2}\rho_A a_t(\bar{b}R)^3\{(\bar{a} - \tfrac{1}{2})U_T\Delta\dot{\alpha}(t)$$

$$+ \bar{a}[\Delta\ddot{h}(t) - \dot{U}_p(t)] + \bar{a}\dot{U}_T(t)[\alpha_0 + \Delta\alpha(t)] - \bar{b}R(\tfrac{1}{8} + \bar{a}^2)\Delta\ddot{\alpha}(t)\} \tag{4.8}$$

$$L_c(t) = \rho_A a_t(\bar{b}R)U_T(t)[0.006825(\frac{U_{T0}}{\bar{b}R})^2 X_1(t) + 0.10805(\frac{U_{T0}}{\bar{b}R})X_2(t)]$$

$$+ \frac{1}{2}\rho_A a_t(\bar{b}R)U_T(t)Q(t) \tag{4.9}$$

$$M_c(t) = \bar{b}R(\bar{a} + \tfrac{1}{2})L_c(t) - \underline{\frac{1}{2}\rho_A a_t(\bar{b}R)^2 U_T(t)Q(t)} \tag{4.10}$$

where the two underlined terms cancel each other and U_{T0} is the constant portion of U_T. From Fig. 4.1 it can be seen that the ¾ chord downwash velocity Q(t) will have contributions due to oncoming velocity $U_T(t)$, vertical velocity $\Delta\dot{h}(t) - U_p(t)$, and angular rotation $\Delta\dot{\alpha}(t)$:

$$Q(t) = U_T(t)[\alpha_0 + \Delta\alpha(t)] + [\Delta\dot{h}(t) - U_p(t)] + \bar{b}R(\tfrac{1}{2} - \bar{a})\Delta\dot{\alpha}(t) \tag{4.11}$$

The augmented states X_1 and X_2 are governed by a first order differential equation:

$$\begin{Bmatrix} \dot{X}_1(t) \\ \dot{X}_2(t) \end{Bmatrix} = \begin{bmatrix} 0 & 1 \\ -0.01365(\frac{U_{T0}}{\bar{b}R})^2 & -0.3455(\frac{U_{T0}}{\bar{b}R}) \end{bmatrix} \begin{Bmatrix} X_1(t) \\ X_2(t) \end{Bmatrix} + \begin{Bmatrix} 0 \\ Q(t) \end{Bmatrix} \tag{4.12}$$

4.2.3 *Lift and Moment in Terms of Local Blade Velocities*

To apply Eqns. 4.7 through 4.10 to the present problem, it is convenient to consider, as was done in Ref. 57, a system of unit vectors $\hat{e}''_x$, $\hat{e}''_y$, and $\hat{e}''_z$, where the double prime system has been rotated by an angle of $-\phi\hat{e}'_x$ from the deformed blade coordinate system. The transformation between the unit vec-

tors is given by Eqn. 2.6. From this transformation the velocities in the two systems are related by:

$$U''_y = U'_y \cos\phi - U'_z \sin\phi$$

$$U''_z = U'_y \sin\phi + U'_z \cos\phi \tag{4.13}$$

The velocities used in this derivation will be velocities of the elastic axis, as were used in Ref. 12, rather than velocities relative to the elastic axis, as were used in Ref. 57. With this convention, the following relations can be identified:

$$U_T = U''_y\,, \quad \alpha_0 + \Delta\alpha = \theta_G + \phi\,, \quad U_p - \Delta\dot{h} = U''_z \tag{4.14}$$

By substituting the above velocity terms in Eqns. 4.7 through 4.10 and using the following notation:

$$\frac{\partial}{\partial t} = \Omega\frac{\partial}{\partial\psi}\,, \quad \bar{x}_A = \frac{x_A}{\bar{b}R}\,, \quad \bar{a} = (\bar{x}_A - \tfrac{1}{2})\,, \quad \bar{R} = \frac{R}{\ell}\,,$$

$$\bar{U}_y = \frac{U_y}{\Omega\ell}\,, \quad \bar{U}_z = \frac{U_z}{\Omega\ell}\,, \quad \bar{X}_1 = \frac{\Omega}{\ell}X_1\,, \quad \bar{X}_2 = \frac{X_2}{\ell}\,,$$

$$\bar{L}_{nc} = \frac{L_{nc}}{a_i\rho_A(\bar{b}R)(\Omega\ell)^2}\,, \qquad \bar{M}_{nc} = \frac{M_{nc}}{a_i\rho_A(\bar{b}R)^2(\Omega\ell)^2}$$

$$\bar{L}_c = \frac{L_c}{a_i\rho_A(\bar{b}R)(\Omega\ell)^2}\,, \qquad \bar{M}_c = \frac{M_c}{a_i\rho_A(\bar{b}R)^2(\Omega\ell)^2} \tag{4.15}$$

the noncirculatory lift and moment become:

$$\bar{L}_{nc} = \frac{\overline{bR}}{2}\{\bar{U}''_y(\overset{*}{\theta}_G + \overset{*}{\phi}) - \overset{*}{\bar{U}}''_z - \overline{bR}(\bar{x}_A - \tfrac{1}{2})(\overset{**}{\theta}_G + \overset{**}{\phi}) + \overset{*}{\bar{U}}''_y(\theta_G + \phi)\} \tag{4.16}$$

$$\overline{M}_{nc} = \frac{\overline{bR}}{2}\{(\overline{x}_A - 1)\overline{U}''_y(\dot{\theta}_G + \dot{\phi}) - (\overline{x}_A - \tfrac{1}{2})\dot{\overline{U}}''_z + (\overline{x}_A - \tfrac{1}{2})\dot{\overline{U}}''_y(\theta_G + \phi)$$

$$- \overline{bR}(3/8 + \overline{x}_A^2 - \overline{x}_A)(\ddot{\theta}_G + \ddot{\phi})\} \tag{4.17}$$

and the ¾ chord downwash velocity becomes:

$$\overline{Q}(t) = \overline{U}''_y(\theta_G + \phi) - \overline{U}''_z + \overline{bR}(1 - \overline{x}_A)(\dot{\theta}_G + \dot{\phi}) \tag{4.18}$$

The circulatory lift and moment can be expressed as:

$$\overline{L}_c = \overline{U}''_y[0.006825(\frac{\overline{U}''_{y0}}{\overline{bR}})^2\overline{X}_1(\psi) + 0.10805(\frac{\overline{U}''_{y0}}{\overline{bR}})\overline{X}_2(\psi)] + \tfrac{1}{2}\overline{U}''_y\overline{Q} \tag{4.19}$$

$$\overline{M}_c = \overline{x}_A\overline{L}_c \tag{4.20}$$

where the nondimensional augmented states are now governed by:

$$\begin{Bmatrix} \dot{\overline{X}}_1 \\ \dot{\overline{X}}_2 \end{Bmatrix} = \begin{bmatrix} 0 & 1 \\ -0.01365(\frac{\overline{U}''_{y0}}{\overline{bR}})^2 & -0.3455(\frac{\overline{U}''_{y0}}{\overline{bR}}) \end{bmatrix} \begin{Bmatrix} \overline{X}_1 \\ \overline{X}_2 \end{Bmatrix} + \begin{Bmatrix} 0 \\ \overline{Q} \end{Bmatrix} \tag{4.21}$$

The circlatory lift can be written in a more convenient form if a quantity associated with unsteady effects is defined as:

$$H = [0.006825(\frac{\overline{U}''_{y0}}{\overline{bR}})^2\overline{X}_1(\psi) + 0.10805(\frac{\overline{U}''_{y0}}{\overline{bR}})\overline{X}_2(\psi)] \tag{4.22}$$

with this expression the circulatory lift becomes:

$$\overline{L}_c = \overline{U}''_y[H + \tfrac{1}{2}\overline{Q}] \tag{4.23}$$

4.2.4 *A Previous Formulation for the Circulatory Lift*

In Ref. 12, the circulatory lift and moment were written in a different form. As will be shown, this introduced a spurious instability at higher advance ratios which was a consequence of the particular details of the formulation, and was not an inherent property of the time domain aerodynamics. The circulatory lift and moment were expressed in terms of their quasisteady values multiplied by a time domain lift deficiency function, leading to the following expressions[12]:

$$\overline{L}_c = \frac{L_c}{\rho_A a_l(\bar{b}R)(\Omega\ell)^2} = [\tfrac{1}{2} + F]\overline{U}''_y\overline{Q} \tag{4.24}$$

$$\overline{M}_c = \frac{M_c}{\rho_A a_l(\bar{b}R)^2(\Omega\ell)^2} = \bar{x}_A[\tfrac{1}{2} + F]\overline{U}''_y\overline{Q} \tag{4.25}$$

Where the function F was a lift deficiency function in the time domain calculated using the ¾ chord downwash velocity corresponding to a typical blade section located at the three quarter span station of the blade. The quantity F was assumed to be a function of time only, and valid for the entire blade span:

$F(\overline{X}_{TS1}, \overline{X}_{TS2}, \overline{Q}_{TS}) =$

$$\frac{[0.006825(\frac{\overline{U}_{TS0}}{\overline{bR}})^2]\overline{X}_{TS1} + [0.10805(\frac{\overline{U}_{TS0}}{\overline{bR}})]\overline{X}_{TS2}}{\overline{Q}_{TS}} \tag{4.26}$$

where:

$\bar{x}_{TS}$ = nondimensional radial position of the typical section

$\overline{Q}_{TS} = \overline{Q}$ evaluated at $\bar{x}_0 = \bar{x}_{TS}$

$\overline{U}_{TS0} = \bar{x}_{TS} + \bar{e}$ = constant portion of $\overline{U}''_y$ evaluated at the typical section.

The differential equation governing the augmented states was given by:

$$\begin{Bmatrix} \overset{*}{\overline{X}}_{TS1} \\ \overset{*}{\overline{X}}_{TS2} \end{Bmatrix} = \begin{bmatrix} 0 & 1 \\ -0.01365(\frac{\overline{U}_{TS0}}{\overline{bR}})^2 & -0.3455(\frac{\overline{U}_{TS0}}{\overline{bR}}) \end{bmatrix} \begin{Bmatrix} \overline{X}_{TS1} \\ \overline{X}_{TS2} \end{Bmatrix} + \begin{Bmatrix} 0 \\ \overline{Q}_{TS} \end{Bmatrix} \quad (4.27)$$

The purpose of this formulation for the lift and moment was to simplify the solution of the aeroelastic response and stability problem by having the augmented states governing the unsteady aerodynamics be only functions of time. Thus the augmented states were independent of the spanwise locations of the cross sections of the blade. While the formulation was successful in accomplishing this objective, it also introduced a spurious singularity in the circulatory loads at high advance ratios.

For typical rotor blades, the ¾ chord downwash velocity $\overline{Q}$ can become zero on the advancing side of the rotor at sufficiently high advance ratios. From Eqn. 4.26 it can be seen that when $\overline{Q}_{TS}$ approaches zero the lift defficiency function F will approach infinity. If the circulatory lift is being calculated at the typical section, this produces no algebraic problem because from Eqn. 4.24, F is multiplied by $\overline{Q}$ which cancels with the denominator in Eqn. 4.26. If the circulatory lift is being calculated anywhere but at the typical section, $\overline{Q}$ and $\overline{Q}_{TS}$ do not cancel and as $\overline{Q}_{TS}$ approaches zero the circulatory lift approaches infinity.

This singularity in the circulatory lift leads to a spurious instability in the flap degree of freedom at an advance ratio of 0.45 in the flap-lag study presented in Ref. 12. When this version of the formulation of the unsteady loads is used, the spurious instability is also reproduced in the present flap-lag-torsional study. With the correct formulation of the circulatory loads, given in Eqns. 4.18 through 4.23, no such instability is found. A comparison of results due to the two formulations is given in Ch. 7.

4.2.5 *General Expressions for Aerodynamic Forces and Moments*

Forces and moments per unit span in the deformed blade coordinate system must now be found. The loads will have components due to circulatory lift, which is assumed to act perpendicular to the resultant velocity at the elastic axis, noncirculatory lift, which is assumed to act perpendicular to the blade chord, and an additional profile drag force which is parallel to the resultant velocity of the elastic axis. These orientations are shown in figure 4.2. Drag is calculated using:

$$D = \rho_A U^2 \bar{b} R C_{D0}, \quad \text{where: } U^2 = U_y''^2 + U_z''^2$$

$$\bar{D} = \frac{D}{\rho_A a_i \bar{b} R (\Omega \ell)^2} = \frac{C_{D0}}{a_i}(\bar{U}_y''^2 + \bar{U}_z''^2) \tag{4.28}$$

Using these assumptions concerning the direction of the lift and drag forces (per unit span), the loads per unit length in the double primed system become:

$$\overline{P}''_{za} = \overline{L}_c \cos[\tan^{-1}(\frac{\overline{U}''_z}{\overline{U}''_y})] + \overline{L}_{nc} \cos(\theta_G + \phi) \tag{4.29}$$

$$\overline{P}''_{ya} = -\overline{L}_c \sin[\tan^{-1}(\frac{\overline{U}''_z}{\overline{U}''_y})] - \overline{L}_{nc} \sin(\theta_G + \phi) - \overline{D} \tag{4.30}$$

or:

$$\overline{P}''_{za} = \overline{L}_c \frac{\overline{U}''_y}{\sqrt{\overline{U}''^2_y + \overline{U}''^2_z}} + \overline{L}_{nc} \cos(\theta_G + \phi) \tag{4.31}$$

$$\overline{P}''_{ya} = -\overline{L}_c \frac{\overline{U}''_z}{\sqrt{\overline{U}''^2_y + \overline{U}''^2_z}} - \overline{L}_{nc} \sin(\theta_G + \phi) - \frac{C_{D0}}{a_i}(\overline{U}''^2_y + \overline{U}''^2_z) \tag{4.32}$$

$$\overline{q}''_{xa} = \overline{M}_c + \overline{M}_{nc} \tag{4.33}$$

To obtain the forces and moments in the undeformed coned blade coordinate system the transformations given by Eqn. 2.7 must be used. Using these transformations the loads are:

$$\begin{aligned} \overline{P}_{xa} &= -v_{,x}\overline{P}''_{ya} - w_{,x}\overline{P}''_{za} & \overline{q}_{xa} &= \overline{q}''_{xa} \\ \overline{P}_{ya} &= \overline{P}''_{ya} - v_{,x}w_{,x}\overline{P}''_{za} & \overline{q}_{ya} &= v_{,x}\overline{q}''_{xa} \\ \overline{P}_{za} &= \overline{P}''_{za} & \overline{q}_{za} &= w_{,x}\overline{q}''_{xa} \end{aligned} \tag{4.34}$$

4.3 NUMERICAL IMPLEMENTATION OF AERODYNAMIC LOADS

4.3.1 *Introduction*

The values of the expressions for the aerodynamic loads given in Eqn. 4.34 must be calculated at various azimuthal positions and provided as input to the aeroelastic analysis.

In this study two approaches to the overall problem were implemented. In the first approach an algebraic manipulation program was used to derive algebraic expressions for the local velocities. Numerical values for the loads were then computed from these implicitly derived values for the local velocities. This approach avoids the neccessity of introducing assumptions which would allow one to neglect terms to simplify the expressions. In the second approach, assumptions were made for the orders of magnitude of all quantities in the expressions. Using these assumptions, higher order terms were systematically neglected leading to explicit expressions for the aerodynamic loads. This second approach is the same as was used in Refs. 57 and 8. It was implemented for comparison with the implicit formulation to verify that the two approaches gave similar results, which they did. These two approaches are described in the following sections. In both cases the basic approach to finding the local air velocities in terms of blade displacements and the other problem parameters follows the approach used in Ref. 57.

4.3.2 *Implicit Implementation*

To numerically calculate implicit values for the blade loads, values of the lift and moment expressions in Eqns. 4.16 through 4.23 are determined and then these values are numerically substituted in Eqns. 4.31 through 4.33. Subsequently these results are then numerically substituted in Eqn. 4.34 to give the final implicit loads.

The lift and moment quantities in Eqns. 4.16 through 4.23 are in terms of local blade velocities in the double primed coordinate system. Expressions for these velocities in terms of blade slopes and displacements and other problem parameters must therefore be found. The local velocities are due to two components, $\mathbf{V}_{EA}$, the velocity of the elastic axis, and $\mathbf{V}_{A}$, the velocity of airflow due to inflow. The velocity of the elastic axis may be found from:

$$\mathbf{V}_{EA} = \dot{\mathbf{R}}_{EA} + \Omega \times \mathbf{R}_{EA} \tag{4.35}$$

where $\mathbf{R}_{EA}$ and Ω are given by:

$$\mathbf{R}_{EA} = e_1 \hat{i} + (x_0 + u)\hat{e}_x + v\hat{e}_y + w\hat{e}_z \tag{4.36}$$

$$\Omega = \Omega \hat{k} \tag{4.37}$$

Using the transformation of Eqn. 2.2, $\mathbf{R}_{EA}$ and $\dot{\mathbf{R}}_{EA}$ can be expressed in the $\hat{i}$, $\hat{j}$, $\hat{k}$ coordinate system as:

$$\mathbf{R}_{EA} = [e_1 + (x_0 + u)\cos\beta_p - w\sin\beta_p]\,\hat{i}$$

$$+v\hat{j} + [(x_0 + u)\sin\beta_p + w\cos\beta_p]\,\hat{k} \tag{4.38}$$

$$\dot{\mathbf{R}}_{EA} = [\dot{u}\cos\beta_p - \dot{w}\sin\beta_p]\,\hat{i} + \dot{v}\hat{j} + [\dot{u}\sin\beta_p + \dot{w}\cos\beta_p]\,\hat{k} \tag{4.39}$$

The velocity due to inflow is given by:

$$\mathbf{V}_A = \mu\Omega R\cos\psi\,\hat{i} - \mu\Omega R\sin\psi\,\hat{j} - \Omega R\lambda\,\hat{k} \tag{4.40}$$

With higher order terms included, the velocity expressions are as follows:

$$\mathbf{V}_{EA} = \Omega[(w_{,x}v - v_{,x}w)\sin\beta_p + \{v_{,x}(x_0 + u) - v\}\cos\beta_p + v_{,x}(e_1 + \overset{*}{v})$$

$$+ \overset{*}{u} + w_{,x}\overset{*}{w}]\hat{e}'_x + \Omega[(\phi v - w)\sin\beta_p + \{x_0 + u + v(w_{,x}\phi + v_{,x})\}\cos\beta_p$$

$$- \overset{*}{u}(w_{,x}\phi + v_{,x}) + \phi\overset{*}{w} + \overset{*}{v} + e_1]\hat{e}'_y + \Omega[\{v + w(\phi + v_{,x}w_{,x})\}\sin\beta_p$$

$$+ \{w_{,x}v - w_{,x}v_{,x}(x_0 + u) - \phi(v_{,x}v + u + x_0)\}\cos\beta_p$$

$$-w_{,x}v_{,x}(\overset{*}{v} - e_1) - w_{,x}\overset{*}{u} + \phi(v_{,x}\overset{*}{u} - \overset{*}{v} - e_1) + \overset{*}{w}]\hat{e}'_z \tag{4.41}$$

$$\mathbf{V}_A = \Omega R[-v_{,x}\mu\sin\psi + (\cos\beta_p - w_{,x}\sin\beta_p)\mu\cos\psi$$

$$-(\sin\beta_p + w_{,x}\cos\beta_p)\lambda]\hat{e}'_x + \Omega R[-\mu\sin\psi - \{\phi\sin\beta_p$$

$$+ (w_{,x}\phi + v_{,x})\cos\beta_p\}\mu\cos\psi + \{(w_{,x}\phi + v_{,x})\sin\beta_p - \phi\cos\beta_p\}\lambda]\hat{e}'_y$$

$$+ \Omega R[(w_{,x}v_{,x} + \phi)\mu\sin\psi + \{-\sin\beta_p + (\phi v_{,x} - w_{,x})\cos\beta_p\}\mu\cos\psi$$

$$+\{(w_{,x} - \phi v_{,x})\sin\beta_p - \cos\beta_p\}\lambda]\hat{e}'_z \tag{4.42}$$

From these velocities the total velocity of the elastic axis relative to the air can be found from:

$$\mathbf{U} = \mathbf{V}_{EA} - \mathbf{V}_A = U'_x\hat{e}'_x + U'_y\hat{e}'_y + U'_z\hat{e}'_z \tag{4.43}$$

The velocities in the single primed system are:

$$\begin{aligned}
\overline{U}'_z = &- [\overline{w}_{,x}\overline{v}_{,x} + \phi]\overline{R}\mu \sin\psi \\
&+ [\sin\beta_p + \cos\beta_p(\overline{w}_{,x} - \phi\overline{v}_{,x})]\overline{R}\mu\cos\psi \\
&+ [\sin\beta_p(-\overline{w}_{,x} + \phi\overline{v}_{,x}) + \cos\beta_p]\overline{R}\lambda \\
&+ \sin\beta_p(\overline{w}_{,x}\overline{v}_{,x}\overline{w} + \phi\overline{w} + \overline{v}) \\
&+ \cos\beta_p(-\overline{w}_{,x}\overline{v}_{,x}\overline{u} - \overline{w}_{,x}\overline{v}_{,x}\overline{x}_o + \overline{w}_{,x}\overline{v} - \phi\overline{v}_{,x}\overline{v} - \phi\overline{u} - \phi\overline{x}_0) \\
&- \overline{w}_{,x}\overline{v}_{,x}\overset{*}{\overline{v}} - \overline{w}_{,x}\overline{v}_{,x}\overline{e}_1 - \overline{w}_{,x}\overset{*}{\overline{u}} + \phi\overline{v}_{,x}\overset{*}{\overline{u}} - \phi\overset{*}{\overline{v}} - \phi\overline{e}_1 + \overset{*}{\overline{w}}
\end{aligned} \tag{4.44}$$

$$\begin{aligned}
\overline{U}'_y = &\ \overline{R}\mu\sin\psi + [\phi\sin\beta_p + \cos\beta_p(\overline{w}_{,x}\phi + \overline{v}_{,x})]\overline{R}\mu\cos\psi \\
&+ [-\sin\beta_p(\overline{w}_{,x}\phi + \overline{v}_{,x}) + \phi\cos\beta_p]\overline{R}\lambda \\
&+ \sin\beta_p(\phi\overline{v} - \overline{w}) + \cos\beta_p(\overline{w}_{,x}\phi\overline{v} + \overline{v}_{,x}\overline{v} + \overline{u} + \overline{x}_0) \\
&- \overline{w}_{,x}\phi\overset{*}{\overline{u}} + \phi\overset{*}{\overline{w}} - \overline{v}_{,x}\overset{*}{\overline{u}} + \overset{*}{\overline{v}} + \overline{e}_1
\end{aligned} \tag{4.45}$$

Since apparent mass terms are retained in the expressions for the loads, the derivatives of the velocities with respect to ψ are also needed. These are given by the following expressions:

$$\overset{*}{\bar{U}}{}'_z = [-\sin\beta_p + \cos\beta_p(-\bar{w}_{,x} + \phi\bar{v}_{,x}) - (\bar{w}_{,x}\overset{*}{\bar{v}}_{,x} + \bar{v}_{,x}\overset{*}{\bar{w}}_{,x} + \overset{*}{\phi})]\bar{R}\mu\sin\psi$$

$$+ [\cos\beta_p(-\phi\overset{*}{\bar{v}} - \bar{v}_{,x}\overset{*}{\phi} + \overset{*}{\bar{w}}_{,x}) - (\bar{w}_{,x}\bar{v}_{,x} + \phi)]\bar{R}\mu\cos\psi$$

$$+ [\sin\beta_p(\phi\overset{*}{\bar{v}} + \bar{v}_{,x}\overset{*}{\phi} - \overset{*}{\bar{w}}_{,x})]\bar{R}\lambda$$

$$+ \sin\beta_p(\bar{w}_{,x}\bar{v}_{,x}\overset{*}{\bar{w}} + \bar{w}_{,x}\overset{*}{\bar{v}}_{,x}\bar{w} + \phi\overset{*}{\bar{w}} + \bar{v}_{,x}\overset{*}{\bar{w}}_{,x}\bar{w} + \overset{*}{\phi}\bar{w} + \overset{*}{\bar{v}})$$

$$+ \cos\beta_p(-\bar{w}_{,x}\bar{v}_{,x}\overset{*}{\bar{u}} - \bar{w}_{,x}\overset{*}{\bar{v}}_{,x}\bar{u} - \bar{w}_{,x}\overset{*}{\bar{v}}_{,x}\bar{x}_0 + \bar{w}_{,x}\overset{*}{\bar{v}} - \phi\bar{v}_{,x}\overset{*}{\bar{v}}$$

$$- \phi\overset{*}{\bar{v}}_{,x}\bar{v} - \phi\overset{*}{\bar{u}} - \bar{v}_{,x}\overset{*}{\phi}\bar{v} - \bar{v}_{,x}\overset{*}{\bar{w}}_{,x}\bar{u} - \bar{v}_{,x}\overset{*}{\bar{w}}_{,x}\bar{x}_0 - \overset{*}{\phi}\bar{u} - \overset{*}{\phi}\bar{x}_0 + \overset{*}{\bar{w}}_{,x}\bar{v})$$

$$- \bar{w}_{,x}\bar{v}_{,x}\overset{**}{\bar{v}} - \bar{w}_{,x}\overset{**}{\bar{u}} - \bar{w}_{,x}\overset{*}{\bar{v}}_{,x}\overset{*}{\bar{v}} - \bar{w}_{,x}\overset{*}{\bar{v}}_{,x}\bar{e}_1 + \phi\bar{v}_{,x}\overset{**}{\bar{u}} - \phi\overset{**}{\bar{v}} + \phi\overset{*}{\bar{v}}_{,x}\overset{*}{\bar{u}}$$

$$+ \bar{v}_{,x}\overset{*}{\phi}\overset{*}{\bar{u}} - \bar{v}_{,x}\overset{*}{\bar{w}}_{,x}\overset{*}{\bar{v}} - \bar{v}_{,x}\overset{*}{\bar{w}}_{,x}\bar{e}_1 + \overset{**}{\bar{w}} - \overset{*}{\phi}\overset{*}{\bar{v}} - \overset{*}{\phi}\bar{e}_1 - \overset{*}{\bar{w}}_{,x}\overset{*}{\bar{u}} \tag{4.46}$$

$$\overset{*}{\bar{U}}{}'_y = [-\phi\sin\beta_p - \cos\beta_p(\bar{w}_{,x}\phi + \bar{v}_{,x})]\bar{R}\mu\sin\psi$$

$$+ [\overset{*}{\phi}\sin\beta_p + \cos\beta_p(\bar{w}_{,x}\overset{*}{\phi} + \phi\overset{*}{\bar{w}}_{,x} + \overset{*}{\bar{v}}_{,x}) + 1]\bar{R}\mu\cos\psi$$

$$+ [-\sin\beta_p(\bar{w}_{,x}\overset{*}{\phi} + \phi\overset{*}{\bar{w}}_{,x} + \overset{*}{\bar{v}}_{,x}) + \overset{*}{\phi}\cos\beta_p]\bar{R}\lambda$$

$$+ \sin\beta_p(\phi\overset{*}{\bar{v}} + \overset{*}{\phi}\bar{v} - \overset{*}{\bar{w}}) + \cos\beta_p(\bar{w}_{,x}\phi\overset{*}{\bar{v}} + \bar{w}_{,x}\overset{*}{\phi}\bar{v} + \phi\overset{*}{\bar{w}}_{,x}\bar{v} + \bar{v}_{,x}\overset{*}{\bar{v}} + \overset{*}{\bar{v}}_{,x}\bar{v} + \overset{*}{\bar{u}})$$

$$- \bar{w}_{,x}\phi\overset{**}{\bar{u}} - \bar{w}_{,x}\overset{*}{\phi}\overset{*}{\bar{u}} + \phi\overset{**}{\bar{w}} - \phi\overset{*}{\bar{w}}_{,x}\overset{*}{\bar{u}} - \bar{v}_{,x}\overset{**}{\bar{u}} + \overset{*}{\phi}\overset{*}{\bar{w}} + \overset{**}{\bar{v}} - \overset{*}{\bar{v}}_{,x}\overset{*}{\bar{u}} \tag{4.47}$$

Given the velocities in the single primed system, the velocities in the double primed system can be found by using Eqn. 4.13. By diferentiating Eqn. 4.13 the following expressions for the ψ derivatives of the velocities in the double primed coordinates are found.

$$\overset{*}{\overline{U}}{}''_y = -\overset{*}{\phi}\overline{U}'_y \sin\phi + \overset{*}{\overline{U}}{}'_y \cos\phi - \overset{*}{\phi}\overline{U}'_z \cos\phi - \overset{*}{\overline{U}}{}'_z \sin\phi \tag{4.48}$$

$$\overset{*}{\overline{U}}{}''_z = \overset{*}{\phi}\overline{U}'_y \cos\phi + \overset{*}{\overline{U}}{}'_y \sin\phi - \overset{*}{\phi}\overline{U}'_z \sin\phi + \overset{*}{\overline{U}}{}'_z \cos\phi \tag{4.49}$$

In actual implementation, the axial displacement terms u , $\dot{u}$, and $\ddot{u}$ are neglected in calculating the aerodynamic loads. This is because with the implicit nature of the aerodynamic formulation, there are no provisions for the calculation of axial displacements in the aerodynamic section of the program. In fact these are quite small terms which should have little effect on the aerodynamic loads.

4.3.3 *Explicit Implementation*

To determine explicit expressions for the aerodynamic loads, an ordering scheme is adopted by which higher order terms are systematically neglected. This ordering scheme is consistent with that used in deriving the equations of motion given in Eqns. 4.3 through 4.6 and include additional assumptions on the order of $\ddot{\theta}_G$ which lead to the retention of some terms which may be important when high frequency excitations such as HHC are present. Again, following Eqn. 4.2, terms having an order of magnitude comparable to the

square of the blade slopes, i.e. $O(\varepsilon^2)$, are neglected when compared to terms of order one.

The orders of magnitude assigned to various parameters in this study are given below:

$$O(\varepsilon^{-1/2}): \quad \ddot{\theta}_G$$

$$O(1): \quad \sin\psi\,, \quad \cos\psi\,, \quad \mu\,, \quad \bar{x}_0 = \frac{x_0}{\ell}\,, \quad \bar{R} = \frac{R}{\ell}\,, \quad \frac{\partial}{\partial \bar{x}_0} = (\ )_{,x}$$

$$O(1): \quad \frac{\partial}{\partial \psi} = \frac{1}{\Omega}\frac{\partial}{\partial t} \quad \text{(except when applied to } \theta_G\text{)}$$

$$O(\varepsilon^{1/2}): \quad \theta_G\,, \quad \sin\theta_G\,, \quad \dot{\theta}_G$$

$$O(\varepsilon): \quad \phi\,, \quad \beta_p\,, \quad \lambda\,, \quad \bar{x}_A = \frac{x_A}{\bar{b}R}\,, \quad \bar{b} = \frac{b}{R}\,, \quad \bar{e}_1 = \frac{e_1}{\ell}\,, \quad \bar{w}_{,x} = \frac{\partial \bar{w}}{\partial \bar{x}_0}\,,$$

$$\bar{v}_{,x} = \frac{\partial \bar{v}}{\partial \bar{x}_0}\,, \quad \bar{v} = \frac{v}{\ell}\,, \quad \bar{w} = \frac{w}{\ell}\,, \quad \frac{x_I}{\bar{b}R}\,, \quad \frac{k_{m2}}{\ell}\,, \quad \frac{k_{m3}}{\ell}$$

$$O(\varepsilon^{3/2}): \quad \frac{C_{DO}}{a_i}$$

$$O(\varepsilon^2): \quad \bar{u} = \frac{u}{\ell}\,, \quad \bar{x}_I = \frac{x_I}{\ell}$$

The main difference from Ref. 8 is in the magnitude assigned to $\ddot{\theta}_G$. In this study HHC inputs are included in θ_G as shown in Eqn. 4.1. Because HHC is

input at high frequencies, the angular accelerations due to it can be quite large and this is reflected in a larger assigned magnitude for $\ddot{\theta}_G$ than would be otherwise expected.

The forces and moments in the undeformed coned blade coordinate system are obtained by algebraically substituting the velocities given by Eqns. 4.44 through 4.47 in Eqn. 4.13 and substituting this result in the expressions for lift and moment given by Eqns. 4.16 through 4.23. Using the ordering scheme leads to the neglect of numerous higher order terms. With the use of a small angle assumption, Eqns. 4.29 through 4.33 reduce to:

$$\overline{P}''_{za} = \overline{L}_c + \overline{L}_{nc} \tag{4.50}$$

$$\overline{P}''_{ya} = -\,\overline{U}''_z(H + \frac{1}{2}\overline{Q}) - \overline{L}_{nc}(\theta_G + \phi) - \frac{C_{D0}}{a_i}(\overline{U}''_y)^2 \tag{4.51}$$

$$\overline{q}''_{xa} = \overline{M}_c + \overline{M}_{nc} \tag{4.52}$$

The simplified algebraic expressions for lift and moment are substituted in Eqns. 4.50 through 4.52. Subsequently these expressions are further algebraically substituted in the expressions for forces and moments in Eqn. 4.34. Carrying out the various algebraic manipulations and applying the ordering scheme produces the following final expressions for the forces and moments:

$$\overline{P}_{za} = H\{\dot{\overline{v}} + \overline{v}_{,x}F_3 + F_1\} + \frac{1}{2}\{F_1(F_1\theta_G + F_4\dot{\theta}_G - F_2)$$

$$- F_1\beta_p\overline{v} + (2F_1F_3\theta_G - F_2F_3)\overline{v}_{,x} - F_1F_3\overline{w}_{,x} + F_1^2\phi - F_1\overline{v}\,\overline{w}_{,x}$$

$$+ (F_1^2 - F_3^2)\bar{v}_{,x}\bar{w}_{,x} + 2F_1F_3\bar{v}_{,x}\phi + (2F_1\theta_G - F_2)\overset{*}{\bar{v}} - F_1\overset{*}{\bar{w}} + F_1F_4\overset{*}{\phi}$$

$$+2F_1\phi\overset{*}{\bar{v}} - F_3\bar{w}_{,x}\overset{*}{\bar{v}} - F_3\bar{v}_{,x}\overset{*}{\bar{w}} - \overset{*}{\bar{v}}\overset{*}{\bar{v}}\} + \frac{\overline{bR}}{2}\{\overset{*}{\theta}_G F_1 - \overset{**}{\theta}_G F_5$$

$$+ \beta_p F_6 + \theta_G F_3 + F_6\bar{w}_{,x} + F_3\phi - F_3\overset{*}{\bar{w}}_{,x} - \overset{**}{\bar{w}} + F_1\overset{*}{\phi}\} \tag{4.53}$$

$$\bar{P}_{ya} = - H\{F_2 + \overset{*}{\bar{w}} + \overset{*}{\bar{v}}\bar{v}_{,x}\bar{w}_{,x} + \bar{v}\bar{w}_{,x} + \bar{v}\beta_p + \bar{v}_{,x}^2\bar{w}_{,x}F_3 + \bar{w}_{,x}F_3\}$$

$$- \frac{1}{2}\{(F_1\theta_G + F_4\overset{*}{\theta}_G - F_2)F_2 + \beta_p(\theta_G F_1 - 2F_2)\bar{v} + \theta_G F_3 F_2\bar{v}_{,x}$$

$$+ F_3(F_1\theta_G + F_4\overset{*}{\theta}_G - 2F_2)\bar{w}_{,x} + F_1F_2\phi + (F_1\theta_G - 2F_2 - 2\beta_p F_3)\bar{v}\bar{w}_{,x}$$

$$+ (\theta_G F_3^2 + F_1F_2)\bar{v}_{,x}\bar{w}_{,x} - F_3^2\bar{w}_{,x}^2 + (F_1\beta_p\bar{v} + F_2F_3\bar{v}_{,x} + F_1F_3\bar{w}_{,x})\phi$$

$$+ (F_1\bar{v}_{,x} - 2\bar{v})F_3\bar{w}_{,x}^2 + (F_1\bar{v} + F_3^2\bar{v}_{,x})\bar{w}_{,x}\phi + F_2\theta_G\overset{*}{\bar{v}}$$

$$+ (F_1\theta_G + F_4\overset{*}{\theta}_G - 2F_2)\overset{*}{\bar{w}} + F_2F_4\overset{*}{\phi} + (F_3\theta_G\bar{w}_{,x} + F_2\phi)\overset{*}{\bar{v}}$$

$$+ (F_1\phi + F_3\theta_G\bar{v}_{,x} - 2\beta_p\bar{v} - 2F_3\bar{w}_{,x})\overset{*}{\bar{w}} + F_3F_4\bar{w}_{,x}\overset{*}{\phi} + F_3\phi\bar{w}_{,x}\overset{*}{\bar{v}}$$

$$+ (F_3\phi\bar{v}_{,x} + F_1\bar{v}_{,x}\bar{w}_{,x} - 2\bar{v}\bar{w}_{,x})\overset{*}{\bar{w}} + \theta_G\overset{*}{\bar{v}}\overset{*}{\bar{w}} - \overset{*}{\bar{w}}^2 + F_4\overset{*}{\bar{w}}\overset{*}{\phi} + \phi\overset{*}{\bar{v}}\overset{*}{\bar{w}}\}$$

$$- \frac{1}{2}\{\theta_G(F_1\overset{*}{\theta}_G - F_5\overset{**}{\theta}_G + F_3\theta_G) + \theta_G\beta_p F_6 + \theta_G(\overset{*}{\theta}_G F_3 - \theta_G F_6)\bar{v}_{,x}$$

$$+ \theta_G F_6\bar{w}_{,x} + (\overset{*}{\theta}_G F_1 - F_5\overset{**}{\theta}_G + 2F_3\theta_G + \beta_p F_6)\phi + F_6\phi\bar{w}_{,x}$$

$$+ F_3\phi^2 + \theta_G\overset{*}{\theta}_G\overset{*}{\bar{v}} + \theta_G^2 F_3\overset{*}{\bar{v}}_{,x} - F_3\theta_G\overset{*}{\bar{w}}_{,x} + \theta_G F_1\overset{*}{\phi} + F_1\phi\overset{*}{\phi}$$

$$- F_3\phi\overset{*}{\bar{w}}_{,x} - \theta_G\overset{**}{\bar{w}} + \theta_G^2\overset{**}{\bar{v}} - \phi\overset{**}{\bar{w}}\} - \frac{C_{D0}}{a_i}\{F_1^2 + 2F_1\overset{*}{\bar{v}} + 2F_1F_3\bar{v}_{,x}\} \tag{4.54}$$

$$\bar{q}_{xa} = H\bar{x}_A\{\overset{*}{\bar{v}} + \bar{v}_{,x}F_3 + F_1\} + \frac{\bar{x}_A}{2}\{F_1(F_1\theta_G + F_4\overset{*}{\theta}_G - F_2)$$

$$- F_1\beta_p\bar{v} + (2F_1F_3\theta_G - F_2F_3)\bar{v}_{,x} - F_1F_3\bar{w}_{,x} + F_1^2\phi - F_1\bar{v}\bar{w}_{,x}$$

$$+ (F_1^2 - F_3^2)\bar{v}_{,x}\bar{w}_{,x} + 2F_1F_3\bar{v}_{,x}\phi + (2F_1\theta_G - F_2)\overset{*}{\bar{v}} - F_1\overset{*}{\bar{w}} + F_1F_4\overset{*}{\phi}$$

$$+ 2F_1\phi\overset{*}{\bar{v}} - F_3\bar{w}_{,x}\overset{*}{\bar{v}} - F_3\bar{v}_{,x}\overset{*}{\bar{w}} - \overset{*}{\bar{v}}\overset{*}{\bar{w}}\} + \frac{1}{2}\{(F_3F_5\theta_G + F_5F_6\beta_p$$

$$- F_1F_4\overset{*}{\theta}_G - \overline{bR}F_7\overset{**}{\theta}_G) - (F_3F_4\overset{*}{\theta}_G + F_5F_6\theta_G)\bar{v}_{,x} + F_5F_6\bar{w}_{,x}$$

$$+ F_3F_5\phi + F_3F_5\bar{v}_{,x}\bar{w}_{,x} - F_5F_6\bar{v}_{,x}\phi - (F_4\overset{*}{\theta}_G + F_5\beta_p)\overset{*}{\bar{v}} - F_1F_4\overset{*}{\phi}$$

$$- (F_4\overset{*}{\phi} + F_5\bar{w}_{,x})\overset{*}{\bar{v}} - F_3F_4\bar{v}_{,x}\overset{*}{\phi} + (F_1F_5\bar{w}_{,x} + F_3F_5\phi + F_3F_5\theta_G)\overset{*}{\bar{v}}_{,x}$$

$$+ (F_1F_5\bar{v}_{,x} - F_3\bar{v}F_3F_5)\overset{*}{\bar{w}}_{,x} - F_5\overset{**}{\bar{w}} + F_5\theta_G\overset{**}{\bar{w}} - \overline{bR}F_7\overset{**}{\phi} + F_5\phi\overset{**}{\bar{v}}\} \tag{4.55}$$

where the quantities F_1 through F_7 are defined by:

$F_1 = \bar{e}_1 + \bar{x}_0 + \bar{R}\mu\sin\psi$

$F_2 = \lambda\bar{R} + \mu\bar{R}\beta_p\cos\psi$

$F_3 = \mu\bar{R}\cos\psi$

$F_4 = \overline{bR}(1 - \bar{x}_A)$

$F_5 = \overline{bR}(\bar{x}_A - 1/2)$

$F_6 = \bar{R}\mu\sin\psi$

$F_7 = \overline{bR}(3/8 + \bar{x}_A^2 - \bar{x}_A)$

4.3.4 *Solving Numerically for the Augmented States*

The differential equation governing the augmented states, Eqn. 4.21, can be rewritten as:

$$\begin{Bmatrix} \overset{*}{\overline{X}}_1 \\ \overset{*}{\overline{X}}_2 \end{Bmatrix} = \begin{bmatrix} 0 & 1 \\ A_{21} & A_{22} \end{bmatrix} \begin{Bmatrix} \overline{X}_1 \\ \overline{X}_2 \end{Bmatrix} + \begin{Bmatrix} 0 \\ \overline{Q} \end{Bmatrix} \tag{4.56}$$

where:

$$A_{21} = -\,0.01365\left(\frac{\overline{U}''_{y0}}{\overline{bR}}\right)^2 , \quad A_{22} = -\,0.3455\left(\frac{\overline{U}''_{y0}}{\overline{bR}}\right) \tag{4.57}$$

This equation is forced by the ¾ chord downwash velocity $\overline{Q}$. In quasilinearization a time history for $\overline{Q}$ from the previous iteration is known and this can be used to determine the augmented states for the current iteration.

A Fourier analysis may be applied to the time history of $\overline{Q}$ from the last iteration of quasilinearization, then $\overline{Q}$ may be expressed as:

$$\overline{Q} = \overline{Q}_0 + \sum_{n=1}^{NH} [\overline{Q}_{sn} \sin n\psi + \overline{Q}_{cn} \cos n\psi] \tag{4.58}$$

where NH is the number of harmonics retained in the Fourier analysis. The quantities $\overline{X}_1$ and $\overline{X}_2$ may then be solved for in terms of their Fourier coefficients.

$$\overline{X}_1 = \overline{X}_{10} + \sum_{n=1}^{NH} [\overline{X}_{1sn} \sin n\psi + \overline{X}_{1cn} \cos n\psi] \tag{4.59}$$

$$\overline{X}_2 = \overline{X}_{20} + \sum_{n=1}^{NH} [\overline{X}_{2sn} \sin n\psi + \overline{X}_{2cn} \cos n\psi] \tag{4.60}$$

Substituting Eqns. 4.58, 4.59, and 4.60 in Eqn. 4.56 and equating coefficients of sine and cosine leads to the following solution for the Fourier coefficients of the augmented states $\overline{X}_1$ and $\overline{X}_2$:

$$\overline{X}_{10} = \frac{-\overline{Q}_0}{A_{21}} \ , \qquad \overline{X}_{20} = 0$$

$$\overline{X}_{1sn} = \frac{-(A_{21} + n^2)\overline{Q}_{sn} - nA_{22}\overline{Q}_{cn}}{(A_{21} + n^2)^2 + n^2 A_{22}^2}$$

$$\overline{X}_{1cn} = \frac{nA_{22}\overline{Q}_{sn} - (A_{21} + n^2)\overline{Q}_{cn}}{(A_{21} + n^2)^2 + n^2 A_{22}^2}$$

$$\overline{X}_{2sn} = -n\overline{X}_{1cn} \ , \qquad \overline{X}_{2cn} = n\overline{X}_{1sn} \tag{4.61}$$

If Eqn. 4.57 is substituted in Eqn. 4.22, an expression for H in terms of A_{21} and A_{22} can be found and is given below:

$$H = -\frac{1}{2}A_{21}\overline{X}_1 - \frac{2162}{6910}A_{22}\overline{X}_2 \tag{4.62}$$

The quantity H is also assumed to have a Fourier series representation.

$$H = H_0 + \sum_{n=1}^{NH} [H_{sn} \sin n\psi + H_{cn} \cos n\psi] \tag{4.63}$$

If Eqns. 4.59, 4.60, and 4.61 are substituted in Eqn. 4.62 and this is set equal to Eqn. 4.63, the following Fourier coefficients for H are found.

$$H_0 = \frac{\overline{Q}_0}{2} \tag{4.64}$$

$$H_{cn} = [\frac{B_1}{B_3}]\overline{Q}_{sn} + [\frac{B_2}{B_3}]\overline{Q}_{cn} \tag{4.65}$$

$$H_{sn} = [\frac{B_2}{B_3}]\overline{Q}_{sn} + [\frac{-B_1}{B_3}]\overline{Q}_{cn} \tag{4.66}$$

where the following abreviations have been used:

$$B_1 = -1294A_{21}A_{22}n + 2162A_{22}n^3$$

$$B_2 = 3455A_{21}(A_{21} + n^2) + 2162A_{22}^2n^2$$

$$B_3 = 6910[(A_{21} + n^2)^2 + n^2A_{22}^2]$$

For a given point along the blade, the augmented states are driven by the time varying ¾ chord downwash at that point. To perform the Fourier analysis described above and solve for H every time the aerodynamic loads are required would use excessive amounts of computer time. However the Fourier coefficients of H are independent of the azimuth and thus have to be determined only once for each radial coordinate where the airloads are required. When implementing this procedure, the airloads are only solved for at a finite number of radial stations where the airloads are needed for use in Gaussian integration. Each time an airload at a given radius is needed, computer memory is searched to see if the Fourier coefficients for H at that radius have already been computed. If this data is available it is read from memory. If it

is not available it is calculated and stored for future use. Typically for a five element representation of the blade and eight point Gaussian integration this will involve the storing of forty sets of Fourier coefficients for H. When H is needed for a particular value of ψ, the Fourier coefficients from Eqns. 4.64 through 4.66 are substituted in Eqn. 4.63 to give the needed value of H at that azimuth.

Chapter V

CALCULATION OF HUB FORCES AND MOMENTS

5.1 INTRODUCTION

Hub forces and moments are calculated using a direct force integration technique. A blade response in the form of a Fourier series representation of the generalized coordinates is assumed to be known and the hub loads are calculated based on this. The procedure used consists of three loops, one over the blade azimuth, one over the four blades of the rotor, and one over the blade radius. A description of the sequence of calculations is provided below:

1. For a given blade azimuth, the local aerodynamic and inertia loads are calculated at a number of radial stations along the blade.
2. The forces and moments at the blade root due to the local loads are then calculated and are numerically integrated along the blade to give the root loads at a given azimuth.
3. The root blade loads due to the four blades are combined to give the total rotor hub loads for a given azimuth.
4. A Fourier analysis of the total rotor hub loads around the blade azimuth is carried out.

From the resultant Fourier series, characteristics of the rotor hub loads may be reconstructed. A flow chart showing this procedure is given in Fig. 5.1 and

a detailed mathematical treatment of these calculations is provided in this chapter.

Calculation of hub loads in this study differ from that in Ref. 8 principally in that aerodynamic loads have been calculated in an implicit manner and the blade modeling is more general. Implicit load calculations imply the retention of various higher order terms which were previously neglected, and the elimination of the small angle assumption. The current study allows the inclusion of HHC inputs in the computations of the hub loads and includes provisions for the modeling of a control system stiffness and articulated blades with or without spring restraints.

Details of the calculations are given in the following sections.

5.2 CALCULATION OF LOCAL LOADS

5.2.1 *Local Aerodynamic Loads*

Expressions for local aerodynamic forces and moments in the coned, undeformed coordinate system, as developed in Ch. 4, are used. These forces and moments are: $\overline{P}_{xa}$, $\overline{P}_{ya}$, $\overline{P}_{za}$, $\overline{q}_{xa}$, $\overline{q}_{ya}$, and $\overline{q}_{za}$.

5.2.2 *Local Inertia Loads*

Inertia loads per unit span of the blade are calculated using D'Alembert's principle and integrating over the cross section of the blade. Referring to the geometry of the blade shown in Figs. 2.3 through 2.4, these loads can be expressed as:

$$\overline{\mathbf{P}}_i = \overline{P}_{xi}\hat{e}_x + \overline{P}_{yi}\hat{e}_y + \overline{P}_{zi}\hat{e}_z = \frac{-1}{m_0\Omega^2\ell}\int_{A_x} \rho \mathbf{a} dA_x \tag{5.1}$$

$$\overline{\mathbf{q}}_i = \overline{q}_{xi}\hat{e}_x + \overline{q}_{yi}\hat{e}_y + \overline{q}_{zi}\hat{e}_z = \frac{-1}{m_0\Omega^2\ell^2}\int_{A_x} \rho \mathbf{R_p}\times\mathbf{a} dA_x \tag{5.2}$$

The acceleration of a point on the blade is given by:

$$\mathbf{a} = \ddot{\overline{\mathbf{R}}} + 2\Omega\times\dot{\mathbf{R}} + \Omega\times(\Omega\times\mathbf{R}) \tag{5.3}$$

where the position vector of a point in the blade cross section, relative to the axis of rotation is given by:

$$\mathbf{R} = e_1\hat{i} + (x_0 + u)\hat{e}_x + v\hat{e}_y + w\hat{e}_z + y_0\hat{e}'_y + z_0\hat{e}'_z \tag{5.4}$$

the rotor angular velocity vector is given by:

$$\Omega = \Omega\hat{k} \tag{5.5}$$

and the position vector of a point in the blade cross section relative to the elastic axis is given by:

$$\mathbf{R_p} = y_0\hat{e}'_y + z_0\hat{e}'_z \tag{5.6}$$

Using the coordinate transformations given in Eqns. 2.3 through 2.4, these vectors may be expressed in the coned undeformed coordinate system as:

$$\mathbf{R} = [(x_0 + u) + e_1 \cos\beta_p - y_0(v_{,x} + \phi w_{,x}) - z_0(w_{,x} - \phi v_{,x})]\hat{e}_x$$

$$+ [v + y_0 - z_0(\phi + w_{,x}v_{,x})]\hat{e}_y + [w - e_1 \sin\beta_p + y_0\phi + z_0]\hat{e}_z \tag{5.7}$$

$$\mathbf{R_p} = [-y_0(v_{,x} + \phi w_{,x}) - z_0(w_{,x} - \phi v_{,x})]\hat{e}_x$$

$$+ [y_0 - z_0(\phi + v_{,x}w_{,x})]\hat{e}_y + [y_0\phi + z_0]\hat{e}_z \tag{5.8}$$

$$\Omega = \Omega \sin\beta_p \hat{e}_x + \Omega \cos\beta_p \hat{e}_z \tag{5.9}$$

The first and second time derivatives of **R** are then:

$$\dot{\mathbf{R}} = [\dot{u} - y_0(\dot{v}_{,x} + \phi\dot{w}_{,x} + \dot{\phi}w_{,x}) - \dot{y}_0(v_{,x} + \phi w_{,x}) - z_0(\dot{w}_{,x} - \phi\dot{v}_{,x} - \dot{\phi}v_{,x})$$

$$- \dot{z}_0(w_{,x} - \phi v_{,x})]\hat{e}_x + [\dot{v} + \dot{y}_0 - z_0(\dot{\phi} + \dot{w}_{,x}v_{,x} + w_{,x}\dot{v}_{,x})$$

$$- \dot{z}_0(\phi + w_{,x}v_{,x})]\hat{e}_y + [\dot{w} + \dot{y}_0\phi + y_0\dot{\phi} + \dot{z}_0]\hat{e}_z \tag{5.10}$$

$$\ddot{\mathbf{R}} = [\ddot{u} - y_0(\ddot{v}_{,x} + \phi\ddot{w}_{,x} + 2\dot{\phi}\dot{w}_{,x} + \ddot{\phi}w_{,x}) - 2\dot{y}_0(\dot{v}_{,x} + \phi\dot{w}_{,x} + \dot{\phi}w_{,x})$$

$$- \ddot{y}_0(v_{,x} + \phi w_{,x}) - z_0(\ddot{w}_{,x} - \phi\ddot{v}_{,x} - 2\dot{\phi}\dot{v}_{,x} - \ddot{\phi}v_{,x})$$

$$-2\dot{z}_0(\dot{w}_{,x} - \phi\dot{v}_{,x} - \dot{\phi}v_{,x}) - \ddot{z}_0(w_{,x} - \phi v_{,x})]\hat{e}_x$$

$$+ [\ddot{v} + \ddot{y}_0 - z_0(\ddot{\phi} + \ddot{w}_{,x}v_{,x} + 2\dot{w}_{,x}\dot{v}_{,x} + w_{,x}\ddot{v}_{,x})$$

$$-2\dot{z}_0(\dot{\phi} + \dot{w}_{,x}v_{,x} + w_{,x}\dot{v}_{,x}) - \ddot{z}_0(\phi + w_{,x}v_{,x})]\hat{e}_y$$

$$+ [\ddot{w} + \ddot{y}_0\phi + 2\dot{y}_0\dot{\phi} + y_0\ddot{\phi} + \ddot{z}_0]\hat{e}_z \tag{5.11}$$

To develop the inertia loads implicitly, Eqns. 5.7, 5.9, 5.10, and 5.11 are substituted in Eqn. 5.3 and subsequently this result and Eqn. 5.8 are substituted in Eqns. 5.1 and 5.2. The following quantities arising from integration over the blade cross section can be defined:

$$\int_A \rho y_0 dA = m x_I \cos\theta_G \tag{5.12}$$

$$\int_A \rho z_0 dA = m x_I \sin\theta_G \tag{5.13}$$

$$\int_A \rho \dot{y}_0 dA = -m x_I \dot{\theta}_G \sin\theta_G \tag{5.14}$$

$$\int_A \rho \dot{z}_0 dA = m x_I \dot{\theta}_G \cos\theta_G \tag{5.15}$$

$$\int_A \rho \ddot{y}_0 dA = -m x_I (\dot{\theta}_G^2 \cos\theta_G + \ddot{\theta}_G \sin\theta_G) \tag{5.16}$$

$$\int_A \rho \ddot{z}_0 dA = m x_I (-\dot{\theta}_G^2 \sin\theta_G + \ddot{\theta}_G \cos\theta_G) \tag{5.17}$$

$$\int_A \rho y_0^2 dA = I_{m2} \cos^2\theta_G + I_{m3} \sin^2\theta_G \tag{5.18}$$

$$\int_A \rho y_0 \dot{y}_0 dA = (I_{m3} - I_{m2})\dot{\theta}_G \sin\theta_G \cos\theta_G \tag{5.19}$$

$$\int_A \rho y_0 \ddot{y}_0 dA = -I_{m2}\cos\theta_G(\dot{\theta}_G^2 \cos\theta_G + \ddot{\theta}_G \sin\theta_G)$$

$$+ I_{m3}\sin\theta_G(-\dot{\theta}_G^2 \sin\theta_G + \ddot{\theta}_G \cos\theta_G) \tag{5.20}$$

$$\int_A \rho y_0 z_0 dA = (I_{m2} - I_{m3})\sin\theta_G \cos\theta_G \tag{5.21}$$

$$\int_A \rho y_0 \dot{z}_0 dA = I_{m2}\dot{\theta}_G \cos^2\theta_G + I_{m3}\dot{\theta}_G \sin^2\theta_G \tag{5.22}$$

$$\int_A \rho y_0 \ddot{z}_0 dA = I_{m2}\cos\theta_G(-\dot{\theta}_G^2 \sin\theta_G + \ddot{\theta}_G \cos\theta_G)$$

$$+ I_{m3}\sin\theta_G(\dot{\theta}_G^2 \cos\theta_G + \ddot{\theta}_G \sin\theta_G) \tag{5.23}$$

$$\int_A \rho z_0^2 dA = I_{m2}\sin^2\theta_G + I_{m3}\cos^2\theta_G \tag{5.24}$$

$$\int_A \rho z_0 \dot{z}_0 dA = (I_{m2} - I_{m3})\dot{\theta}_G \sin\theta_G \cos\theta_G \tag{5.25}$$

$$\int_A \rho z_0 \ddot{z}_0 dA = I_{m2}\sin\theta_G(-\dot{\theta}_G^2 \sin\theta_G + \ddot{\theta}_G \cos\theta_G)$$

$$- I_{m3}\cos\theta_G(\dot{\theta}_G^2 \cos\theta_G + \ddot{\theta}_G \sin\theta_G) \tag{5.26}$$

$$\int_A \rho z_0 \dot{y}_0 dA = -I_{m2}\dot{\theta}_G \sin^2\theta_G - I_{m3}\dot{\theta}_G \cos^2\theta_G \tag{5.27}$$

$$\int_A \rho z_0 \ddot{y}_0 dA = -I_{m2} \sin\theta_G(\dot{\theta}_G^2 \cos\theta_G + \ddot{\theta}_G \sin\theta_G)$$

$$- I_{m3} \cos\theta_G(- \dot{\theta}_G^2 \sin\theta_G + \ddot{\theta}_G \cos\theta_G) \tag{5.28}$$

This procedure leads to implicit expressions which would be extremely lengthy if written out but which can be easily calculated by the numerical program carrying out the analysis. In order to compare with Ref. 8 and verify the implicit expressions, explicit inertia loads were also derived using the ordering scheme detailed in Ch. 4. These expressions contain some previously neglected higher order terms which can be important when HHC is being applied. These expressions are given below:

$$\bar{P}_{xi} = \bar{m}[\bar{x}_0 + \bar{e}_1 + 2\overset{*}{\bar{v}}] \tag{5.29}$$

$$\bar{P}_{yi} = \bar{m}[- \overset{**}{\bar{v}} - 2\overset{*}{\bar{u}} + 2\beta_p\overset{*}{\bar{w}} + \bar{v} + \bar{x}_I \cos\theta_G + x_I\overset{**}{\theta}_G(\sin\theta_G + \phi \cos\theta_G)] \tag{5.30}$$

$$\bar{P}_{zi} = - \bar{m}[\overset{**}{\bar{w}} + 2\beta_p\overset{*}{\bar{v}} + \beta_p(\bar{x}_0 + \bar{e}_1) + x_I\overset{**}{\theta}_G \cos\theta_G] \tag{5.31}$$

$$\bar{q}_{xi} = - \bar{m}\bar{x}_I \cos\theta_G[\overset{**}{\bar{w}} + 2\beta_p\overset{*}{\bar{v}} + \beta_p(\bar{x}_0 + \bar{e}_1) - \phi\overset{**}{\bar{v}} + \bar{v}\phi]$$

$$- \bar{m}\bar{x}_I \sin\theta_G[\bar{v} - \overset{**}{\bar{v}}] - (\bar{I}_{m2} + \bar{I}_{m3})[\overset{**}{\theta}_G + \overset{**}{\phi} + \phi^2\overset{**}{\theta}_G]$$

$$- \bar{I}_{m2}[(1 + 2\overset{*}{\bar{v}}_{,x}) \sin\theta_G \cos\theta_G + (2\phi\overset{*}{\bar{v}}_{,x} - \beta_p\bar{v}_{,x} + \phi) \cos^2\theta_G$$

$$+ (2\overset{*}{\bar{w}}_{,x} - \phi)\sin^2\theta_G + 2\bar{w}_{,x}\overset{*}{\theta}_G \sin\theta_G \cos\theta_G] - \bar{I}_{m3}[\phi \sin^2\theta_G$$

$$- (1 + 2\overset{*}{\bar{v}}_{,x})\sin\theta_G \cos\theta_G + (\overset{**}{\bar{w}}_{,x}\bar{v}_{,x} + 2\overset{*}{\bar{w}}_{,x}\overset{*}{\bar{v}}_{,x} + \bar{w}_{,x}\overset{**}{\bar{v}}_{,x} + 2\overset{*}{\bar{w}}_{,x} - 2\phi\overset{*}{\bar{v}}_{,x} - 2\overset{*}{\phi}\bar{v}_{,x}$$

$$- \phi - \bar{w}_{,x}\bar{v}_{,x})\cos^2\theta_G - 2\bar{w}_{,x}\overset{*}{\theta}_G \sin\theta_G \cos\theta_G - 2\bar{v}_{,x}\overset{*}{\theta}_G \cos^2\theta_G] \tag{5.32}$$

$$\bar{q}_{yi} = -\bar{m}\bar{x}_I \cos\theta_G[\bar{v}_{,x}(\overset{**}{\bar{w}} + \beta_p(\bar{x}_0 + \bar{e}_1)) - \phi(\bar{x}_0 + \bar{e}_1 + 2\overset{*}{\bar{v}})]$$

$$+ \bar{m}\bar{x}_I \sin\theta_G[\bar{x}_0 + \bar{e}_1 + 2\overset{*}{\bar{v}}] - (\bar{I}_{m2} + \bar{I}_{m3})[\bar{v}_{,x}\overset{**}{\theta}_G]$$

$$- \bar{I}_{m2}[(\phi\bar{v}_{,x} - \phi\overset{**}{\bar{v}}_{,x} + \bar{v}_{,x}\overset{**}{\phi})\cos^2_G + 2(2\phi - \overset{*}{\bar{w}}_{,x})\overset{*}{\theta}_G \sin\theta_G \cos\theta_G$$

$$+ (\bar{v}_{,x} - \overset{**}{\bar{v}}_{,x})\sin\theta_G \cos\theta_G + (\bar{w}_{,x} + \beta_p + 2\overset{*}{\phi} - \overset{**}{\bar{w}}_{,x})\sin^2\theta_G + 2\overset{*}{\theta}_G \sin^2\theta_G]$$

$$- \bar{I}_{m3}[\cos^2\theta_G(\beta_p - \phi\bar{v}_{,x} + \bar{w}_{,x} + 2\bar{w}_{,x}\overset{*}{\bar{v}}_{,x} + 2\bar{v}_{,x}\overset{*}{\bar{w}}_{,x} + 2\overset{*}{\phi}$$

$$+ \overset{**}{\phi}\bar{v}_{,x} + 2\overset{*}{\phi}\overset{*}{\bar{v}}_{,x} + \phi\overset{**}{\bar{v}}_{,x} - \overset{**}{\bar{w}}_{,x}) + (\overset{**}{\bar{v}}_{,x} - \bar{v}_{,x})\sin\theta_G \cos\theta_G$$

$$-2(2\phi - \overset{*}{\bar{w}}_{,x})\overset{*}{\theta}_G \sin\theta_G \cos\theta_G + 2\overset{*}{\theta}_G \cos^2\theta_G(1 + \overset{*}{\bar{v}}_{,x})] \tag{5.33}$$

$$\bar{q}_{zi} = -\bar{m}\bar{x}_I \cos\theta_G[\bar{x}_0 + \bar{e}_1 + 2\overset{*}{\bar{v}}] + + \bar{m}\bar{x}_I \sin\theta_G[\phi(\bar{x}_0 + \bar{e}_1)]$$

$$- \bar{I}_{m2}[\overset{**}{\bar{v}}_{,x}\cos^2\theta_G - 2\overset{*}{\theta}_G \sin\theta_G \cos\theta_G + \sin\theta_G \cos\theta_G(\overset{**}{\bar{w}}_{,x} - 2\overset{*}{\phi} - \beta_p)$$

$$+ \overset{*}{\theta}_G \cos^2\theta_G(2\overset{*}{\bar{w}}_{,x} - 2\phi)] - (\bar{I}_{m2} + \bar{I}_{m3})[\bar{w}_{,x}\overset{**}{\theta}_G]$$

$$- \bar{I}_{m3}[2\overset{*}{\theta}_G \sin\theta_G \cos\theta_G - \sin\theta_G \cos\theta_G(\overset{**}{\bar{w}} - 2\overset{*}{\phi} - \beta_p) + 2\phi\overset{*}{\theta}_G \cos^2\theta_G] \quad (5.34)$$

To be consistent with the quasilinearization analysis, the axial displacements $\bar{u}$ in these expressions were neglected in the actual numerical implementation of the shear calculations.

5.3 CALCULATION OF ROOT LOADS

5.3.1 *Summation of Local Aerodynamic and Inertia Loads*

Aerodynamic and inertia loads are combined at each local point of application before any further calculations are performed. Because inertia and aerodynamic loads have been nondimensionalized by different factors, a proportionality constant must be used before they can be combined:

$$\bar{\mathbf{P}} = \bar{\mathbf{P}}_i + \Gamma\bar{\mathbf{P}}_a \; ; \qquad \bar{\mathbf{q}} = \bar{\mathbf{q}}_i + \bar{b}\bar{R}\Gamma\bar{\mathbf{q}}_a \quad (5.35)$$

The proportionality constant is found from the ratio of the nondimensionalization factors:

$$\Gamma = \frac{a_i \rho_a \bar{b} R \Omega^2 \ell^2}{m_0 \Omega^2 \ell} = \frac{\gamma \bar{I}_b}{2\bar{R}^4} \quad (5.36)$$

where it has been assumed that the blade semi-chord used in calculating the Lock number γ is equal to the local blade semi-chord.

5.3.2 *Expressions for Local Contributions to Root Loads*

The local forces and moments produce resultant forces and moments at the blade axis of rotation. These loads must be found in the unconed hub coordinate system. Using Eqn. 2.2 the blade root forces are found by transforming the local aerodynamic and inertia forces which have been calculated in the undeformed, coned blade coordinate system to the undeformed, unconed coordinate system.

$$\overline{P}_x^R = \overline{P}_x \cos\beta_p - \overline{P}_z \sin\beta_p$$

$$\overline{P}_y^R = \overline{P}_y$$

$$\overline{P}_z^R = \overline{P}_x \sin\beta_p + \overline{P}_z \cos\beta_p \tag{5.37}$$

The blade root moments consist of contributions due to the local moments transformed to the hub coordinate system and due to the local forces acting through a moment arm from the blade center of rotation to a given point on the blade. The local moments are transformed to the unconed coordinate system in the same manner as the forces in Eqn. 5.37.

$$\overline{q}_x^{R1} = \overline{q}_x \cos\beta_p - \overline{q}_z \sin\beta_p$$

$$\overline{q}_y^{R1} = \overline{q}_y$$

$$\overline{q}_z^{R1} = \overline{q}_x \sin\beta_p + \overline{q}_z \cos\beta_p \tag{5.38}$$

Moments due to the local forces can be calculated from:

$$\mathbf{q}^{R2} = \mathbf{R}_c \times \mathbf{P}^R \tag{5.39}$$

where $\mathbf{R}_c$ is the position vector of a point on the elastic axis of the blade relative to the center of rotation in the unconed coordinate system:

$$\mathbf{R}_c = (\bar{e}_1 + \bar{x}_0 \cos\beta_p - \bar{w}\sin\beta_p)\hat{i} + \bar{v}\hat{j} + (\bar{x}_0 \sin\beta_p + \bar{w}\cos\beta_p)\hat{k} \tag{5.40}$$

and $\mathbf{P}^R$ is the vector of local forces in the unconed coordinate system.

$$\mathbf{P}^R = \bar{P}_x^R\hat{i} + \bar{P}_y^R\hat{j} + \bar{P}_z^R\hat{k} \tag{5.41}$$

Combining Eqns. 5.39 through 5.41 produces the following expressions for the total blade root moments:

$$\bar{q}_x^R = -\bar{P}_y^R(\bar{x}_0 \sin\beta_p + \bar{w}\cos\beta_p) + \bar{P}_z^R\bar{v} + \bar{q}_x^{R1} \tag{5.42}$$

$$\bar{q}_y^R = \bar{P}_x^R(\bar{x}_0 \sin\beta_p + \bar{w}\cos\beta_p) - \bar{P}_z^R(\bar{e}_1 + \bar{x}_0\cos\beta_p - \bar{w}\sin\beta_p) + \bar{q}_y^{R1} \tag{5.43}$$

$$\bar{q}_z^R = -\bar{P}_x^R\bar{v} + \bar{P}_y^R(\bar{e}_1 + \bar{x}_0\cos\beta_p - \bar{w}\sin\beta_p) + \bar{q}_z^{R1} \tag{5.44}$$

These expressions are calculated based on an equilibrium blade response which has been calculated using the mode shapes for a given blade and so are valid for either hingeless or articulated blades.

5.3.3 *Integration of Loads Over the Blade*

The total blade root forces and moments are calculated by integrating the expressions for the local blade root loads over the length of the blade. The integrals for these expressions are given below:

$$\overline{P}_x^B(\psi) = \int_{\bar{e}_1}^{\overline{R}} \overline{P}_x^R(\bar{x}, \psi) d\bar{x} \qquad \bar{q}_x^B(\psi) = \int_{\bar{e}_1}^{\overline{R}} \bar{q}_x^R(\bar{x}, \psi) d\bar{x} \tag{5.45}$$

$$\overline{P}_y^B(\psi) = \int_{\bar{e}_1}^{\overline{R}} \overline{P}_y^R(\bar{x}, \psi) d\bar{x} \qquad \bar{q}_y^B(\psi) = \int_{\bar{e}_1}^{\overline{R}} \bar{q}_y^R(\bar{x}, \psi) d\bar{x} \tag{5.46}$$

$$\overline{P}_z^B(\psi) = \int_{\bar{e}_1}^{\overline{R}} \overline{P}_z^R(\bar{x}, \psi) d\bar{x} \qquad \bar{q}_z^B(\psi) = \int_{\bar{e}_1}^{\overline{R}} \bar{q}_z^R(\bar{x}, \psi) d\bar{x} \tag{5.47}$$

These integrals are calculated by a spanwise integration using a 16 point Gauss-Legendre integration formula.

5.4 CALCULATION OF TOTAL HUB FORCES AND MOMENTS

5.4.1 *Transformation to the Nonrotating Hub Coordinate System*

Using Eqn. 2.1, the loads in the rotating system can be converted to the blade root loads in the nonrotating hub fixed coordinate system. The expressions for the various components of the hub shears and moments in the nonrotating coordinate system are presented below.

Vertical Shear:

C-2.

$$\bar{S}^B_{vt}(\psi) = \bar{P}^B_z(\psi) \tag{5.48}$$

Lateral Shear:

$$\bar{S}^B_{lt}(\psi) = \bar{P}^B_x(\psi)\sin\psi + \bar{P}^B_y(\psi)\cos\psi \tag{5.49}$$

Longitudinal Shear:

$$\bar{S}^B_{\ln}(\psi) = \bar{P}^B_x(\psi)\cos\psi - \bar{P}^B_y(\psi)\sin\psi \tag{5.50}$$

Pitching Moment:

$$\bar{M}^B_{pt}(\psi) = \bar{q}^B_x(\psi)\sin\psi + \bar{q}^B_y(\psi)\cos\psi \tag{5.51}$$

Rolling Moment:

$$\bar{M}^B_{rt}(\psi) = \bar{q}^B_x(\psi)\cos\psi - \bar{q}^B_y(\psi)\sin\psi \tag{5.52}$$

Yawing Moment:

$$\bar{M}^B_{yw}(\psi) = \bar{q}^B_z(\psi) \tag{5.53}$$

5.4.2 *Summation Over the Blades*

Since each individual blade undergoes the same periodic response around the azimuth, the total hub loads for a given azimuth of the reference blade may be found by summing the loads for a single blade calculated at azimuths appropriately phased from that of the reference blade. This procedure is carried out in the following manner:

$$\bar{S}_{vt}(\psi) = \sum_{i=1}^{NB} \bar{S}_{vt}^{B}(\psi_i) \quad \text{where } \psi_i = \psi + \frac{2\pi(i-1)}{NB} \tag{5.54}$$

where NB is the number of blades. Expressions for the other hub loads, $\bar{S}_{lt}$, $\bar{S}_{ln}$, $\bar{M}_{pt}$, $\bar{M}_{rt}$, and $\bar{M}_{yw}$ are found in a similar manner.

5.5 HARMONIC ANALYSIS OF THE HUB LOADS

The total hub loads are functions of blade azimuth and thus are expanded into a Fourier series and stored in this form. For example the Fourier expansion of $\bar{S}_{vt}(\psi)$ is:

$$\bar{S}_{vt}(\psi) = s_{vt0} + \sum_{n=1}^{NHR} (s_{vtcn} \cos n\psi + s_{vtsn} \sin n\psi) \tag{5.55}$$

where the number of harmonics retained in the analysis is typically NHR = 5 and the Fourier coefficients are given by:

$$s_{vt0} = \frac{1}{2\pi} \int_0^{2\pi} \bar{S}_{vt}(\psi) d\psi$$

$$s_{vtcn} = \frac{1}{\pi} \int_0^{2\pi} \bar{S}_{vt}(\psi) \cos n\psi \, d\psi$$

$$s_{vtsn} = \frac{1}{\pi} \int_0^{2\pi} \bar{S}_{vt}(\psi) \sin n\psi \, d\psi \tag{5.56}$$

These coefficients are calculated using a trapezoidal integration rule. The constant portion of each load, required for the calculation of the trim state of

the helicopter and for determining thrust and power coefficients, are just the constant coefficients in the Fourier series for each load.

5.6 PERFORMANCE COEFFICIENTS AND NORMALIZATION

The constant part of the rotor thrust, power, and inplane force are conventionally expressed in nondimensional coefficient form as:

$$C_T = \frac{T}{\rho_a A(\Omega R)^2} \; ; \quad C_P = \frac{P}{\rho_a A(\Omega R)^3} \; ; \quad C_H = \frac{F_H}{\rho_a A(\Omega R)^2} \tag{5.57}$$

where T, P, and F_H are average rotor thrust, power, and inplane force, and A is the rotor area. These coefficients may be expressed in terms of the nondimensional loads as:

$$C_T = \frac{4\bar{b}\bar{R}}{\gamma \bar{I}_b}\bar{S}_{vt} \; ; \quad C_P = \frac{-4\bar{b}}{\gamma \bar{I}_b}\bar{M}_{yw} \; ; \quad C_H = \frac{4\bar{b}\bar{R}}{\gamma \bar{I}_b}\bar{S}_{\ln} \tag{5.58}$$

Hub shear and moment results used in this study are normalized by the nondimensional blade mass moment of inertia in flapping, $\bar{I}_b$. For example:

$$\bar{\bar{S}}_{vt}(\psi) = \frac{\bar{S}_{vt}(\psi)}{\bar{I}_b} \tag{5.59}$$

where $\bar{S}_{vt}(\psi)$ has already been nondimensionalized by $m_0\Omega^2\ell^2$. The nondimensional form of the sine and cosine components of the 4/rev. hub forces and moments are used in the HHC calculations. They are represented by:

$$\bar{\bar{s}}_{vts4}\,; \quad \bar{\bar{s}}_{vtc4}\,; \quad \bar{\bar{s}}_{lts4}\,; \quad \bar{\bar{s}}_{ltc4}\,; \quad \bar{\bar{s}}_{lns4}\,; \quad \bar{\bar{s}}_{lnc4}$$

$$\overline{\overline{m}}_{pts4}\,; \quad \overline{\overline{m}}_{ptc4}\,; \quad \overline{\overline{m}}_{rls4}\,; \quad \overline{\overline{m}}_{rlc4}\,; \quad \overline{\overline{m}}_{yws4}\,; \quad \overline{\overline{m}}_{ywc4} \tag{5.60}$$

Referring to Fig. 2.1, the pitching, rolling, and yawing moments are as shown, and the vertical, lateral, and longitudinal shears are respectively in the directions of the Z_{nr}, Y_{nr}, and X_{nr} axes.

Chapter VI

HHC FOR VIBRATION REDUCTION

6.1 PREVIOUS WORK

In 1974 McCloud and Kretz[39] tested multicyclic control applied in the rotating system on a wind tunnel model of a jet-flap rotor. They investigated the effects of HHC on the rotor loads and blade stresses. The concept of a linear, quasi-static representation of the relationship between harmonics of the rotor loads and harmonics of the HHC was developed. An offline weighted least square error technique was used to calculate the transfer matrix relating response harmonics to control harmonics and the notation "T" was introduced for this matrix. Open-loop control needed to minimize a quadratic performance function was calculated. Further open-loop studies using this method were conducted on a Multicyclic Controllable Twist Rotor by McCloud and Weisbrich[40] and Brown and McCloud[5]. The control needed to reduce both blade loads and test module accelerations was considered including the influence of weights in the performance index. The effect of rotor lift, propulsive force and speed on open-loop control were also examined.

In 1974 Sissingh and Donham[60] conducted wind tunnel tests on a hingeless rotor which had HHC introduced by oscillations of the swashplate. Vibratory vertical shear and hub moment due to HHC were measured and

from this a transfer matrix was identified off-line by a least square error technique. The sensed vibrations and a transfer matrix calculated by direct inversion were used to calculate control to be applied to the rotor.

In 1980 Shaw and Albion[58] measured the response to HHC of a hingeless rotor in a wind tunnel. The transfer matrix was identified using a Kalman filter and was then inverted and used with feedback of measured vibrations to reduce rotor loads. This controller worked very well at an advance ratio of $\mu = 0.1$ but was less successful at other speeds because the required HHC exceeded an externally imposed limit of 1.5°. Shaw continued this research in 1985[59]. Fixed gain, scheduled gain, and adaptive controllers were evaluated with wind tunnel tests. Response to HHC was found to be essentially linear up to angles of $\pm$ 3°. The most significant finding was that a fixed gain controller provided 90% multi-axis vibration suppression over a wide range of operating conditions from hover to 188 knots and at varying load factors.

In 1980 Taylor et al.[62,63] conducted numerical studies using the G400 nonlinear aeroelastic helicopter simulation[2]. A Kalman filter was used for on-line identification of the transfer matrix and deterministic closed-loop gains were found to minimize a quadratic function of the vibrations and control inputs. Changes in the transfer matrix due to system nonlinearity and variation in the flight condition were accounted for only by the Kalman filter identification of the transfer matrix. The control system showed good convergence and significantly reduced vibrations.

In 1980 Hammond[30] conducted wind tunnel tests of an articualted rotor. The vibratory hub moments and vertical shear due to HHC inputs were measured. Both a deterministic controller with external rate limiting and a cautious controller based on a global HHC model were considered. The transfer matrix and the uncontrolled vibration level were identified using a Kalman filter. Feedback of measured vibrations was used to minimize a quadratic performance function. The cautious controller was found to be less erratic than the deterministic controller. Vertical vibratory shears were reduced significantly, however hub moment reductions were smaller. In 1981 Molusis, Hammond, and Cline[45] extended this investigation with an analytical development of six controllers, four of which were then tested in a wind tunnel. Vertical, longitudinal, and lateral hub shears were used as feedback to reduce a quadratic performance function. A cautious controller tested worked smoothly and reduced vertical and longitudinal vibrations but actually led to higher lateral vibrations at low speeds. A controller identifying only the uncontrolled vibration level was not successful when tested in the wind tunnel. A dual controller incorporating probing terms designed to enhance system identification was derived but not tested.

Since 1980 Wood et al.[67,68,25] have developed software and hardware for HHC implementation on an OH6-A and have conducted the first successful flight tests with active HHC. The cautious controller developed by Molusis[45] was used in closed-loop studies and additionally, open-loop results showing phasing of HHC for shear minimization were presented. A

Kalman filter was used to identify the transfer matrix and the uncontrolled vibration level. This approach was successful in reducing fuselage vibrations at low to moderate speeds and during moderate transient maneuvers.

In 1982 Johnson[36] wrote a comprehensive review including the analytical development and evaluation of essentially all the control algorithms used to that date. The discussion of the algorithms was based on single-input single-output system models and did not include actual helicopter simulations.

In 1983 Molusis[46] and Molusis, Mookerjee, and Bar-Shalom[47] performed analytical studies of the effects of nonlinearity on controller performance. In Ref. 46 performance of a deterministic controller and a cautious controller were compared using a simple, arbitrary nonlinear simulation model not based on an actual helicopter analysis. Reference 47 used a nonlinear Volterra series analytical system model with parameters derived from a nonlinear aeroelastic vibration analysis using the G400 computer simulation. This model was used to consider the effects of nonlinearity on controller performance and Kalman filter stability.

Ham[28,29] and McKillip[41,42] have developed the concept of Individual Blade Control (IBC). The pitch of each blade is controlled individually, either through swashplate actuators for three or less blades, or by individual actuators in the rotating system for more than three blades. Blade mounted accelerometers are used to sense blade motion and feed this information back to the controller. These references include analytical studies using simple models not

based on actual helicopter aeroelastic simulations, and limited wind tunnel testing. Results indicate that IBC can be used to reduce helicopter vibrations using relatively simple controllers at the expense of a more conplicated physical implementation due to components in the rotating system.

In 1983 Chopra and McCloud[10] developed a linear, quasi-static, frequency-domain model for the response of a rotor to HHC. This model related six harmonics of vibration to six harmonics of HHC input through use of a transfer function based on experimental data. This model was used to evaluate the performance of a deterministic controller for various flight speeds and in the presence of simulated measurement noise and inaccurate initial estimates of model parameters.

In 1983 Jacob and Lehmann[34] presented an analytical study of HHC. Two simulations were used, one a rigid spring restrained blade, and one a fully elastic blade with one mode modeled in each of flap, lag, and torsion. Simulation was basically of an open-loop type but a static search algorithm was used to find the HHC necessary to minimize a performance criterion. In 1985 Lehmann[37] continued this work with the wind tunnel testing of a four bladed hingeless rotor. The effect of open-loop HHC consisting of 3, 4, and 5/rev pitch changes in the rotating system was investigated. In 1988 Lehmann and Kube[38] successfully reduced 4/rev. hub vibrations using closed-loop HHC applied to the same rotor. A frequency domain, minimum variance controller based on a local HHC model and using Kalman filter identification of the transfer matrix was used.

Davis[11] in 1984 produced a computer simulation using the G400 code. Deterministic, cautious, and dual controllers using both local and global HHC models were investigated. These controllers employed Kalman filter identification of the vibrations and/or transfer matrix. A general controller which can be specialized to any of these cases by changing certain parameters was presented. Vibration reductions of 75 to 95 percent were achieved with each of the controllers when they were properly tuned. Control amplitudes of less than one degree were needed for these reductions.

In 1986 Miao, Kottapalli, and Frye[43] and Walsh[64] presented results of HHC flight tests using an S-76A helicopter. Only open-loop HHC was implemented. Substantial vibration reductions were achieved but at high speeds these reductions were constrained by hardware limitations which would not allow high enough HHC amplitudes. Various combinations of HHC inputs were used to reduce combinations of several vibratory quantities.

In 1986 Polychroniadis and Achache[53] presented flight test results for closed-loop HHC applied to an SA 349 Gazelle. One deterministic and two stochastic controllers, each based on a global HHC model, were tested. All three controllers gave good vibration reductions of up to 90% in steady state flight and differed mainly in their self-adaptive performance. Since HHC amplitudes in this study were limited to one degree, it was speculated that by allowing higher values of HHC greater reductions in vibratory loads could be obtained.

In 1986 Jacklin[32,33] presented an analysis of system identification techniques for HHC. Least squares and Kalman filter type identification techniques were reviewed and a new mean least squares algorithm was developed. Various aspects of these algorithms were compared. The mean least square algorithm uses equations similar to those of a Kalman filter however these equations turned out to be simpler. It was found that this algorithm converged to the correct estimate only when a signal averaging method over several iterations was employed.

In 1986 Hanagud et al.[31] produced an analytical, coupled rotor-airframe analysis of HHC using a one degree of freedom, flap only, rotor model. A global HHC model was assumed and a deterministic control law was used. The transfer matrix was calculated by a method which required the matrix to be consistent with measured vibration data while at the same time being as close as possible to some a priori estimate of the transfer matrix. This approach led to reductions in vibration levels.

Gupta[26], Gupta and DuVal[27], and DuVal, Gregory, and Gupta[15] have developed an extension of linear-quadratic-Gaussian (LQG) design methods using frequency-shaped cost functionals. A vibration controller was obtained by minimizing a cost functional which places a large penalty on fuselage accelerations at set vibration frequencies. The optimal control solution involved feedback of fuselage accelerations through undamped oscillators, tuned to the frequency at which vibrations are to be suppressed. This approach has the advantage that on-line harmonic analysis of the vibrations is

not required and the resultant controller is simple to implement because it is a constant gain regulator with filters in the feedback loops. A dynamic model of the rotor-fuselage combination is needed in the LQG design procedure. Since this model will change with flight condition, gain scheduling is required to account for these different conditions. This control law was implemented using a blade-element simulation of the Rotor Systems Research Aircraft (RSRA). Accelerations were reduced by at least 80% in all channels except the vertical, in which the initial vibration level was two orders of magnitude below that of the other channels.

In the appendices to Murphy's 1987 report[48], Motyka et al. developed an approach to HHC implementation using a Linear Quadratic Guassian with Loop Transfer Recovery (LQG/LTR) design methodology. Baseline controllers for various operating conditions were designed using LQG/LTR to ensure robustness. These model based compensators contained elements of a linear system model of the helicopter and so had to be implemented with a gain scheduling or table look-up approach for implementaion at different flight conditions. Attempts were made to enhance these controllers using various adaptive control techniques. Numerical simulations of the control algorithms were carried out on an elastic model of a helicopter. The basic model based compensators were very effective in reducing vibrations with vibration reductions of 99% in vertical, 94% in lateral, and 68% in longitudinal directions. Various adaptive enhancement approaches did not improve control performance.

6.2 THE HHC MODELS

6.2.1 *Linearity of HHC*

It is generally assumed that the relationship between the vector of HHC input harmonics θ and the vector of vibration output harmonics Z can be represented by a linear, quasi-static, frequency-domain model. A discrete time model of the helicopter is assumed such that the sampling time step Δt is sufficient for all transients to die out and for the vibration harmonics to be measured. This time step would typically be one rotor revolution. The actual helicopter being modeled, and the mechanisms being used to control it, are of course complicated continuous time systems. A schematic of such a helicopter model is shown in Fig. 6.1. This figure shows a helicopter, with given flight conditions, which produces some time history of vibrations. A harmonic analysis of these vibrations is carried out and a discrete set of vibration harmonics is fed to the controller. These harmonics are used, typically in a Kalman filter, to identify problem parameters. From these parameters and stored information from previous samplings, gain calculations are made and harmonics of an HHC feedback to minimize vibrations are calculated. From these harmonics a time history of HHC inputs is calculated and this is fed to electro-hydraulic servo-actuators in the helicopter which set the actual blade pitch angles. These HHC inputs modify the helicopter dynamics producing new vibration levels which are used to begin another iteration of the process.

The baseline uncontrolled vibration level of the helicopter, Z_0, is a nonlinear function of the helicopter operating condition and is dependent on nonlinear phenomena associated with aerodynamic, structural, and inertial aspects of the helicopter dynamics. Linearity is being assumed only in the response to HHC inputs. Previous experimental studies[30,59] have indicated that only 0°-3° of HHC inputs are needed to alleviate vibration, so the assumption of linearity is thought to be reasonable. Still, some studies[46,47] have found evidence of nonlinear response to HHC over this amplitude range, in which case the locally linearized model explained in the next section may be needed.

6.2.2 *Global Model*

The global model of the helicopter response to HHC assumes linearity over the entire range of control application:

$$Z(i+1) = Z_0 + T\theta(i) \tag{6.1}$$

The vibration vector Z at time step $i+1$ is equal to the baseline vibration Z_0 plus the product of the transfer matrix T and the HHC vector θ at time step i. This implies that T, the transfer matrix relating HHC input harmonics to vibration output harmonics, is independent of $\theta(i)$. This concept of a linear quasi-static representation of the relationship between harmonics of helicopter response and harmonics of HHC was introduced in Ref. 39 where the notation T for this matrix was first used.

6.2.3 *Local Model*

The local model of the helicopter response to HHC is based on a linearization of the response about the response to the current value of the control vector:

$$Z(i+1) = Z(i) + T\,[\theta(i+1) - \theta(i)] \tag{6.2}$$

The vibration vector Z at time step $i+1$ is equal to the vibration vector at time step i plus the product of the transfer matrix and the difference in the control vector from time step i to time step $i+1$. The transfer matrix T now relates changes in the HHC input harmonics to changes in the vibration output harmonics. This allows for variation of the transfer matrix T with input $\theta(i)$. Alternately this may be written as:

$$\Delta Z(i+1) = T\Delta\theta(i+1) \tag{6.3}$$

6.3 IDENTIFICATION

6.3.1 *Assumptions*

In applying HHC algorithms for vibration reduction, it is assumed that the HHC inputs $\theta(i)$ are known without error. Measurements $y(i)$ of the hub vibratory loads $Z(i)$ are made and are assumed to include zero mean white Gaussian measurement noise $V(i)$:

$$y(i) = Z(i) + V(i) \tag{6.4}$$

Based on the measurements $y(i)$, different parameters may be identified for the following cases[36]:

1. Local Model, Identify transfer matrix T
2. Global Model, Identify baseline vibrations Z_0, T assumed known
3. Global Model, Identify T, Z_0 assumed known
4. Global Model, Identify T and Z_0

If the transfer matrix T or the baseline vibration vector Z_0 is to be identified, it is assumed to vary with flight condition and is represented by a random walk model[45]:

$$T(i+1) = T(i) + W(i) \tag{6.5}$$

$$Z_0(i+1) = Z_0(i) + W_0(i) \tag{6.6}$$

where $W(i)$ and $W_0(i)$ are zero mean white Gaussian process noise.

6.3.2 *Kalman Filter Identification*

6.3.2.1 General Kalman Filter

A discrete Kalman filter[6] may be used to estimate a discrete random process x which can be modeled in the form:

$$x_{k+1} = \phi_k x_k + w_k \tag{6.7}$$

Observation of the process occurs at discrete points in time according to:

$$z_k = H_k x_k + v_k \tag{6.8}$$

where:

x_k = $(n \times 1)$ process state vector at time t_k

ϕ_k = $(n \times n)$ matrix relating x_k to x_{k+1} in the absence of a forcing function

w_k = $(n \times 1)$ vector - white (uncorrelated) sequence with known covariance structure

z_k = $(m \times 1)$ vector of measurements at time t_k

H_k = $(m \times n)$ matrix giving the ideal (noiseless) connection between the measurement and the state vector at time t_k

v_k = $(m \times 1)$ vector of measurement errors - white sequence with known covariance structure and uncorrelated with the w_k sequence

The covariance matrices for the w_k and v_k vectors are:

$$E[w_k w_i^T] = \begin{cases} Q_k & i = k \\ 0 & i \neq k \end{cases} \tag{6.9}$$

$$E[v_k v_i^T] = \begin{cases} R_k & i = k \\ 0 & i \neq k \end{cases} \tag{6.10}$$

$$E[w_k v_i^T] = 0 \qquad \text{for all } i \text{ and } k \tag{6.11}$$

The Kalman filter consists of the following algorithm to produce an updated estimate of the state vector $\hat{x}$ with the assumption of some prior estimate $\hat{x}^-$.

Update equation:

$$\hat{x}_k = \hat{x}_k^- + K_k(z_k - H_k\hat{x}_k^-) \tag{6.12}$$

Kalman gain equation:

$$K_k = P_k^- H_k^T (H_k P_k^- H_k^T + R_k)^{-1} \tag{6.13}$$

Error variance matrix equation:

$$P_k = (I - K_k H_k) P_k^- \tag{6.14}$$

State vector projection equation:

$$\hat{x}_{k+1}^- = \phi_k \hat{x}_k \tag{6.15}$$

Error variance matrix projection equation:

$$P_{k+1}^- = \phi_k P_k \phi_k^T + Q_k \tag{6.16}$$

This algorithm is used to identify the transfer matrix T and/or the baseline vibrations Z_0. From the assumptions of Eqns. 6.5 and 6.6 the matrix ϕ_k will always be the identity matrix I. Therefore Eqn. 6.15 becomes:

$$\hat{x}_{k+1}^- = \hat{x}_k \tag{6.17}$$

and Eqn. 6.14 and 6.16 can be combined to give:

$$P_{k+1}^- = P_k^- - K_k H_k P_k^- + Q_k \tag{6.18}$$

If there are no process dynamics, i.e. $Q_k = 0$, then the Kalman filter is equivalent to a recursive weighted least-squares algorithm in which the weighting on the measurement error is equal to $\frac{1}{R_k}$.

6.3.2.2 Kalman Filter for Case 1

For the local HHC model only T is identified. When Eqn. 6.5 is considered one row at a time, one has for the jth row:

$$T_j(i+1) = T_j(i) + w_j(i) \tag{6.19}$$

From Eqns. 6.4 and 6.3 an observation equation for one row of the T matrix, equivalent to Eqn. 6.8, can be written as:

$$\Delta y_j(i) = \Delta\theta^T(i) T_j^T(i) + v(i) \quad . \tag{6.20}$$

where $\Delta y_j(i)$ is the jth componemt of $\Delta y(i)$ and $T_j(i)$ is the jth row of $T(i)$.

By comparing Eqns. 6.20 and 6.5 with Eqns. 6.7 and 6.8, the Kalman filter equations for one row of the T matrix can be obtained as:

$$\hat{T}_j^T(i+1) = \hat{T}_j^T(i) + K(i+1)[\Delta y_j(i+1) - \Delta\theta^T(i)\hat{T}_j^T(i)] \tag{6.21}$$

$$K(i+1) = P_j(i)\Delta\theta(i)[\Delta\theta^T(i)P_j(i)\Delta\theta(i) + R_j(i)]^{-1} \tag{6.22}$$

$$P_j(i+1) = P_j(i) - K(i+1)\Delta\theta^T(i)P_j(i) + Q_j(i) \tag{6.23}$$

If it is <u>assumed</u> that the ratio of parameter and measurement noise variances, $Q_j(i)/R_j(i)$ is the same for every measurement, then Eqn. 6.21 can be written[36] in matrix form as:

$$\hat{T}(i+1) = \hat{T}(i) + [\Delta y(i) - \hat{T}(i)\Delta\theta(i)]K^T(i+1) \tag{6.24}$$

and $K(i+1)$ and $P(i+1)$ only have to be calculated once. There is no reason to expect this assumption to be true, but a great reduction in computation is gained by its acceptance[36].

6.3.2.3 Kalman Filter for Case 2

Using the global HHC model, identifying only the T matrix, and assuming Z_{0j} is known, requires only the substitution in Eqn. 6.21 of $y_j(i+1) - Z_{0j}$ for $\Delta y_j(i+1)$ and $\theta(i)$ for $\Delta\theta(i)$, thus one obtains:

$$\hat{T}_j^T(i+1) = \hat{T}_j^T(i) + K(i+1)[y_j(i+1) - Z_{0j} - \theta^T(i)\hat{T}_j^T(i)] \tag{6.25}$$

$$K(i+1) = P_j(i)\theta^T(i)[\theta^T(i)P_j(i)\theta(i) + R_j(i)]^{-1} \tag{6.26}$$

$$P_j(i+1) = P_j(i) - K(i+1)\theta^T(i)P_j(i) + Q_j(i) \tag{6.27}$$

and the matrix form of these equations may be written similarly to Eqn. 6.24.

6.3.2.4 Kalman Filter for Case 3

Using the global model, identifying only Z_0, and assuming the T matrix is known, requires an observer for Z_0 in the form of Eqn. 6.8. From Eqns. 6.1 and 6.4 this can be written as:

$$y_j(i) - \theta^T(i)T_j^T(i) = Z_{0j}(i) + v(i) \tag{6.28}$$

Comparing Eqns. 6.6 and 6.28 with Eqns. 6.8 and 6.7 the Kalman filter for this case can be seen to be:

$$\hat{Z}_{0j}(i+1) = \hat{Z}_{0j}(i) + K(i+1)[y_j(i+1) - \theta^T(i)T_j^T(i) - \hat{Z}_{0j}(i)] \tag{6.29}$$

$$K(i+1) = P_j(i)[P_j(i) + R_k]^{-1} \tag{6.30}$$

$$P_j(i+1) = P_j(i) - K(i+1)P_j(i) + Q_k \tag{6.31}$$

where now all quantities are scalars. In vector form Eqn. 6.29 can be written as:

$$\hat{Z}_0(i+1) = \hat{Z}_0(i) + [y(i+1) - T(i)\theta(i) - \hat{Z}_0(i)]K(i+1) \tag{6.32}$$

6.3.2.5 Kalman Filter for Case 4

Using the global HHC model and identifying both Z_0 and T requires that elements of Z_0 and T be incorporated in a single vector. From Eqns. 6.1 and 6.4 an observation equation for an element of Z_0 and a row of the T matrix may be written as:

$$y_j(i) = [1 \quad \theta^T(i)]\begin{bmatrix} Z_{0j}(i) \\ T_j^T(i) \end{bmatrix} + v(i) \tag{6.33}$$

or by defining a new vector and matrix as:

$$\underline{\theta}(i) = \begin{bmatrix} 1 \\ \theta(i) \end{bmatrix}; \qquad \underline{C}(i) = [Z_0(i)\ T(i)] \tag{6.34}$$

this becomes:

$$y_j(i) = [\underline{\theta}^T(i)][\underline{C}_j^T(i)] + v(i) \tag{6.35}$$

Comparing Eqns. 6.6, 6.5, and 6.33 with Eqns. 6.7 and 6.8 the Kalman filter for this case can be seen to be:

$$\hat{\underline{C}}_j^T(i+1) = \hat{\underline{C}}_j^T(i) + K(i+1)[y_j(i+1) - \hat{Z}_{0j}(i) - \theta^T(i)\hat{T}_j^T(i)] \tag{6.36}$$

$$K(i+1) = \underline{P}_j(i)\underline{\theta}^T(i)[\underline{\theta}^T(i)\underline{P}_j(i)\underline{\theta}(i) + R_j(i)]^{-1} \tag{6.37}$$

$$\underline{P}_j(i+1) = \underline{P}_j(i) - K(i+1)\underline{\theta}^T(i)\underline{P}_j(i) + Q_j(i) \tag{6.38}$$

where now $\underline{P}_j(i)$ is the covariance matrix for $\underline{C}_j^T(i)$ and is composed in the following manner:

$$\underline{P}_j(i) = \begin{bmatrix} P_{11j} & P_{12j} \\ P_{21j} & P_{22j} \end{bmatrix} \tag{6.39}$$

where P_{11j} is the covariance of Z_{0j}, P_{22j} is the covariance of the jth row of the T matrix, and P_{12j} is the cross covariance of Z_{0j} and the jth row of the T matrix.

Again Eqn. 6.36 may be written in matrix form as:

$$\hat{\underline{C}}(i+1) = \hat{\underline{C}}(i) + [y(i+1) - \hat{Z}_0(i) - \hat{T}(i)\theta(i)]K^T(i+1) \tag{6.40}$$

In summary the inputs to the Kalman filter given in Eqns. 6.12 through 6.18 for the four cases are given in table 6.1.

TABLE 6.1

Kalman Filter Inputs

Case	x	z	H
1	T_j	Δy_j	$\Delta\theta$
2	T_j	$y_j - Z_{0j}$	θ
3	Z_{0j}	$y_j - T_j\theta$	1
4	$[Z_{0j} \quad T_j]$	y_j	$\begin{bmatrix} 1 \\ \theta \end{bmatrix}$

6.3.3 *Least Mean Squares (LMS) Identification*

Jacklin[32,33] has developed an extension of the LMS algorithm of Widrow and Hoff[65,66] to handle multi-input, multi-output helicopter parameter identification problems. He uses this approach with "inverse control," i.e. application of the inverse of the local transfer matrix as a controller to reduce vibrations. Denoting the inverse of T by C , the vibration control commands are produced by:

$$^{*}\Delta\theta(i) = -\, Cy(i) \tag{6.41}$$

$$^{*}\theta(i+1) = \theta(i) + {}^{*}\Delta\theta \tag{6.42}$$

The matrix C need not be a true inverse of T but is a general matrix which performs the inverse function of the T matrix.

The LMS algorithm forms an adaptation error vector consisting of the differences between the actual and estimated changes in HHC input harmonics. Referring to Fig. 6.2:

$$\begin{aligned} \varepsilon &= \Delta\theta - \hat{\Delta\theta} \\ &= \Delta\theta - C\Delta Z \\ &= \Delta\theta - CT\Delta\theta \end{aligned} \tag{6.43}$$

If C were the exact inverse of T, the error vector would be zero. A steepest descent method is used to update C:

$$C(i+1) = C(i) - K_s\left(\frac{\partial^2\varepsilon}{\partial C(i)}\right). \tag{6.44}$$

Here K_s is a gain term governing the amount of correction being made.

The error squared term for one row of C is given by:

$$\varepsilon_j^2 = (\varepsilon_j)(\varepsilon_j)^T = (\Delta\theta_j - C_j\Delta Z)(\Delta\theta_j - \Delta Z^T C_j^T) \tag{6.45}$$

Expanding this and differentiating with respect to C_j^T leads to:

$$\frac{\partial\varepsilon_j^2}{\partial C_j^T} = 2(C_j\Delta Z - \Delta\theta_j)\Delta Z^T \tag{6.46}$$

The update equation for a row of C then becomes:

$$C_j(i+1) = C_j(i) - 2k_j(C_j\Delta Z - \Delta\theta_j)\Delta Z^T \tag{6.47}$$

All the row equations may be combined in matrix form to give:

$$C(i+1) = C(i) + 2[\Delta\theta(i) - C(i)\Delta Z(i)][\overline{\Delta Z}^T] \tag{6.48}$$

where $\overline{\Delta Z}^T$ is a matrix whose jth row is the $\Delta Z^T(i)$ vector multiplied by k_j :

$$\overline{\Delta Z}^T = \begin{bmatrix} k_1 \Delta Z^T(i) \\ k_2 \Delta Z^T(i) \\ \cdot \\ \cdot \\ \cdot \\ k_j \Delta Z^T(i) \end{bmatrix} \tag{6.49}$$

In the investigations of Refs. 32 and 33 it was found that the values of k_j needed to be tuned for optimal performance.

6.4 CONTROL ALGORITHMS

6.4.1 *Minimum Varaince Control Algorithms*

The vast majority of all HHC investigations[67,68,53,45,59,37,62,10,34] to date have used linear optimal control solutions based on a quadratic cost functional. Minimum variance control is based on the minimization of a cost functional which is the expected value of a weighted sum of the mean squares of the control and vibration variables.

Minimum variance controllers are obtained by minimization of the cost functional:

$$J = E\left\{Z^T(i)W_Z Z(i) + \theta^T(i)W_\theta \theta(i) + \Delta\theta^T(i)W_{\Delta\theta}\Delta\theta(i)\right\} \tag{6.50}$$

where:

$E\{\}$	=	indicates expected value, accounting for uncertainty in the system
$\Delta\theta(i)$	=	$\theta(i) - \theta(i-1)$
W_z	=	diagonal weighting matrix on vibrations
W_θ	=	diagonal weighting on control amplitudes
$W_{\Delta\theta}$	=	diagonal weighting matrix on rate of change of the control amplitudes

Typically Z, θ, and $\Delta\theta$ consist of the sine and cosine components of the N/rev vibrations and HHC inputs. The weightings of each of these parameters may be changed to make it more or less important than the other components.

The minimum variance controllers are obtained by taking the partial derivative of J with respect to $\theta(i)$ and setting this equal to zero:

$$\frac{\partial J}{\partial \theta(i)} = 0 \tag{6.51}$$

The resulting set of equations may be solved for the optimal HHC input $^*\theta(i)$.

The form of the resulting algorithm will depend on whether the global or local system model is used and on whether a deterministic, cautious, or dual controller is desired. For the dual controller the cost functional must be modified to include system probing terms. Detailed descriptions of these algorithms including the terminology for deterministic, cautious, and dual controllers are given in the following sections.

6.4.1.1 Deterministic Controller

For deterministic control, uncertainties in T and Z_0 are ignored and all system parameters are assumed to be known exactly. The cost functional then becomes:

$$J = Z^T(i)W_z Z(i) + \theta^T(i)W_\theta \theta(i) + \Delta\theta^T(i)W_{\Delta\theta}\Delta\theta(i) \tag{6.52}$$

For the local model Eqn. 6.2 is substituted for $Z(i)$ and setting the derivative equal to zero in Eqn. 6.51 leads to an expression for the optimal control. The algebra involved is quite lengthy but will be outlined for this one case. First substituting Eqn.6.2 in Eqn. 6.52 gives:

$$J = [Z(i-1) + T(\theta(i) - \theta(i-1))]^T W_z [Z(i-1) + T(\theta(i) - \theta(i-1))]$$

$$+ \theta^T(i)W_\theta \theta(i) + [\theta(i) - \theta(i-1)]^T W_{\Delta\theta}[\theta(i) - \theta(i-1)] \tag{6.53}$$

Expanding the transposes gives:

$$J = [Z^T(i-1)W_z T - \theta^T(i-1)T^T W_z T - \theta^T(i-1)W_{\Delta\theta}]\theta(i)$$

$$+ \theta^T(i)[T^T W_z Z(i-1) - T^T W_z T\theta(i-1) - W_{\Delta\theta}\theta(i-1)]$$

$$+ \theta^T(i)[T^T W_z T + W_\theta + W_{\Delta\theta}]\theta(i) + Z^T(i-1)W_z(Z(i-1) - T\theta(i-1))$$

$$+ \theta^T(i-1)[W_{\Delta\theta}\theta(i-1) - T^T W_z(Z(i-1) - T\theta(i-1))] \tag{6.54}$$

Taking the derivative with respect to $\theta(i)$ gives:

$$\frac{\partial J}{\partial \theta(i)} = [Z^T(i-1)W_z T - \theta^T(i-1)T^T W_z T - \theta^T(i-1)W_{\Delta\theta}]$$

$$+ [T^T W_z Z(i-1) - T^T W_z T\theta(i-1) - W_{\Delta\theta}\theta(i-1)]$$

$$+ 2[T^T W_z T + W_\theta + W_{\Delta\theta}]\theta(i) = 0 \tag{6.55}$$

Solving for the optimal control $^*\theta(i)$ gives:

$$^*\theta(i) = D\Big[-T^T W_z Z(i) + W_{\Delta\theta}\theta(i) + T^T W_z T\theta(i)\Big] \tag{6.56}$$

where:

$$D = \Big[T^T W_z T + W_\theta + W_{\Delta\theta}\Big]^{-1} \tag{6.57}$$

Subtracting $\theta(i)$ from both sides gives:

$$^*\Delta\theta(i+1) = D\Big[-T^T W_z Z(i) - W_\theta\theta(i)\Big] \tag{6.58}$$

For the global model, using Eqn. 6.1, $Z_0 + T\theta(i)$ may be substituted for $Z(i)$ giving:

$$^*\theta(i+1) = D\Big[-T^T W_z Z_0 + W_{\Delta\theta}\theta(i)\Big] \tag{6.59}$$

or:

$$^*\Delta\theta(i+1) = D\Big[-T^T W_z Z_0 + W_\theta\theta(i) - T^T W_z T\theta(i)\Big] \tag{6.60}$$

6.4.1.2 Cautious Controller

A cautious controller takes account for system parameter uncertainties by taking the expected value of the cost functional. The control θ is assumed to be explicitly known so that all uncertainty is in the vibrations Z. The cost functional then becomes:

$$J = E\left\{\sum_j W_{zjj} Z_j^2(i)\right\} + \theta^T(i) W_\theta \theta(i) + \Delta\theta^T(i) W_{\Delta\theta} \Delta\theta(i) \tag{6.61}$$

For the local HHC model, Eqn. 6.2 is used for $Z(i)$ and the covariance of the jth row of the T matrix, $P_j(i)$, is taken from the Kalman filter for the local case, giving:

$$E\left\{\sum_j W_{zjj} Z_j^2(i)\right\} = Z^T(i) W_z Z(i) + \Delta\theta^T(i)\left(\sum_j W_{zjj} P_j(i)\right)\Delta\theta(i) \tag{6.62}$$

The solution may be found by defining an effective $W_{\Delta\theta}$ as:

$$W_{\Delta\theta_{eff}} = W_{\Delta\theta} + \sum_j W_{zjj} P_j(i) \tag{6.63}$$

and substituting in Eqn. 6.56. The optimal control is then:

$$^*\theta(i+1) = D\left[-T^T W_z Z(i) + \left(W_{\Delta\theta} + T^T W_z T + \lambda_c \sum_j W_{zjj} P_j(i)\right)\theta(i)\right] \tag{6.64}$$

$$^*\Delta\theta(i+1) = D\left[-T^T W_z Z(i) - W_\theta \theta(i)\right] \tag{6.65}$$

where:

$$D = \left[T^T W_z T + W_\theta + W_{\Delta\theta} + \lambda_c \sum_j W_{zjj} P_j(i) \right]^{-1} \tag{6.66}$$

The constant λ_c has been introduced to allow modification of the amount of caution in the controller. For $\lambda_c = 0$ this reduces to the deterministic controller. This controller introduces a constraint on the rate of change of control similar to $W_{\Delta\theta}$. This control is proportional to the uncertainty in the T matrix. As the covariance of the T matrix increases, the rate of change allowed by the cautious controller is reduced.

For the global HHC model, Eqn. 6.1 is used for $Z(i)$. Uncertainties in $Z(i)$ are now due to both Z_0 and T. This gives:

$$E\left\{ \sum_j W_{zjj} Z_j^2(i) \right\} = Z^T(i) W_z Z(i) + \underline{\theta}^T(i) \left(\sum_j W_{zjj} \underline{P}_j(i) \right) \underline{\theta}(i) \tag{6.67}$$

where $\underline{\theta}$ and $\underline{P}_j$ are defined in Eqns. 6.34 and 6.39. The optimal control is found by using J as defined in Eqns. 6.61 and 6.67 in Eqn. 6.51. After algebraic manipulations similar to Eqns. 6.53 through 6.55 the optimal solution is:

$$^*\theta(i+1) = D\left[-T^T W_z Z_0 + W_{\Delta\theta}\theta(i) - \lambda_c \sum_j W_{zjj} P_{12j}^T \right] \tag{6.68}$$

where now:

$$D = \left[T^T W_z T + W_\theta + W_{\Delta\theta} + \lambda_c \sum_j W_{zjj} P_{22j}(i) \right]^{-1} \tag{6.69}$$

The constant λ_c has been added in again as in the local cautious controller. This controller introduces a constraint on the magnitude of the total control angles proportional to the covariance of the T matrix. It also adds a constant term to the solution which is proportional to the cross covariance P_{12}.

6.4.1.3 Dual Controller

A dual controller attempts to improve long term system identification by actively probing the system while at the same time maintaining good control. Optimal dual controllers generally are too conplex for practical implementation. the sub-optimal dual controller presented here is taken from Ref. 23 and is presented in Refs. 36 and 11. In this approach, the cost functional J of Eqn. 6.52 is modified by having a term added which is a function of the estimation error and acts to probe the system. The new cost functional is:

$$J_D = J - \lambda_D \frac{|P(i)|}{|P(i+1)|} \tag{6.70}$$

Here $|\,|$ indicates the determinant of a matrix. The controller therefore attempts to provide good control by minimizing J while furthermore attempting to reduce $P(i)$ in comparison to $P(i+1)$, i.e. improve identification, in order to reduce the second term in Eqn. 6.70. The constant λ_D allows tuning of the degree of probing by the algorithm. In Ref. 23 it is shown that:

$$\lambda_D \frac{|P(i)|}{|P(i+1)|} = \lambda_D \left[1 + \frac{\Delta\theta^T(i) P(i) \Delta\theta(i)}{R} \right] \qquad \text{(local)} \tag{6.71}$$

$$\lambda_D \frac{|P(i)|}{|P(i+1)|} = \lambda_D \left[1 + \frac{\underline{\theta}^T(i) P(i) \underline{\theta}(i)}{R} \right] \qquad \text{(global)} \tag{6.72}$$

Because this gives a quadratic term in J, it allows the minumum variance solution to be easily found.

For the local HHC model the cost functional is given by Eqns. 6.70 and 6.71. The dual control solution may be found by replacing $W_{\Delta\theta}$ by an effective $W_{\Delta\theta}$ in Eqns. 6.56 through 6.58.

$$W_{\Delta\theta_{eff}} = W_{\Delta\theta} - \lambda_D \frac{P(i)}{R} \tag{6.73}$$

This leads to the following solution:

$$^*\theta(i+1) = D\left[-T^T W_z Z(i) + \left(W_{\Delta\theta} + T^T W_z T - \lambda_D \frac{P(i)}{R} \right) \theta(i) \right] \tag{6.74}$$

where:

$$D = \left[T^T W_z T + W_\theta + W_{\Delta\theta} - \lambda_D \frac{P(i)}{R} \right]^{-1} \tag{6.75}$$

Subtracting $\theta(i)$ from both sides gives:

$$^*\Delta\theta(i+1) = D\left[-T^T W_z Z(i) - W_\theta \theta(i) \right] \tag{6.76}$$

The probing term in the local model control leads to a reduction in the constraint on the rate of change of the control proportional to the covariance of the T matrix.

For the global HHC model the cost functional is given by Eqns. 6.70 and 6.72. This gives:

$$J_D = Z^T(i)W_z Z(i) + \theta^T(i)W_\theta \theta(i) + \Delta\theta^T(i)W_{\Delta\theta}\Delta\theta(i)$$

$$- \lambda_D \underline{\theta}^T(i)\frac{P(i)}{R}\underline{\theta}(i) \tag{6.77}$$

Comparing this with the cautious controller in Eqns. 6.61, 6.62, and 6.64 through 6.66 leads to the following dual controller:

$$^*\theta(i+1) = D\left[-T^T W_z Z_0 + W_{\Delta\theta}\theta(i) - \lambda_D \frac{P_{12}^T}{R} \right] \tag{6.78}$$

where now:

$$D = \left[T^T W_z T + W_\theta + W_{\Delta\theta} - \lambda_D \frac{P_{22}}{R} \right]^{-1} \tag{6.79}$$

Again P_{12} and P_{22} are as defined in Eqn. 6.39.

The probing term in the global HHC model dual controller reduces the effective constraint on control magnitude in proportion to the covariance of the T matrix. In addition a constant term is added to the control which is proportional to the crosscovariance P_{12} .

6.4.1.4 General Minimum Variance Controller

Reference 11 suggests that the deterministic, cautious, and dual controllers just outlined can be programmed into two combined algorithms, one for the

local and one for the global HHC model. This form depends on the assumption that the noise characteristics for each row of Z_0 and the T matrix are the same so that P is the same for each row. In these algorithms the appropriate controller can be implemented by changing the value of a parameter β. The algorithms are as follows:

Local Model

$$^{*}\Delta\theta(i+1) = -D\left[W_\theta\theta(i) + T^T W_z Z(i)\right] \tag{6.80}$$

$$D = \left[T^T W_z T + W_\theta + W_{\Delta\theta} + \beta\lambda P\sum_j W_{zjj}\right]^{-1} \tag{6.81}$$

Global Model

$$^{*}\Delta\theta(i+1) = -D$$

$$\times\left[\left(T^T W_z T + W_\theta + \beta\lambda P_{22}\sum_j W_{zjj}\right)\theta(i) + T^T W_z Z_0 + \beta\lambda P_{12}^T\sum_j W_{zjj}\right] \tag{6.82}$$

$$D = \left[T^T W_z T + W_\theta + W_{\Delta\theta} + \beta\lambda P_{22}\sum_j W_{zjj}\right]^{-1} \tag{6.83}$$

In each case the value of β is given by:

Controller	Value of β
Deterministic	0
Cautious	1
Dual	$\dfrac{-1}{R\sum_j W_{zjj}}$

6.4.2 *LMS Direct Inverse Control*

Direct inverse control with LMS identification of the inverse matrix was implemented by Jacklin[32,33]. From Eqn. 6.2, if $T\Delta\theta$ is equal to $-Z(i)$ then vibration will be eliminated. This leads to the inverse control $\Delta\theta$ given by Eqn. 6.41. As in Eqns. 6.41 and 6.42, the optimal change in HHC, ${}^{*}\Delta\theta(i)$, is found by direct multiplication of the C matrix and the total vibration vector $y(i)$. The C matrix performs the inverse of the operation carried out by the T matrix however it does not have to be the formal inverse, in a mathematical sense, of the T matrix. The inverse matrix C is identified using the LMS identification algorithm explained previously. In Ref. 32 it was found that even when vibrations were nearly eliminated, a steady-state error in inverse matrix identification remained because as vibrations went to zero the update term for the inverse matrix also went to zero. To improve identification, a control relaxation parameter was used allowing the implemented control to be only a fraction of commanded control:

$$ {}^{*}\theta(i+1) = \theta(i) + K_{cr}{}^{*}\Delta\theta \tag{6.84} $$

The use of control relaxation was shown to produce lower steady-state identification errors at the expense of slower vibration reduction.

6.5 HHC IMPLEMENTATION

6.5.1 *HHC Input Formulation*

Required HHC pitch commands are introduced into the structural model as time varying changes in the blade root pitch angle. Two methods of formulating the HHC inputs will be presented. The first method expresses HHC components in terms of the magnitude and phase of a sine input. This is useful when dealing with open loop applications of HHC but does not allow each degree of freedom to be varied while all others remain zero. The second method of formulation expresses HHC components in terms of the amplitudes of sine and cosine inputs. This allows the degrees of freedom to be individually incremented and lends itself to implementation of automatic controllers.

<u>First Formulation</u>

$$\theta_{HH} = [\theta_0 \sin(\overline{\omega}_{HH}\psi + \phi_o)] + [\theta_C \sin(\overline{\omega}_{HH}\psi + \phi_c)] \cos\psi$$

$$+ [\theta_S \sin(\overline{\omega}_{HH}\psi + \phi_s)] \sin\psi \tag{6.85}$$

where $\overline{\omega}_{HH} = \dfrac{\omega_{HH}}{\Omega}$ and θ_0, θ_C, θ_S, ϕ_o, ϕ_c, ϕ_s, and $\overline{\omega}_{HH}$ are constant with respect to ψ.

In addition, expressions for the first and second derivatives of θ_{HH} with respect to ψ are needed. They are as follows.

$$\overset{*}{\theta}_{HH} = [\theta_0 \overline{\omega}_{HH} \cos(\overline{\omega}_{HH}\psi + \phi_o)]$$

$$+ [\theta_S \overline{\omega}_{HH} \cos(\overline{\omega}_{HH}\psi + \phi_s) - \theta_C \sin(\overline{\omega}_{HH}\psi + \phi_c)] \sin \psi$$

$$+ [\theta_C \overline{\omega}_{HH} \cos(\overline{\omega}_{HH}\psi + \phi_c) + \theta_S \sin(\overline{\omega}_{HH}\psi + \phi_s)] \cos \psi \tag{6.86}$$

$$\overset{**}{\theta}_{HH} = [- \theta_0 \overline{\omega}_{HH}^2 \sin(\overline{\omega}_{HH}\psi + \phi_o)]$$

$$+ [2\theta_S \overline{\omega}_{HH} \cos(\overline{\omega}_{HH}\psi + \phi_s) - \theta_C(1 + \overline{\omega}_{HH}^2) \sin(\overline{\omega}_{HH}\psi + \phi_c)] \cos \psi$$

$$+ [-2\theta_C \overline{\omega}_{HH} \cos(\overline{\omega}_{HH}\psi + \phi_c) - \theta_S(1 + \overline{\omega}_{HH}^2) \sin(\overline{\omega}_{HH}\psi + \phi_s)] \sin \psi \tag{6.87}$$

<u>Second Formulation</u>

$$\theta_{HH} = [\theta_{0S} \sin \overline{\omega}_{HH}\psi + \theta_{0C} \cos \overline{\omega}_{HH}\psi]$$

$$+ [\theta_{CS} \sin \overline{\omega}_{HH}\psi + \theta_{CC} \cos \overline{\omega}_{HH}\psi] \cos \psi$$

$$+ [\theta_{SS} \sin \overline{\omega}_{HH}\psi + \theta_{SC} \cos \overline{\omega}_{HH}\psi] \sin \psi \tag{6.88}$$

where θ_{0C}, θ_{0S}, θ_{CS}, θ_{CC}, θ_{SS}, and θ_{SC} are constant with respect to ψ.

The first and second derivatives of θ_{HH} with respect to ψ are as follows.

$$\overset{*}{\theta}_{HH} = [\theta_{0S} \overline{\omega}_{HH} \cos \overline{\omega}_{HH}\psi - \theta_{0C} \overline{\omega}_{HH} \sin \overline{\omega}_{HH}\psi]$$

$$+ [(\theta_{CS} \overline{\omega}_{HH} + \theta_{SC}) \cos \overline{\omega}_{HH}\psi + (-\theta_{CC} \overline{\omega}_{HH} + \theta_{SS}) \sin \overline{\omega}_{HH}\psi] \cos \psi$$

$$+ [(\theta_{SS} \overline{\omega}_{HH} - \theta_{CC}) \cos \overline{\omega}_{HH}\psi - (\theta_{SC} \overline{\omega}_{HH} + \theta_{CS}) \sin \overline{\omega}_{HH}\psi] \sin \psi \tag{6.89}$$

$$\overset{**}{\theta}_{HH} = [- \theta_{0S} \overline{\omega}_{HH}^2 \sin \overline{\omega}_{HH}\psi - \theta_{0C} \overline{\omega}_{HH}^2 \cos \overline{\omega}_{HH}\psi]$$

$$+ [-\{\theta_{CS}(\overline{\omega}_{HH}^2 + 1) + 2\theta_{SC} \overline{\omega}_{HH}\} \sin \overline{\omega}_{HH}\psi$$

$$+\{2\theta_{SS}\overline{\omega}_{HH} - \theta_{CC}(\overline{\omega}_{HH}^2 + 1)\} \cos \overline{\omega}_{HH}\psi] \cos \psi$$

$$+ [\{2\theta_{CC}\overline{\omega}_{HH} - \theta_{SS}(\overline{\omega}_{HH}^2 + 1)\} \sin \overline{\omega}_{HH}\psi$$

$$-\{2\theta_{CS}\overline{\omega}_{HH} + \theta_{SC}(\overline{\omega}_{HH}^2 + 1)\} \cos \overline{\omega}_{HH}\psi] \sin \psi \tag{6.90}$$

The two formulations can be made equivalent through the use of a trigonometric identity.

$$\theta \sin(\omega\psi + \phi) = \theta(\sin \omega\psi \cos \phi + \cos \omega\psi \sin \phi)$$

Using the above identity, the two formulations can be seen to be equivalent if:

$$\theta_{0S} = \theta_0 \cos \phi_o \qquad \theta_{CC} = \theta_C \sin \phi_c$$

$$\theta_{0C} = \theta_0 \sin \phi_o \qquad \theta_{SS} = \theta_S \cos \phi_s$$

$$\theta_{CS} = \theta_C \cos \phi_c \qquad \theta_{SC} = \theta_S \sin \phi_s \tag{6.91}$$

For the closed-loop HHC implementation, the control vector θ will be defined as:

$$\theta = \{\theta_{0s} \quad \theta_{0c} \quad \theta_{cs} \quad \theta_{cc} \quad \theta_{ss} \quad \theta_{sc}\}^T \tag{6.92}$$

or an appropriate subset of this vector.

6.5.2 *Minimization Objectives*

From the calculations described and presented in Ch. 5, rotor hub forces and moments are available in three orthogonal directions. In the absence of any modeling of the fuselage dynamics, these give the best available indication of helicopter vibration levels. Sine and cosine components of the 4/rev. forces and moments are available as well as their peak-to-peak values. Any combination of these quantities could be used as an indication of vibration levels and therefore be chosen to be minimized. In this study the sine and cosine components of the 4/rev. hub forces in the vertical, lateral, and longitudinal directions are chosen to be minimized. Decreases in vibration levels will be given in terms of the peak-to-peak values of these forces. For closed-loop HHC studies, using the notation of Ch. 5, the vector of hub vibratory shears Z will be defined as:

$$Z = \{\bar{\bar{s}}_{vts4} \quad \bar{\bar{s}}_{vtc4} \quad \bar{\bar{s}}_{lts4} \quad \bar{\bar{s}}_{ltc4} \quad \bar{\bar{s}}_{lns4} \quad \bar{\bar{s}}_{lnc4}\}^T \tag{6.93}$$

or an appropriate subset of this vector.

Chapter VII

RESULTS SHOWING EFFECTS OF UNSTEADY AERODYNAMICS

7.1 BASELINE BLADE CONFIGURATIONS

The results presented in this chapter were calculated using two baseline blade configurations. A soft-in-plane and a stiff-in-plane hingeless configuration identical to those used in Ref. 8 were used. All results in this chapter except those comparing the trim procedures were calculated using the flap trim procedure.

The baseline soft-in-plane blade has fundamental, rotating, uncoupled natural frequencies in lag, flap, and torsion of 0.735/rev, 1.123/rev, and 3.17/rev respectively. The rotor consists of four blades. The Lock number is $\gamma = 5.5$, the rotor solidity is $\sigma = 0.07$, and the rotor thrust coefficient is $C_T = 0.005$. The blade has zero precone β_p, zero root offset e_1 , and no built in twist. The offset between the elastic axis and the center of gravity, x_I, and the offset between the elastic axis and the aerodynamic center, x_A, are both zero. All blade properties are uniform across the span. The blade chord is $c = 0.055R$, the lift curve slope is $a = 2\pi$, and the profile drag coefficient is $C_{D0} = 0.01$.

The baseline stiff-in-plane blade is identical to the baseline soft-in-plane blade except that the fundamental rotating lag frequency is 1.42/rev.

7.2 COMPARISON WITH PREVIOUS UNSTEADY RESULTS

In Ref. 13 finite-state time-domain unsteady aerodynamics were incorporated in a simple rigid blade, offset hinged spring model of a blade with flap and lag degrees of freedom. The intent of this study was to simulate the same soft-in-plane blade described in the last section, except that the torsional degree of freedom was not included. Unsteady effects were incorporated using two augmented states governing the unsteady aerodynamics at a typical section at 3/4R. These two augmented states were solved for as explicit state variables along with those for flap and lag.

The present study uses an elastic hingeless blade with coupled flap-lag-torsional degrees of freedom which is a much more realistic model of an actual blade. The current model can be made to give results quite similar to the model of Ref. 13 by increasing the torsional stiffness of the blade so that it resembles a torsionally rigid blade. With this in mind, a model identical to the baseline soft-in-plane blade, but with a fundamental torsional frequency of 6.4/rev. was used to determine aeroelastic response and stability of the blade using the unsteady aerodynamic formulation of Ref. 13. This blade will be referred to as the baseline torsionally stiff blade.

Figure 7.1 presents the flap and lag blade tip responses as a function of azimuth. Plots taken from Ref. 13 for the rigid offset hinged spring restrained soft-in-plane blade are also included. The flap responses from Ref. 13 and for the torsionally stiff blade are quite similar while the lag responses show the

same variation with azimuth but differ considerably in magnitude. These differences are reasonable since the structural models are completely different. Decreasing the torsional stiffness to a more realistic level, that of the soft-in-plane blade, leads to a considerably different flap response.

Figure 7.2 presents the stability in the first flap and first lag modes for the same three cases. Basic stability trends are the same in all three cases and the instability of Ref. 13 is present in the first flap mode for each model. Although the first flap eigenvalue branch point for the soft-in-plane blade is at a slightly higher advance ratio, all three cases become unstable at the same advance ratio of $\mu = 0.45$.

As was explained in Chapt. 4, the instability of Ref. 13 was due to an error in formulation which led to a singularity in flap loads at high advance ratios. The formulation of this study eliminates this singularity and in addition applies the aerodynamics in a more realistic manner.

Figure 7.3 presents the blade tip response in flap, lag, and torsion, at an advance ratio of $\mu = 0.4$, for the soft-in-plane blade using the aerodynamic formulation of Ref. 13 and the inproved formulation of this study. Because the singularity of Ref. 13 was sharply localized at $\mu = 0.45$, even at an advance ratio of $\mu = 0.4$ the vertical aerodynamic loads are reasonable. Much of the difference in response is due to the new formulation allowing the augmented states to vary along the blade.

Figure 7.4 shows the variation in first flap and first lag eigenvalues with advance ratio. Lag stability differs very little for the two cases. The sudden instability at $\mu = 0.45$ found using the aerodynamic formulation of Ref. 13 is eliminated using the formulation of this study.

7.3 COMPARISON OF QUASISTEADY AND UNSTEADY RESULTS

7.3.1 *Response and Stability*

Response and stability calculations were carried out for the baseline soft-in-plane and stiff-in-plane blades using the quasisteady aerodynamics of Ref. 8 and the unsteady formulation of this study. Blade tip response in flap, lag, and torsion have been plotted for the two cases at advance ratios of $\mu = 0.2$ and $\mu = 0.4$. Figures 7.5 and 7.6 show the responses for the soft-in-plane blade at $\mu = 0.2$ and $\mu = 0.4$. Figures 7.7 and 7.8 show the same responses for the stiff-in-plane blade.

It can bee seen that the unsteady effects produce only moderate differences in the flap and lag responses. The response in the presense of the unsteady loads tends to lag behind that with quasisteady loads due to the phase lag and amplitude modulation associated with the unsteady aerodynamics[13]. As is evident from Figs. 7.6 and 7.8, the influence of the unsteady aerodynamics on the torsional response is more pronounced. This is due in part to the inclusion of several higher order apparent mass terms in Eqn. 4.17,-the expression for

the noncirculatory aerodynamic moment in the unsteady aerodynamic formulation, which were not included in the quasisteady formulation.

In order to determine the importance of these terms, response calculations were carried out at an advance ratio of $\mu = 0.4$ using a quasisteady aerodynamic formulation which included these apparent mass terms. Figures 7.9 and 7.10 show the flap, lag, and torsional response using quasisteady aerodynamics without the apparent mass terms, quasisteady aerodynamics with the apparent mass terms, and unsteady aerodynamics. It can be seen that the apparent mass terms effect all three responses to some degree, but that there is a significant change in the torsional response. This indicates that these apparent mass terms can be important and should not be neglected as they have been in may previous aerodynamic formulations.

For the case of hover, there is no unsteadiness in the aerodynamics and the apparent mass terms are zero. The response therefore is identical to that of the quasisteady aerodynamics of Ref. 8. There are slight differences in hover stability due to the unsteady effects on time derivatives in hover.

Stability plots for the soft and stiff-in-plane blades are shown in Figs. 7.11 through 7.14. The variation with advance ratio of the real part of the characteristic exponent associated with each mode is plotted. The influence of time domain unsteady aerodynamics on lag and torsional mode stability is small. This is reasonable since the primary correction in the unsteady aerodynamics theory is to the lift. The influence of the unsteadiness on the drag, which in-

fluences the lead lag motion, is small. There is however a noticeable effect of unsteady aerodynamics on the flap modes, particularly at higher advance ratios and with the soft-in-plane blade.

7.3.2 *Hub Vibratory Loads*

In Ref. 8, 4/rev. vertical hub shears were calculated using quasisteady aerodynamics. The blade structure was then optimized to reduce these shears. As described in Ch. 3, Ref. 8 used a less precise convergence criterion than the convergence control parameter used in this study when determining whether convergence of quasilinearization had occured. Furthermore, less stringent local error bounds were used when solving the differential equation associated with quasilinearization. The procedure employed in Ref. 8 was adequate for determining the low frequency response and stability of the blade, but led to response solutions which were not actually converged in the higher harmonics. This led to incorrect values of the 4/rev. shears which may have contributed to the inconsistent behavior of the optimization results.

As an example, Fig. 7.15 shows the variation with advance ratio of the 4/rev. vertical and lateral hub shears for the soft-in-plane blade as calculated in Ref. 8 and their comparison to the response solution obtained in this study. In both cases the same quasisteady aerodynamic formulation was used. The response solution obtained in this study was calculated by carrying out one additional iteration of quasilinearization beyond that used in Ref. 8 with in

addition much tighter local error bounds. From Fig. 7.15 it can be seen that the not completely converged response solution produces substantially different vertical hub shears. With the converged response of this study, the peculiar dip in vertical hub shears at an advance ratio of $\mu = 0.3$ completely disappeared. The effect of this convergence problem on the lateral hub shear is much less severe, as is evident from Fig. 7.15.

Hub shear and moment calculations were carried out for the baseline soft-in-plane and stiff-in-plane blades using the quasisteady aerodynamics of Ref. 8 and the unsteady formulation of this study. Figures 7.16 through 7.21 plot the variation with advance ratio of the six different 4/rev. hub shears and moments. All shears and moments vary somewhat depending on the aerodynamics used. The most significant variation is in vertical shears which show a large difference in magnitude which increases with advance ratio. This is reasonable since the primary correction in the unsteady aerodynamic theory is that due to the lift.

7.4 COMPARISON OF OLD AND NEW TRIM RESULTS

The flap trim and full trim procedures described in Ch. 3 were used to determine the collective pitch θ_0, cyclic pitch θ_{1s} and θ_{1c}, inflow ratio λ, and rotor angle of attack α_R which are required to trim the rotor.

With the full trim procedure, essentially identical results were found using quasisteady and unsteady aerodynamics. At hover, the quasisteady and un-

steady aerodynamic models give identical air loads and so the trim conditions are identical. With the simplified aeroelastic model used in the full trim analysis, only the constant and 1/rev components of each generalized coordinate are retained in forward flight. The high frequency motions which contribute to unsteady airloads are therefore not modeled and it is to be expected that nearly identical trim states should result. Furthermore it should be noted that the flap trim procedure does not have the provision for incorporating the unsteady aerodynamics.

Figures 7.22 and 7.23 depict changes in the trim parameters with advance ratio for the flap trim and full trim procedures using the baseline soft-in-plane blade. From Fig. 7.22 the value of the collective pitch θ_0 can be seen to differ most at hover and to become essentially identical at $\mu = 0.3$ or above. Conversely the value of the inflow ratio λ is nearly identical up to $\mu = 0.1$ and then the difference increases somewhat at higher advance ratios. The rotor angle of attack α_R varies considerably above hover, but since α_R is not an explicit variable in the quasilinearization routine, this does not directly effect the rotor response. From Fig. 7.23 the cosine cyclic θ_{1c} varies only slightly between the two procedures while the sine cyclic θ_{1s} differs somewhat at advance ratios above $\mu = 0.2$.

Overall the two trim procedures produce quite similar results for the soft-in-plane blade. It is expected that more realistic blades, having for instance cross-sectional offsets and non-uniform properties, which cannot be modeled

by the flap trim procedure, will show more significant differences between the two procedures.

Figure 7.24 shows blade tip response for the flap trim and full trim procedures applied to the soft-in-plane blade. In each case the trim values determined from the trim procedure were used in the full aeroelastic model with unsteady aerodynamics at an advance ratio of $\mu = 0.3$. The nonlinear response solution was determined and the nondimensional tip displacements in flap, lag, and torsion are plotted versus blade azimuth. Lag and torsional response vary little between the two cases, however the flap response changes considerably. The change in magnitude of the flap response is due primarily to the change in the inflow ratio λ at this advance ratio, while the different value of the sine cyclic pitch θ_{1s} changes the phase of the response somewhat.

The two trim procedures led to almost identical stability eigenvalues for the blade. The largest difference in value of the real part of the eigenvalue for any mode at any advance ratio was less than 2%. Therefore these results are not presented here.

The 4/rev. hub shears and moments were calculated for the soft-in-plane blade using the response solution obtained with both the flap trim and the full trim. Figures 7.25 through 7.27 dipict of the variation, with advance ratio, of the six shears and moments. Application of the coupled trim procedure resulted in somewhat higher hub shears and somewhat lower hub moments than those due to flap trim. The largest difference was in the vertical hub shears.

This behavior is reasonable since the vertical hub shears are dependent on the flapping response which was shown to differ considerably for the two trim formulations.

Chapter VIII

OPEN LOOP RESULTS

8.1 INTRODUCTION

This section presents the results obtained during the open-loop application of HHC. The primary objective here is to gain an understanding of basic trends in rotor response to HHC and to provide initial estimates of the HHC transfer matrix T which is required for starting the closed-loop HHC algorithms. The baseline soft-in-plane blade, as described in Ch. 7, was used in all these calculations. Trim was calculated using the full trim procedure.

8.2 HUB LOAD VARIATION WITH HHC PHASE

As shown in Ch. 6, the HHC inputs can be expressed as a sine function with a phase offset, applied to each of the collective, lateral, and longitudinal control channels. A 1/3° HHC pitch input of the form:

$$\theta_{HH} = 1/3^\circ \sin(\psi - \phi_{HH}) \tag{8.1}$$

was applied to each of the three control channels with the phase ϕ_{HH} being allowed to vary from 0° to 360° in 90° increments. These calculations were carried out for both the quasisteady and the unsteady aerodynamic models.

Figures 8.1 through 8.9 present the variation in hub shears and moments with HHC phase angle in the three control channels for quasisteady and unsteady aerodynamics. Generally for a given shear or moment, if HHC in any of the three control channels is phased correctly, a minimum value of the shear or moment can be obtained. Except for the case of yawing moments, and vertical shears with collective or lateral inputs, this minimum is below the baseline value.

The major difference in responses to HHC between quasisteady and unsteady aerodynamics are in the vertical shears. For all the control channels, the HHC phase at which minimum vertical shears with unsteady aerodynamics are obtained, leads the value calculated with quasisteady aerodynamics by about 90°. In the case of collective and lateral HHC input, the unsteady formulation shows shears above the baseline values for any phasing, while the quasisteady formulation indicates a minimum below the baseline value. With longitudinal input both the aerodynamic models show substantial decreases below the baseline for vertical shears with correct HHC phasing. In actual flights tests[67] also, longitudinal control has been shown to be most effective in alleviating vertical shears.

Rolling and pitching moments show similar behavior of the responses with both aerodynamic formulations and for control inputs in all three channels. Lateral and longitudinal shears show similar response patterns for the two formulations. The responses have similar phases and magnitudes of excursion

from the baseline but are offset by the difference in baseline peak-to-peak shear values.

8.3 LINEARITY OF RESPONSE TO HHC

Linear optimal control theory assumes linear response to control input. It is therefore important that actual response of the model be at least fairly linear over some reasonable range for the HHC to be most effective. The assumption used in the control formulation is that the 4/rev. sine and cosine harmonics of the hub shears vary linearly with the 4/rev. sine and cosine HHC harmonic inputs. To verify this assumption, HHC inputs of -1/3° through 3° in 2/3° increments were applied to the θ_{CC} HHC degree of freedom, i.e. the cosine component in the longitudinal control channel. The calculations were carried out for quasisteady and unsteady aerodynamics at an advance ratio of $\mu = 0.3$.

The variations in the sine and cosine harmonics of the 4/rev. hub shears with HHC input pitch magnitude are shown in Figs. 8.10 and 8.11. The relationship between control harmonics can be seen to be quite linear over this range for both aerodynamic formulations. The difference in response between the two aerodynamic models can be seen to vary from slight offsets to substantially different slopes and intercepts. Thus the transfer matrices needed for control implementation can be expected to differ greatly for the two formulations. The variation of peak-to-peak hub shears with HHC magnitude are shown in Fig. 8.12. The peak-to-peak shears are a function of the squares

of the sine and cosine harmonics and thus are not linear with HHC magnitude. As can be seen, they show distinct minima, with HHC magnitudes above or below this value giving higher shears.

8.4 TRANSFER MATRIX CALCULATION

Initial estimates for the HHC transfer matrix at the baseline were calculated by incrementing each of the six control degrees of freedom by 1/3°. From Eqn. 6.1 and 6.2 it can be seen that at the baseline, with no initial HHC input, both the local and the global HHC models reduce to:

$$\Delta Z = T\Delta\theta \tag{8.2}$$

From this it can be seen that, assuming low process and measurement noise, the columns of the T matrix can be calculated by incrementing each element of θ individually, calculating the changes in hub shears due to this increment, and dividing their values by the magnitude of the control increment. For instance setting the first element of θ to one and all other elements to zero, and multiplying this vector times the T matrix, will result in a vector identical to the first column of the T matrix. Baseline transfer matrices were calculated using quasisteady and unsteady aerodynamics and are given in tables 8.1 and 8.2.

The calculated baseline transfer matrices for the quasisteady and unsteady aerodynamic cases differ greatly. In order to see basic trends for the two cases, the bar chart given in Fig. 8.13 has been constructed showing the proportional

TABLE 8.1

Quasisteady HHC Transfer Matrix

0.3145325	-0.2224358	-0.0447006	0.0600985	-0.1066384	-0.2511157
-0.2216286	-0.3188984	0.0572526	0.0441021	-0.2526287	0.1064007
-0.0680207	-0.0575412	0.0156767	0.0122215	-0.0879807	0.0091254
-0.0569284	0.0649546	0.0097563	-0.0127674	0.0093927	0.0814574
0.0041394	0.0806664	-0.0532560	0.0065953	-0.0125365	-0.0249821
0.0734329	-0.0100913	0.0120377	0.0480450	-0.0136280	0.0000364

TABLE 8.2

Unsteady HHC Transfer Matrix

0.3975075	-0.0000851	-0.0326116	0.0052673	0.0276221	-0.2291952
0.0018428	-0.3944278	0.0092679	0.0358874	-0.2285797	-0.0251755
-0.0298565	-0.0405612	-0.0071383	0.0244647	-0.0822938	0.0075192
-0.0408923	0.0294869	0.0244328	0.0068263	0.0067259	0.0820623
-0.0094324	0.0419992	-0.0516340	0.0210999	0.0071792	-0.0322288
0.0422244	0.0102764	0.0220154	0.0528939	-0.0321438	-0.0064157

changes in shears due to each of the 1/3° HHC incrementations. From this chart some general observations can be made. The vertical shears are effected much more by HHC than the lateral or longitudinal shears. The difference in response with quasisteady and unsteady aerodynamics is greatest for vertical shears which are most directly dependent on the aerodynamic lift where the two formulations differ. Collective and longitudinal HHC inputs have a greater relative effect on shears than lateral HHC inputs.

Chapter IX

CLOSED-LOOP CONTROL RESULTS

9.1 INTRODUCTION

One of the main objectives of this study was to reduce the vertical, lateral, and longitudinal 4/rev. hub shears. Sine and cosine components of each of these three shears were to be minimized by the control algorithms. In applying the control algorithms to the quasilinearization model, a control vector was first calculated using the baseline response. The vibratory response of the rotor with this control was then found and this information was used in calculating an improved control vector. Physically this is equivalent to allowing all transients to die out between control changes. The response due to the new control values was then calculated and the process was continued for a given number of iterations or until no further decrease in shears was observed.

The baseline soft-in-plane blade described in Ch. 7 was used in all these studies. Unless otherwise stated, all the control calculations were done at an advance ratio of $\mu = 0.3$. Trim was calculated using the full trim procedure. The initial baseline transfer matrices for the quasisteady and unsteady aerodynamic models at this advance ratio were those calculated in Ch. 8.

9.2 FIXED GAIN CONTROL

The baseline HHC transfer matrices were used to construct fixed gain controllers. For these controllers, there was no identification of control parameters and the hub shears were assumed known exactly. Control was therefore determined by a simple inverse relation:

$$\theta(i+1) = T^{-1}Z(i) \tag{9.1}$$

This assumes the local HHC model for multistep application. The first step is the same as a global controller, which is a one step process when parameters cannot change through identification.

With quasisteady aerodynamic modeling the HHC input angles, as shown in Fig. 9.1, moved smoothly to their optimums with almost no overshoot or oscillation. The peak-to-peak values of the three shears were reduced smoothly to less than 2% of their baseline values within five iterations as shown in Fig. 9.2. With unsteady aerodynamic modeling the HHC input angles also moved smoothly to their optimums, as shown in Fig. 9.3. With unsteady aerodynamic modeling the hub shears were reduced to less than 5% of their baseline values in two iterations but the vertical shear had risen to 10% of its baseline value by the fifth iteration.

These results indicate that both transfer matrices were quite good estimates of the actual relationship between HHC input and hub shear harmonics at the optimal HHC angles. The increase in vertical shear with continued iterations

for the unsteady case indicates that this transfer matrix was not quite as good an estimate as the quasisteady transfer matrix.

9.3 ADAPTIVE CONTROL AT DESIGN FLIGHT CONDITION

The minimum variance controller described in Ch. 6 provides for one local and three global controller designs using different Kalman identification schemes. These were referred to as controllers 1, 2, 3, and 4. Each of these controllers may be implemented as a deterministic, cautious, or dual controller. Throughout this study equal weighting was given to the different shear components and no weighting was applied to the control input magnitudes or rates of change. It should be stressed that in these simulations a change in step index from i to $i + 1$ indicates an iteration of quasilinearization rather than any real time increment. Also the Kalman filter identifies computer code output parameters which move in an unpredictable manner but does not have to deal with any articficially introduced noise.

In the initial phase of this investigation the deterministic versions of the four controllers were were implemented for the quasisteady and unsteady aeroelastic models. For these calculations the Kalman filters were initialized by assuming the variances W_0 and W_T, and the initial values of the elements of the covariance matrix P, to be equal with a value of $0.5 \cdot 10^{-2}$, and assuming the variance V to have a value of $0.3 \cdot 10^{-7}$.

Figures 9.5 through 9.7 give the iteration history for the three hub shear conponents for the four controllers applied to the quasisteady model. In each case the first step is identical for deterministic control. The results for cases 1 and 2 are quite similar as are the results for cases 3 and 4. When these controllers were applied to the unsteady model, all four controllers produced almost identical hub shear histories with only vertical shear showing some spread in the responses. All four controllers gave staisfactory results and of the global controllers, controller 4 appeared to give the best results after several iterations. It was decided therefore to continue with more extensive studies using the deterministic and cautious versions of just two controllers, controller 1, a local controller with identification of only the HHC transfer matrix, and controller 4, a global controller with identification of the baseline vibrations and the HHC transfer matrix. In these additional studies the Kalman filter was initialized by assuming the variances V, W, and W_0 to be equal with a value of 0.3×10^{-7} and by initializing the elements of the covariance matrix P as 0.3×10^{-5}.

With quasisteady aerodynamics the difference in control sequence between the deterministic and cautious controllers was relatively small, reflecting the excellent initial transfer matrix. Figures 9.8, 9.9, and 9.10 show the iteration history of the six HHC inputs and the three hub shears for deterministic and cautious versions of the local controller. Figures 9.11 through 9.13 show the same iteration histories for the global controller. All four controllers led to the same control solution for hub shear minimization.

With unsteady aerodynamics the cautious and deterministic controllers show more difference in control values initially but all four quickly converge to the same control values. The deterministic controller tends to slightly overshoot the optimal control on the first iteration. Figures 9.14, through 9.19 show the iteration histories of the HHC inputs and hub shears for the local and global controllers with unsteady aerodynamics.

When applied to either the quasisteady or unsteady model, HHC was able to eliminate essentially all the 4/rev. hub shears. With local control applied to the unsteady model, the vertical shears rise slowly after the second iteration indicating that the transfer matrix identification has not been ideal. Since the control input is changing only slowly and identification of the local T matrix is based on changes in control, this result can be easily anticipated.

Figures 9.20 and 9.21 compare the final hub shear values after five iterations for the four control cases as a percentage of their baseline values. When unsteady aerodynamic effects are included the vertical shear becomes the critical component, being decreased much less than the lateral and longitudinal shears. With quasisteady aerodynamics there is no discernible pattern of one shear being reduced more than another. The unsteady baseline vertical shear started at 1/3 the level of the quasisteady baseline, so in absolute terms rather than as percentages of the baseline, the global controllers produced similar vertical shear magnitudes using the two aerodynamic formulations. The local controllers however were much less successful when used with the unsteady model than they were with the quasisteady model. Figure 9.22 compares the

optimal HHC inputs after five iterations of the local controller using quasi-steady versus unsteady aerodynamics. Completely different, but similarly effective, control inputs are needed for hub shear reductions depending on the type of aerodynamic representation used in the aeroelastic model.

The LMS Direct Inverse Control algorithm described in Ch. 6 provides a simple alternative method of determining HHC inputs for hub shear minimization. This algorithm was implemented using the unsteady aerodynamic model. In Ref. 32, values of the gain term K_s of between 0 and 5 were used. A very simple matrix representation of rotor response to HHC was used, and often on the order of 100 or more iterations were carried out for convergence. When a value of $K_s = 0.3$ was used to implement this control, the results in terms of HHC angle and shear minimization iteration histories were essentially identical to those results already presented for fixed gain HHC calculations and shown in Figs. 9.3 and 9.4. This was because changes in the identified C matrix were too slow to be detectable within five iterations. It was necessary to increase K_s far beyond the range in which stability problems were found in Ref. 32 before appreciable changes in convergence within five iterations were found. Unfortunately the high computational cost of the aeroelastic analysis used here precludes the investigation of convergence characteristics much beyond the fifth HHC iteration.

In order to determine the effect of HHC on overall blade response, the elastic tip deformations in flap, lag, and torsion were plotted for the baseline response and for the optimal response for the case of controller 4, the global

cautious controller. From Fig. 9.23 it can be seen that the principal differences in elastic response are in the flap and torsional degrees of freedom. The torsional response is somewhat missleading in that the actual tip angular deflection includes also a rigid body rotation due to the total blade root angle associated with trim and HHC, and a rotation of the form $w_{,x}v_{,x}$ due to the bending of the blade. When these geometric rotations are added to the tip elastic torsional deflection, the total tip angular displacement shown in Fig. 9.24 results. The term $w_{,x}v_{,x}$ accounts for less than 2% of this total angular displacement. This plot indicates that vibration reduction through HHC is achieved not by reducing overall blade response, but by introducing modified airloads on the blade which cancel out the vibratory hub loads.

9.4 CONTROL WITH STEP CHANGE IN FLIGHT CONDITION

A practical controller must be able to adapt to changing flight conditions. As a test of this ability a step change in flight condition from $\mu = 0.3$ to $\mu = 0.35$ was applied to the deterministic and cautious versions of the local and global controllers. This was done by starting with the converged optimal solution and its response at $\mu = 0.3$, changing the propulsive trim values to those for $\mu = 0.35$, and proceeding with iterative control calculations and quasilinearization solutions.

When this procedure was applied to the local controller there were large oscillations in the calculated control inputs and the resultant hub shears. As

can be seen from Figs. 9.25 and 9.26, these oscillations had damped out considerably by the sixth iteration and all the shears were considerably below the baseline values for this advance ratio.

When this step change in μ was applied to the global controller, there was little oscillation in the required control inputs and the controller moved fairly smoothly from an initial large increase in shears toward a minimum. Figures 9.27 and 9.28 show the iteration history of the HHC inputs and hub shears for this case. The procedure was stopped at five iterations but the shears were continuing to decrease at that point.

A comparison of the three shear components and their baseline values for the local and global controllers is given in Fig. 9.29. As can be seen, the global controller has been more successful in reducing shears. Additional iterations of the analysis would be expected to reduce the shears to lower levels. The less effective performance exhibited by the local controllers is attributed to the method employed for the calculation of the transfer matrices, which is based on changes in control input rather than the total control magnitudes. Since the controllers quickly reached minimum shear levels from the baseline, changes in control became very small and the transfer matrices were not completely identified. When a sudden change in flight condition occurred this uncertainty degraded the controller performance.

Chapter X

HHC FOR ARTICULATED VERSUS HINGELESS ROTORS

10.1 INTRODUCTION

In this chapter the effects of HHC on a hingeless rotor and a roughly equivalent articulated rotor are investigated. This includes comparisons of required control angles, shear minimization, accompanying changes in hub moments, attempts at shear and moment minimization, changes in rotating blade loads, changes in blade stability, and changes in power requirements.

The hingeless rotor used in the study is the same as the baseline soft-in-plane rotor described in Ch. 4 except that a blade root offset from the center of rotation of 5% of the blade elastic length has been introduced. The articulated rotor used was produced from this rotor by introducing hinges in flap and lag at the same 5% blade root offset. Additionally a rotational damper was applied to the articulated blade root lag hinge as is generally required to maintain stability in articulated rotors. This was a viscous damper and gave a nondimensional damping coefficient of:

$$\overline{C} = \frac{C}{m_0 \Omega \ell^3} = 0.02 \tag{10.1}$$

The value 0.02 was chosen as being approximately the value of the damper on an OH6A helicopter rotor blade.

The hingeless blade had fundamental uncoupled rotating natural frequencies in lag, flap, and torsion of 0.783/rev., 1.158/rev., and 3.176/rev. The articulated blade had natural frequencies in lag, flap, and torsion of 0.274/rev., 1.037/rev., and 3.176/rev. Mode shapes for the first six modes were very similar for the two blades except in the area of the blade root where the two structural boundary conditions were different.

Trim calculations were carried out for the hingeless and articulated blades at an advance ratio of $\mu = 0.3$ using the full trim procedure. The required collective and sine cyclic angles were almost identical for the two rotors. The hingeless rotor required a rotor shaft angle 1% higher and a cosine cyclic angle 10% lower than that of the articulated rotor.

Using these trim values, baseline response and stability were calculated for the articulated and hingeless blades at an advance ratio of $\mu = 0.3$. Subsequent HHC calculations were carried out from these baselines. All calculations in this chapter were carried using unsteady aerodynamics.

10.2 REDUCTION OF HUB SHEARS

From the baseline flight condition at an advance ratio of $\mu = 0.3$, initial estimates of the HHC transfer matrices for the hingeless and articulated rotors were calculated using the method described in Ch. 8. Using these initial transfer matrices, controller 4, the cautious global controller of Ch. 6, was applied to reduce 4/rev. vibratory hub shears. Five iterations of the shear min-

imization procedure using HHC were performed for each rotor. All results in this chapter used this same HHC algorithm.

Figure 10.1 shows the iteration history of the HHC angles required to reduce hub shears for the hingeless rotor. The maximum HHC angle required was 4°. By the second iteration the HHC angles had essentially reached their optimum values. Figure 10.2 shows the iteration history of the 4/rev. hub shears being minimized. All three hub shears were greatly reduced. The lateral and longitudinal hub shears were reduced to less than 2% of their baseline values by the fifth iteration. The vertical shear, which started at one fifth the level of the inplane shears, was reduced to 13% of its baseline value. While the shears were being minimized, the hub vibratory moments increased greatly. Figure 10.3 shows the iteration history of these moments. The rolling moment and pitching moment rose to respectively 6 times and 4 times their baseline values when HHC was applied. The yawing moment started at a very small value and rose to 250 times its baseline value. The yawing moment does not act directly on the fuselage but acts indirectly through the helicopter powerplant. Typically rotor torque is developed through complicated fluid forces acting on the power turbine of a gas turbine powerplant. Therefore the significance of this large increase in yawing vibratory moment is not at all obvious.

Figure 10.4 shows the iteration history of the HHC angles required to reduce hub shears for the articulated rotor. The maximum HHC angle required to minimize the hub shears was 0.9° but intermediate values of up to 1.1° were

used. By the second iteration the HHC angles had essentially reached their optimum values. The HHC angles required for hub shear reduction with the articulated blade were much lower than those required with the hingeless blade. Figure 10.5 shows the iteration history of the 4/rev. hub shears being minimized for the articulated blade. The lateral and longitudinal shears were reduced to less than 0.4% of their baseline values. The vertical shear was initially much lower and was reduced to 9% of its baseline value.

Figure 10.6 shows the iteration history of the 4/rev. hub vibratory moments as the shears were being minimized. For the articulated rotor, the zero moment condition at the blade root flap hinge and the low vibratory moment transmitted by the rotational damper at the lag hinge kept the vibratory pitching and rolling hub moments from rising greatly as they had for the hingeless blade. The greatest increases in moment were when HHC was first applied. At the first iteration of HHC the hub rolling, pitching, and yawing moments rose respectively to 1.6, 3.4, and 4.0 times their baseline values. These values for the pitching and rolling moments were still only slightly above the baseline values for the hingeless rotor. From the second HHC iteration onward the hub rolling, pitching, and yawing moments were 1.3, 0.8, and 2.2 times their baseline values. These values were an order of magnitude lower that those for the hingeless rotor. The moderate peaks in moment on the first HHC iteration were associated with the first, poor approximation to the optimum HHC angles and it is felt they could be avoided by tuning the controller to give a more cautious first estimate of HHC requirements.

10.3 REDUCTION OF SHEARS AND MOMENTS

Vibrations at a point in a helicopter fuselage will depend on both the hub shears and the hub moments being fed from the rotor into the fuselage. In actual implementation[68], the quantities being minimized by the HHC algorithm would normally be three linear orthogonal acceleration components at some point in the fuselage such as the pilot's seat. Due to the offset of this point from the rotor hub, angular accelerations are transformed into linear accelerations, and therefore hub vibratory moments also contribute to the accelerations experienced at the pilot's seat. The dynamic properties of the fuselage will also act as a filter changing the phase and magnitude of the forces and moments felt at this point due to the hub loads. Because of these factors, minimizing vibrations at a specific point in the fuselage may actually increase some loads at the rotor hub. Conversely, trying to reduce all hub loads may not be the most effective way to reduce vibrations at a specific point in the fuselage. The model used in this study is only capable of modeling hub shears and moments and has no provision for calculating fuselage vibrations.

In the last section it was seen that minimizing hub shears could lead to greatly increased hub moments, particularly for the hingeless blade rotor. It is therefore interesting to attempt to minimize both the hub shears and the hub moments simultaneously. The same cautious global HHC algorithm is used to reduce the hub loads, however now the problem is slightly redefined:

$$Z(i+1) = Z_0 + T\theta(i) \tag{10.2}$$

Where the vibration vector Z is now of length 12 and consists of the sine and cosine harmonics of the three 4/rev. hub shears and the three 4/rev. hub moments. The transfer matrix T is therefore redefined to be a 12×6 matrix relating these 12 hub load harmonics to the 6 HHC input harmonics. There are now 12 hub load harmonics being minimized using only 6 HHC harmonics as input, so the number of quantities being minimized is larger than the number of input variables.

Figure 10.7 shows the iteration history of the HHC angles required by the 12×6 HHC algorithm applied to the hingeless blade. As with the 6×6 algorithm, the optimum HHC angles were essentially reached by the second iteration. The maximum HHC angle was 0.7°, which was much smaller than the 4° commanded by the 6×6 algorithm. Figure 10.8 shows the iteration history of the hub vibratory shears. With the 6×12 algorithm, there was no minimization of the vertical shear and the lateral and longitudinal shears were only reduced by 20% to 30%. Figure 10.9 shows the iteration history of the hub vibratory moments. The pitching and rolling moments were reduced to about 40% of their baseline values and the yawing moment increased to about 24 times its baseline value.

The results for the 6×6 and 6×12 HHC algorithms are summarized in Fig. 10.10 where they are compared to the baseline values for the hingeless blade. It can be seen that including the requirement for hub moment minimizations in the HHC algorithm eliminated the high hub moments of the 6×6 controller, but at the expense of very poor hub shear reductions. As was said earlier, this

does not necessarily mean vibrations cannot be minimized in some area of the fuselage, but the implication is that this may be more difficult with a hingeless rotor than with an articulated rotor for which vibratory hub moments are inherently smaller.

Figure 10.11 shows the iteration history of the HHC angles commanded by the 6×12 control algorithm for the articulated blade. By the second iteration the angles had essentially reached their optimum values. The maximum HHC angle commanded was 0.8°. Comparing Figs. 10.4 and 10.11 it can be seen that almost the same HHC input was commanded by the 6×6 and 6×12 controllers. Figure 10.12 shows the iteration history of the hub vibratory shears. The lateral and longitudinal shears were reduced to about 5% of their baseline values while the vertical shear was reduced to a similar numerical value but only 30% of its baseline value. Figure 10.13 shows the iteration history of the hub moments. Again there were moderate peaks in the pitching and yawing moments at the first HHC iteration. The hub moments then settled at nearly the same values as with the 6×6 algorithm. The pitching moment was 60%, the rolling moment 130%, and the yawing 170% of its baseline value.

The results for the 6×6 and 6×12 HHC algorithms applied to the articulated rotor are summarized in Fig. 10.14. For the articulated rotor, the increases in hub moments associated with the 6×6 algorithm were small. Including moment minimization in the control algorithm had relatively small effects, leading to slightly poorer shear reductions but slightly lower hub moments. For the

articulated rotor, the large trade off between shear and moment reductions observed in the hingeless rotor was not evident.

10.4 ROTATING BLADE ROOT LOADS

In the last two sections, changes in vibratory hub loads in a fixed, non-rotating reference frame were investigated as HHC was applied. It is important to determine whether minimization of non-rotating loads was attained at the expense of higher vibratory loads in the rotating system. Higher rotating peak-to-peak loads could lead to fatigue problems while higher maximum rotating loads could cause blade failure. With an articulated blade, the flap and lag hinges reduce blade bending moments to zero at the blade root. With a hingeless blade however, these moments could become undesirably large. Large increases in peak-to-peak blade root shears or feathering moment would also be undesirable.

In order to investigate rotating blade root loads, the procedure described in Ch. 5 for calculating hub forces and moments was modified. A Fourier analysis of blade root loads was carried out in the rotating system calculating forces and moments at the blade root offset rather than at the center of rotation, and the summation process over the four blades was deleted. This analysis provided a constant component and sine and cosine components in the first five harmonics for axial, cordwise, and vertical blade root shear and feathering,

flapping, and lagging blade root moments. The maximum peak-to-peak value and maximum absolute value of each load were also calculated.

Figure 10.15 shows the variation with iteration number of peak-to-peak vibratory blade root shears for the hingeless blade. The vertical peak-to-peak shear increased by 40% as HHC was applied while the cordwise and axial shears increased by about 25%. Figure 10.16 shows the variation in blade root moments as HHC was applied. The peak-to-peak feathering moment increased to 10 times its baseline value while the flapping moment increased to 1.7 times its baseline value and the lagging moment to 1.5 times its baseline value.

Similar calculations were carried out for the articulated blade. For this case blade root shears increased by less than 5%. The blade root feathering moment increased to 2.5 times its baseline value. For the hingeless and to a lesser degree the articulated blade, the increases in peak-to-peak blade root feathering moment would need to be accounted for when determining the fatigue life estimates of the rotor blade on which HHC is applied. Furthermore, the moderate increases in peak-to-peak blade root bending moments and shears encountered for the hingeless blade could lead to fatigue problems.

Figure 10.17 shows the variation in the maximum absolute value of the blade root moments as HHC was applied to the hingeless blade. The maximum feathering moment increased to 4 times its baseline value while the lagging moment increased by 50% and the flapping moment increased by 15%.

For the articulated blade again there were essentially no increases in maximum blade root shears while the feathering moment increased by 50%. These increased maximum absolute blade root loads, particularly for the hingeless blade, may imply the need for increased blade strength and cause weight penalties.

10.5 POWER REQUIREMENTS AND STABILITY

Operating the electro-hydraulic actuators needed to implement HHC will of course require power from the helicopter powerplant. In addition, the helicopter rotor may require more or less power than at the baseline condition because of the additional aerodynamic loads which are imposed on it by the HHC inputs. In the flight tests of Ref. 67 a small decrease in rotor power required was observed when HHC was applied. If any such decrease in required power could be relied on, it could compensate somewhat for the additional power required to run the HHC servo-actuators.

When HHC was applied to the hingeless rotor, power required increased by 0.58% at the first iteration and remained between 0.90% and 1.03% above the baseline from the second through the fifth HHC iteration. This increase in required power was accompanied by a 0.2% increase in rotor thrust. In actual flight the pilot would retrim the helicopter after the application of HHC by decreasing the collective angle slightly to return to the baseline thrust value. This would alleviate part of the rise in required power seen in this simulation.

When HHC was applied to the articulated rotor, the rotor power required increased by 0.19% on the first iteration and then remained constant at 0.15% above the baseline for iterations two through five. The increase in required power was accompanied by a 0.06% decrease in rotor thrust, meaning that when the rotor was retrimmed the increase in required power would be somewhat greater. The hingeless rotor therefore had a six times greater increase in power required with application of HHC than the articulated rotor, but this difference was somewhat mitigated by the increase in thrust of the hingeless rotor and decrease in thrust for the articulated rotor. In both cases the increase in required power was less than 1%. There was no indication of any decrease in power requirements when HHC was applied.

Another possible problem area with the application of HHC would be any substantial decrease in the blade aeroelastic stability margins. With this in mind, the real parts of the characteristic exponents for the six generalized coordinates, which determine the stability of the six blade modes, were calculated at the baseline and at each iteration of the shear minimization process. The characteristic exponents for the articulated blade were all very insensitive to HHC application. The maximum changes in the real part of the characteristic exponent values were from -0.05% to +0.04%. For the hingeless blade all but the second lag mode characteristic exponent had changes of between -0.34% and +0.58%. The real part of the characteristic exponent for the second lag mode, which was the closest to its stability margin, had an increase in stability of between 27% and 30%. Thus one can conclude that overall stability mar-

gins were not adversely effected by the application of HHC to either hingeless or articulated blades.

Chapter XI

MODELING THE OH6A HELICOPTER

11.1 INTRODUCTION

This chapter presents the results of a simulation aimed at modeling the response to HHC of an OH6A light helicopter rotor. This helicopter was used for extensive flight testing of open-loop and closed-loop HHC by the McDonnell Douglas Helicopter Company (MDHC, then Hughes Helicopters). The aeroelastic simulation employed in this study has certain limitations in its ability to model the OH6A rotor as will be discussed later. However another a fundamental limitation of this aeroelastic analysis is the lack of any representation of the fuselage dynamics. Vibration data for the OH6A flight tests were recorded as accelerations at a particular point in the fuselage, namely the pilot's seat, therefore finding close correlation between the flight test data and the hub loads calculated in this study is not anticipated. The main objective of the simulations conducted was to identify similar trends, to those observed during the flight tests, when HHC was used.

The OH6A is a light turbine powered helicopter with a fully articulated four bladed rotor. Basic descriptive data for the helicopter and its rotor are given in Table 11.1. Geometric, structural, and mass properties for the OH6A rotor were provided by MDHC along with information on usual methods used in

TABLE 11.1

OH6A Basic Data

Gross Weight	2550 lbs
Equivalent Flat Plate Area	5.0 ft^2
Rotor Diameter	26.33 ft
Blade Chord	6.75 in
Blade Twist	-9° (linear)
Flap Hinge Offset	5.5 in
Lag Hinge Offset	16.19 in
Rotor RPM	483
Lock Number	4.919
Precone	0°

modeling the rotor. An illustration of the OH6A rotor hub is given in Fig. 11.1. Plots were provided by MDHC for the cordwise position of the blade center of mass, shear center, and feathering axis. Additional data in the form of plots for the values of the blade chordwise, flapwise, and torsional stiffnesses as a function of blade span together with the radial distribution of lumped blade mass and lumped blade chordwise mass moment, were also provided by MDHC. Several important aspects of the modeling process for this rotor configuration are presented below:

1. Control system stiffness is modeled by a torsional spring acting on the pitch case about the feathering axis.
2. The lead-lag friction damper is usually modeled by a torsional dashpot acting between the blade root and the pitch case about the vertical axis with an equivalent viscous damping coefficient of 1016 in-lbf-sec/radian.
3. The pitchcase/strap pack chordwise elastic bending stiffness is modeled as an 884,800 in-lbf/radian torsional spring acting about the vertical axis between the root and flap/feather bearing.
4. The pitch case flapwise elastic bending stiffness is considered infinite.
5. The masses of the strap pack, pitch link, pitchcase, and damper are lumped at the lag hinge to give an equivalent first mass moment about the center of rotation.

Natural rotating frequencies and mode shapes were provided for model verification. These were calculated at a collective angle such that the 3/4 radius collective angle was zero.

The aeroelastic simulation used in this study has two main limitations in its ability to model this rotor:

1. The feathering and elastic axis are required to be coincident whereas for the OH6A blade the elastic axis is 1.2 inches (0.178×chord) ahead of the feathering axis.
2. Non-coincident flap and lag hinges cannot be modeled whereas the lag hinge is 10.69 inches outboard of the flap hinge for the OH6A.

11.2 SIMPLIFIED OH6A BLADE

In this study, a simplified model of the OH6A blade was developed. The objective here was to model the basic design characteristics of the blade as closely as possible within the constraints imposed by limitations of the analysis. In general, blade properties and their distributions were used as given. The major compromises made in the modeling are listed below:

1. Since non-coincident elastic and feathering axes could not be modeled, these were assumed to be coincident at the elastic axis.
2. Flap and lag hinges were assumed to be coincident at the flap hinge offset of 5.5 inches as given. Changes in the lag mode characteristics were minimized by tuning the torsional spring representing the strap pack cordwise flexibility so as to give the best possible first lag frequency.
3. The torsional spring representing control system stiffness was tuned to give the best possible first torsional frequency.

Other than these compromises, the data on the OH6A blade was used as given. Using this simplified model of the OH6A blade, natural rotating frequencies and mode shapes were calculated. Table 11.2 compares the first six rotating natural frequencies obtained from model of this study and the actual OH6A blade.

The first mode in each of flap, lag, and torsion for the simplified model closely matched the frequencies and mode shapes provided for the OH6A. The

TABLE 11.2

OH6A Rotating Natural Frequencies

OH6A	Simplified Model
1L, 0.442/rev.	1L, 0.441/rev.
1F, 1.028/rev.	1F, 1.028/rev.
2F, 2.701/rev.	2F, 2.389/rev.
1T, 3.143/rev.	1T, 3.144/rev.
3F, 4.645/rev.	2L, 4.442/rev.
2L, 4.809/rev.	3F, 4.687/rev.

torsional components of the last three modes differed substantially from those given in the OH6A modal data. Furthermore, the last two modal natural frequencies appear in a reversed order. Within the constraints of the aeroelastic model used, it was felt that the representation of the modal characteristics provided above, was adequate.

11.3 OPEN-LOOP HHC FOR THE OH6A

In Ref. 67 open and closed-loop HHC flight tests were carried out at flight speeds of 60, 70, 80, and 100 knots. It was decided to do simulations at the highest of these speeds, where vibrations were most severe. The speed of 100 knots is equivalent for the OH6A to an advance ratio of $\mu = 0.253$. Plots of the

variation in vertical and lateral vibrations at the pilots seat, given in g's, with the phasing of a 1/3° amplitude lateral HHC input were given in Ref. 67. The plot of vertical and lateral vibrations for the 100 knot flight condition is reproduced in Fig. 11.2. Calculations were made for the model of this study to produce similar plots of the changes in vertical, lateral, and longitudinal hub shears with changes in the phase of collective, lateral, and longitudinal HHC inputs. These plots are presented in Figs. 11.3, 11.4, and 11.5

These plots show that lateral and longitudinal shears respond fairly well to reduction through HHC inputs. Some phasing of HHC input in any one of the three control channels is capable of reducing either the lateral or longitudinal shear considerably below its baseline value with just this 1/3° of HHC amplitude. Vertical shear on the other hand, responds very well to lateral or longitudinal HHC but for collective HHC gives values well above the baseline for any phasing of a 1/3° input. Comparing the results for lateral HHC input from Ref. 67 and this study, the phasing for minimum vertical and lateral shears are coincident at 320° for Fig. 11.2, the plot from Ref. 67, while from the plot of this study, Fig. 11.4, the minimum for lateral shears is at 140° and that for vertical shears is at 85°. For both the lateral and the longitudinal control channels, there is an HHC phasing which reduces all three shears below the baseline for this 1/3° input.

There is little correlation between the fuselage vibrations reported in Ref. 67 and the hub loads determined in this study. For instance Ref. 67 reported the baseline vertical vibration level as being 2.5 times the baseline lateral vi-

bration level. Conversely the vertical hub shear of this study was found to be only 30% of the lateral or longitudinal hub shear. In fact this is not unreasonable. In Ref. 62 an analytical analysis of HHC was done on a model which provided both hub loads and loads at the pilot's seat. Exactly this same inversion was seen with lateral and longitudinal vibrations being predominant at the hub and vertical vibrations being predominant at the pilot's seat. In an actual helicopter, the vibrations at a point in the fuselage due to rotor hub loads will be changed in phase and magnitude due to the dynamic characteristics of the fuselage. In addition, vibrations due to the powerplant, the tail rotor, impingement of the rotor wake on the empennage, and other factors will contribute to fuselage vibrations. Therefore it remains to be shown what locations for vibration sensors will be most effective in minimizing overall vibrations.

11.4 CLOSED-LOOP HHC FOR THE OH6A

The HHC algorithm used for closed-loop flight tests in Ref. 67 was the cautious, global controller referred to as controller 4 in Ch. 6. This same controller was used to apply HHC to the simplified model of the OH6A rotor at a 100 knot or $\mu = 0.253$ flight condition. Five iterations of HHC were carried out. Figure 11.6 shows the iteration history of the HHC input angles commanded by the controller. By the second iteration HHC angles are very close to their optimums. The collective channel was shown in the last section to be

quite ineffective in reducing vertical hub shears, and this is reflected in the two collective HHC inputs being essentially zero.

Figure 11.7 shows the iteration history of the hub shears being minimized by HHC. The shears are essentially totally suppressed, being less than 1% of their baseline values, in all three directions. In Ref. 67 the vertical, lateral, and longitudinal pilot's seat vibrations were reduced to respectively 7%, 23%, and 77% of their baseline values at 100 knots. Figure 11.8 shows the iteration history of the hub vibratory moments as HHC is applied. There is no increase in the yawing moment but substantial changes in the pitching and rolling moments which increase respectively to 5.3 and 2.4 times their baseline values. Again the significance of any increase in moments as shears are reduced is dependent on actual fuselage dynamics, which are not included in this model.

11.5 POWER REQUIREMENTS AND STABILITY

When HHC was applied to the simplified model of the OH6A rotor, the required rotor power increased by ½%. There was no indication of a decrease in required rotor power as was reported in Ref. 67. This small increase in required power would present no problem in itself, but in any actual prediction of required power for HHC implementation, the power requirements of the servo-actuators used to produce the HHC pitch changes would also have to be taken into account. There were no appreciable negative effects on aeroelastic stability when HHC was applied to this rotor. The real part of the

characteristic exponent associated with the second lag mode, which was closest to its stability margin, increased in stability by 18% while the other modes had changes in stability of 4% or less.

Chapter XII

CONCLUDING REMARKS

This study has presented a rotor aeroelastic analysis capable of modeling the effects of HHC in forward flight. This is a major extension of an existing analysis which includes several features which make it a superior model for HHC studies. The original analysis incorporates structural nonlinearities in a consistent manner and provides direct stability information. An improved, implicitly derived, implementation of a finite-state, time-domain unsteady aerodynamic formulation has been incorporated in the model to capture high frequency aerodynamic effects due to HHC pitch changes. Trim values required for the analysis have been calculated using an improved helicopter trim procedure which accounts for flap, lag, and torsional blade deformations. This complete analysis has then been coupled with a procedure for determining the rotor vibratory hub loads and a set of control routines used to calculate the HHC inputs needed to minimize these vibratory loads.

Using this model, a study of the effects of unsteady, as opposed to quasisteady, aerodynamics on a hingeless rotor was carried out. The unsteady aerodynamic formulation, which also included several apparent mass terms which had been neglected in the quasisteady formulation, was found to have moderate effects on the stability and low frequency response of the blade. In order to compare high frequency response, the 4/rev. rotor hub shears were

compared for the two aerodynamic formulations. It was found that there can be large differences in high frequency response between the two aerodynamic formulations especially at higher advance ratios. This difference is noticeable particularly in the vertical hub shear response which is primarily affected by the changes in lift due to the unsteady aerodynamics. The differences were pronounced when the blade was excited at high frequencies in pitch, as is the case with HHC. These results indicate that high frequency unsteady aerodynamic effects should be included when modeling HHC. A flap trim and an improved full trim procedure were compared. The principal differences in trim values were in the collective at low advance ratios and in the cosine cyclic and angle of attack at high advance ratios. The new trim values gave a considerable difference in low frequency flap response and also led to moderate changes in vertical hub shears at advance ratios above $\mu = 0.3$. Blade stability was not appreciably affected by the new trim solution. The convergence criterion used for quasilinearization in this study was more precise than that of Ref. 8 and results were shown indicating that an improper convergence criterion could lead to poorly converged higher harmonics of the response solution. This led to erroneous values for the vertical hub shears which may have contributed to inconsistent optimization results in Ref. 8.

A preliminary study of the effects of open-loop HHC was carried out on a hingeless rotor. HHC inputs of 1/3° in the collective, lateral, and longitudinal control channels were phased at 90° intervals between 0° and 360° and the corresponding changes in vibratory hub shears and moments were calculated.

With appropriate phasing, lateral and longitudinal shears could be driven below the baseline with control input in any channel using either aerodynamic model. Vertical shears could only be reduced below the baseline by longitudinal input for the unsteady aerodynamic model however they could be reduced below the baseline by any channel of input with the quasisteady aerodynamic model. Similar phasing for minimums of lateral and longitudinal shears were found for the two aerodynamic models but the phases for vertical shear minimization differed greatly. Calculations were made to show the variation in 4/rev. harmonics of hub shears as the HHC input angle magnitude was varied for a set phase angle. The relationships were found to be quite linear over the range 0° to 3° of amplitude for both the quasisteady and the unsteady models.

In order to initiate closed-loop studies of HHC, initial estimates of HHC transfer matrices relating HHC inputs to changes in hub vibratory shears were calculated at an advance ratio of $\mu = 0.3$. This was done by individually incrementing each HHC degree of freedom by 1/3° and measuring the resultant changes in hub shears. These transfer matrices were then used to implement fixed gain closed-loop control on both the quasisteady and unsteady aerodynamic models. In both cases shears were very successfully reduced, indicating that the off-line estimates of the transfer matrices were quite accurate. With the unsteady model there was a tendency for the vertical shears to drift upward after minimization. The quasisteady model was next used to compare the performance of a local and three global HHC algorithms. Based on these results, it was decided to conduct the rest of the investigation using two con-

trollers, a local controller using Kalman filter identification of only the transfer matrix, and a global controller using Kalman identification of the transfer matrix and the baseline vibration level.

Next cautious and deterministic versions of these two controllers were implemented for the quasisteady and unsteady aerodynamic models. With quasisteady aerodynamics there were very small differences in control sequence and shear minimizations. With unsteady aerodynamics the deterministic controller tended to slightly overshoot the optimum control values and the local controller was not as effective in holding the vertical shear to its minimum. This was attributed to the identification process of the transfer matrix for the local controller which was based on changes in the HHC inputs, rather than the total magnitude of the HHC inputs in the global case. Thus when the minimum was quickly reached changes in HHC input became essentially zero and identification to improve the transfer matrix estimate stopped. In order to gauge the ability of the controllers to respond to changing flight conditions, calculations were carried out wherein a step change in flight condition from $\mu = 0.3$ to $\mu = 0.35$ was applied from the optimal HHC solution at $\mu = 0.3$. The local controller responded with large oscillations in commanded control inputs and resultant shear minimizations however by the sixth iteration the hub shears were reduced considerably below the baseline for this advance ratio. Under the same conditions, the global controller responded quite smoothly and only small oscillations were observed. The reduced performance of the local

controller was again attributed to poor transfer matrix identification at the original baseline.

In order to compare the differences in effects of HHC on articulated and hingeless rotors, HHC simulations were carried out on two roughly equivalent rotors, one with a hingeless and one with an articulated hub. It was found that in order to achieve a similar reduction in hub shears, the hingeless rotor required HHC angle magnitudes which were four times larger than those for the articulated rotor. This implies that considerably more power might be needed to drive the HHC servo-actuators for a hingeless rotor. While hub shears were being reduced, hub pitching and rolling moments for the hingeless blade rose to four and six times their baseline values while for the articulated rotor they increase to only 1.3 and 0.8 times their baseline values. Moments for the articulated rotor remained low due to the flap and lag hinges which keep moment transfer from the rotor to the non-rotating system to a minimum, and were an order of magnitude less than those for the hingeless blade. Subsequently HHC was used to attempt to suppress simultaneously both the hub shears and the hub moments. For the hingeless blade this led to pitching and rolling moments which became half the baseline values, however this decrease was accomplished only at the expense of shear reductions of less than 30%. For the articulated blade, a small decrease in the moments, which were already small, was accompanied by a minor increase in shears. This shows that overall vibration reductions may be more difficult to achieve with HHC when applied

to hingeless rotors because the simultaneous minimization of both hub shears and moments could be difficult to accomplish.

Rotating blade root loads were also calculated for the hingeless and articulated blades as HHC was applied. Both peak-to-peak and absolute blade root bending moments increased significantly with HHC application for the hingeless blade, and feathering moment increased substantially for both blades. These increases need to be taken into accounted when designing the strength and fatigue properties of rotor blades on which one intends to use HHC. Application of HHC led to increases in required rotor power of less than 1% for both blades. Aeroelastic stability margins for the two blades changed by less than 1% except for the stability of the second lag mode of the hingeless blade, for which the stability margin increased by 30%.

A simulation of application of HHC to the rotor of an OH6A helicopter was conducted and the results were compared to actual flight test data. The model used was somewhat limited due to the inability to model the noncoincident flap and lag hinges and noncoincident elastic and feathering blade axes of the OH6A rotor blade. Within these limitations, the model was designed so as to have similar geometric, structural, and mass properties to the actual rotor blade. Using this model, open-loop HHC simulations were carried out. Phasing or the HHC for shear minimization did not correlate well between the model and actual flight tests, but this may have been caused by the differences in the objective functions being minimized. In the flight tests vibratory accelerations at the pilot's seat were minimized whereas in the simulation hub vi-

bratory shears were minimized. Due to fuselage dynamics and vibrations from sources other than the rotor, vibration minimization at a given point in the fuselage need not correspond to hub shear minimization, and in fact might lead to increases in some hub load components. Lateral and longitudinal HHC inputs were found to be the most effective in reducing hub shears. When closed-loop HHC was applied to this model, all shears were suppressed to less than 1% of their baseline values at a speed of 100 knots. Concurrently, pitching and rolling hub vibratory moments increased to respectively 5.3 and 2.4 times their baseline values. As HHC was applied, rotor required power increased by ½%. The small decrease in rotor power reported in Ref. 67 was not reproduced by the simulation. Aeroelastic stability was not adversely affected by the application of HHC. Because of the lack of fuselage dynamics in the model, these results cannot be construed as any sort of prediction of actual OH6A response to HHC, but serve to show the ability of the analysis to model more realistic rotor configurations.

REFERENCES

1. Bartlett, F.D., "Flight Vibration Optimization Via Conformal Mapping," AHS Journal, Vol. 28, No. 1, January 1983, pp. 49-55.

2. Bielawa, R.L, Cheney, M.C. Jr., and Novak, R.C.,"Investigation of a Bearingless Rotor Concept Having a Composite Primary Structure," NASA CR-2637 (1976).

3. Bielawa, R.L., "Aeroelastic Analysis for Helicopter Rotor Blades With Time-Variable, Nonlinear Structural Twist and Multiple Structural Redundancy - Mathematical Derivation and User's Manual," NASA CR-2638, October 1976.

4. Bir, G.S., and Chopra, I., "Gust Response of Hingeless Rotors," AHS Journal, Vol. 31, No. 2, April 1986, pp. 35-46.

5. Brown, T.J., and McCloud, J.L. III, "Multicyclic Control of a Helicopter Rotor Considering the Influence of Vibration, Loads, and Control Motion," 36th AHS Forum, Washington, D.C., May 1980.

6. Brown, R.G., Introduction to Random Signal Analysis and Kalman Filtering, John Wiley and Sons, New York, 1983.

7. Celi, R., and Friedmann, P.P., "Rotor Blade Aeroelasticity in Forward Flight With an Implicit Aerodynamic Formulation," AIAA Journal, Vol. 26, No. 12, December 1988, pp. 1425-1433.

8. Celi, R., "Aeroelasticity and Structural Optimization of Helicopter Rotor Blades With Swept Tips," Ph.D. Dissertation, Mechanical, Aerospace and Nuclear Engineering Department, University of California, Los Angeles, CA, 1987.

9. Celi, R., and Friedmann, P.P., "Aeroelastic Modeling of Swept Tip Rotor Blades Using Finite Elements," AHS Journal, Vol. 33, No. 2, April 1988, pp. 43-52.

10. Chopra, I., and J.L. McCloud, "A Numerical Simulation Study of Open-Loop, Closed-Loop and Adaptive Multicyclic Control Systems," AHS Journal, Vol. 28, No. 1, January 1983, pp. 63-77.

11. Davis, M.W., "Refinement and Evaluation of Helicopter Real-Time Self-Adaptive Active Vibration Control Algorithms," NASA CR 3821, August 1984.

12. Dinyavari, M.A.H., and Friedmann, P.P., "Application of Time-Domain Unsteady Aerodynamics to Rotary-Wing Aeroelasticity," AIAA Journal, Vol. 24, no. 9, September 1986, pp. 1424-1432.

13. Dinyavari, M.A.H., "Unsteady Aerodynamics in Time and Frequency Domains for Finite-Time Arbitrary-Motion of Helicopter Rotor Blades in Hover and Forward Flight," Ph.D. Dissertation, Mechanical, Aerospace and Nuclear Engineering Department, University of California, Los Angeles, CA, March 1985.

14. Drees, J.M., "A Theory of Airflow Through Rotors and its Application to Some Helicopter Problems," Journal of the Helicopter Association of Great Britain, Vol. 3, No. 2, July-September 1949.

15. Du Val, R.W., Gregory, C.Z., and Gupta, N.K., "Design and Evaluation of a State-Feedback Vibration Controller," AHS Journal, Vol. 29, No. 3, July 1984.

16. Friedmann, P.P., "Formulation and Solution of Rotary-Wing Aeroelastic Stability and Response Problems," Vertica, Vol. 7, No. 2,1983, pp. 101-141.

17. Friedmann, P.P., "Recent Trends in Rotary-Wing Aeroelasticity," Vertica, Vol. 11, No. 1/2, 1987, pp. 1939-170.

18. Friedmann, P., "Application of Modern Structural Optimization to Vibration Reduction in Rotorcraft," Vertica, Vol. 19, No 4, 1985, pp. 363-376.

19. Friedmann, P., and Kottapalli, S.B.R., "Coupled Flap-Lag-Torsional Dynamics of Hingeless Rotor Blades in Forward Flight," AHS Journal, Vol. 27, No. 4 October 1982, pp. 28-36.

20. Friedmann, P.P., "Arbitrary Motion Unsteady Aerodynamics and Its Application to Rotary-Wing Aeroelasticity," Journal of Fluids and Structures, Vol. 1, No. 1, 1987, pp. 71-93.

21. Friedmann, P.P., and Robinson, L., "Time Domain Aerodynamic Effects on Coupled Flap-Lag-Torsional Aeroelastic Stability and Response of Rotor Blades," Proc. 2nd International Conference on Basic Rotorcraft Research, College Park, Maryland, February 1988.

22. Goankar, G. and Peters, D., "Effectiveness of Current Dynamic-inflow Models in Hover and in Forward Flight," AHS Journal, Vol. 31, No. 2, April 1986, pp. 47-57.

23. Goodwin, G.D., and Payne, R.L., Dynamic System Indentification, Experiment Design and System Analysis, Academic Press, New York, 1977.

24. Greenberg, J.M., "Airfoil in Sinusoidal Motion in Pulsating Stream," NACA TN 1326, 1947.

25. Gupta, B.P., Logan, A.H., and Wood, E.R., "Higher Harmonic Control for Rotary Wing Aircraft," AIAA/AHS/ASEE Aircraft Design Systems and Operations Meeting, San Diego, California, October 1984.

26. Gupta, N.K., "Frequency Shaped Cost Functionals: Extension of Linear-Quadratic-Gaussian Design Methods," Journal of Guidance and Control, Vol 3, No. 6, November-December 1980.

27. Gupta, N.K., and Du Val, R.W., "A New Approach for Active Control of Rotorcraft Vibration," Journal of Guidance and Control, Vol 5, No. 2, March-April 1982.

28. Ham, N., "Helicopter Individual-Blade-Control and its Applications," 39th AHS Forum, St. Louis, Missouri, May 1983.

29. Ham, N.D., "Helicopter Gust Alleviation, Attitude Stabilization, and Vibration Alleviation Using Individual-Blade-Control Through a Conventional Swashplate," 41st AHS Forum, Fort Worth, Texas, May 1985.

30. Hammond, C.E., "Wind Tunnel Results Showing Vibratiory Loads Reduction Using Higher Harmonic Blade Pitch," 36th AHS Forum, Washington, D.C., May 1980.

31. Hanagud, S., M. Meyyappa, S. Sarkar, and J.I. Craig, "A Coupled Rotor/Airframe Vibration Model With Higher Harmonic Control Effects," 42nd AHS Forum, Washington D.C., June 1986.

32. Jacklin, S.A., "Adaptive Inverse Control for Rotorcraft Vibration Reduction," NASA TM 86829, October 1985.

33. Jacklin, S.A., "System Identification Techniques for Helicopter Higher Harmonic Control," 42nd AHS Forum, Washington, D.C., June 1986.

34. Jacob, H.G., and G. Lehmann, "Optimization of Blade Pitch Angle for Higher Harmonic Rotor Control," Vertica, Vol.7, No.3, 1983, pp. 271-286.

35. Johnson, W., Helicopter Theory, Princeton University Press, Princton, New Jersey, 1980.

36. Johnson, W., "Self-Tuning Regulators for Multicyclic Control of Helicopter Vibration," NASA TP 1996, 1982.

37. Lehmann, G., "The Effect of Higher Harmonic Control (HHC) on a Four-Bladed Hingeless Model Rotor," Vertica, Vol.9, No.3, 1985, pp. 273-284.

38. Lehmann, G., and Kube, R., "Automatic Vibration Reduction of a Four Bladed Hingeless Model Rotor- a Wind Tunnel Demonstration," 14th European Rotorcraft Forum, Milan, Italy, September 1988.

39. McCloud, J.L. III, and Kretz, M., "Multicyclic Jet-Flap Control for Alleviation of Helicopter Blade Stresses and Fuselage Vibration," Rotorcraft Dynamics, NASA SP-352, 1974, pp. 233-238.

40. McCloud, J.L. III, and Weisbrich, A.L., "Wind Tunnel Test Results of a Full-Scale Multicyclic Controllable Twist Rotor," Paper No. 78-60, 34th AHS Forum, Washington, D.C., May 1978.

41. McKillip, R.M., "Periodic Control of the Individual-Blade-Control Helicopter Rotor," Ph.D. Dissertation, M.I.T. August 1984.

42. McKillip, R.M., "Kinematic Observers for Active Control of Helicopter Rotor Vibration," Vertica, Vol.12, No.1/2, 1988, pp. 1-11.

43. Miao, W., and Frye, H.M., "Flight Demonstration of Higher Harmonic Control (HHC) on S-76," 42nd AHS Forum, Washington, D.C., June 1986.

44. Miura, H., "Application of Numerical Optimization Methods to Helicopter Design Problems-A Survey," Vertica, Vol.9, No.2, 1985, pp. 141-154.

45. Molusis, J.A., Hammond, C.E., and Cline, J.H., "A Unified Approach to the Optimal Design of Adaptive and Gain Scheduled Controllers to Achieve Minimum Helicopter Vibration," AHS Journal, Vol.28, no.2, April 1983, pp. 9-18.

46. Molusis, J.A., "The Importance of Nonlinearity on the Higher Harmonic Control of Helicopter Vibration," 39th AHS Forum, St. Lious, Missouri, May 1983.

47. Molusis, J.A., Mookerjee, P., and Bar-Shalom, Y., "Evaluation of the Effect of Vibration Nonlinearity on Convergence Behavior of Adaptive Higher Harmonic Control," NASA CR-166424, January 1983.

48. Murphy, M.R., "Higher Harmonic Control (HHC) Design Investigation," Aviation Applied Technology Directorate, US Army Aviation Research and Technology Activity (AVSCOM), USAAVSCOM TR-87-D-7, December 1987.

49. Nilakantan, G.H. and Gaonkar, G., "Feasibility of Simplifying Coupled Flap-lag-torsion Models for Rotor Blade Stability in Forward Flight," Vertica, Vol. 9, No. 3, 1985, pp.241-256.

50. Panda, B. and Chopra, I., "Flap-lag-torsion Stability in Forward Flight," AHS Journal, Vol. 30, No. 4, October 1985, pp. 30-39.

51. Peters, D.A., and Hohenemser, K.H., "Application of the Floquet Transition Matrix to the Problem of Lifting Rotor Stability," AHS Journal, Vol. 16, No. 2, October 1982, pp. 28-36.

52. Pitt, D.M., and Peters, D.A., "Theoretical Prediction of Dynamic Inflow Derivatives," Vertica, Vol. 5, No. 1, 1981, pp. 21-34.

53. Polychroniadis, M., and Achache, M., "Higher Harmonic Control: Flight Tests of an Experimental System on SA 349 Research Gazelle," 42nd AHS Forum, Washington, D.C., June 1986.

54. Reddy, T.S.R., and Warmbrodt, W., "Forward Flight Aeroelastic Stability from Symbolically Generated Equations," AHS Journal, Vol. 31, No. 3, July 1986, pp. 35-44.

55. Reichert, G., "Helicopter Vibration Control-A Survey," Vertica, Vol. 5, No. 1, 1981, pp. 1-20.

56. Rosen, A., and Friedmann, P.P., "Nonlinear Equations of Equilibrium for Elastic Helicopter or Wind Turbine Blades Undergoing Moderate Deformation," NASA CR-159478, December 1978.

57. Shamie, J., and Friedmann, P., "Effect of Moderate Deflections on the Aeroelastic Stability of a Rotor Blade in Forward Flight," 3rd European Rotorcraft and Powered Lift Aircraft Forum, Paper No. 24, Aix-en-Provence, France, September 1977.

58. Shaw, J., and Albion, N., "Active Control of the Helicopter Rotor for Vibration Reduction," 36th AHS Forum, Washington, D.C., May 1980.

59. Shaw, J., Albion, A., Hanker, E.J., and Teal, R., "Higher Harmonic Control: Wind Tunnel Demonstration of Fully Effective Vibratory Hub Force Suppression," AHS Journal, Vol.34, no.1, January 1989, pp. 14-25.

60. Sissingh, G.J., and Donham, R.E., "Hingeless Rotor Theory and Experiment on Vibration Reduction by Periodic Variation of Conventional Control," Rotorcraft Dynamics, NASA SP-352, 1974, pp. 261-277.

61. Straub, F.K., and P.P. Friedmann, "Application of the Finite Element Method to Rotary Wing Aeroelasticity," NASA CR-165854, February 1982.

62. Taylor, R.B., Farrar, F.A., and Miao, W., "An Active Control System for Helicopter Vibration Reduction by Higher Harmonic Pitch," AIAA paper No. 80-0672, 36th AHS Forum, Washington D.C., May 1980.

63. Taylor, R.B., Zwicke, P.E., Gold, P., and Miao, W., "Analytical Design and Evaluation of an Active Control System for Helicopter Vibration Reduction and Gust Alleviation," NASA CR-152377, July 1980.

64. Walsh, D.M., "Flight Test of an Open Loop Higher Harmonic Control System on an S-76A Helicopter," 42nd AHS Forum, Washington, D.C., June 1986.

65. Widrow, B., Adaptive Filters, Aspects of Network and System Theory, Holt, Rinehart, and Winston, Inc., New York, 1970.

66. Widrow, B., and Hoff, M.E., Jr., "Adaptive switching Circuits," IRE WFSCON Convention Record, 1960, pp 96-104.

67. Wood, E.R., and Powers, J.H., "Practical Design Considerations for a Flightworthy Higher Harmonic Control System," 36th AHS Forum, Washington, D.C., May 1980.

68. Wood, E.R., Powers, J.H., Cline, J.H., and Hammomd, C.E., "On Developing and Flight Testing a Higher Harmonic Control System," AHS Journal, Vol.30, no.1, January 1985, pp. 3-20.

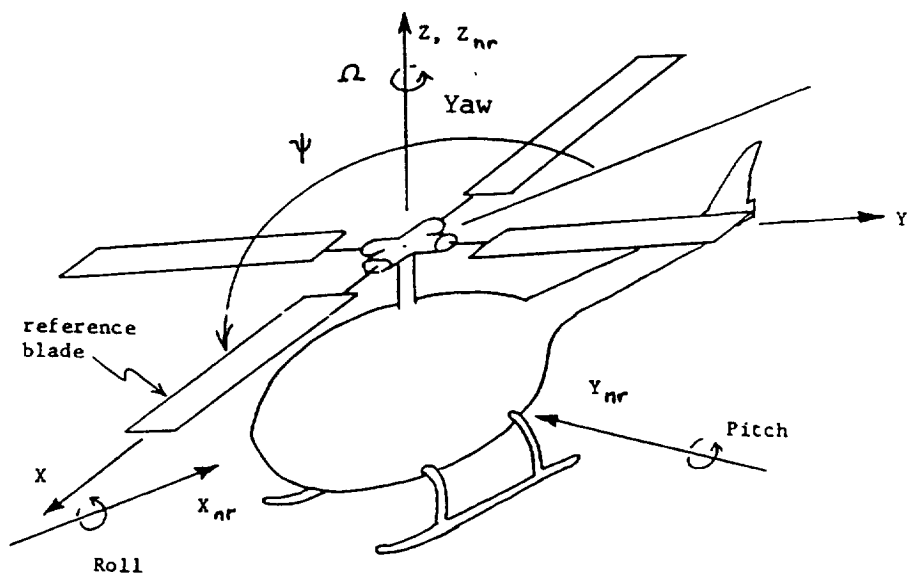

Figure 2.1: Geometry of the Nonrotating Coordinate System and Hub Shears and Moments.

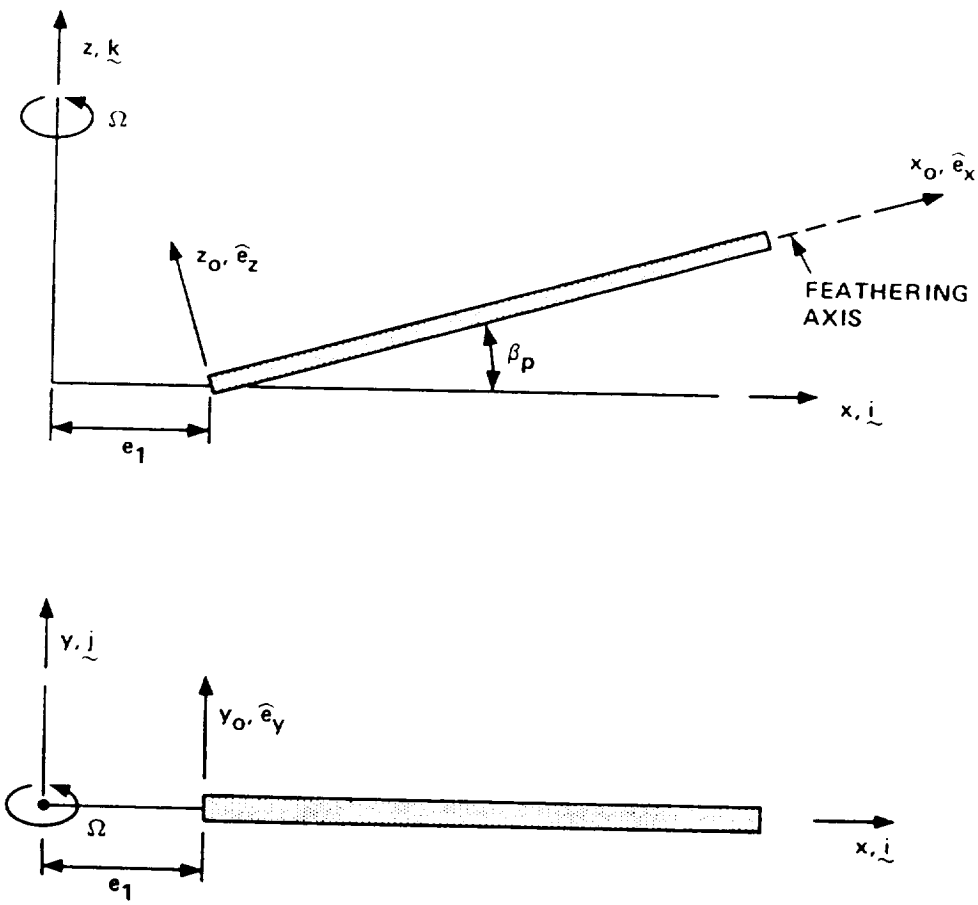

Figure 2.2: Geometry of the Undeformed Blade in the Rotating System.

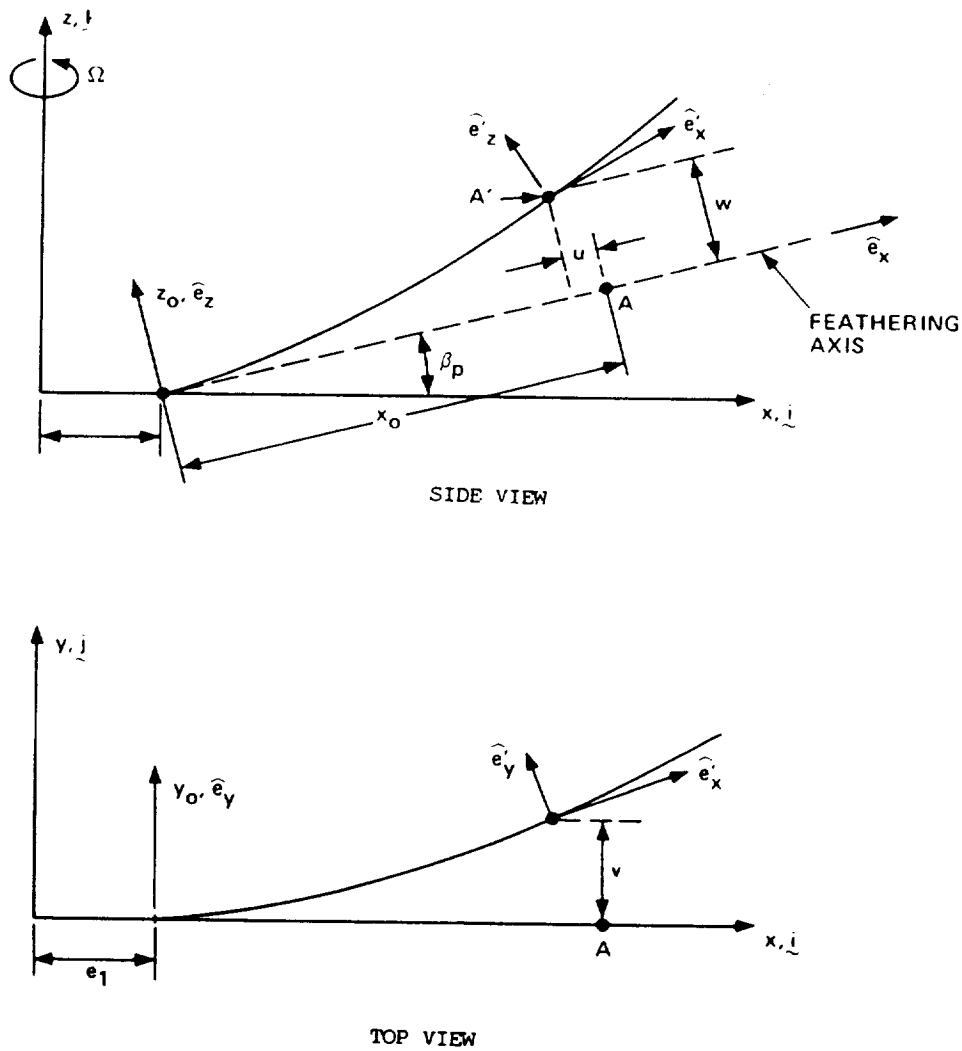

Figure 2.3: Geometry of the Elastic Axis of the Deformed Blade.

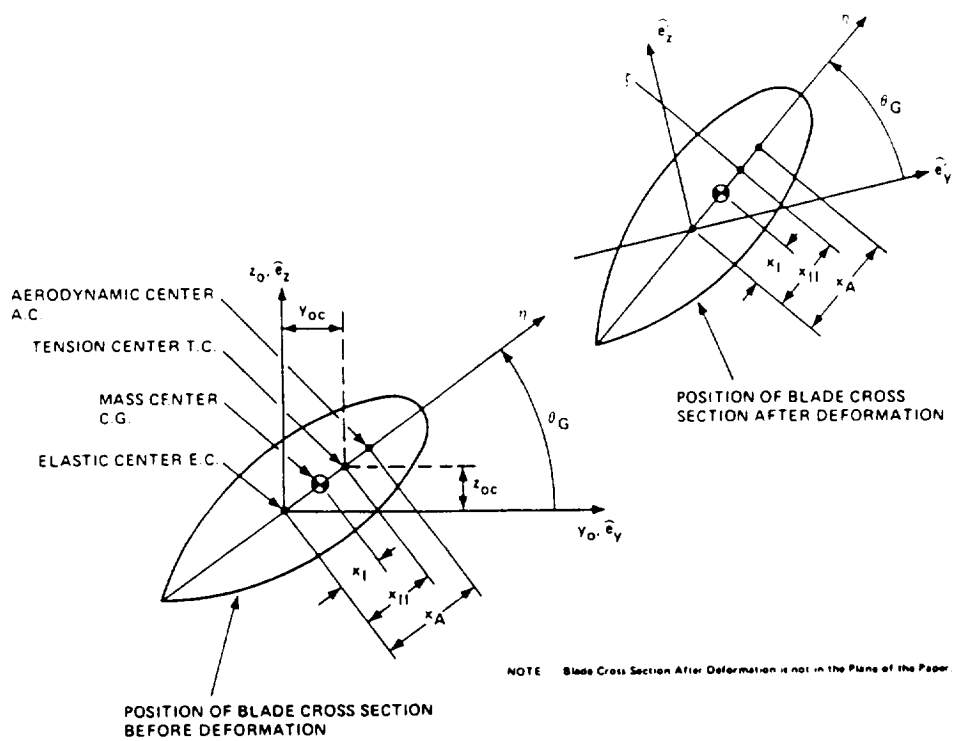

Figure 2.4: Deformed Blade Cross Sectional Geometry.

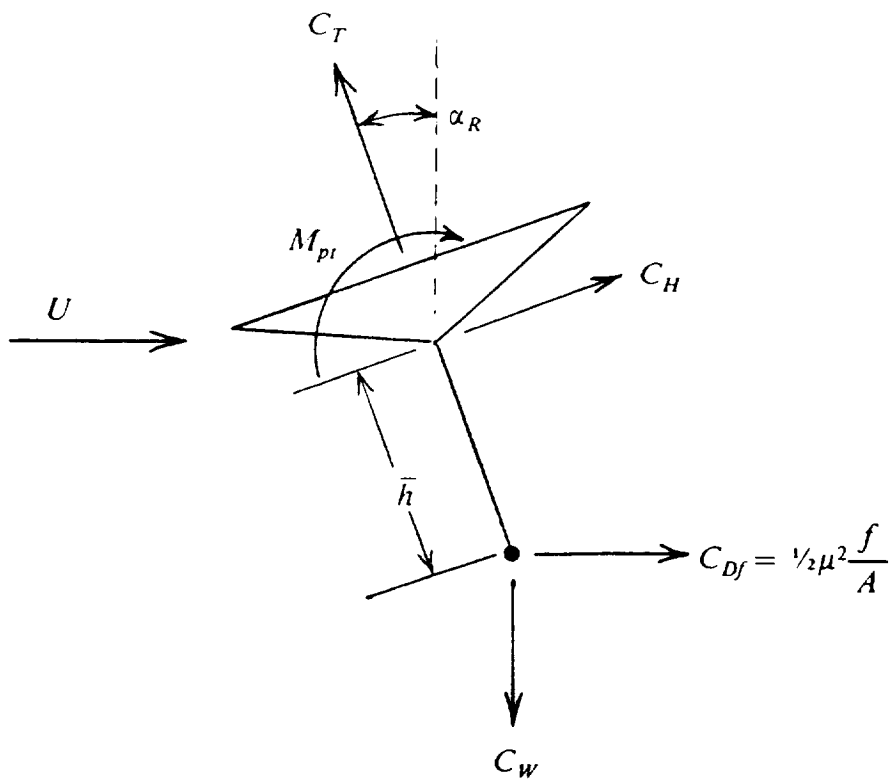

Figure 3.1: Forces and moments on the helicopter in straight and level flight.

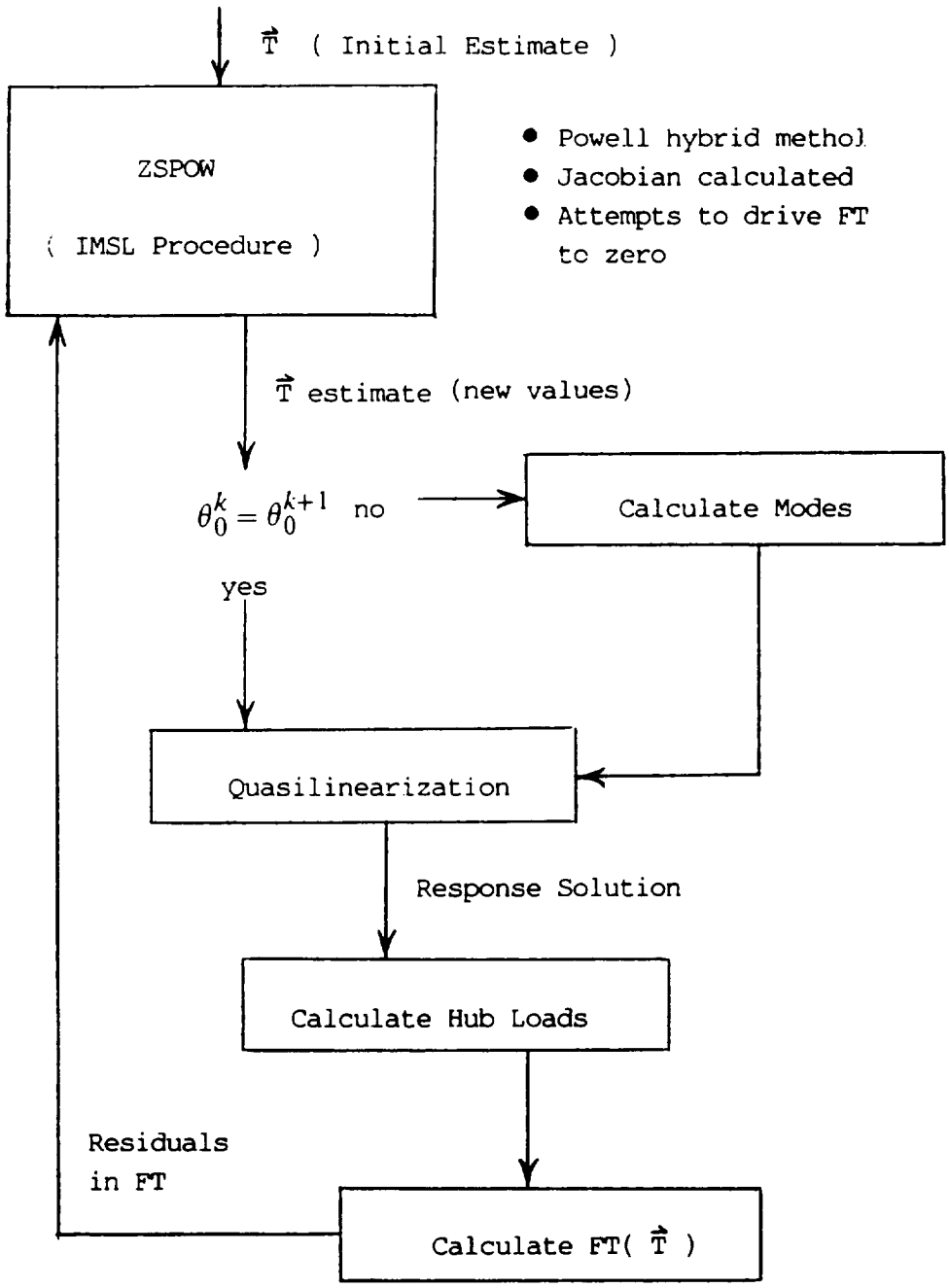

Figure 3.2: Flow chart showing procedure used to solve the full trim equations.

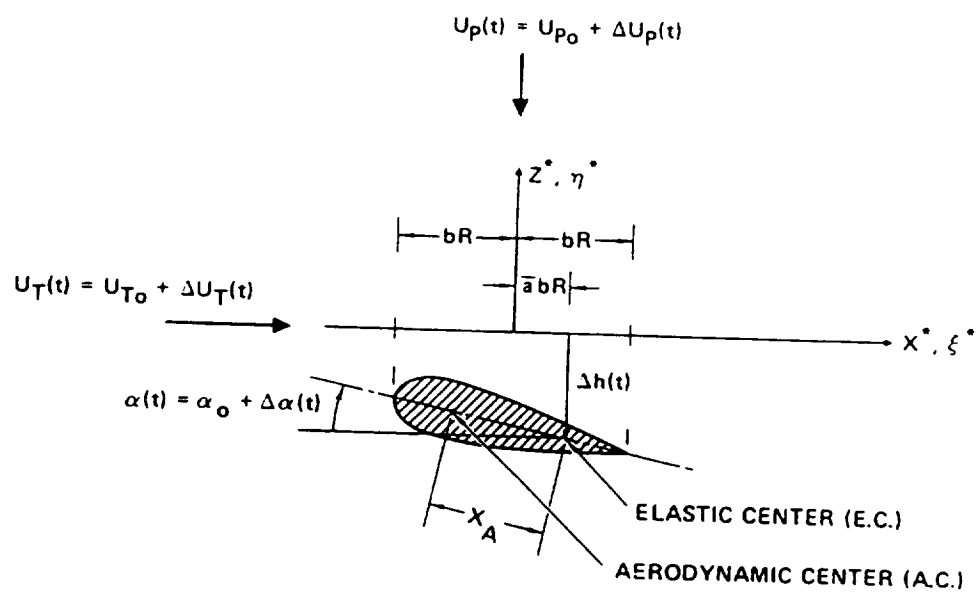

Figure 4.1: Geometry of motion of a typical airfoil.

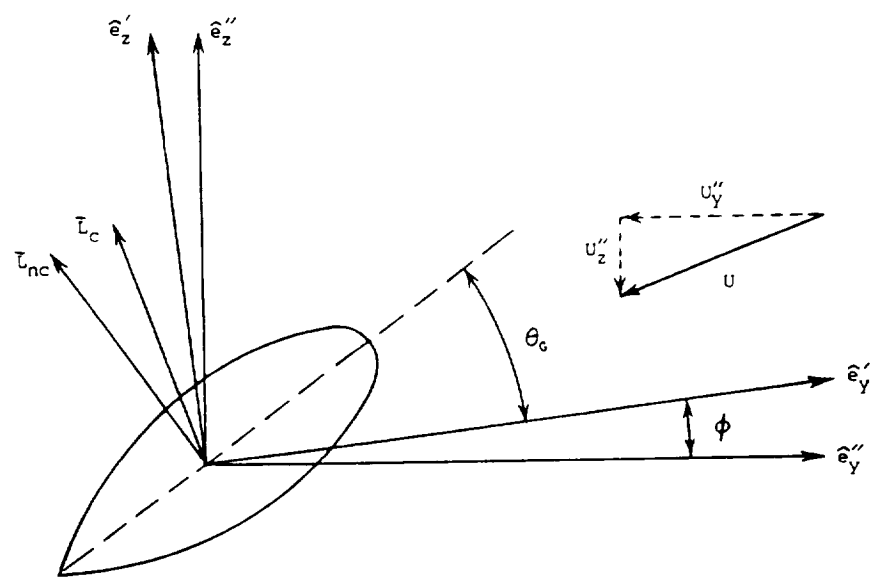

Figure 4.2: Various components of the unsteady loads acting on the airfoil.

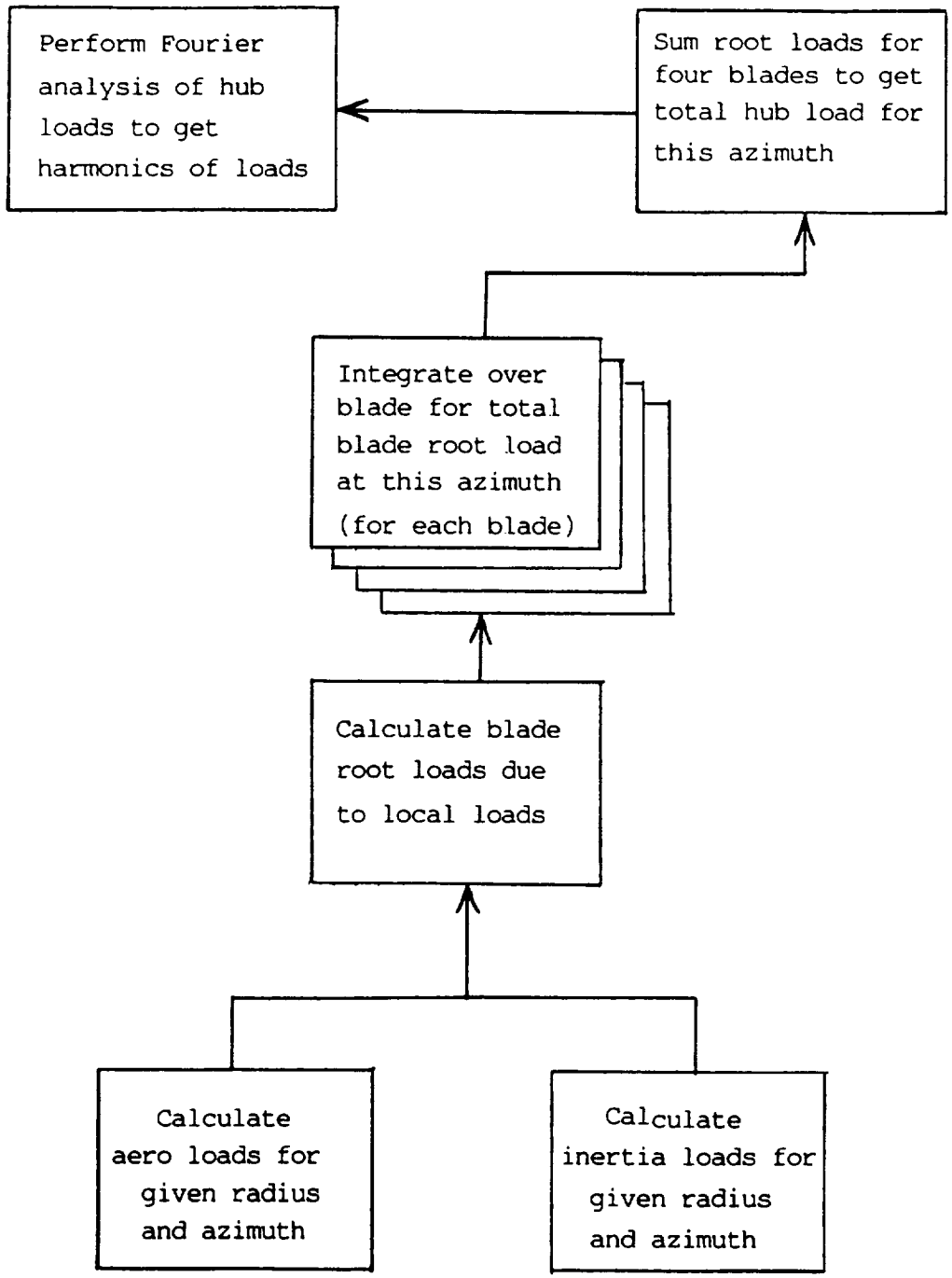

Figure 5.1: Flow chart showing procedure for hub force and moment calculation.

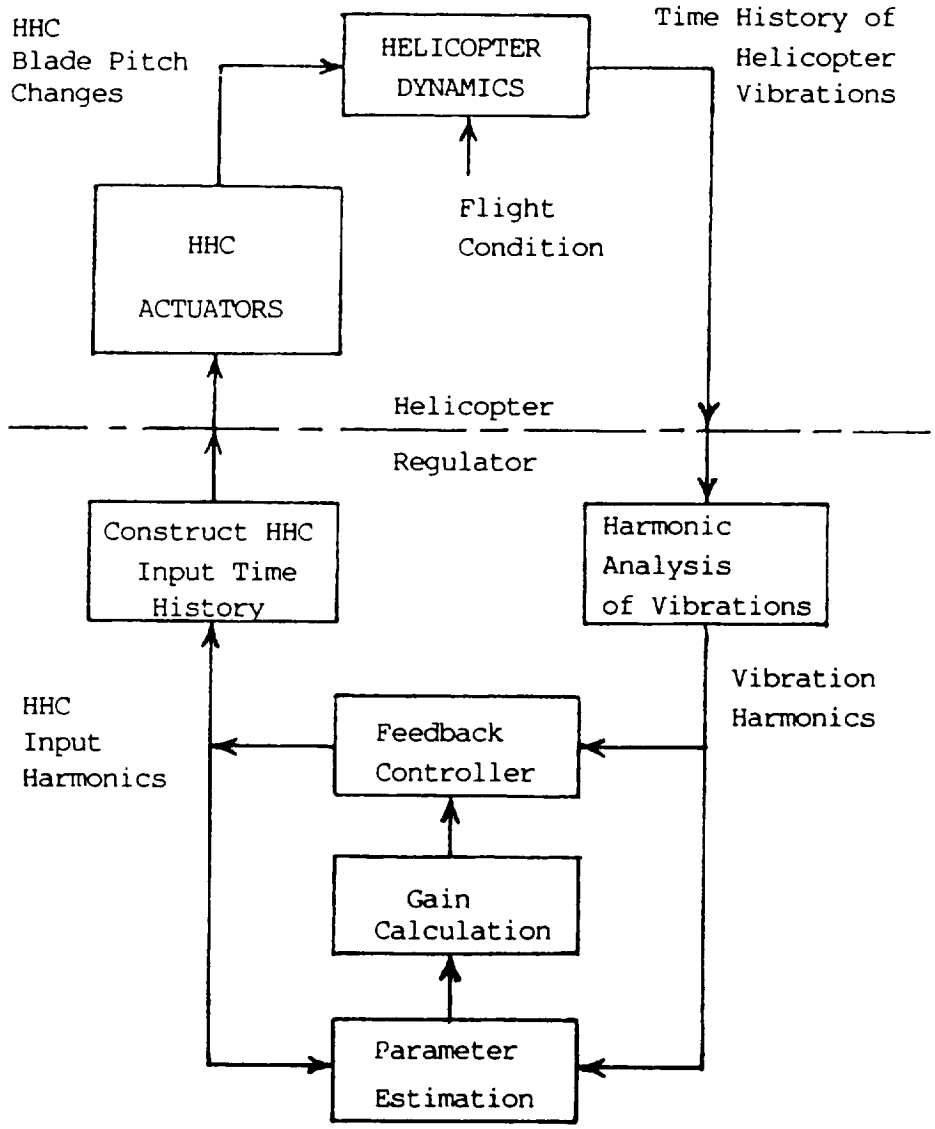

Figure 6.1: Schematic of helicopter plant model.

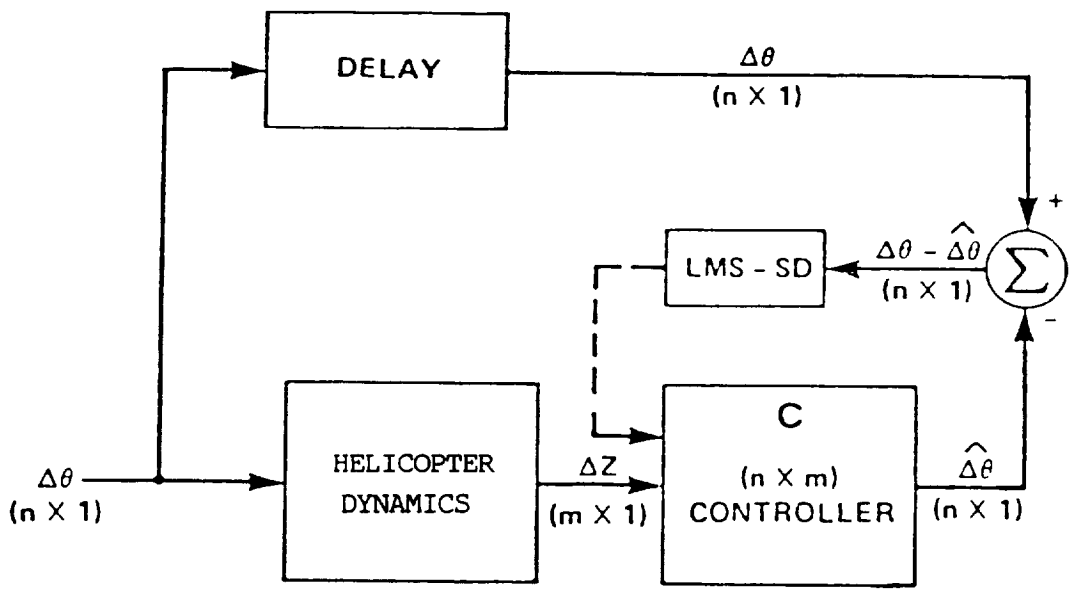

Figure 6.2: Block chart showing generation of the adaptive error vector for the extended LMS identification algorithm.

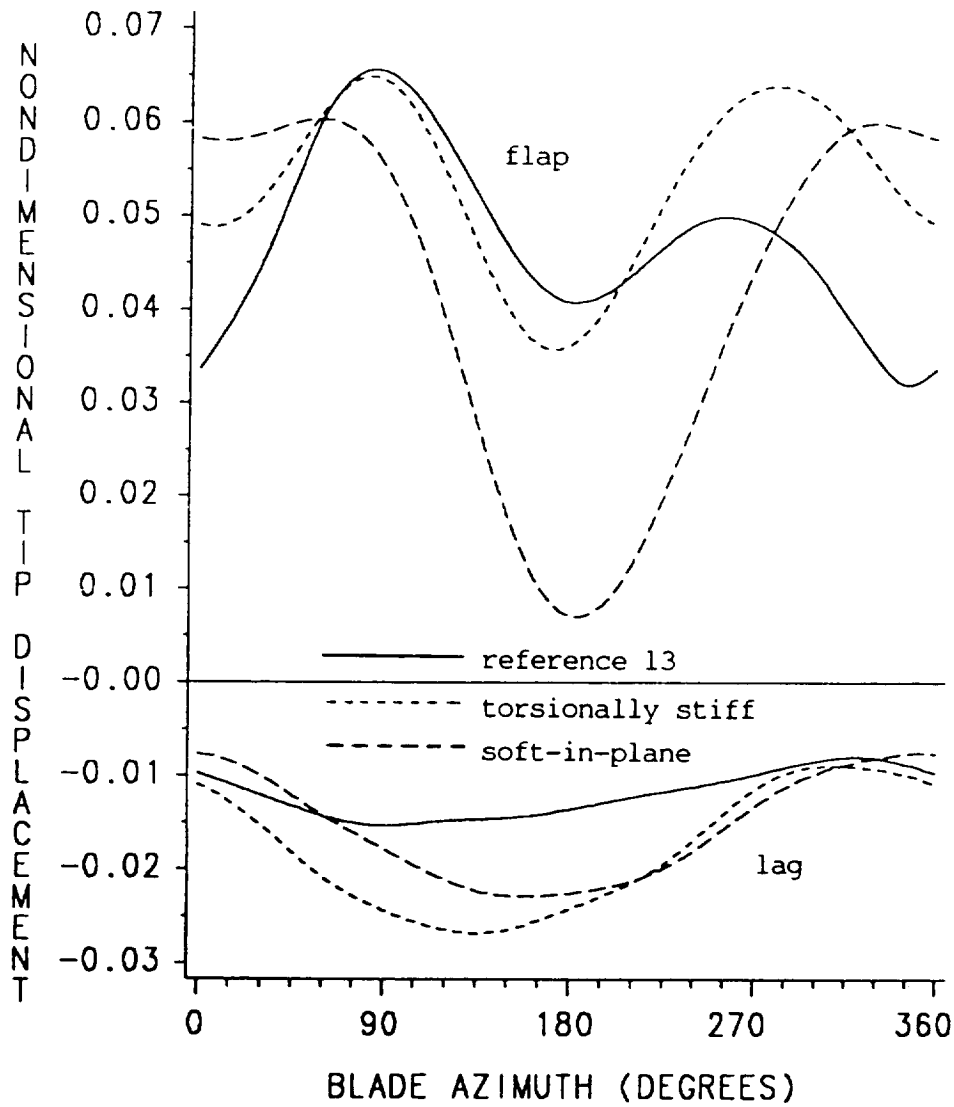

Figure 7.1: Flap and lag response, advance ratio $\mu = 0.4$, results of Ref. 13, torsionally stiff blade, and baseline soft-in-plane blade.

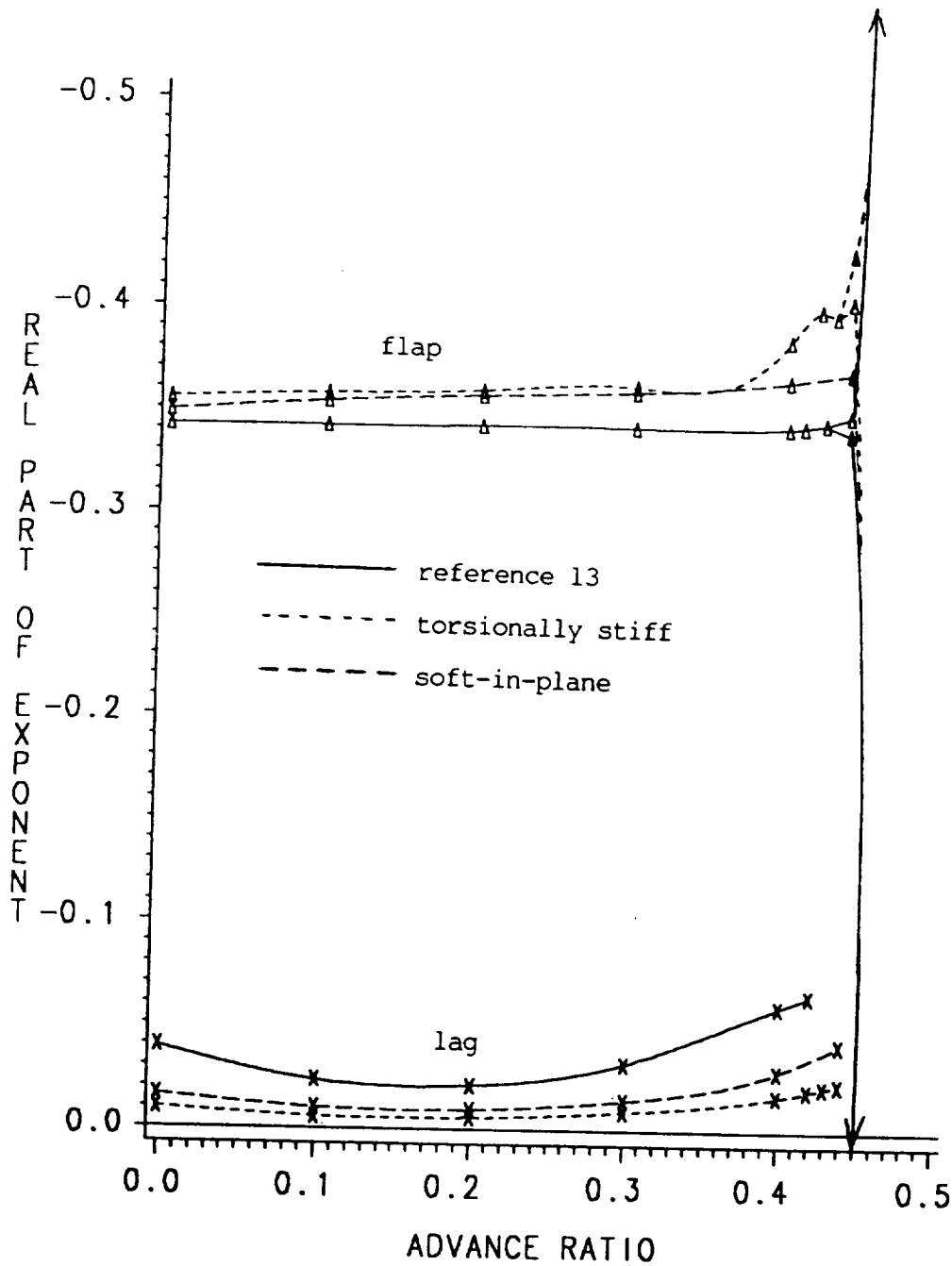

Figure 7.2: Stability eigenvalues for flap and lag for the torsionally stiff blade and the baseline soft-in-plane blade, and their comparison to the results of Ref. 13.

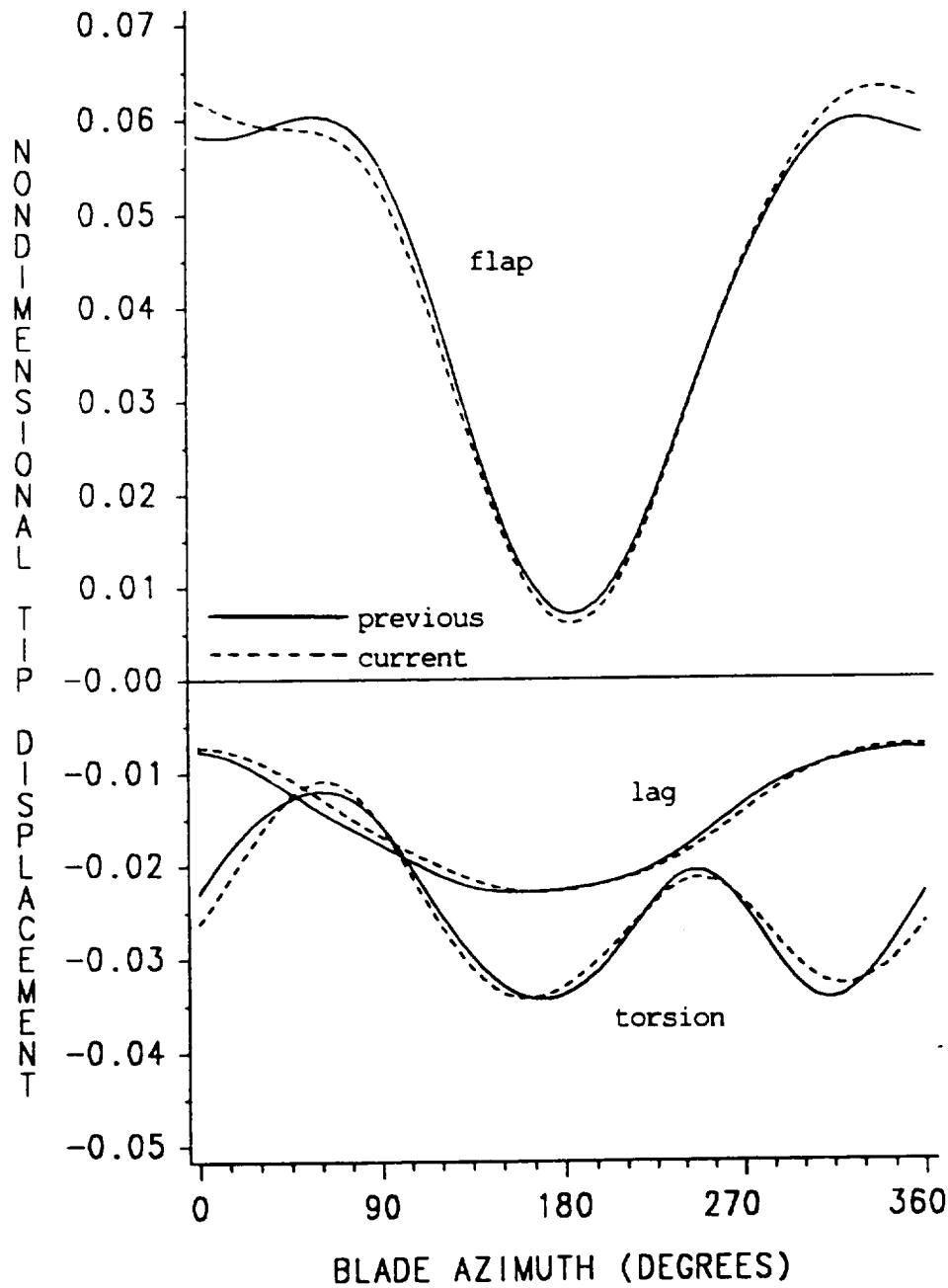

Figure 7.3: Flap, lag, and torsional response, soft-in-plane blade, advance ratio $\mu = 0.4$, previous and current unsteady aerodynamics.

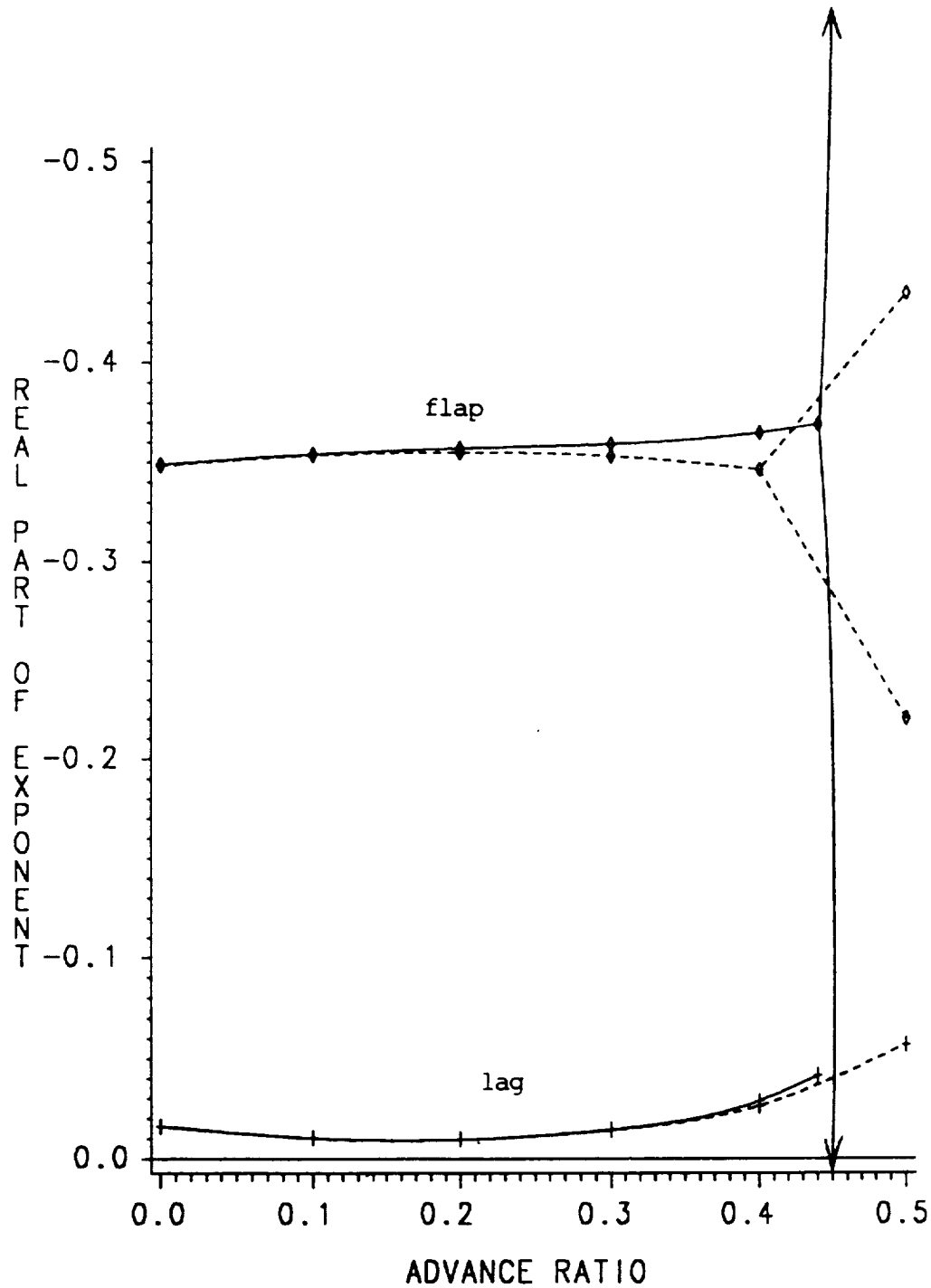

Figure 7.4: Stability eigenvalues for flap and lag, soft-in-plane blade, previous and current unsteady aerodynamics.

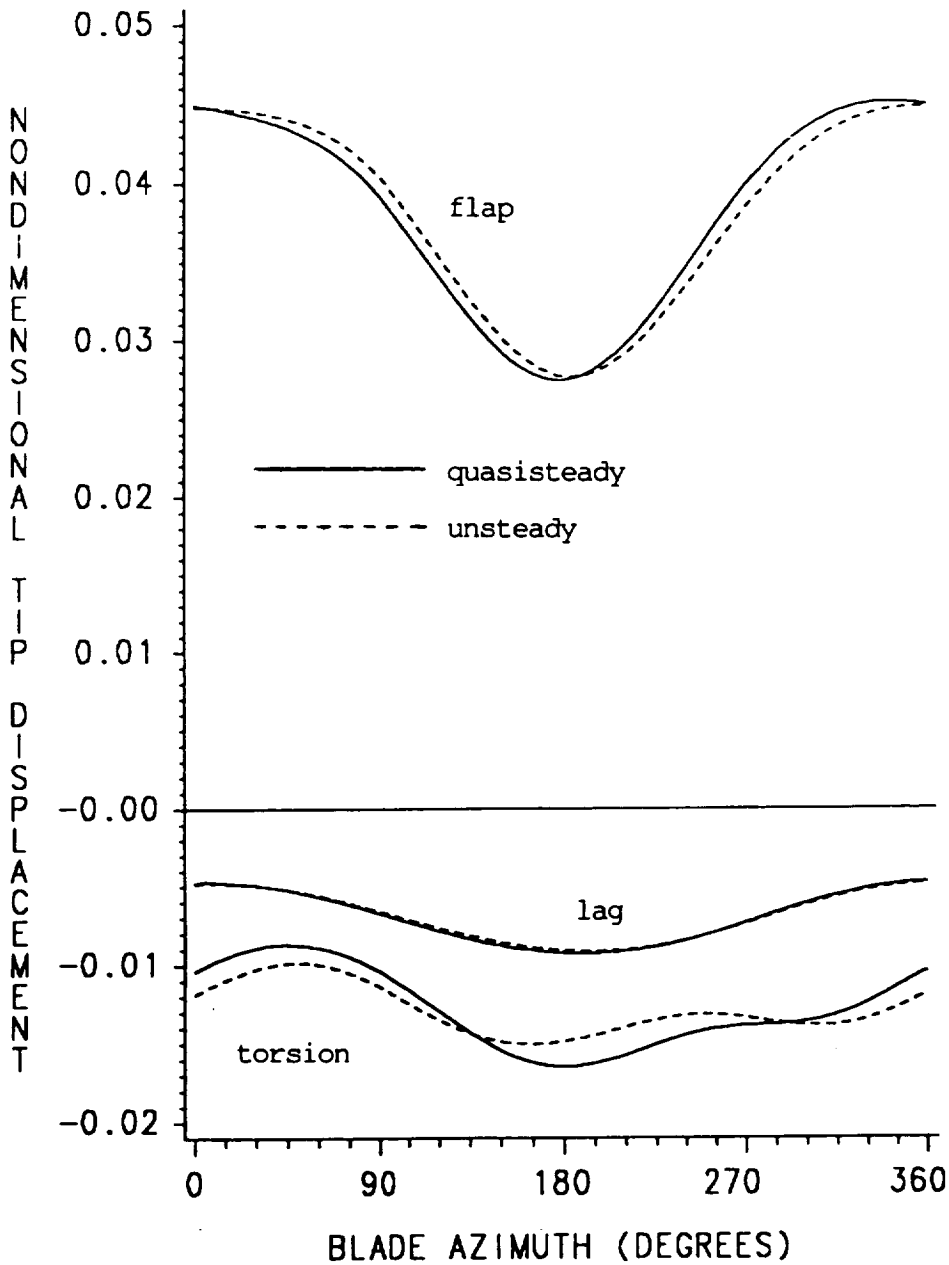

Figure 7.5: Flap, lag, and torsional response, soft-in-plane blade, advance ratio $\mu = 0.2$, quasisteady and unsteady aerodynamics.

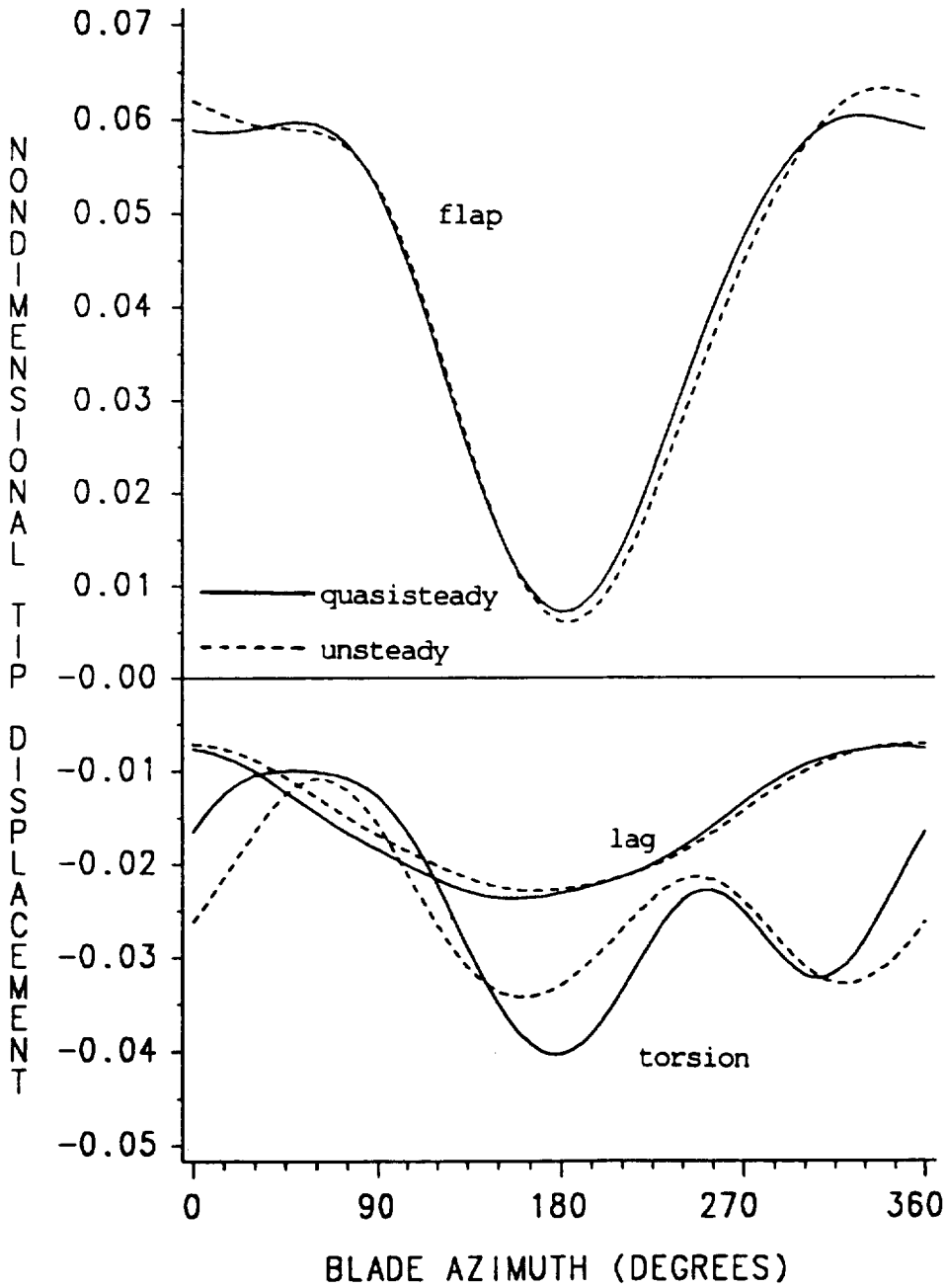

Figure 7.6: Flap, lag, and torsional response, soft-in-plane blade, advance ratio $\mu = 0.4$, quasisteady and unsteady aerodynamics.

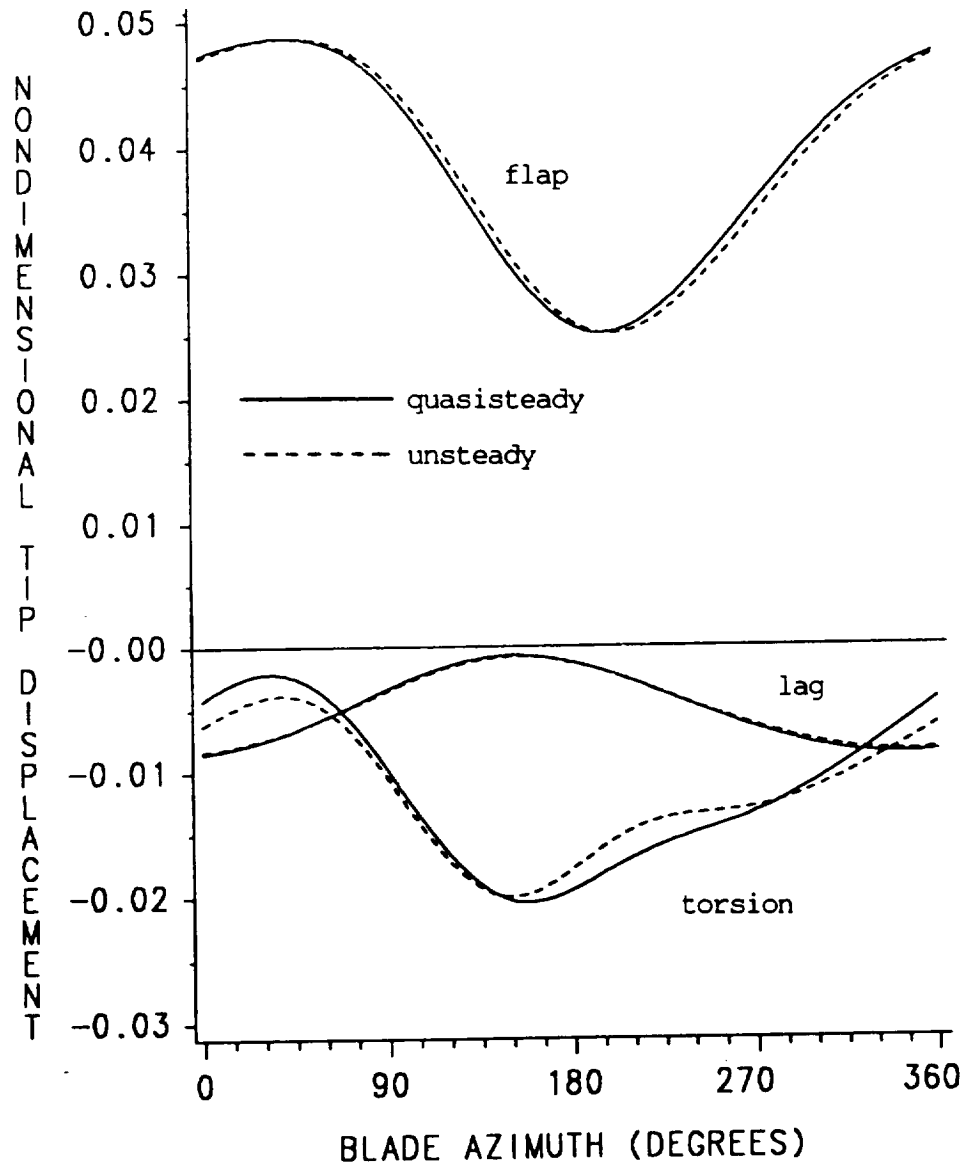

Figure 7.7: Flap, lag, and torsional response, stiff-in-plane blade, advance ratio $\mu = 0.2$, quasisteady and unsteady aerodynamics.

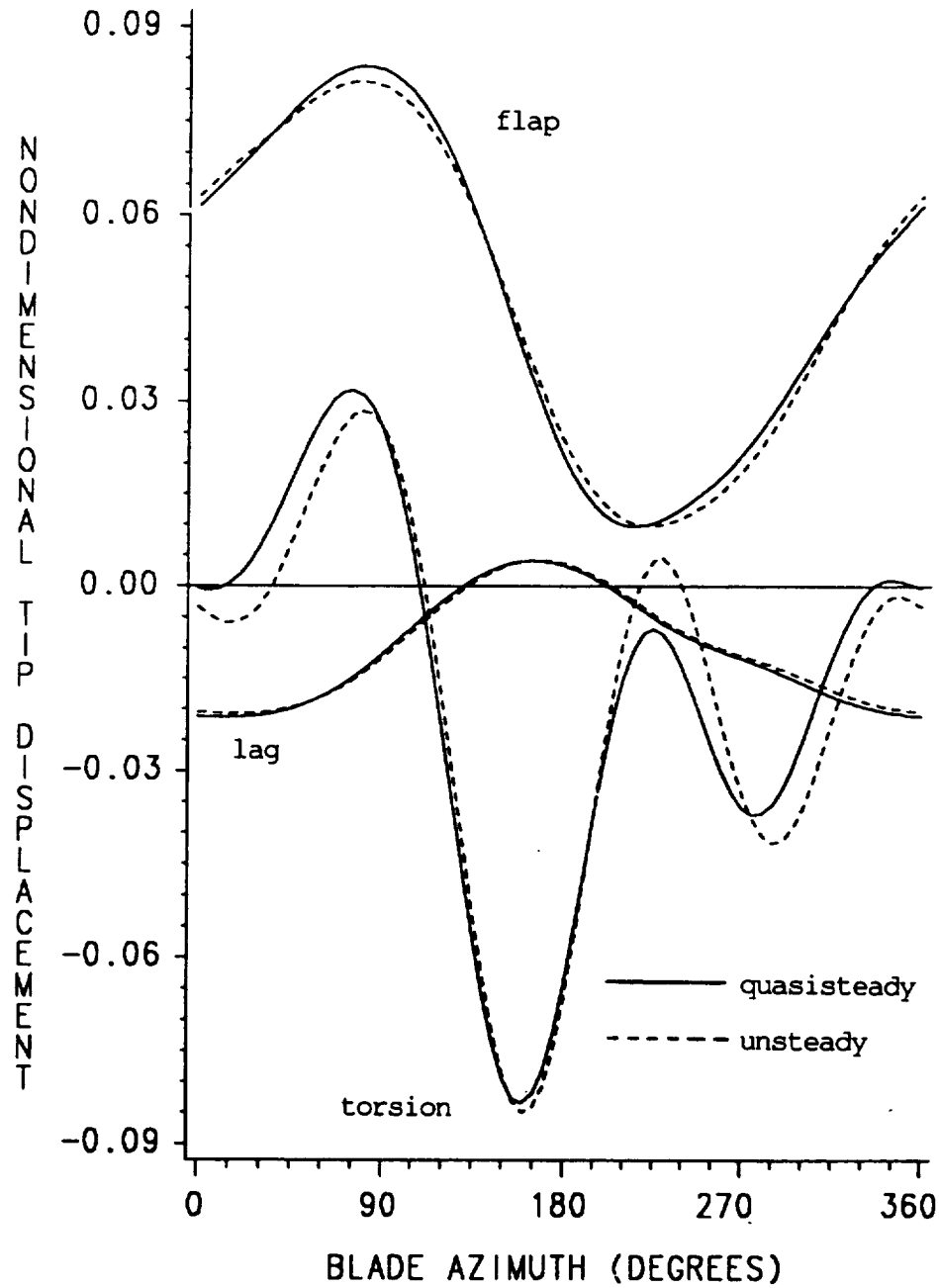

Figure 7.8: Flap, lag, and torsional response, stiff-in-plane blade, advance ratio $\mu = 0.4$, quasisteady and unsteady aerodynamics.

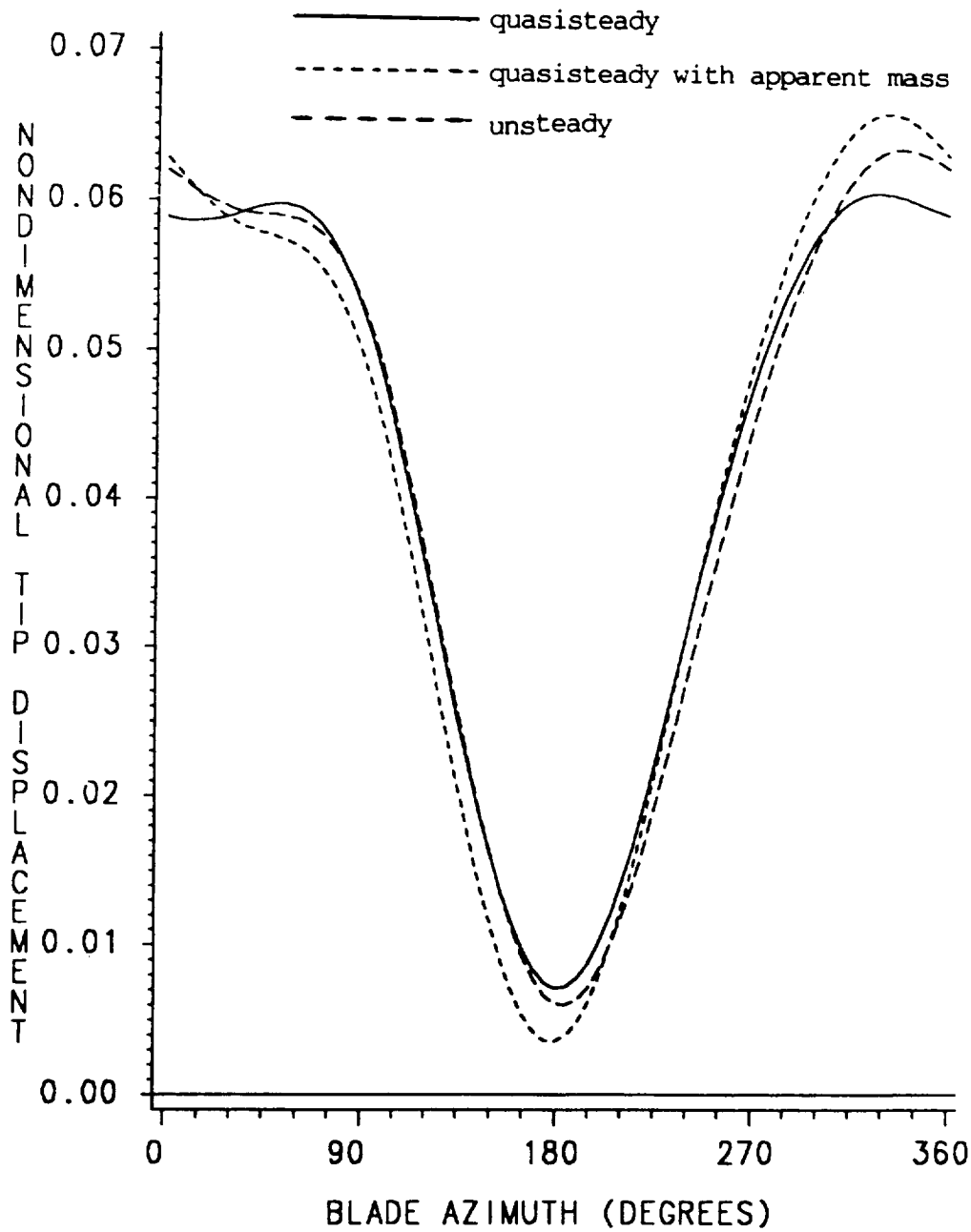

Figure 7.9: Flap response, soft-in-plane blade, advance ratio $\mu = 0.4$, quasisteady, quasisteady with apparent mass, and unsteady aerodynamics.

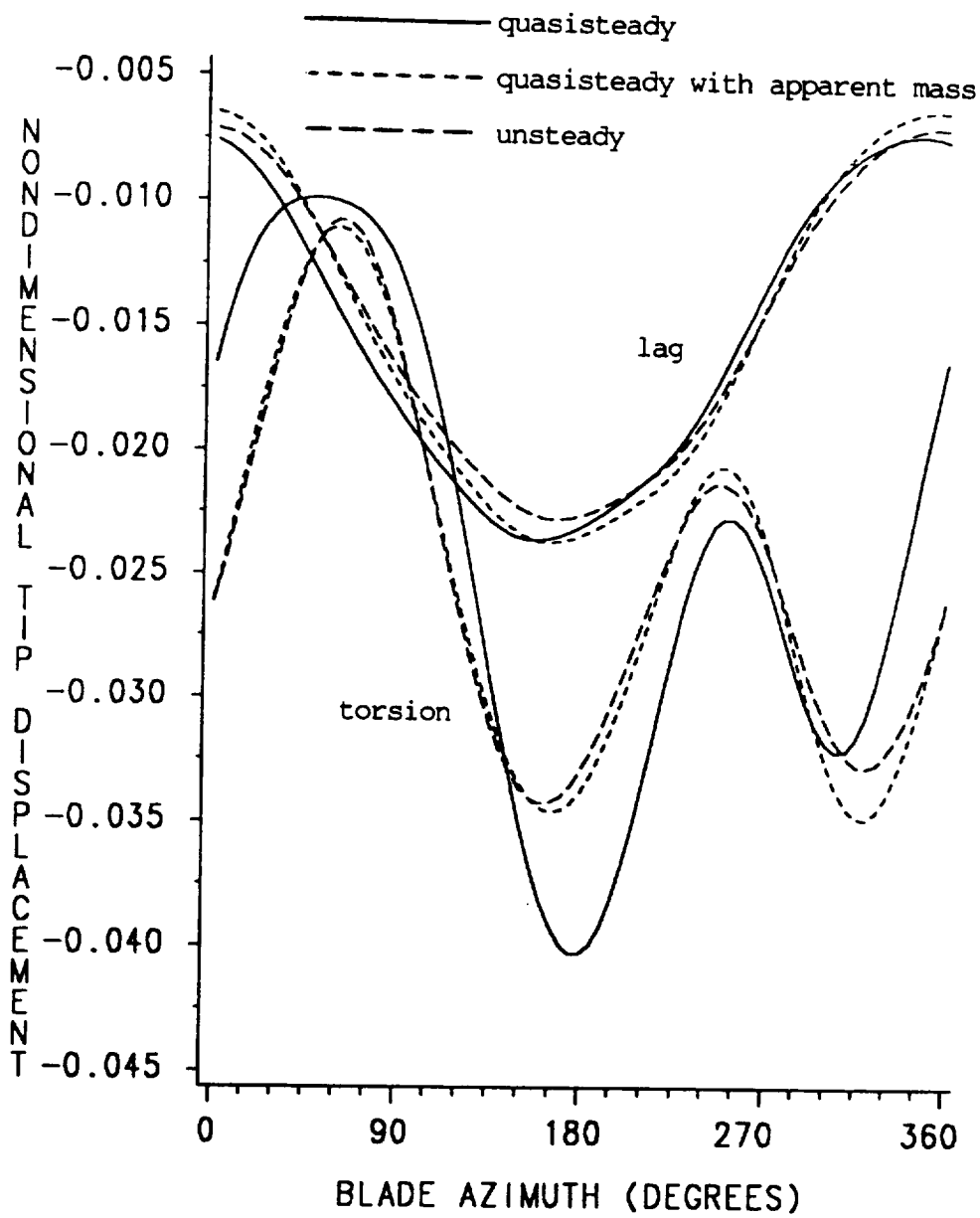

Figure 7.10: Lag and torsional response, soft-in-plane blade, advance ratio $\mu = 0.4$, quasisteady, quasisteady with apparent mass, and unsteady aerodynamics.

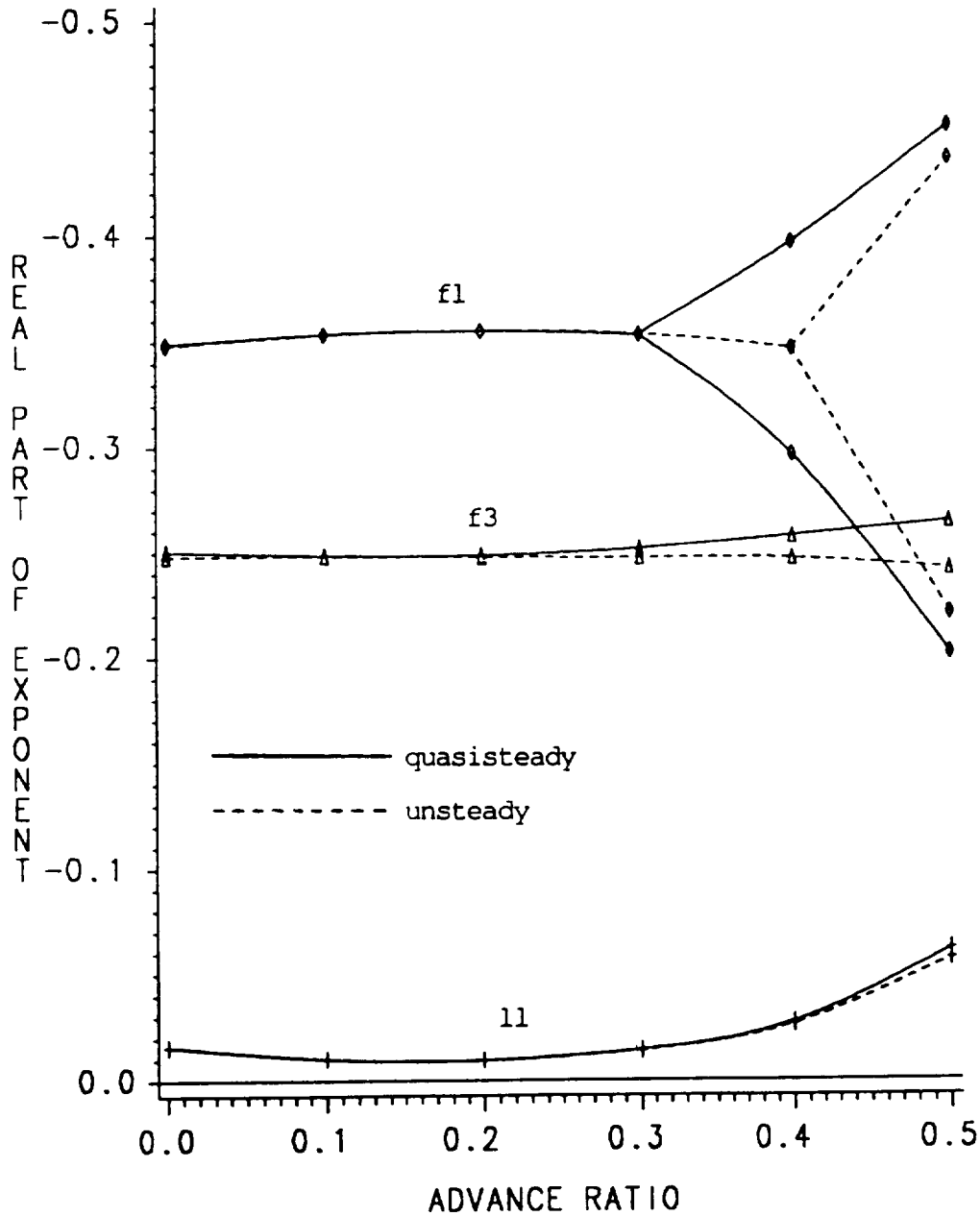

Figure 7.11: Stability eigenvalues for the first lag, first flap, and third flap modes, soft-in-plane blade, quasisteady and unsteady aerodynamics.

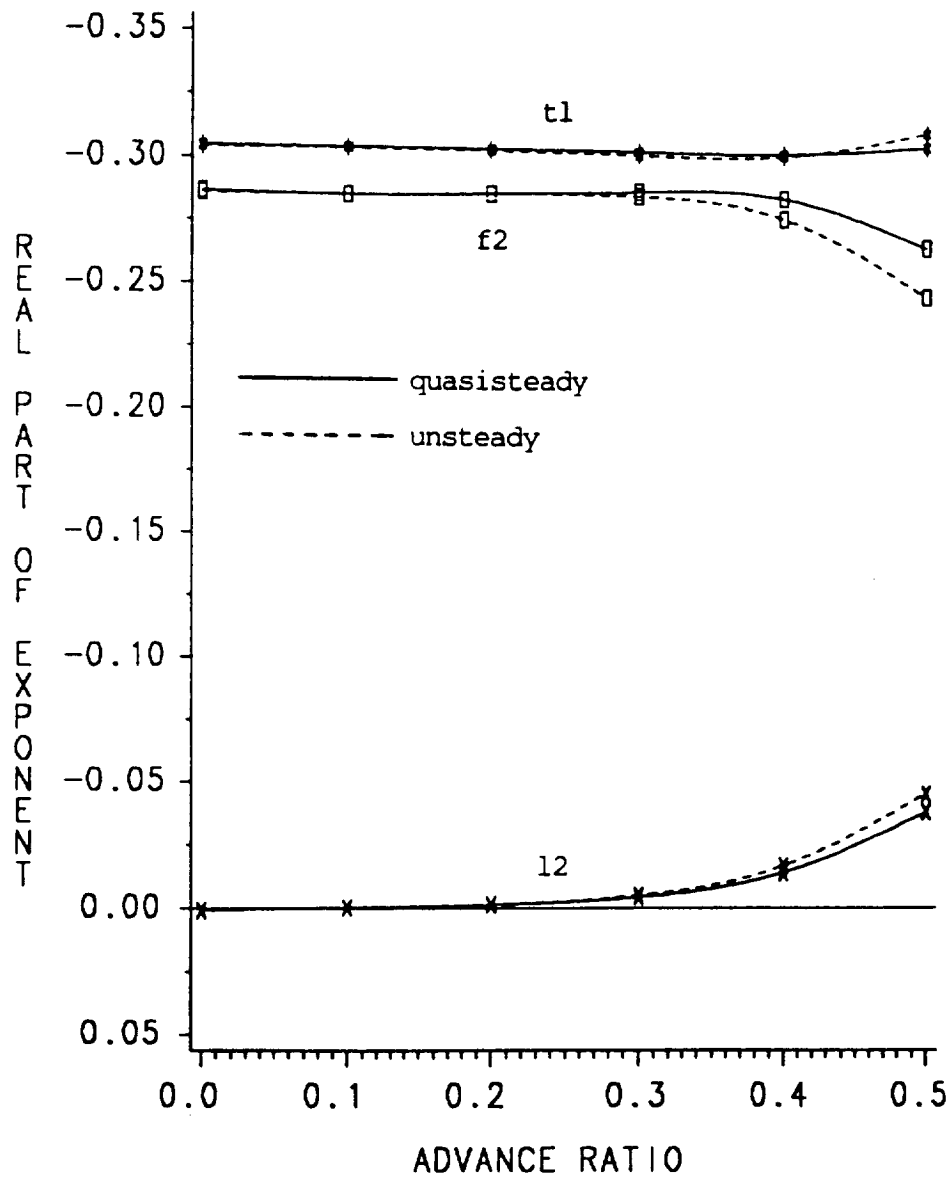

Figure 7.12: Stability eigenvalues for the second lag, second flap, and first torsion modes, soft-in-plane blade, quasisteady and unsteady aerodynamics.

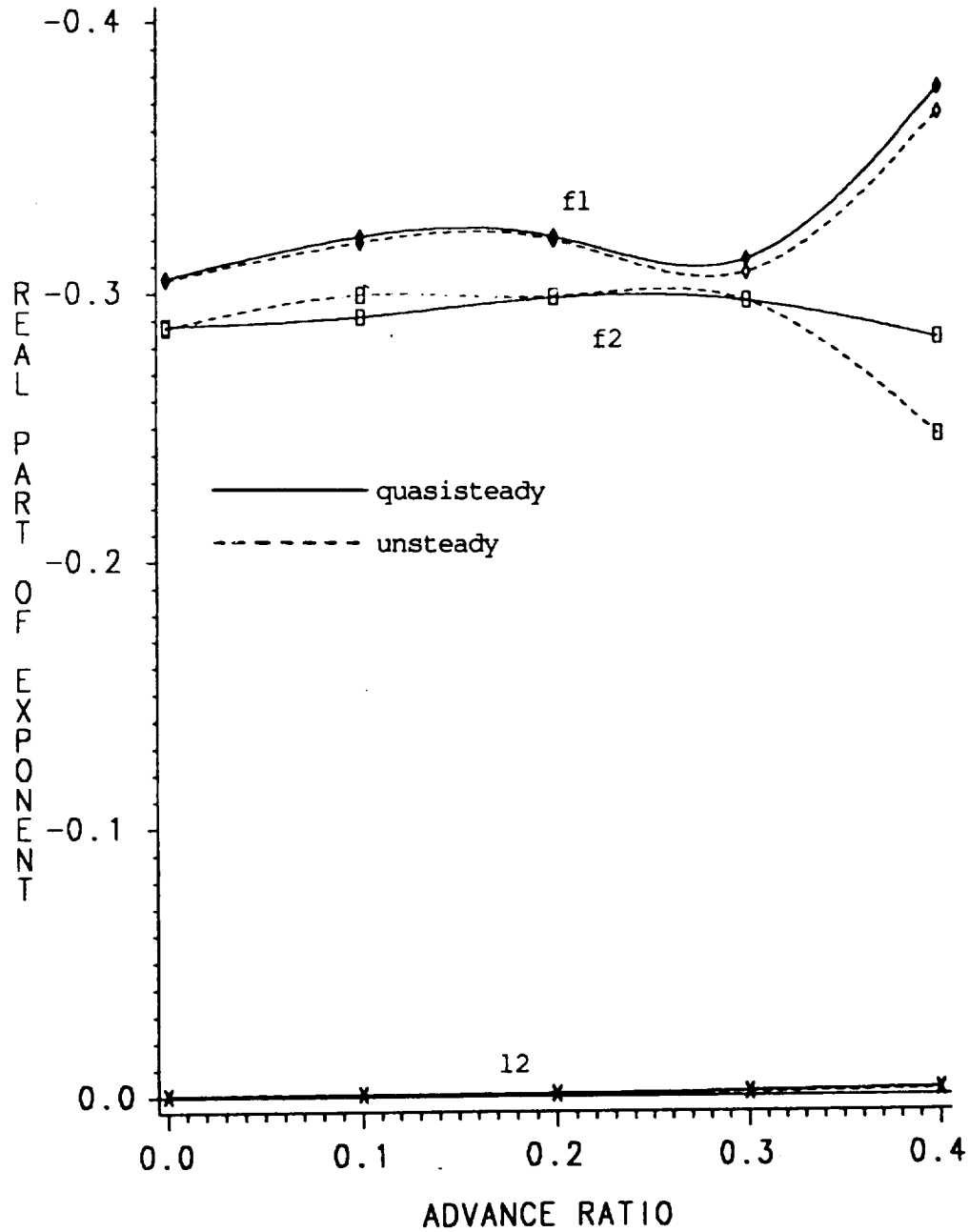

Figure 7.13: Stability eigenvalues for the second lag, first flap, and second flap modes, stiff-in-plane blade, quasisteady and unsteady aerodynamics.

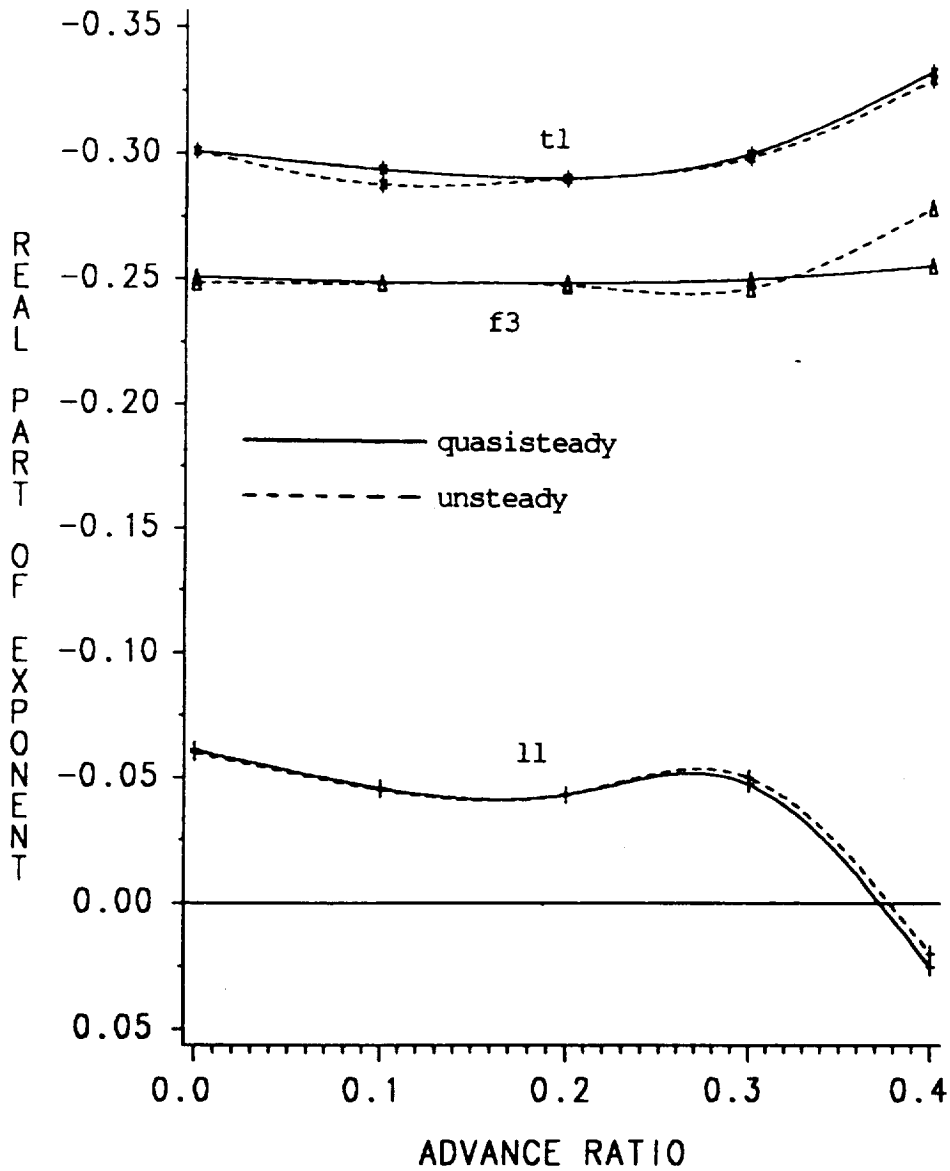

Figure 7.14: Stability eigenvalues for the first lag, third flap, and first torsion modes, stiff-in-plane blade, quasisteady and unsteady aerodynamics.

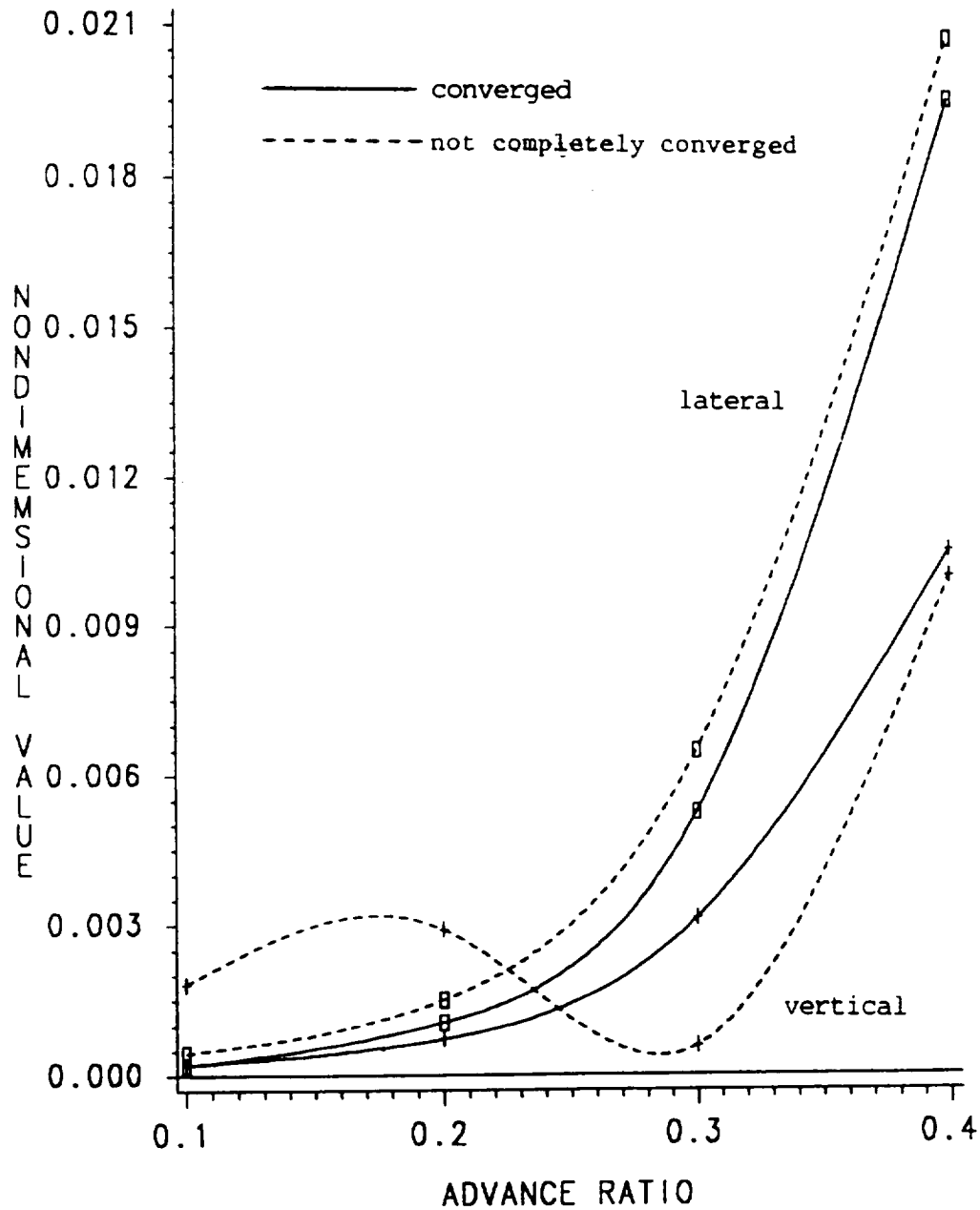

Figure 7.15: Variation of 4/rev. vertical and lateral hub shears with advance ratio, soft-in-plane blade, quasisteady aerodynamics, calculated from converged and unconverged response solutions.

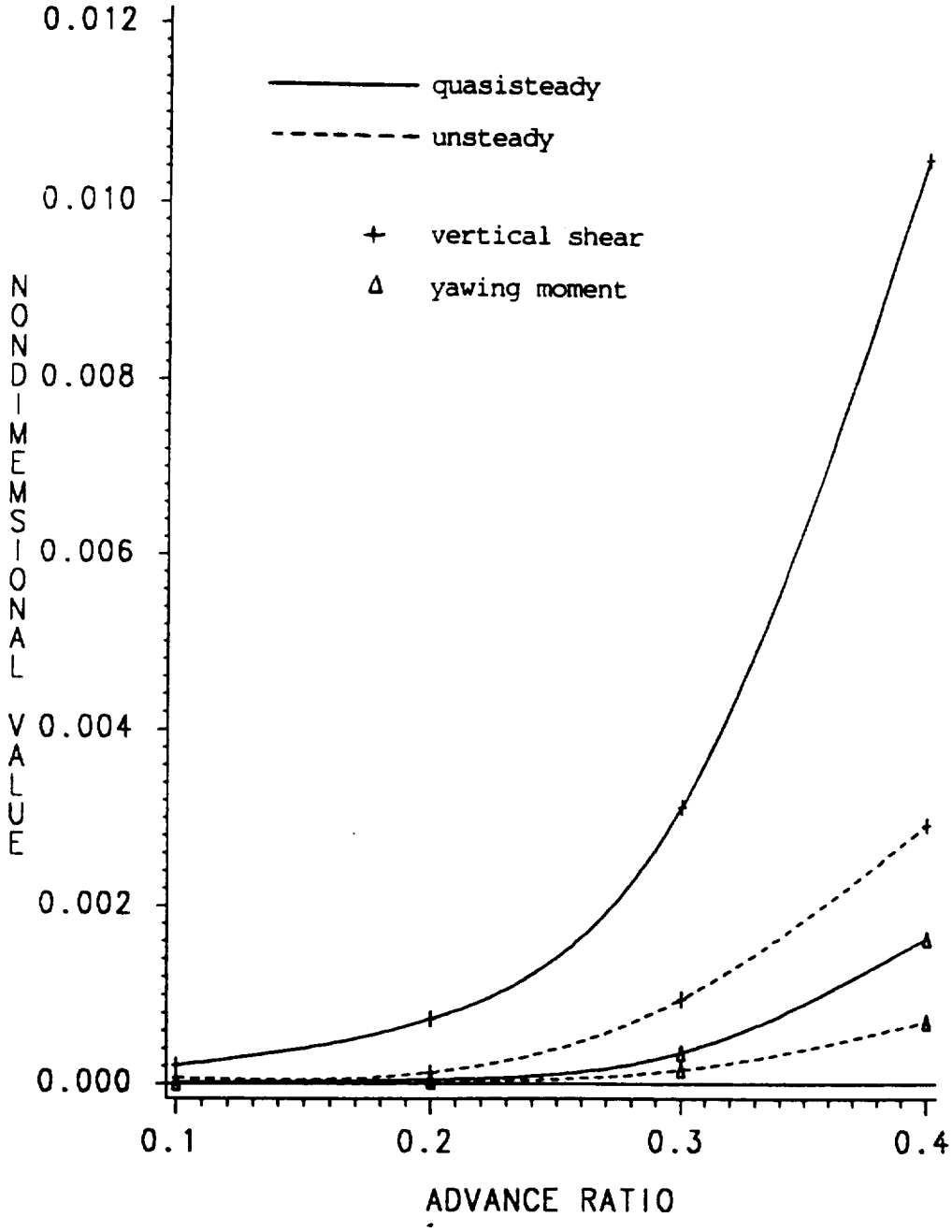

Figure 7.16: Variation of 4/rev. vertical shear and yawing moment with advance ratio, soft-in-plane blade, quasisteady and unsteady aerodynamics.

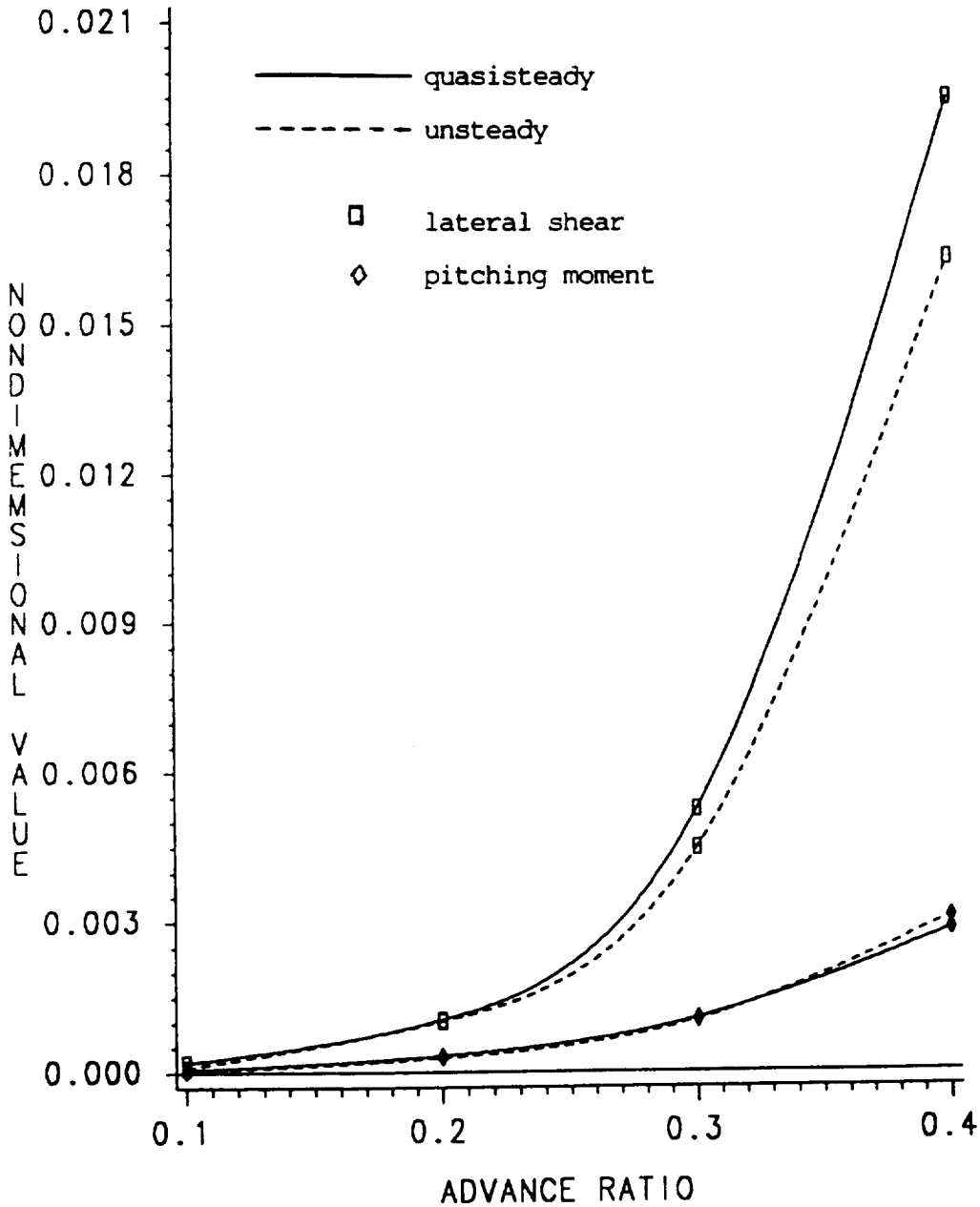

Figure 7.17: Variation of 4/rev. lateral shear and pitching moment with advance ratio, soft-in-plane blade, quasisteady and unsteady aerodynamics.

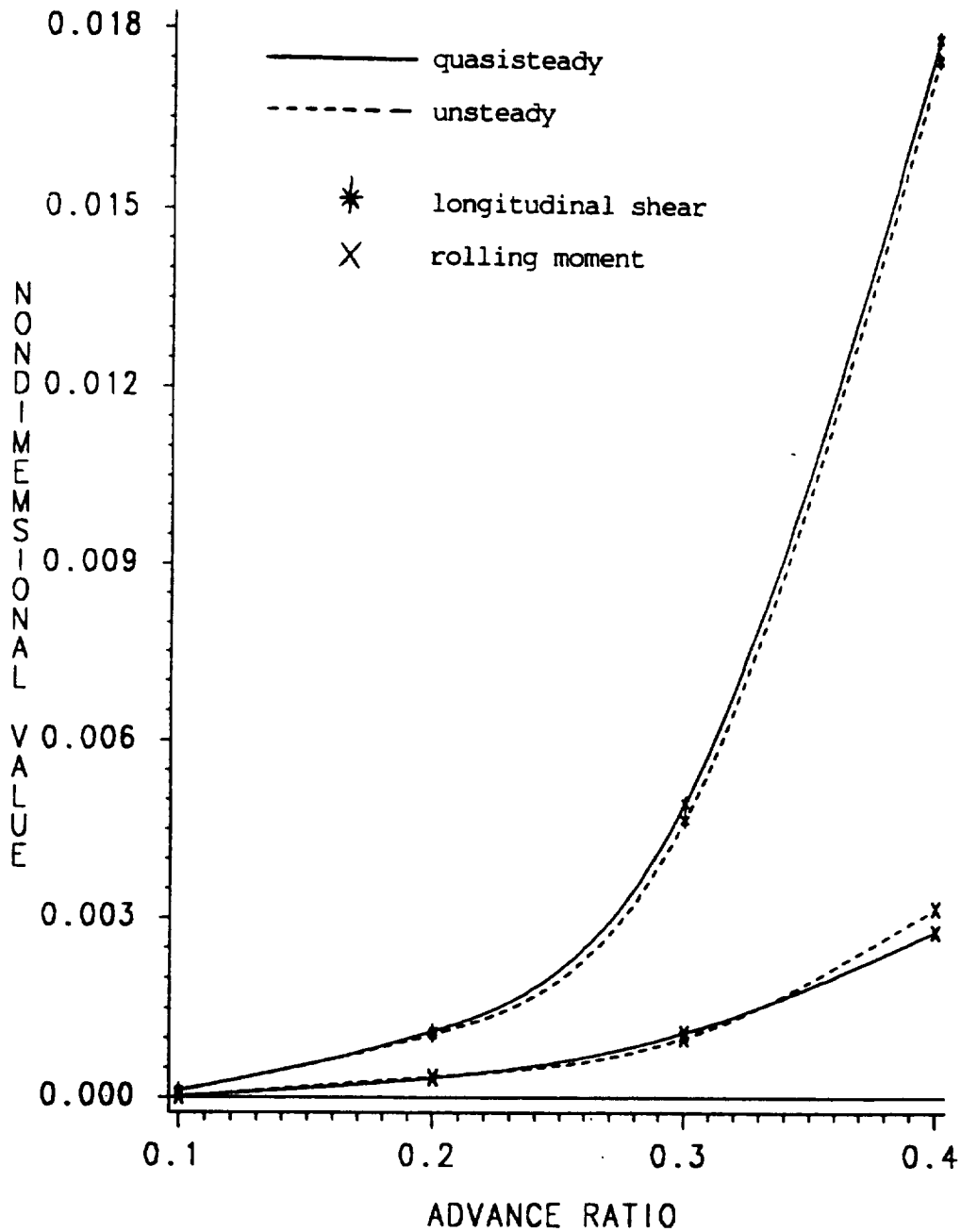

Figure 7.18: Variation of 4/rev. longitudinal shear and rolling moment with advance ratio, soft-in-plane blade, quasisteady and unsteady aerodynamics.

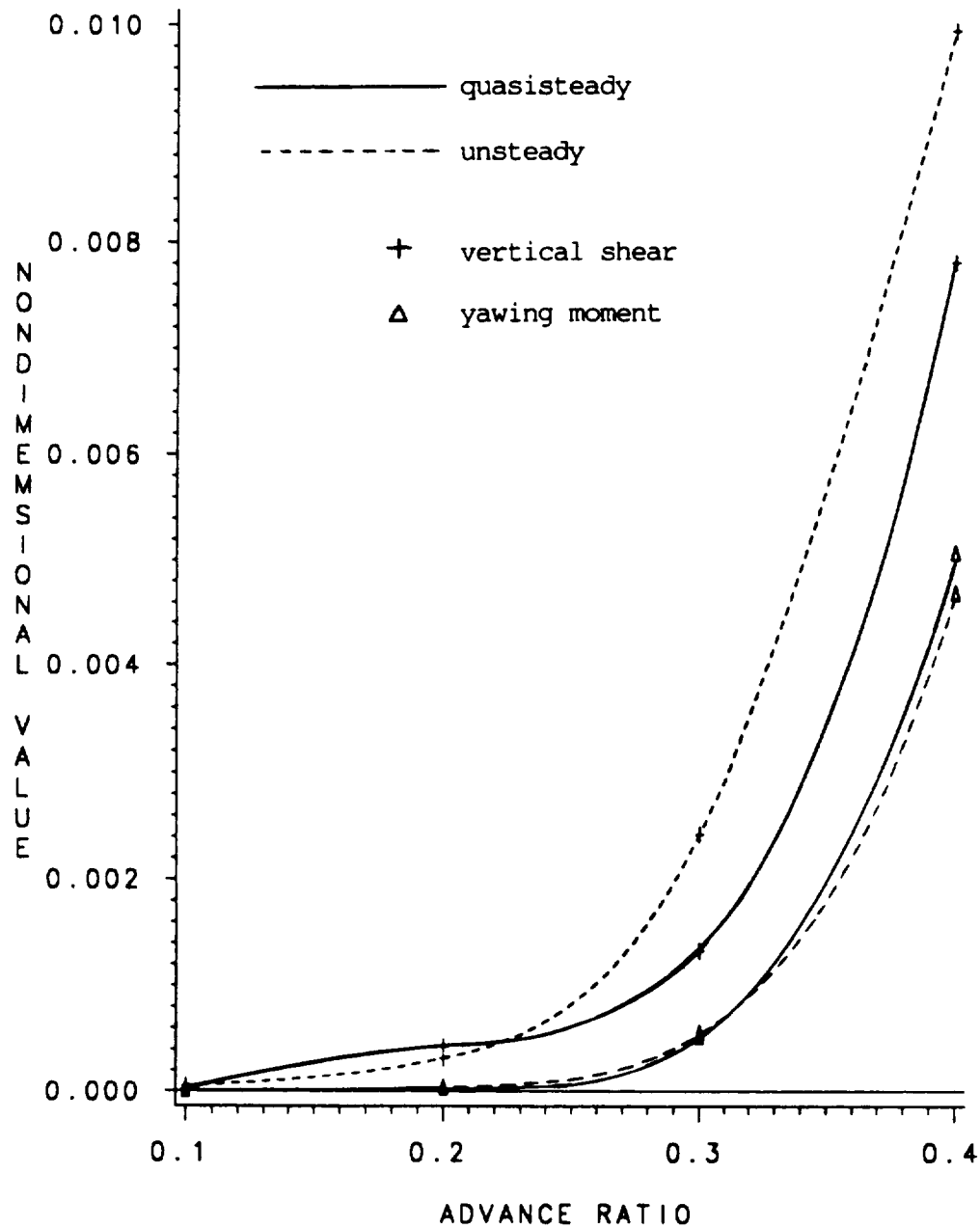

Figure 7.19: Variation of 4/rev. vertical shear and yawing moment with advance ratio, stiff-in-plane blade, quasisteady and unsteady aerodynamics.

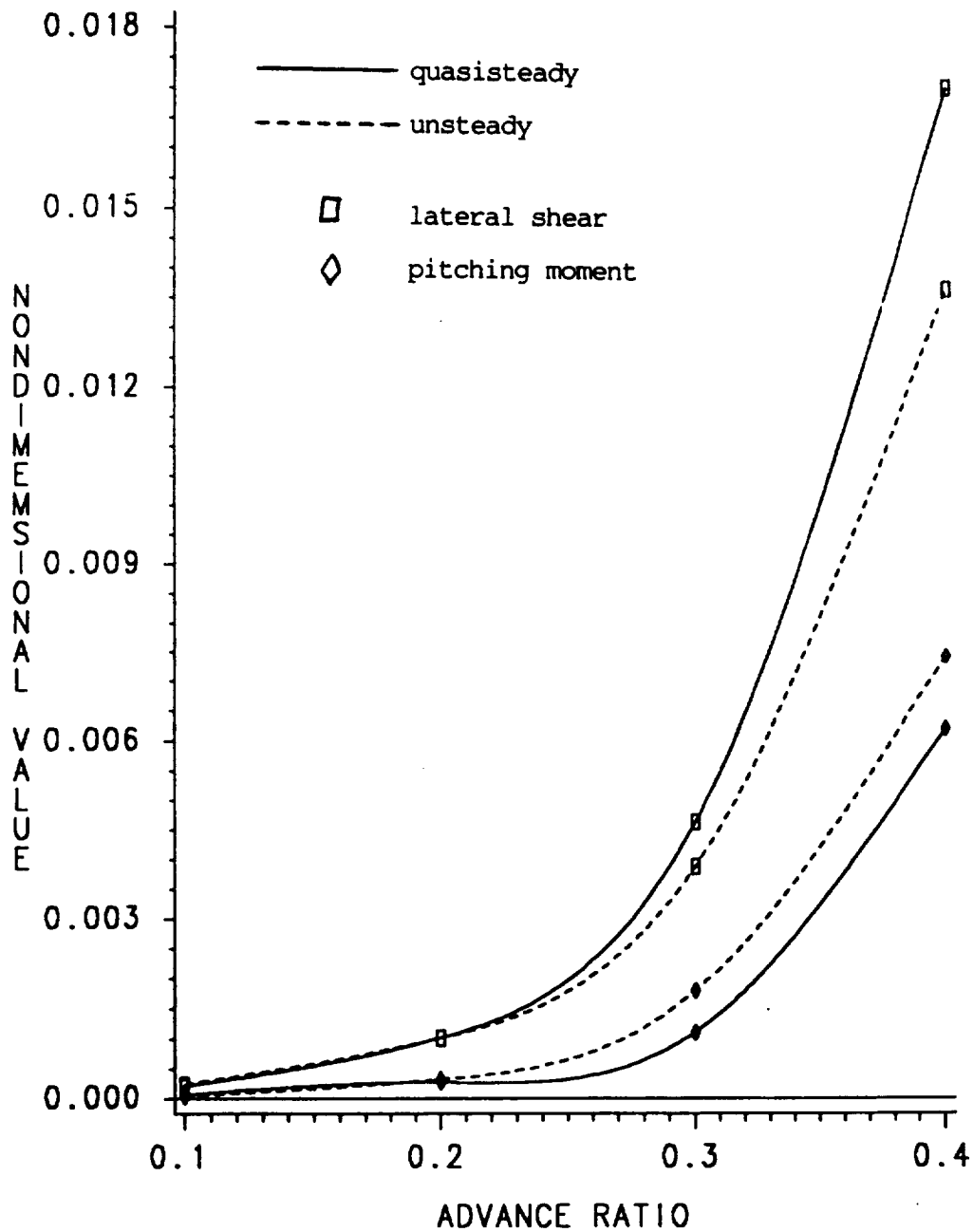

Figure 7.20: Variation of 4/rev. lateral shear and pitching moment with advance ratio, stiff-in-plane blade, quasisteady and unsteady aerodynamics.

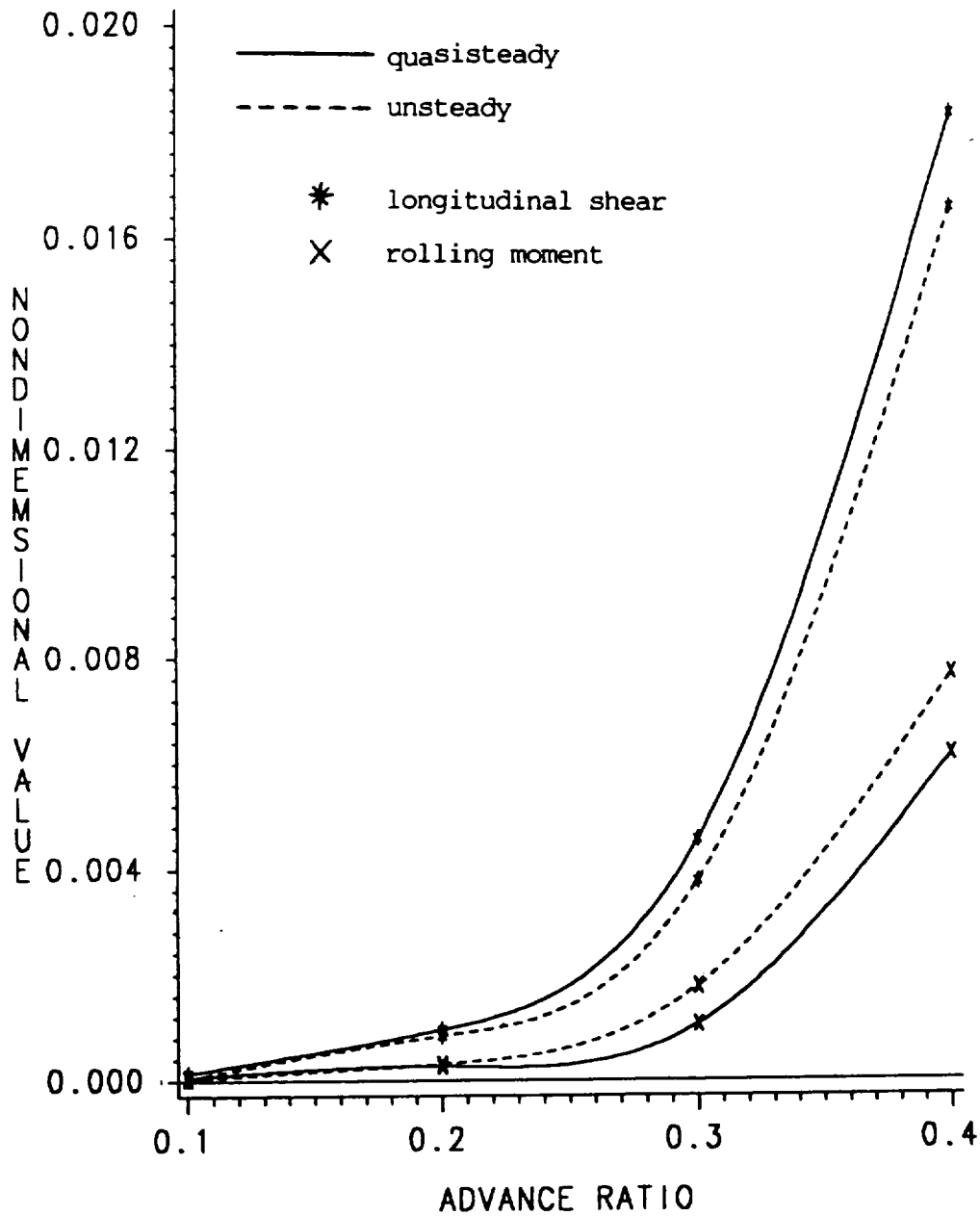

Figure 7.21: Variation of 4/rev. longitudinal shear and rolling moment with advance ratio, stiff-in-plane blade, quasisteady and unsteady aerodynamics.

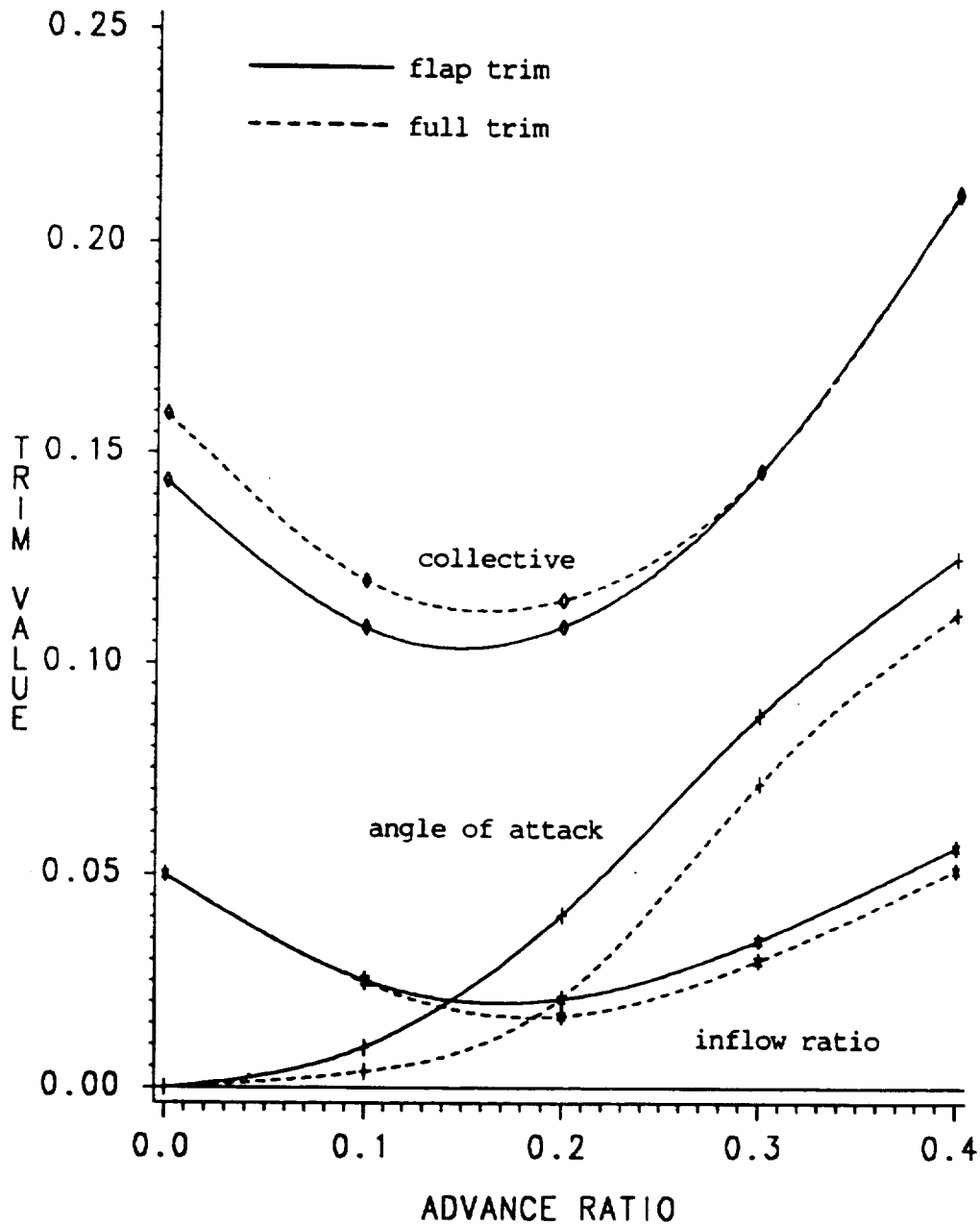

Figure 7.22: Trim values for collective pitch, inflow ratio, and rotor angle of attack, soft-in-plane blade, flap trim and full trim values.

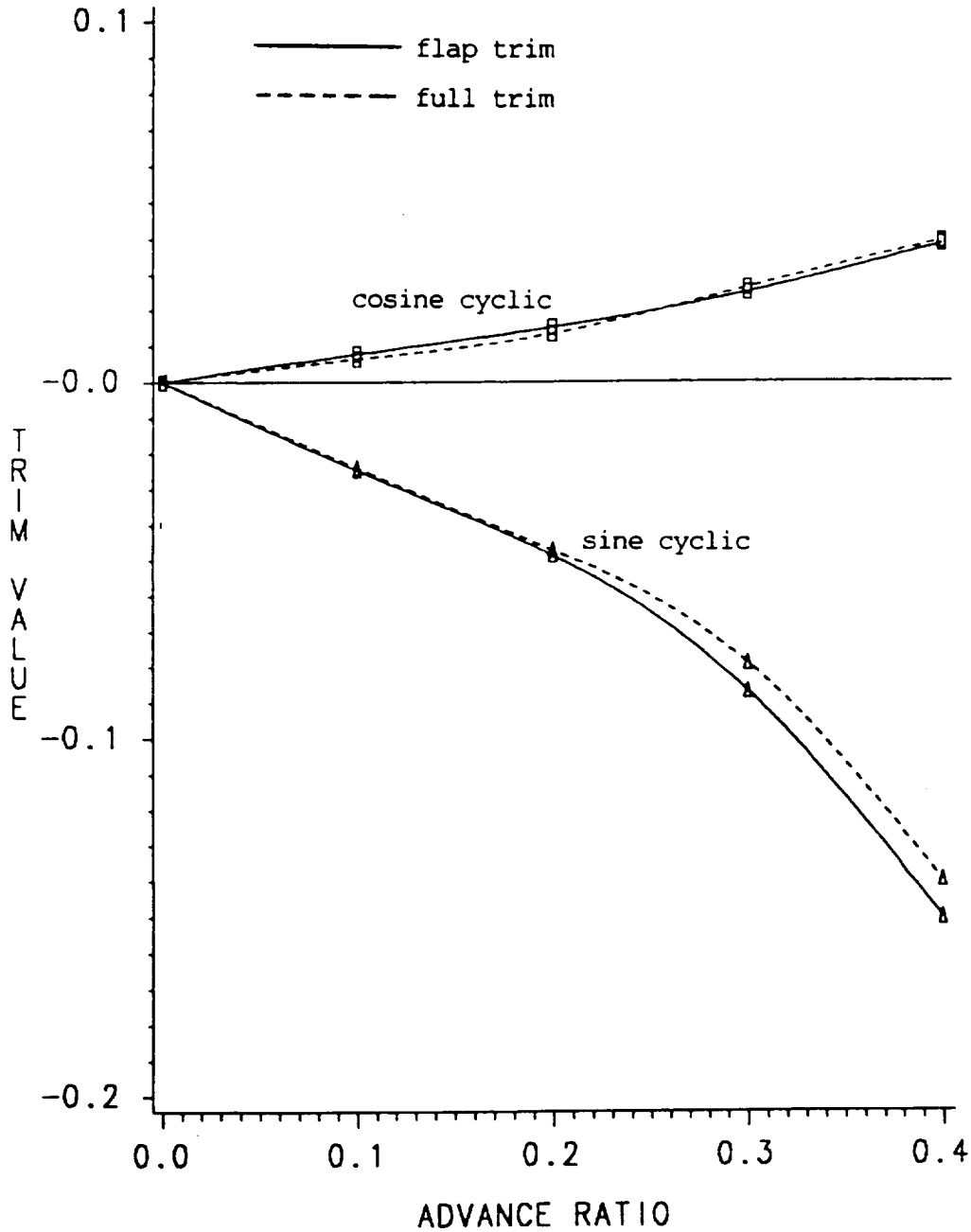

Figure 7.23: Trim values for cosine cyclic pitch and sine cyclic pitch, soft-in-plane blade, flap trim and full trim values.

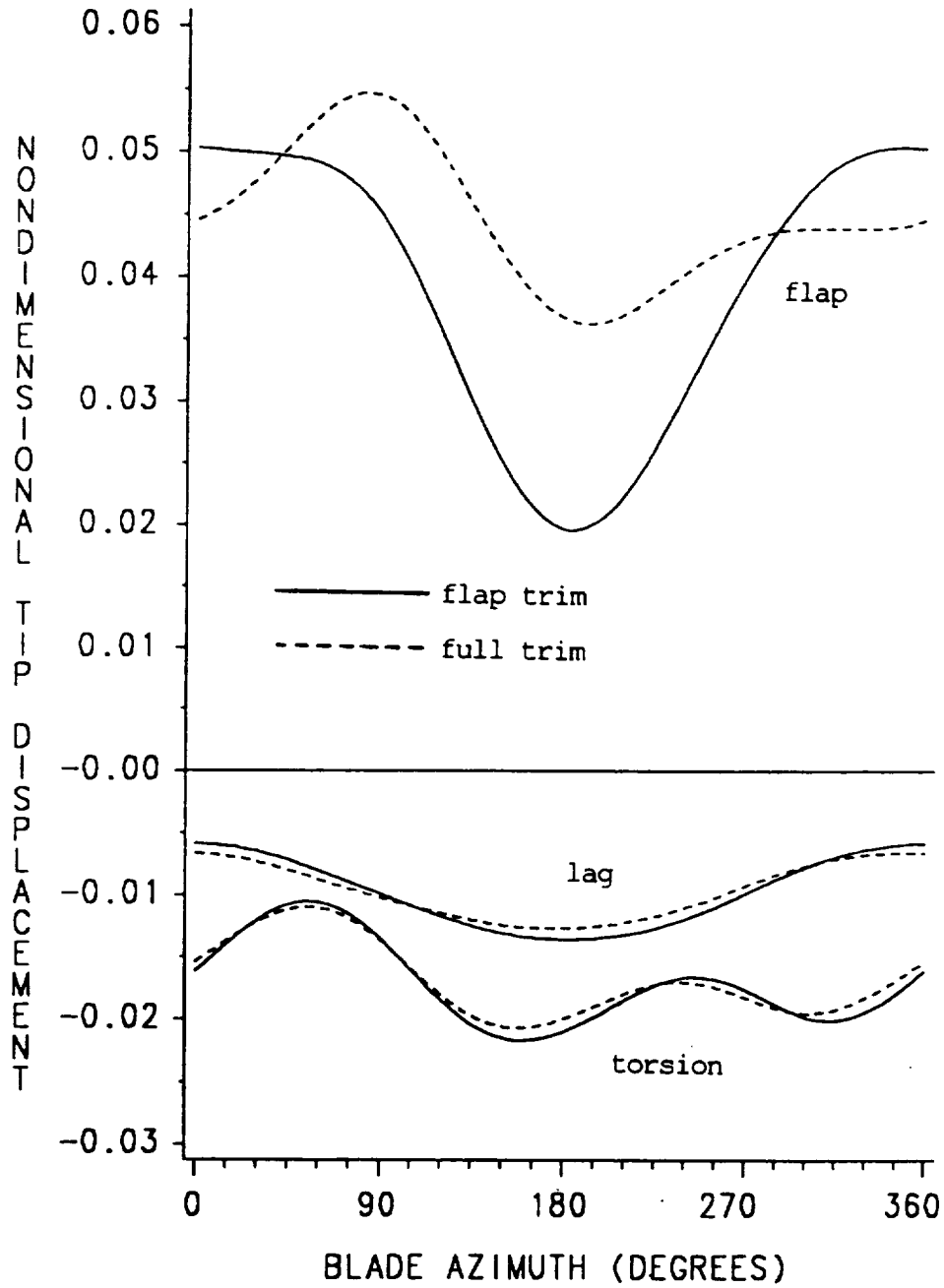

Figure 7.24: Flap, lag, and torsional response, soft-in-plane blade, advance ratio $\mu = 0.3$, unsteady aerodynamics, flap trim and full trim.

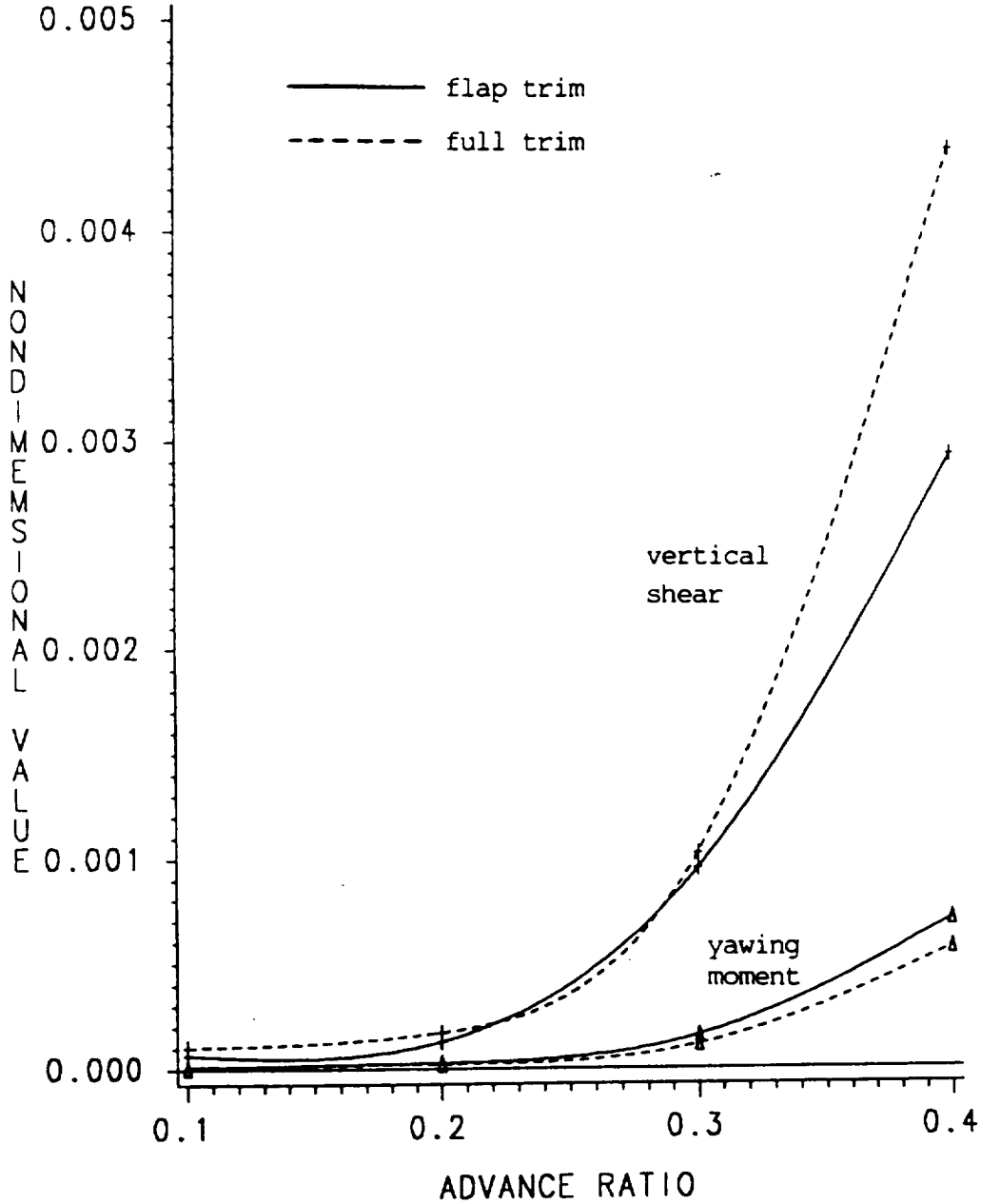

Figure 7.25: Variation of 4/rev. vertical shear and yawing moment with advance ratio, soft-in-plane blade, unsteady aerodynamics, flap trim and full trim.

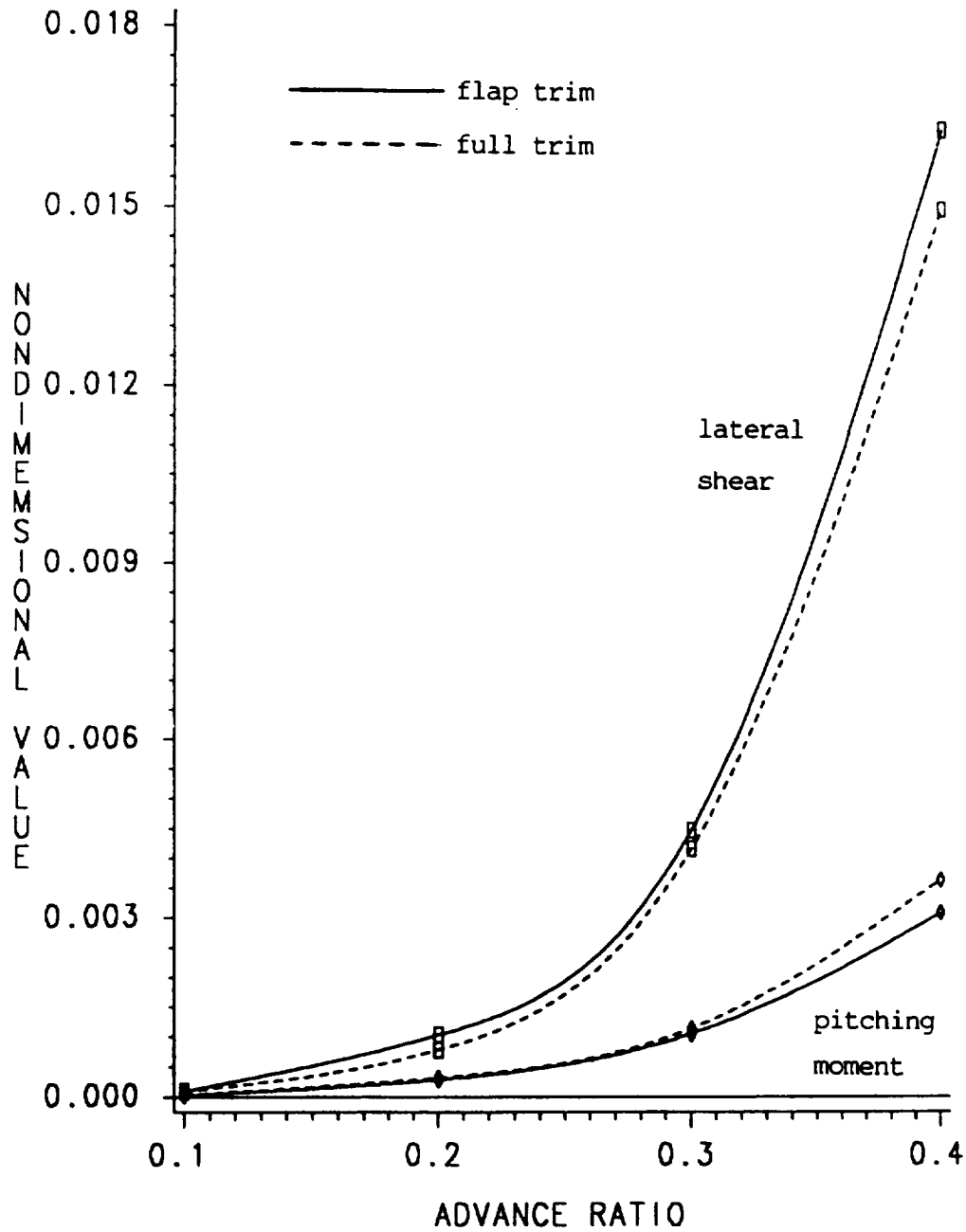

Figure 7.26: Variation of 4/rev. lateral shear and pitching moment with advance ratio, soft-in-plane blade, unsteady aerodynamics, flap trim and full trim.

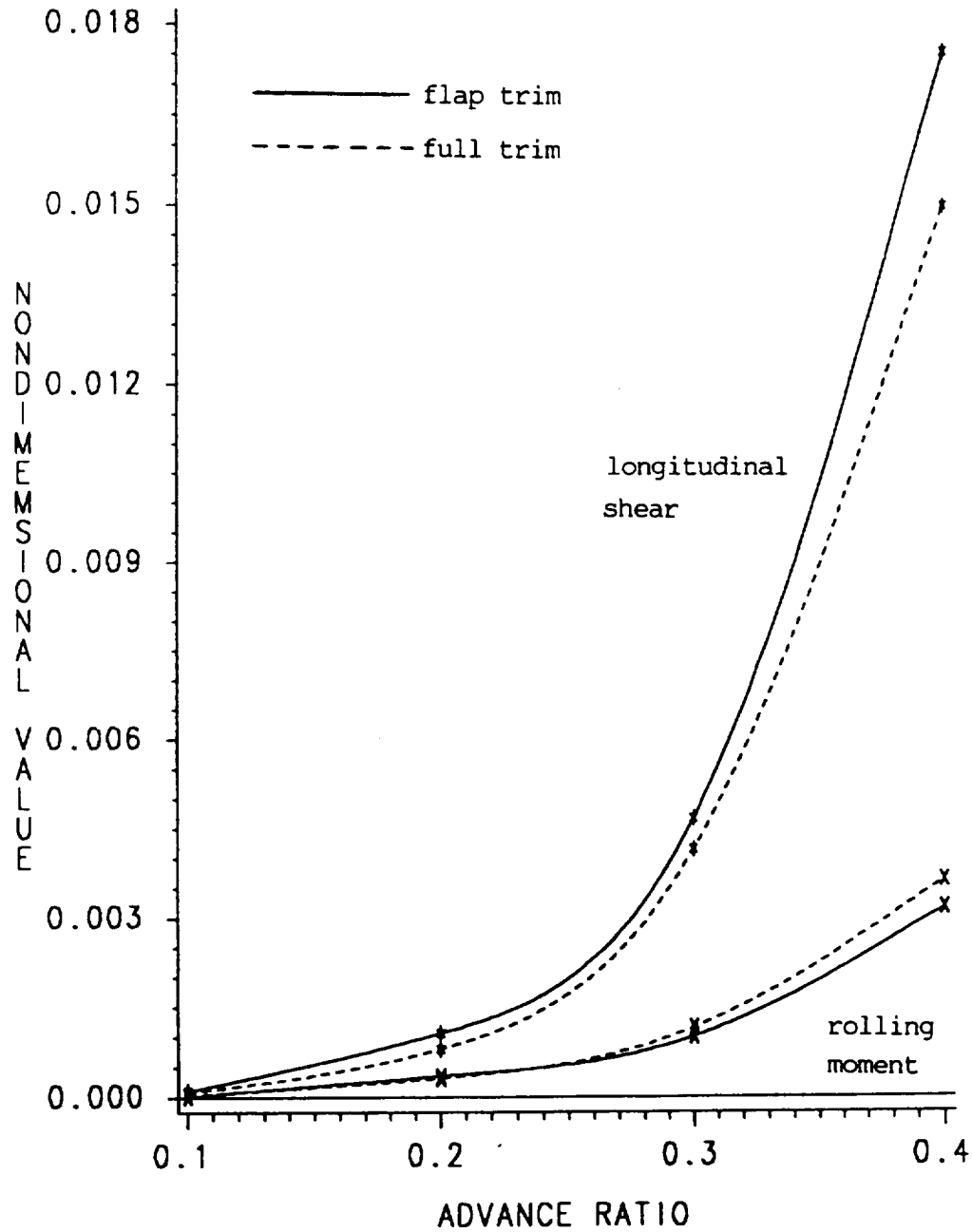

Figure 7.27: Variation of 4/rev. longitudinal shear and rolling moment with advance ratio, soft-in-plane blade, unsteady aerodynamics, flap trim and full trim.

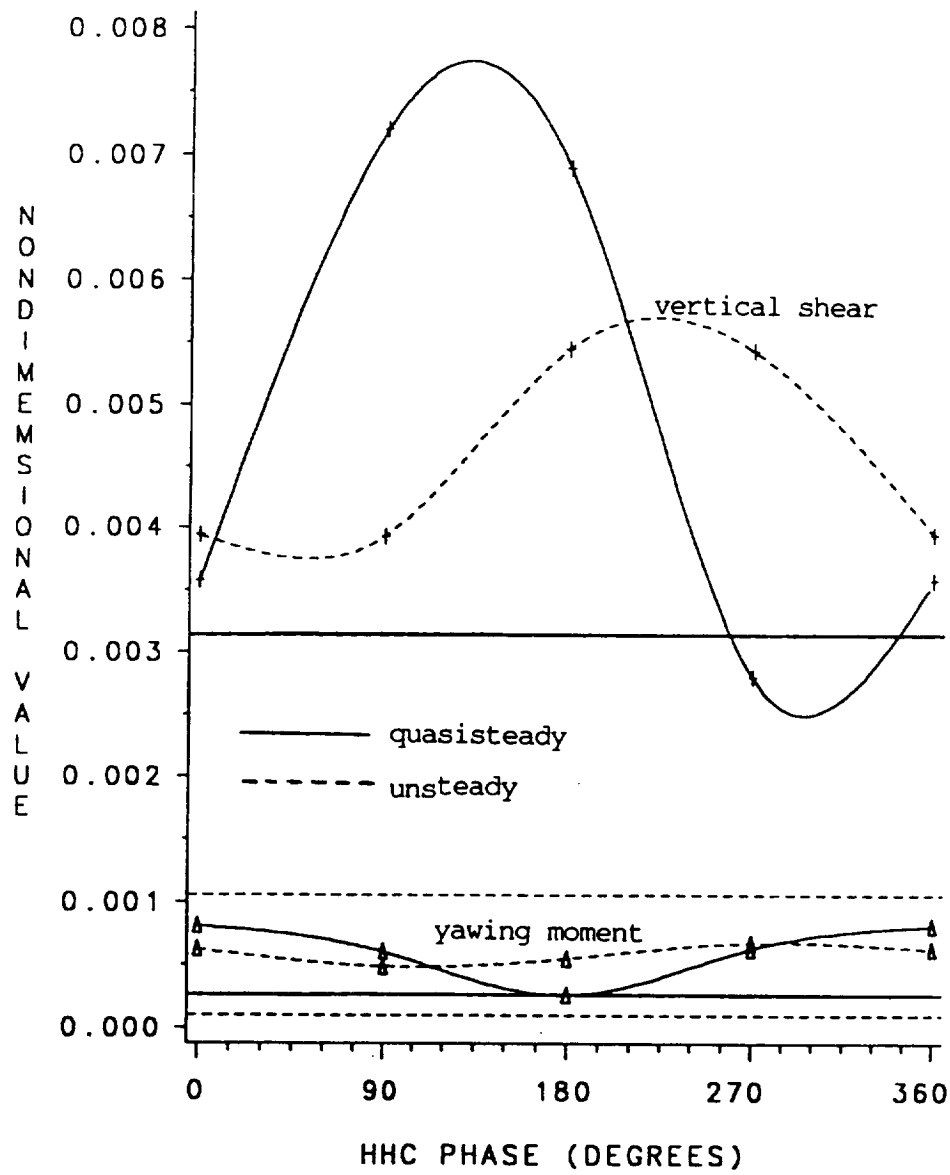

Figure 8.1: Variation of 4/rev. vertical shear and yawing moment with HHC phase, collective input, soft-in-plane blade, quasisteady and unsteady aerodynamics, $\mu = 0.3$.

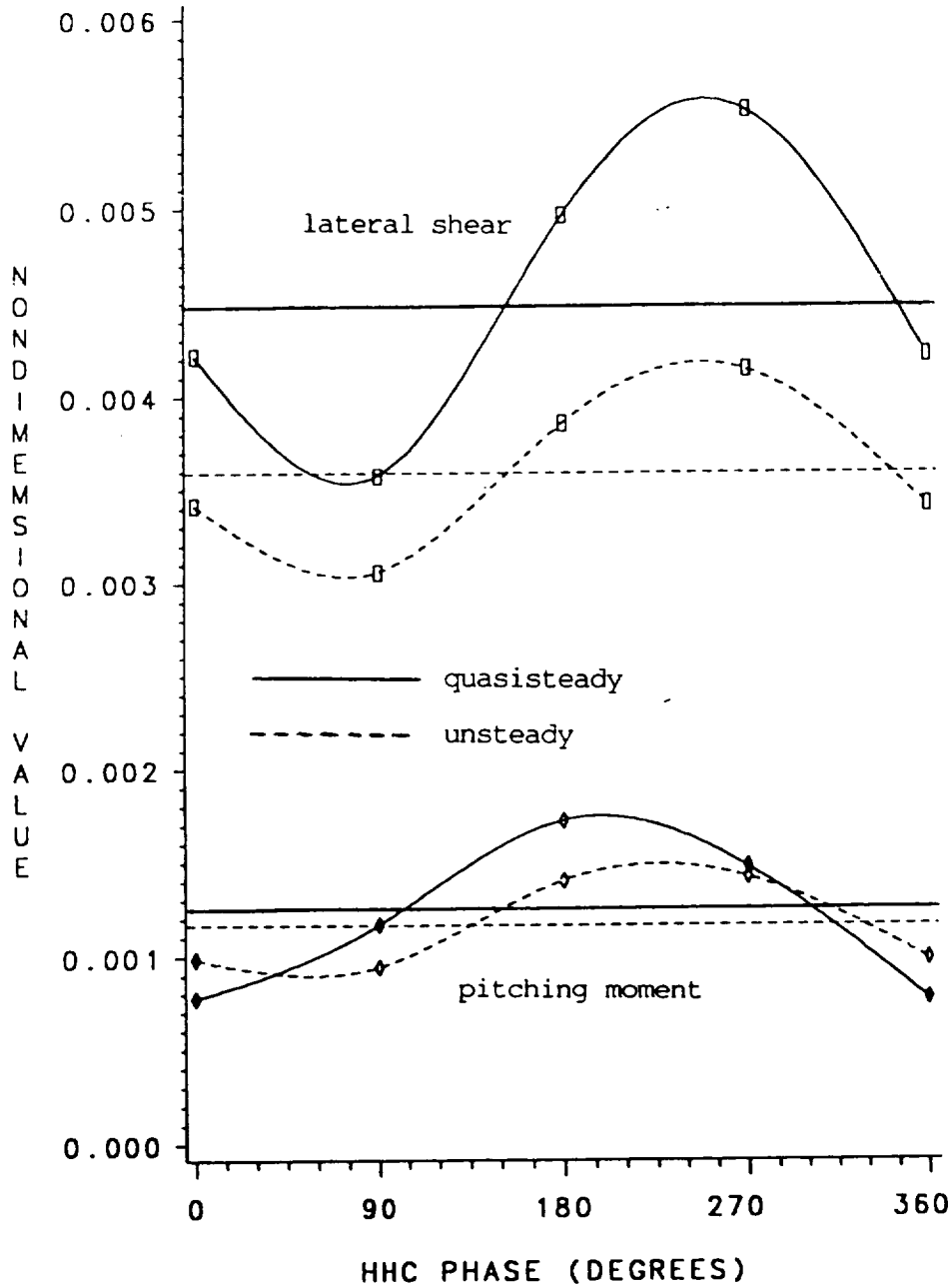

Figure 8.2: Variation of 4/rev. lateral shear and pitching moment with HHC phase, collective input, soft-in-plane blade, quasisteady and unsteady aerodynamics, $\mu = 0.3$.

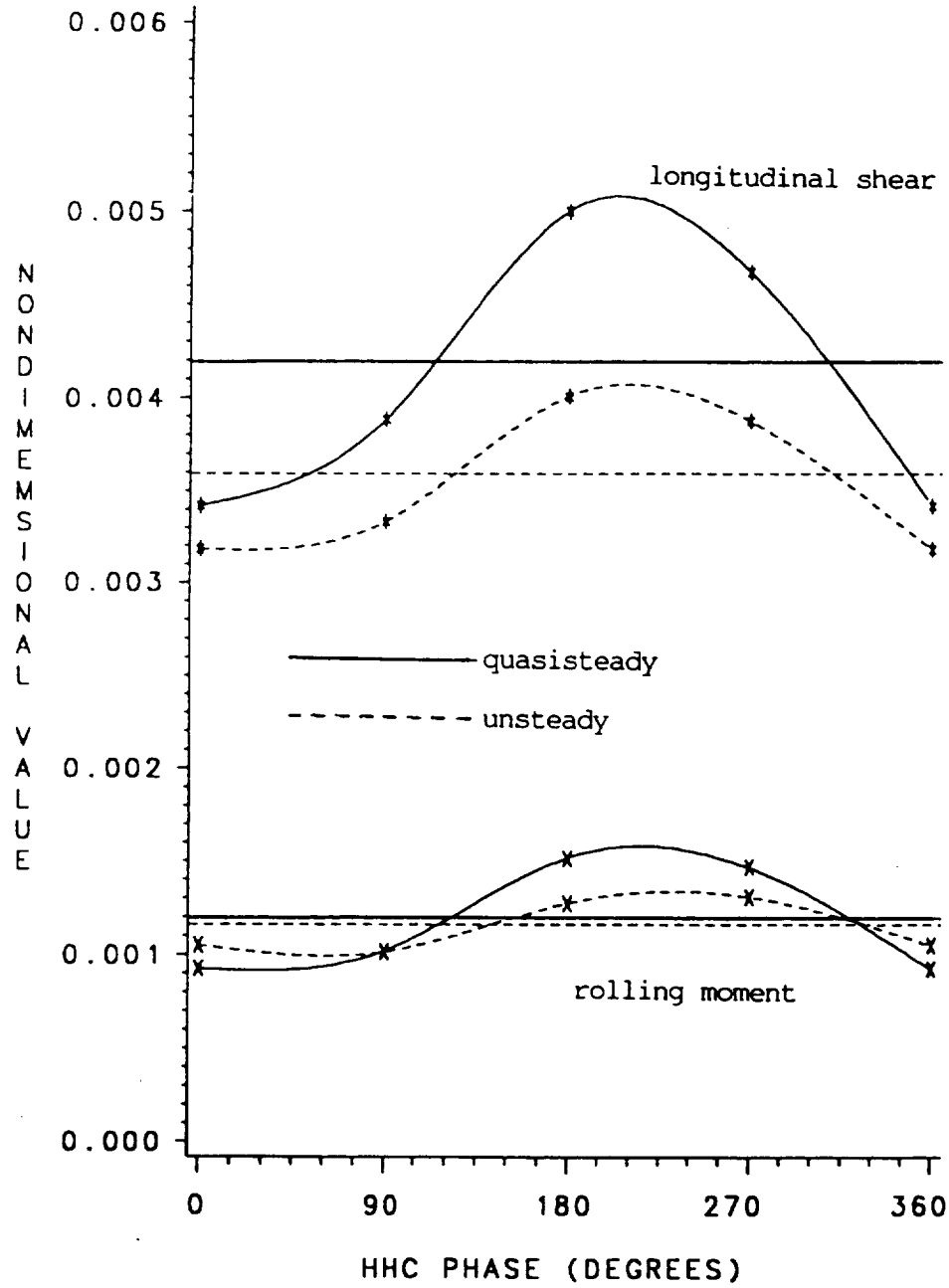

Figure 8.3: Variation of 4/rev. longitudinal shear and rolling moment with HHC phase, collective input, soft-in-plane blade, quasisteady and unsteady aerodynamics, $\mu = 0.3$.

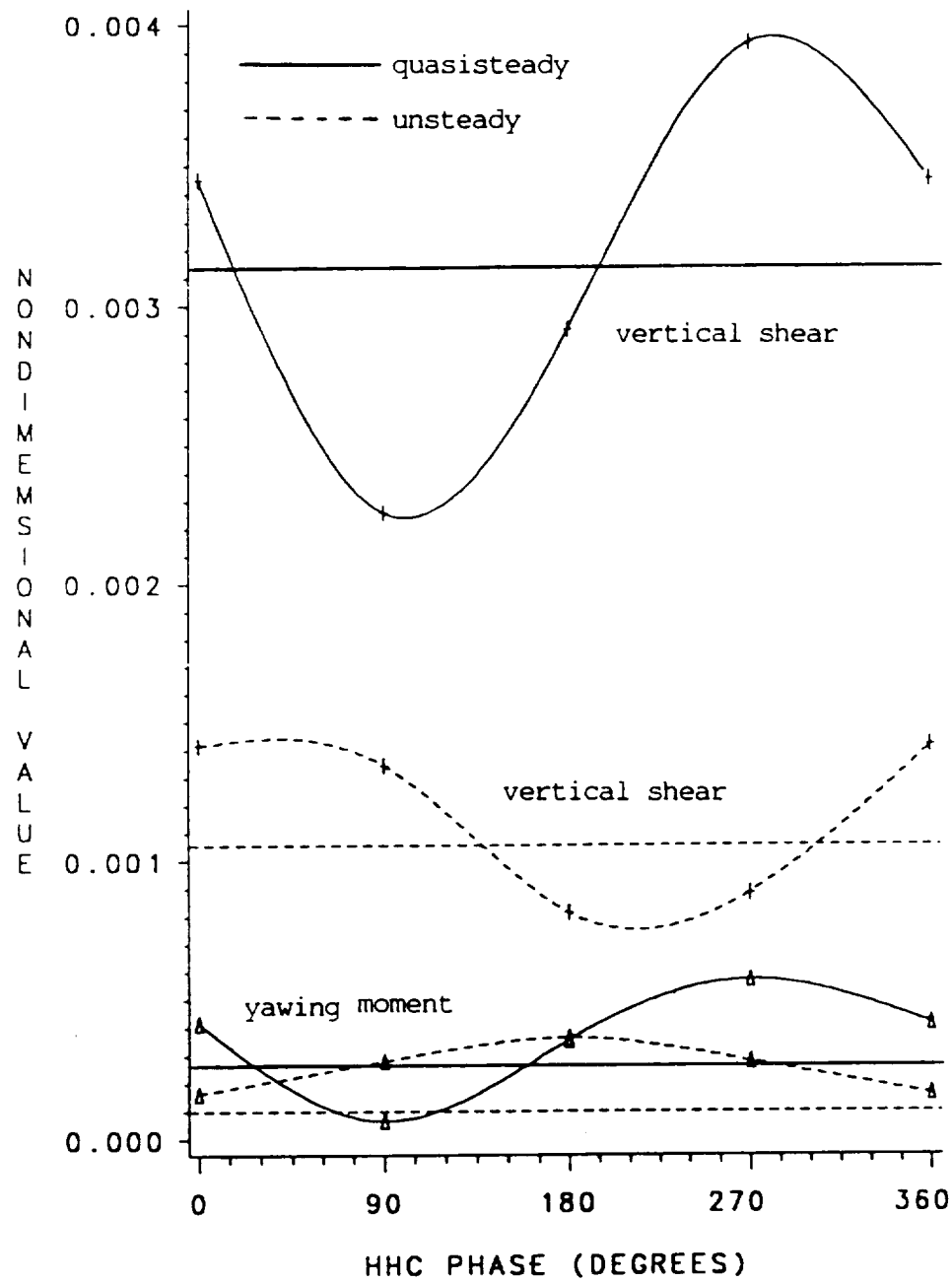

Figure 8.4: Variation of 4/rev. vertical shear and yawing moment with HHC phase, longitudinal input, soft-in-plane blade, quasisteady and unsteady aerodynamics, $\mu = 0.3$.

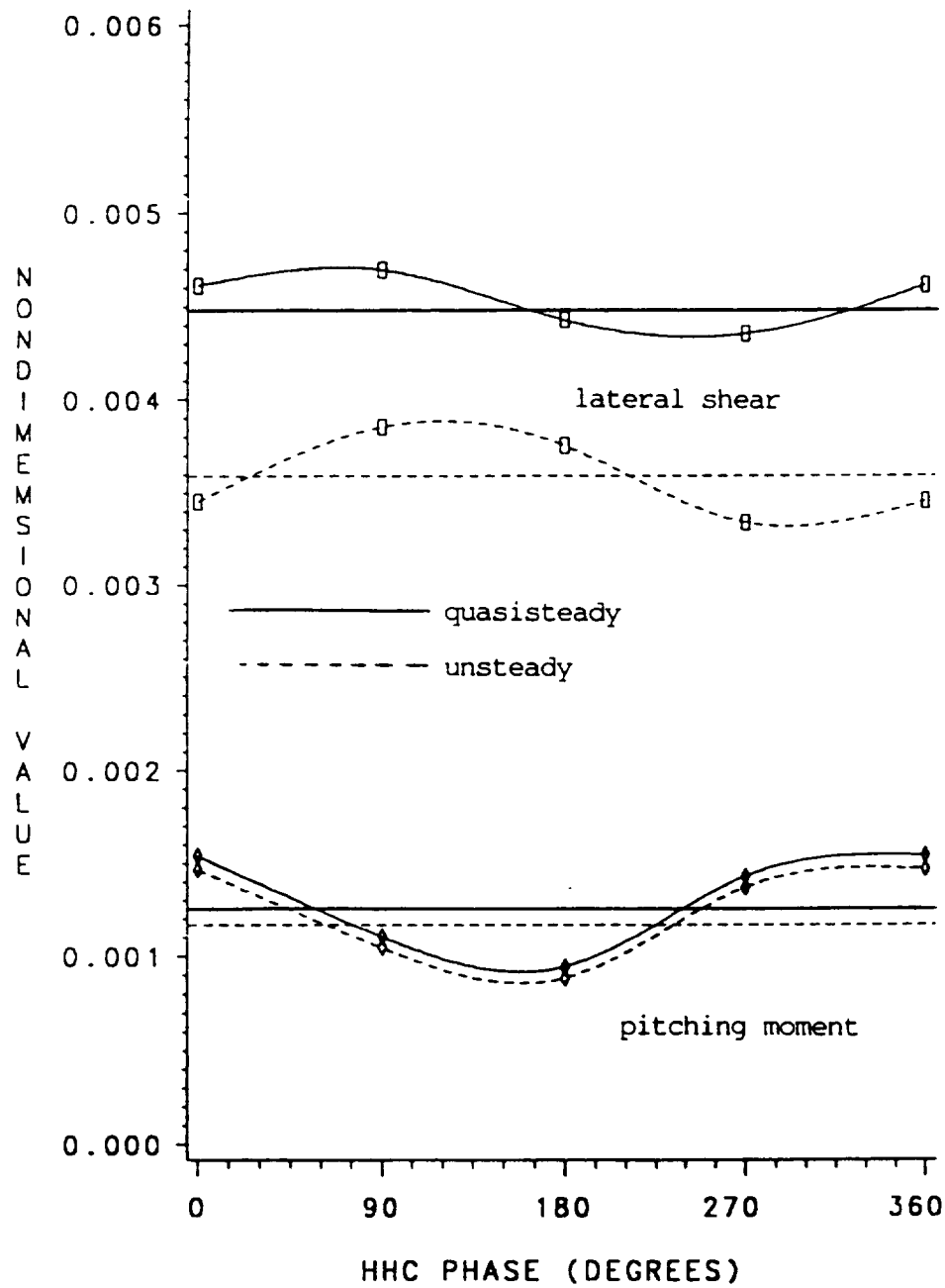

Figure 8.5: Variation of 4/rev. lateral shear and pitching moment with HHC phase, longitudinal input, soft-in-plane blade, quasisteady and unsteady aerodynamics, $\mu = 0.3$.

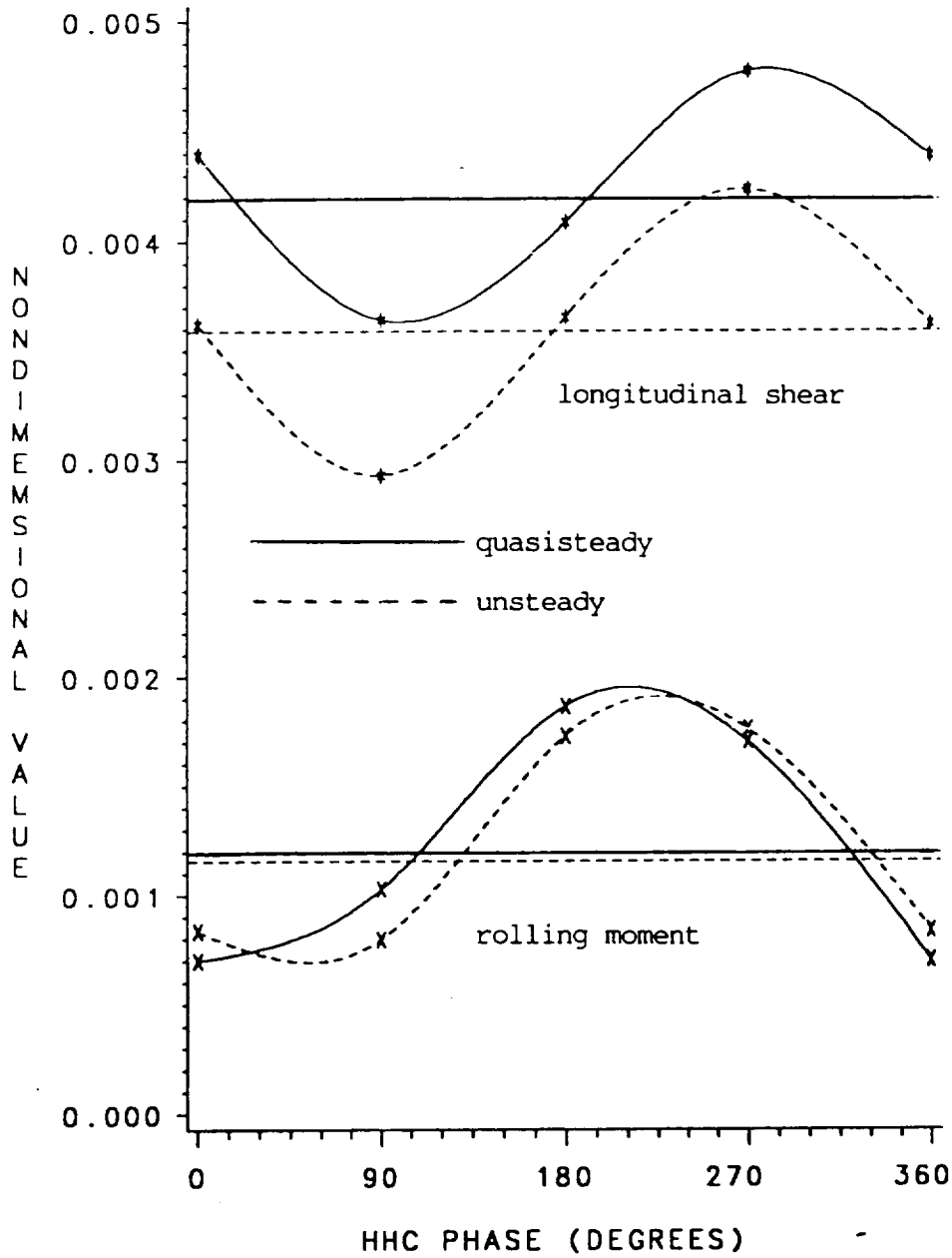

Figure 8.6: Variation of 4/rev. longitudinal shear and rolling moment with HHC phase, longitudinal input, soft-in-plane blade, quasisteady and unsteady aerodynamics, $\mu = 0.3$.

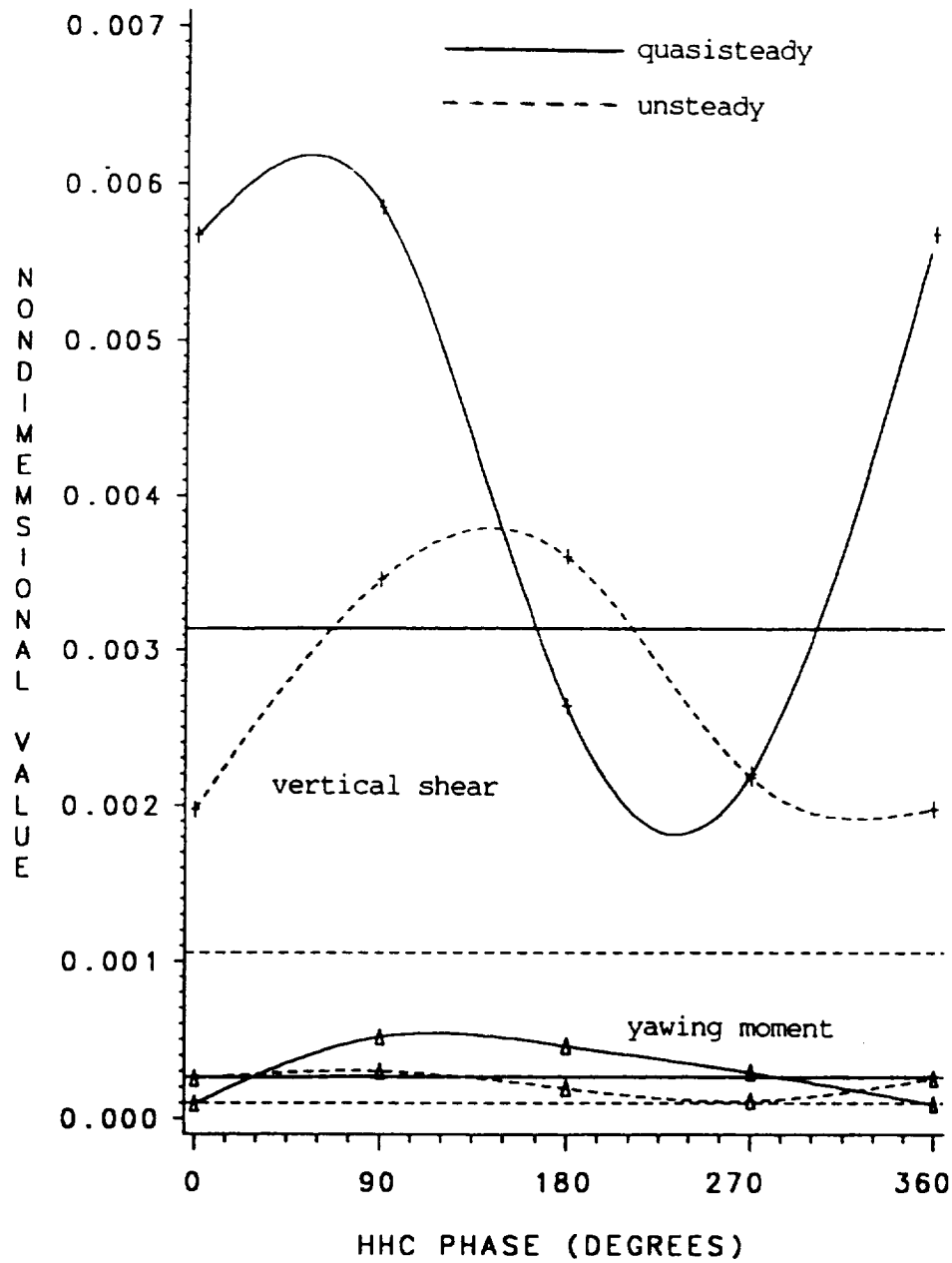

Figure 8.7: Variation of 4/rev. vertical shear and yawing moment with HHC phase, lateral input, soft-in-plane blade, quasisteady and unsteady aerodynamics, $\mu = 0.3$.

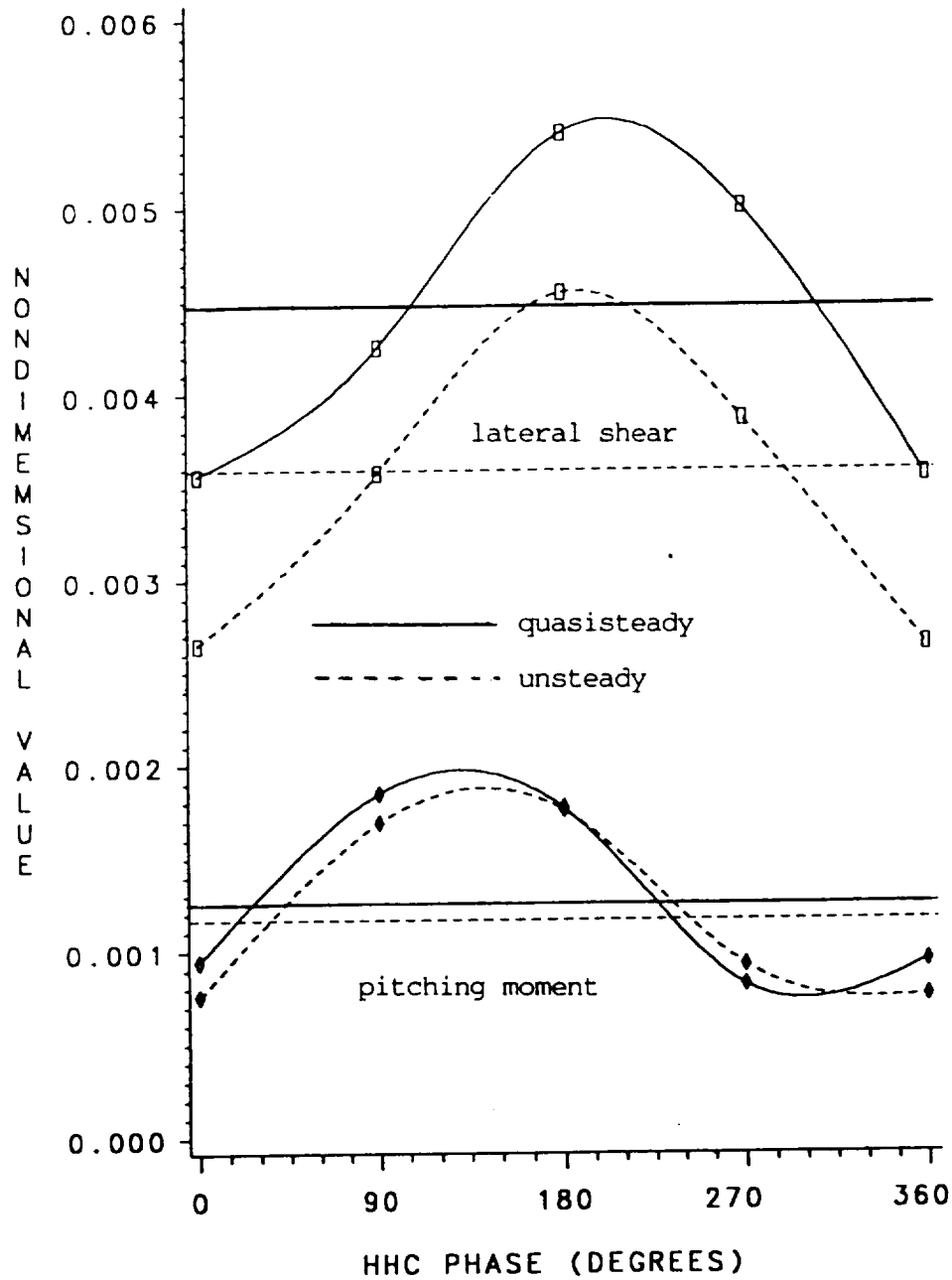

Figure 8.8: Variation of 4/rev. lateral shear and pitching moment with HHC phase, lateral input, soft-in-plane blade, quasisteady and unsteady aerodynamics, $\mu = 0.3$.

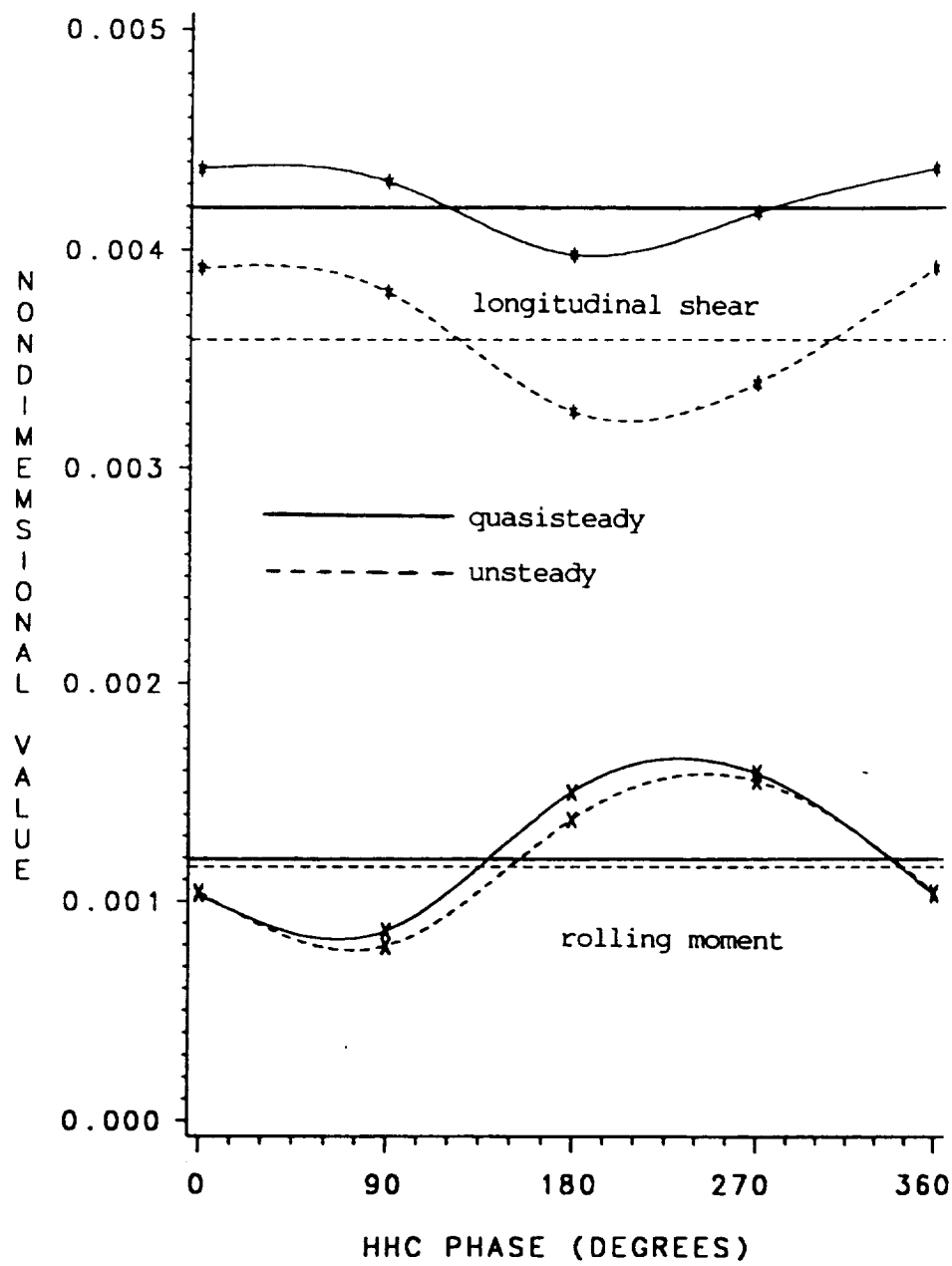

Figure 8.9: Variation of 4/rev. longitudinal shear and rolling moment with HHC phase, lateral input, soft-in-plane blade, quasisteady and unsteady aerodynamics, $\mu = 0.3$.

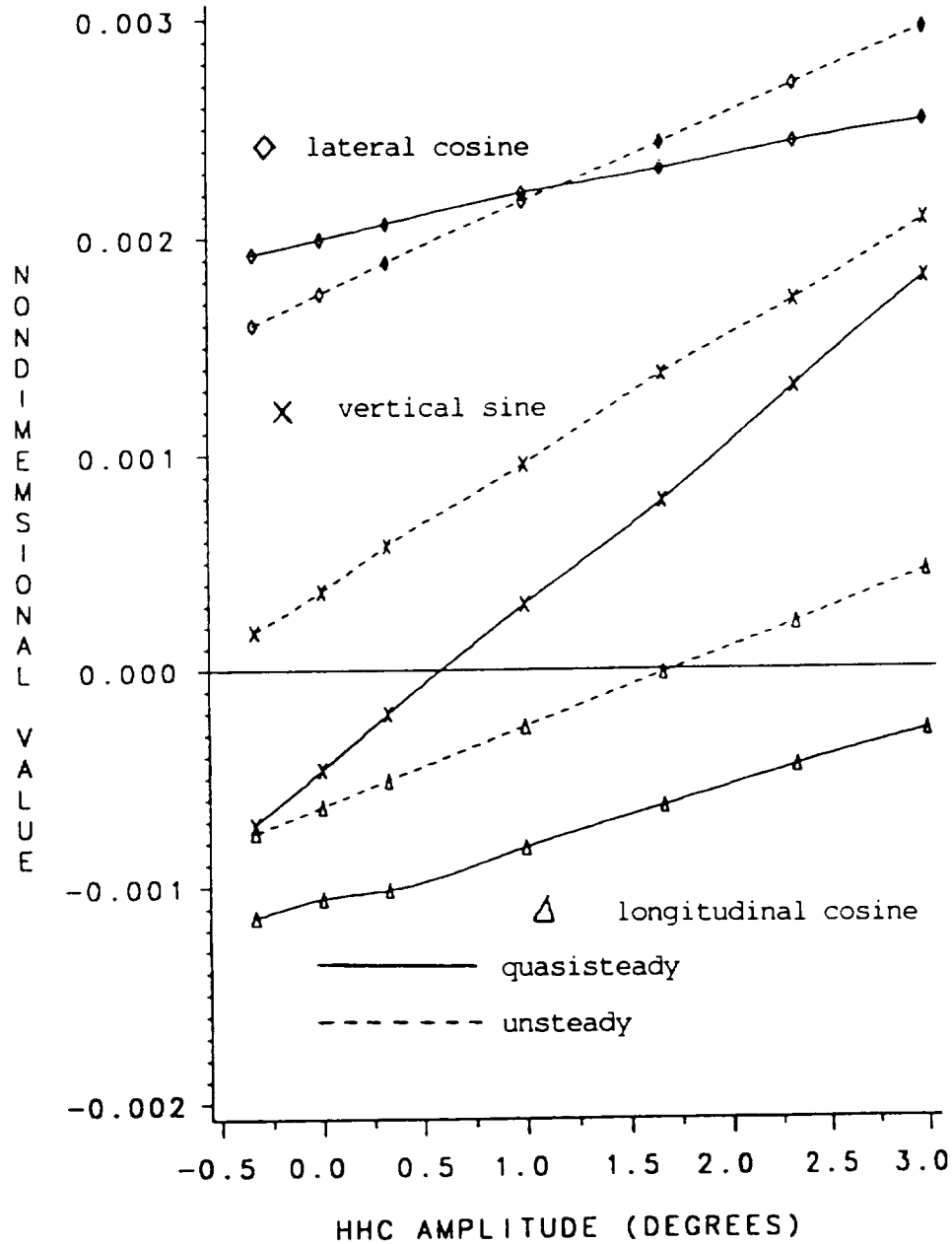

Figure 8.10: Variation of hub shear harmonics with HHC amplitude, quasisteady and unsteady aerodynamics, longitudinal cosine HHC applied, $\mu = .0.3$.

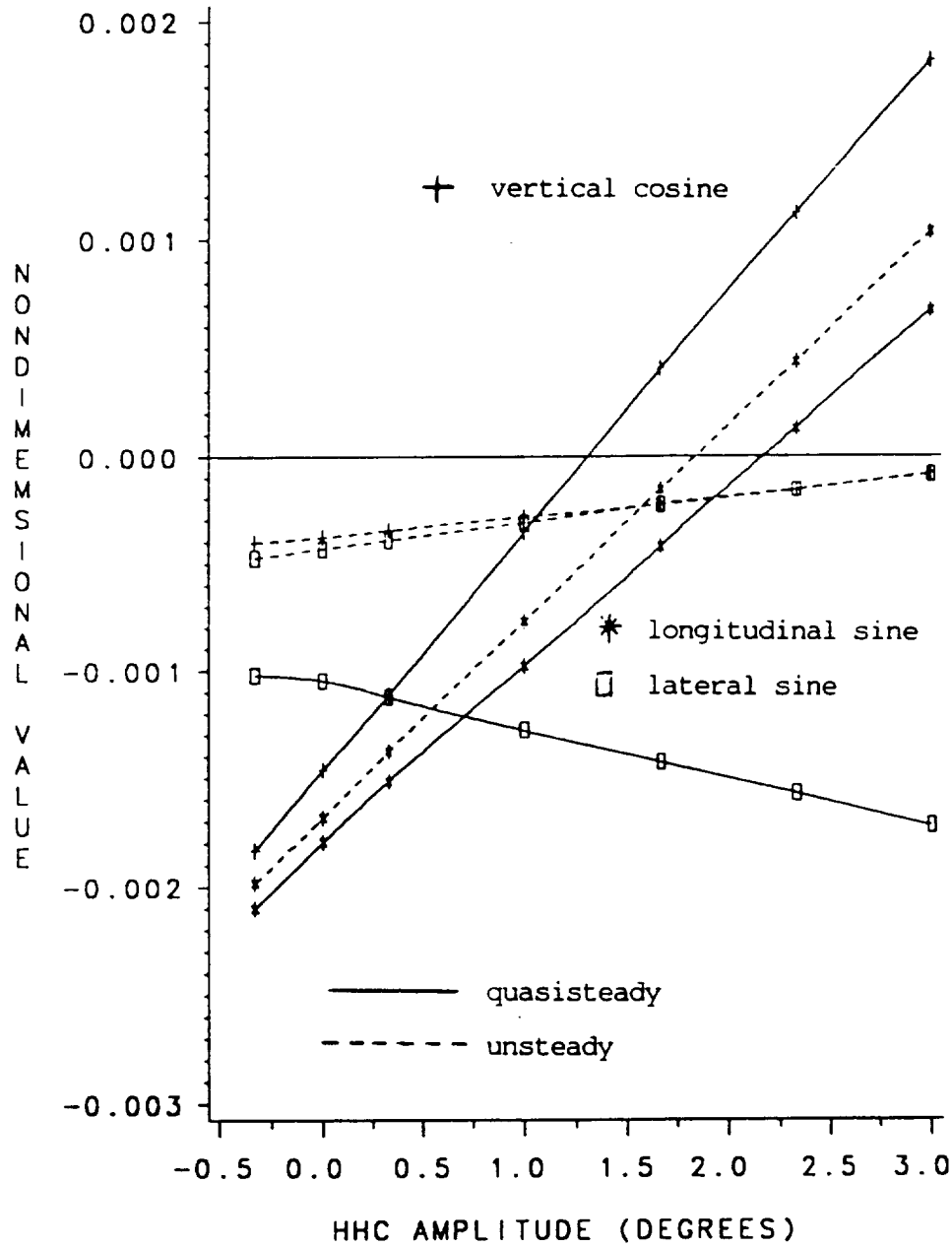

Figure 8.11: Variation of hub shear harmonics with HHC amplitude, quasisteady and unsteady aerodynamics, longitudinal cosine HHC applied, $\mu = 0.3$.

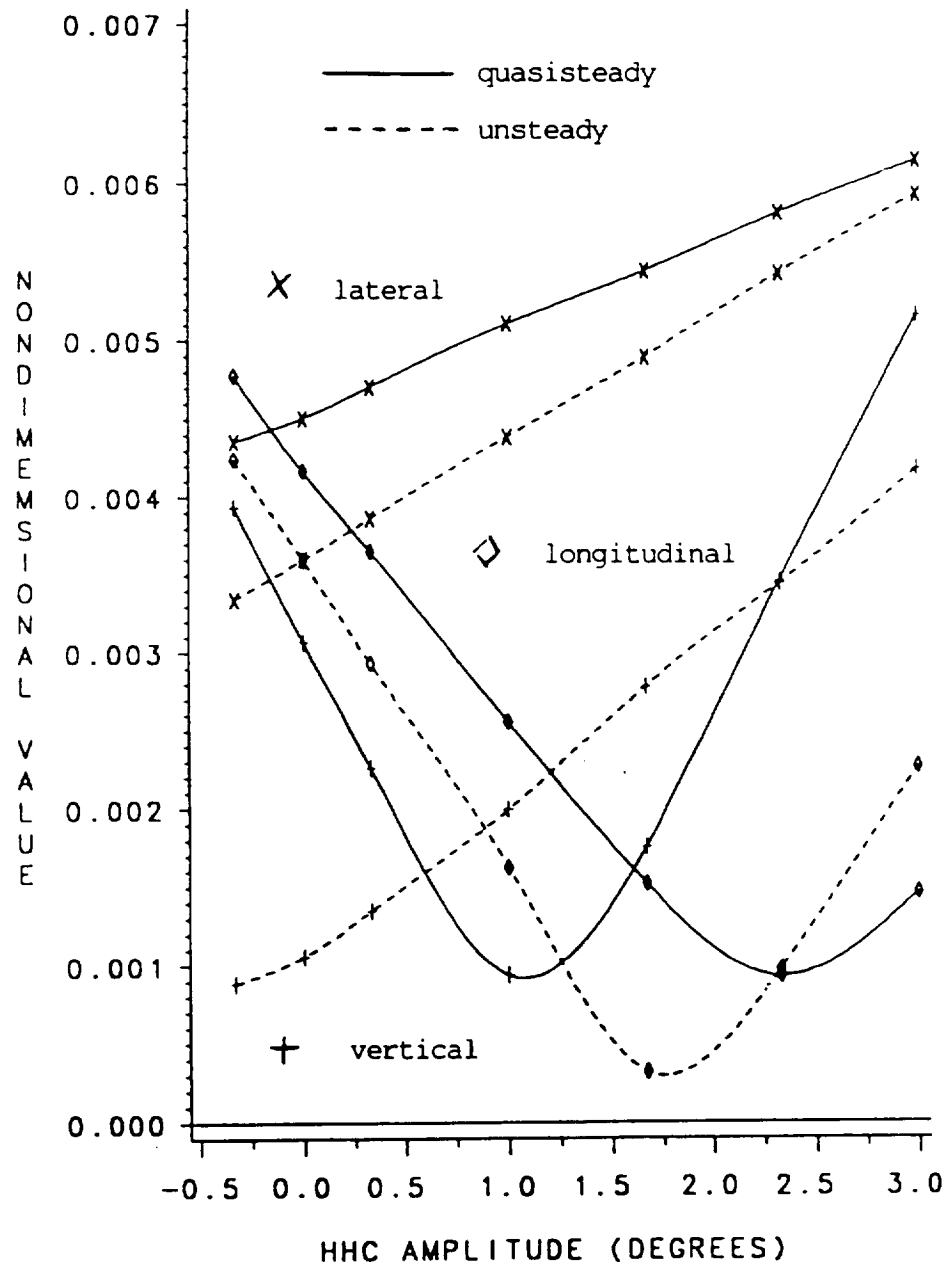

Figure 8.12: Variation of peak-to-peak hub shears with HHC amplitude, quasisteady and unsteady aerodynamics, longitudinal cosine HHC applied, $\mu = 0.3$.

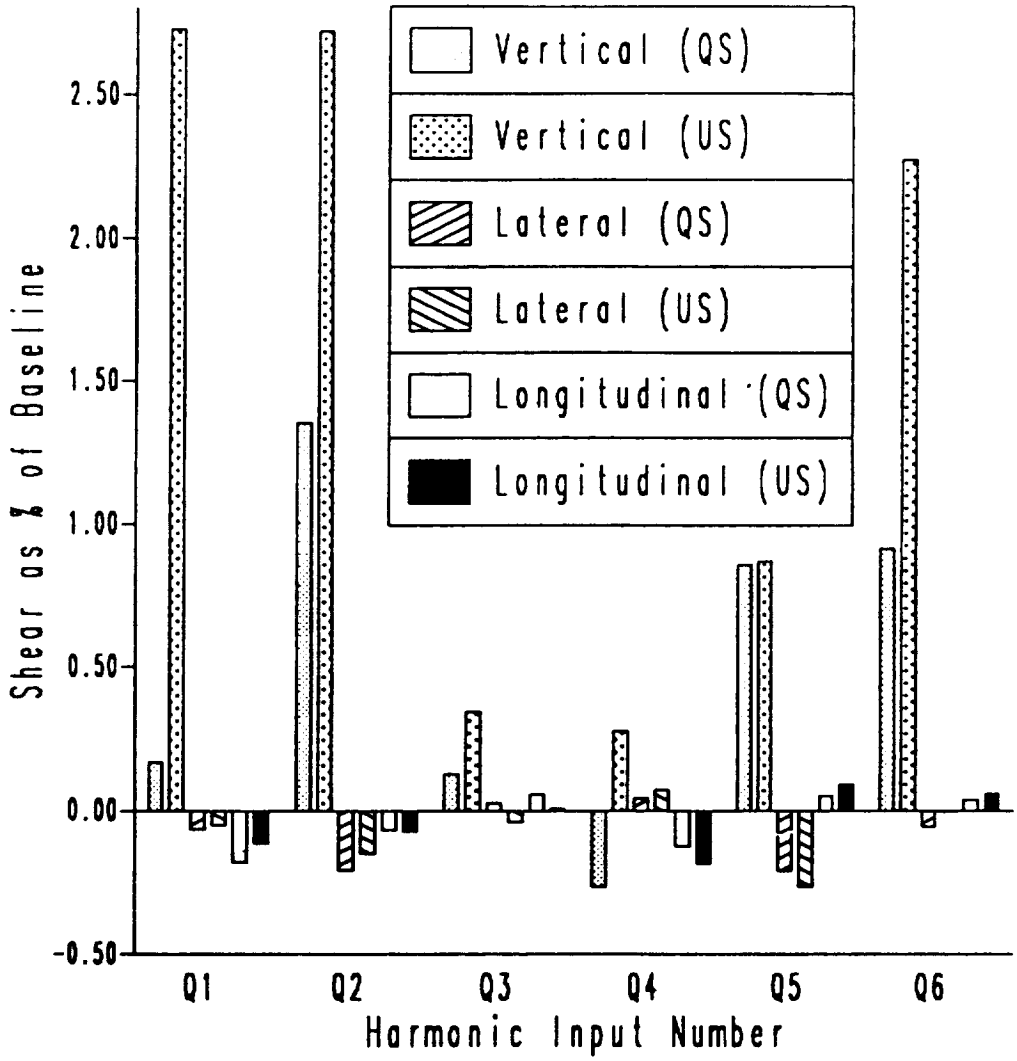

Figure 8.13: Proportional change in hub shears with different 1/3° HHC incrementations, quasisteady and unsteady aerodynamics, soft-in-plane blade, advance ratio $\mu = 0.3$.

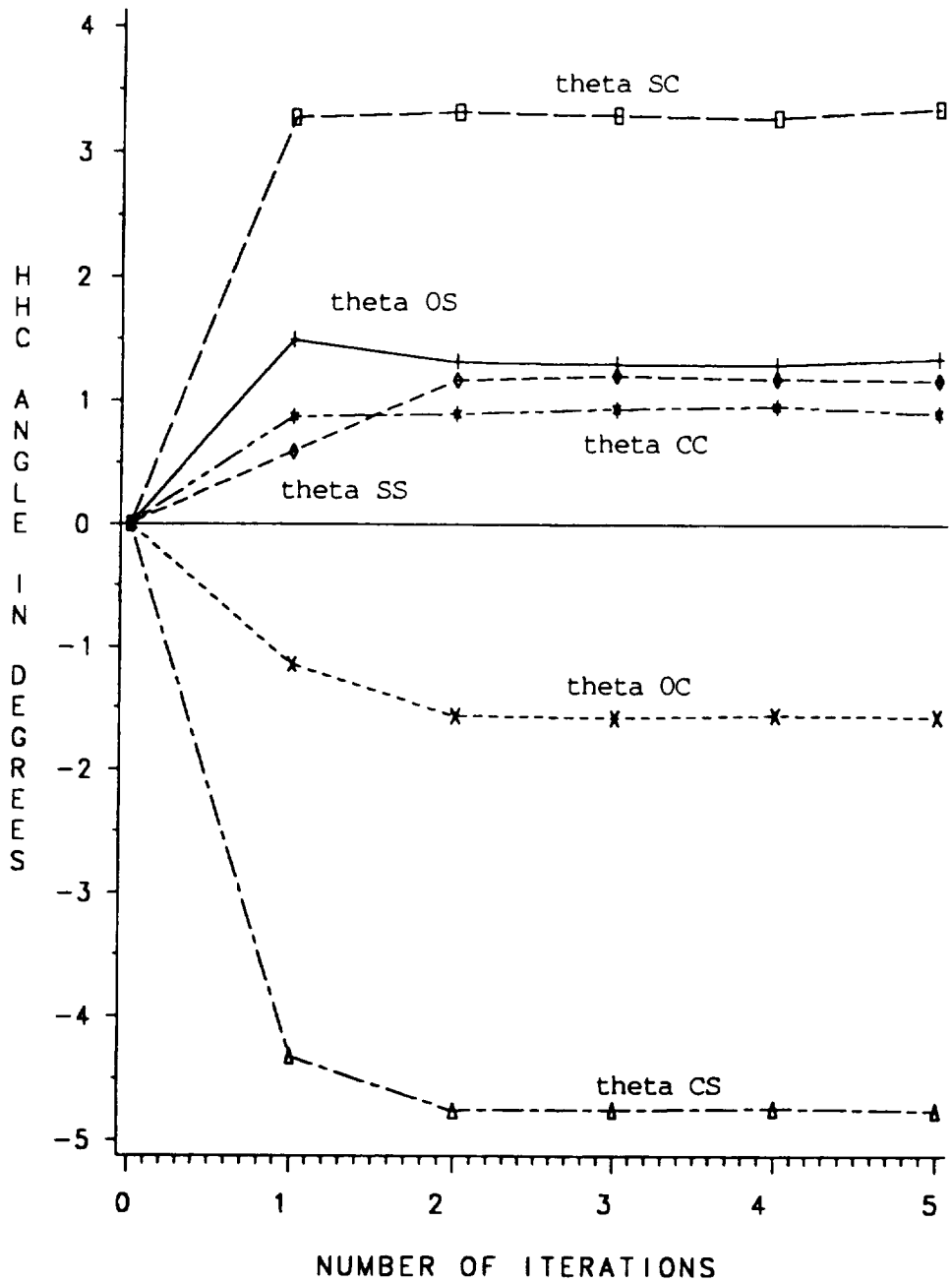

Figure 9.1: Iteration history of HHC input angles for fixed gain control, quasisteady aerodynamics, $\mu = 0.3$.

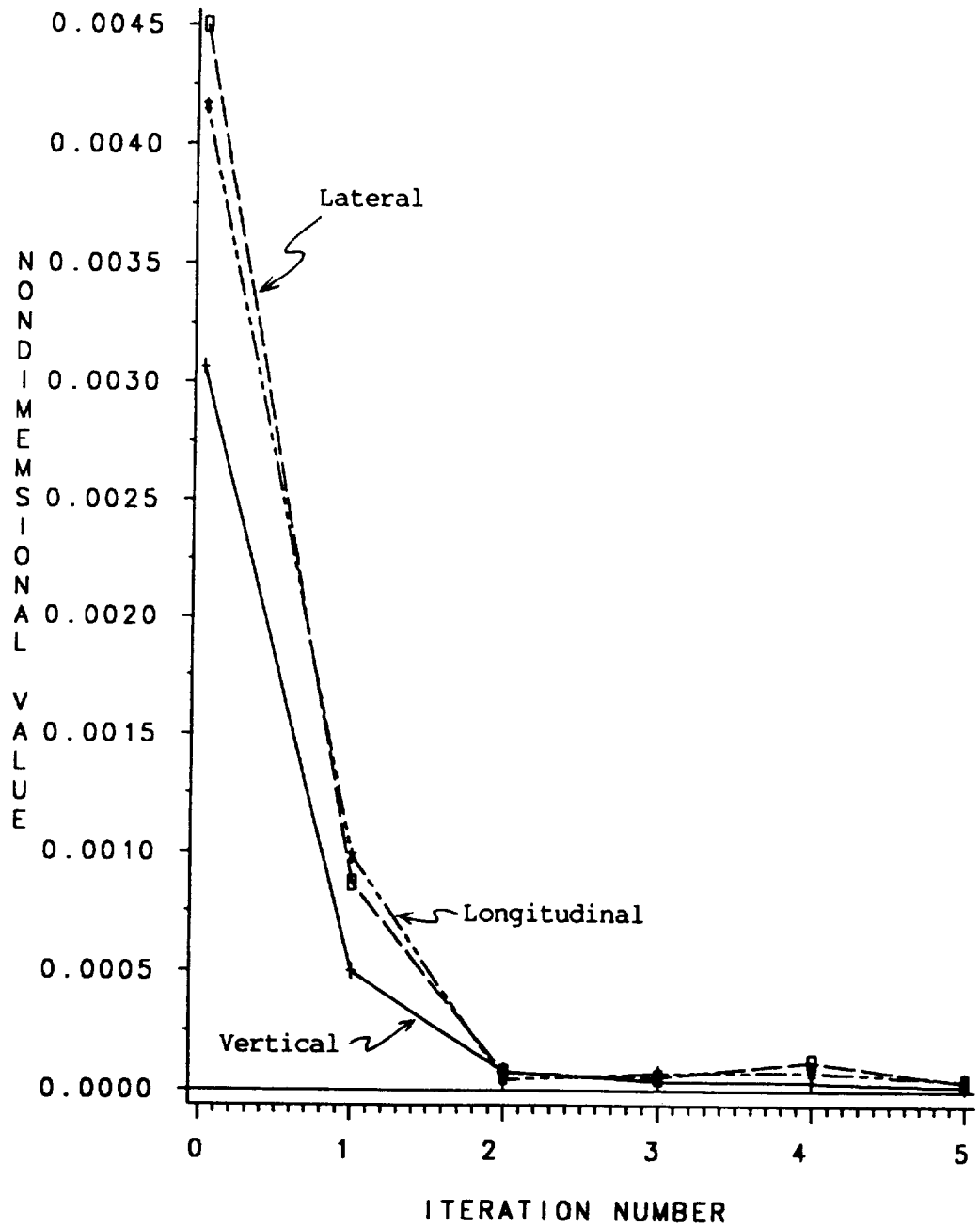

Figure 9.2: Iteration history of vertical, lateral, and longitudinal shears for fixed gain control, quasisteady aerodynamics, $\mu = 0.3$.

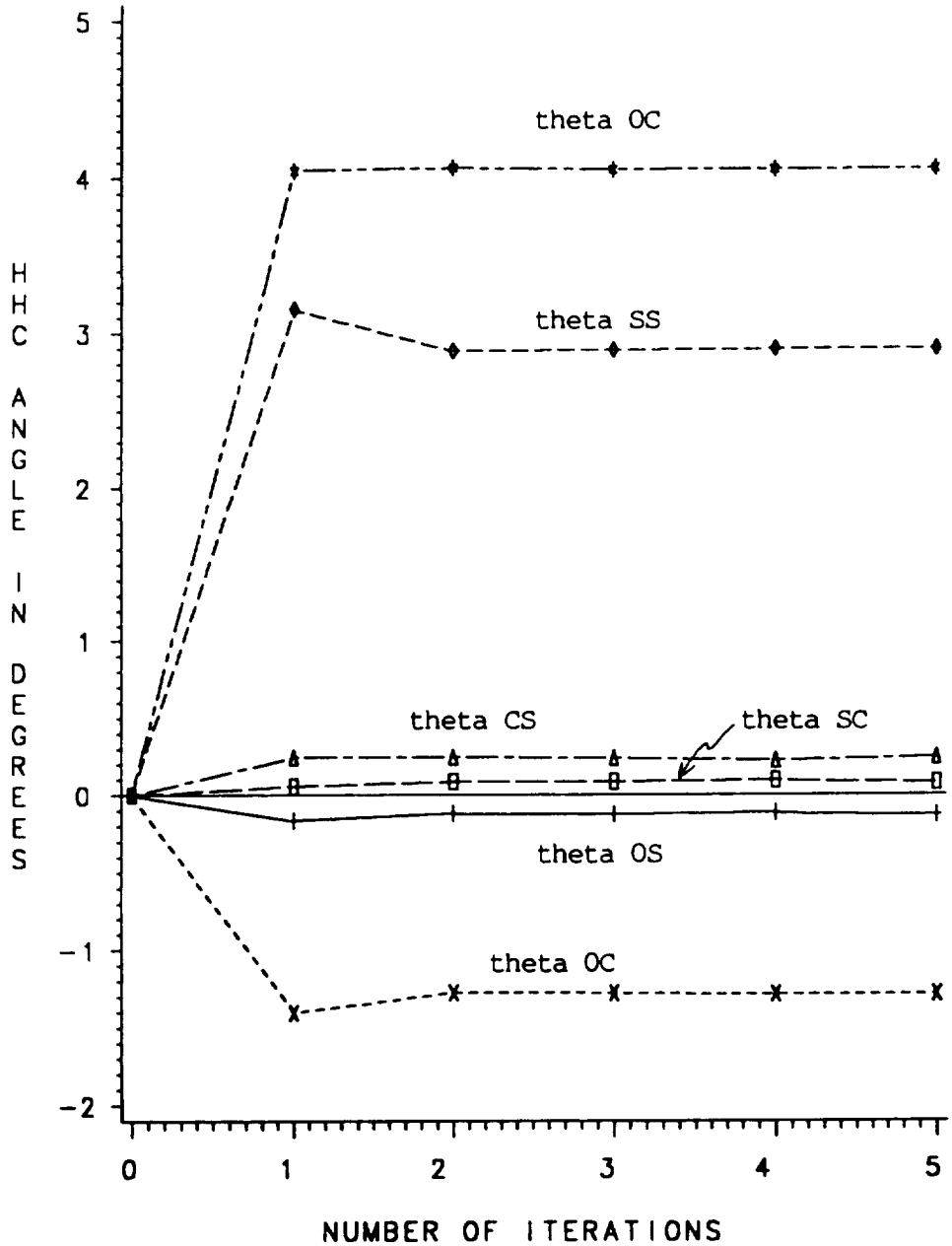

Figure 9.3: Iteration history of HHC input angles for fixed gain control, unsteady aerodynamics, $\mu = 0.3$.

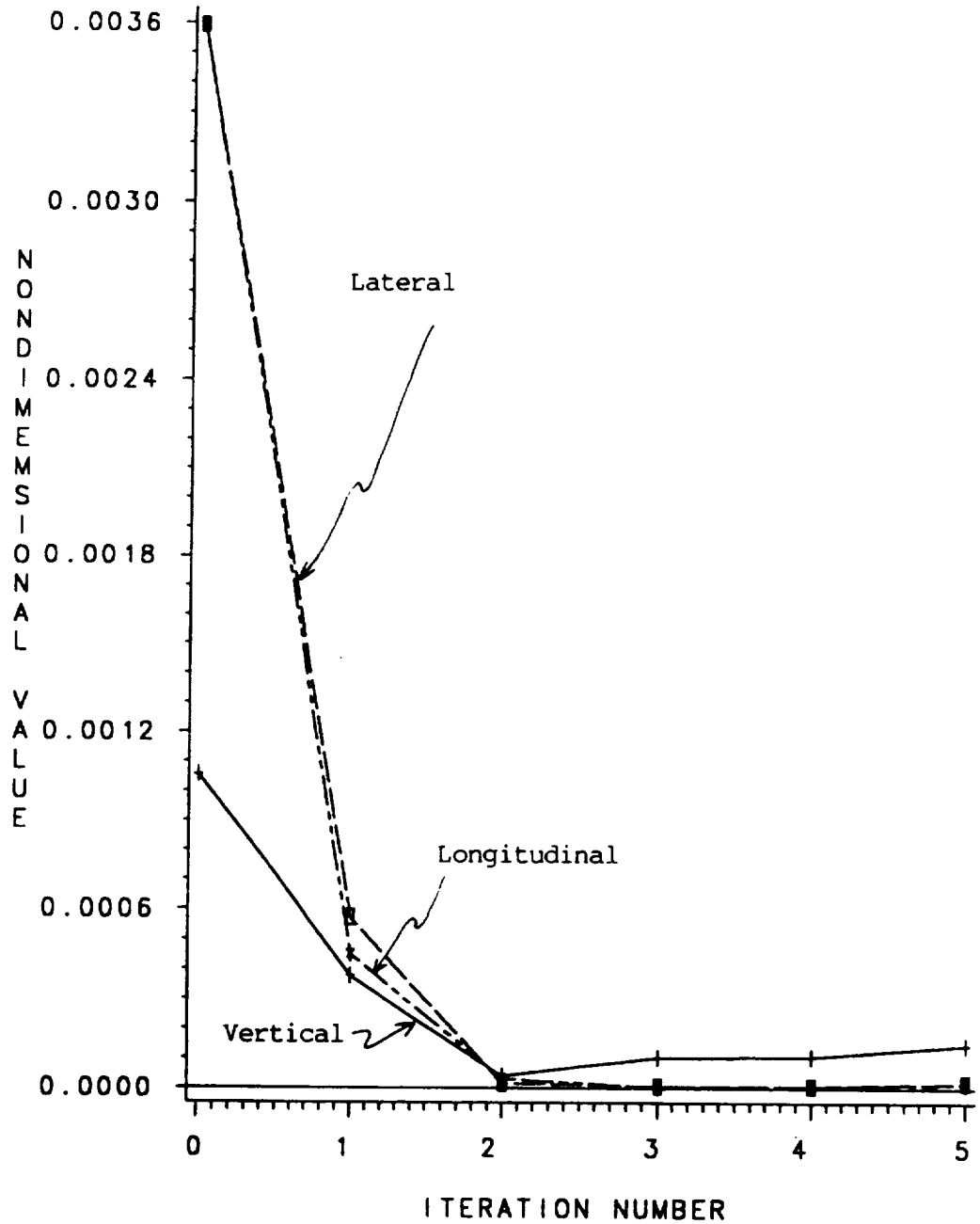

Figure 9.4: Iteration history of vertical, lateral, and longitudinal shears for fixed gain control, unsteady aerodynamics, $\mu = 0.3$.

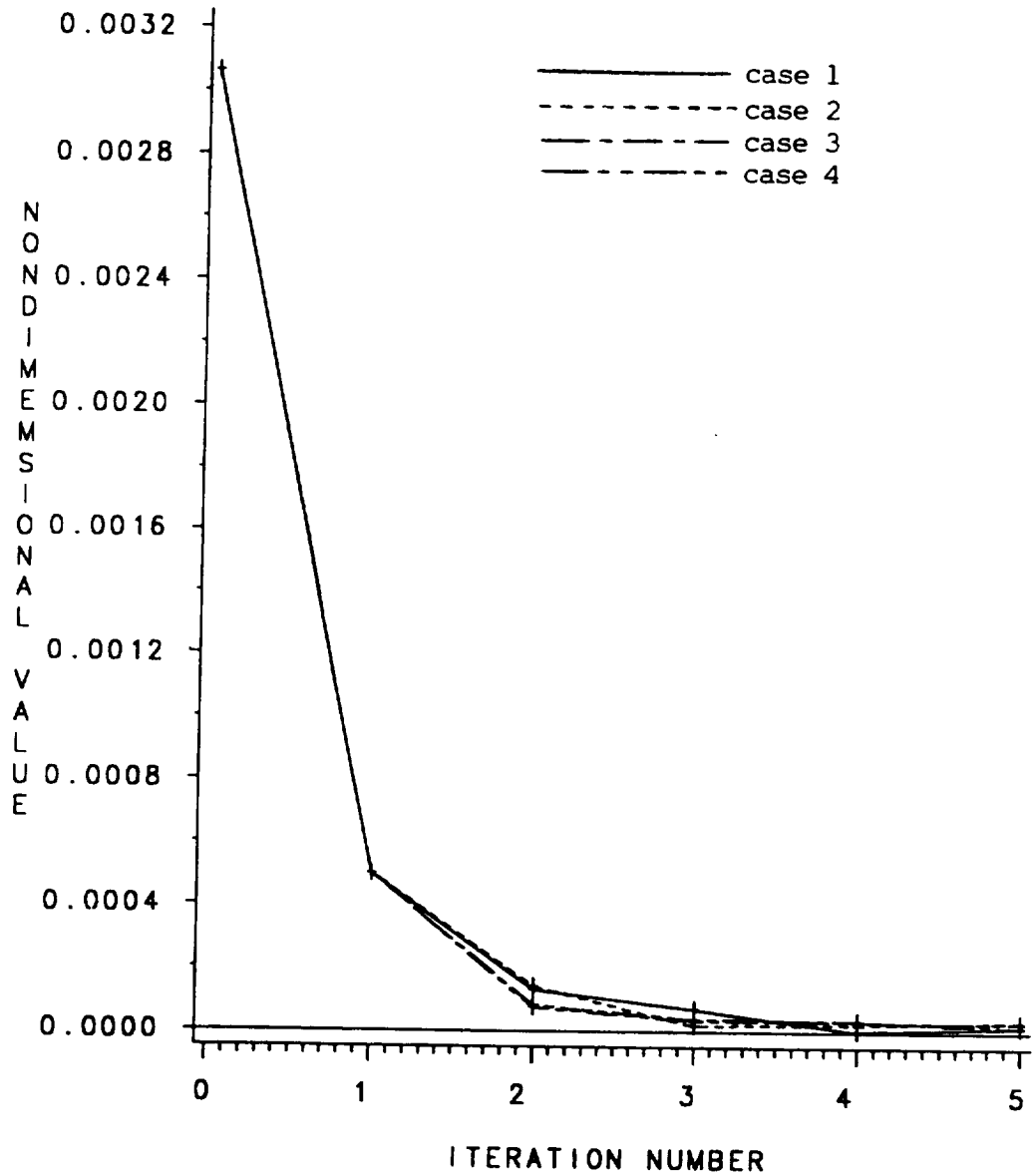

Figure 9.5: Iteration history of vertical shears, four different deterministic controllers, quasisteady aerodynamics, $\mu = 0.3$.

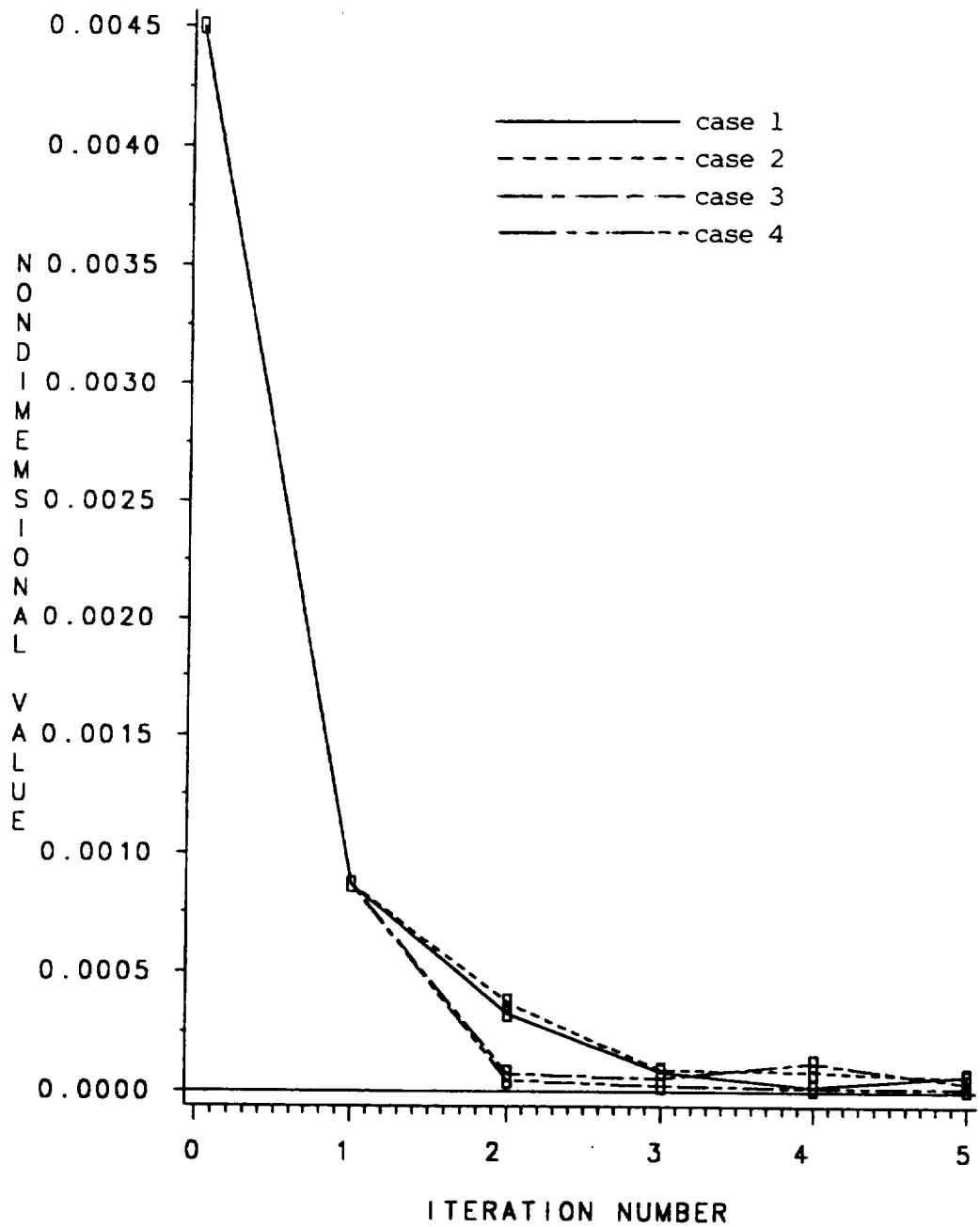

Figure 9.6: Iteration history of lateral shears, four different deterministic controllers, quasisteady aerodynamics, $\mu = 0.3$.

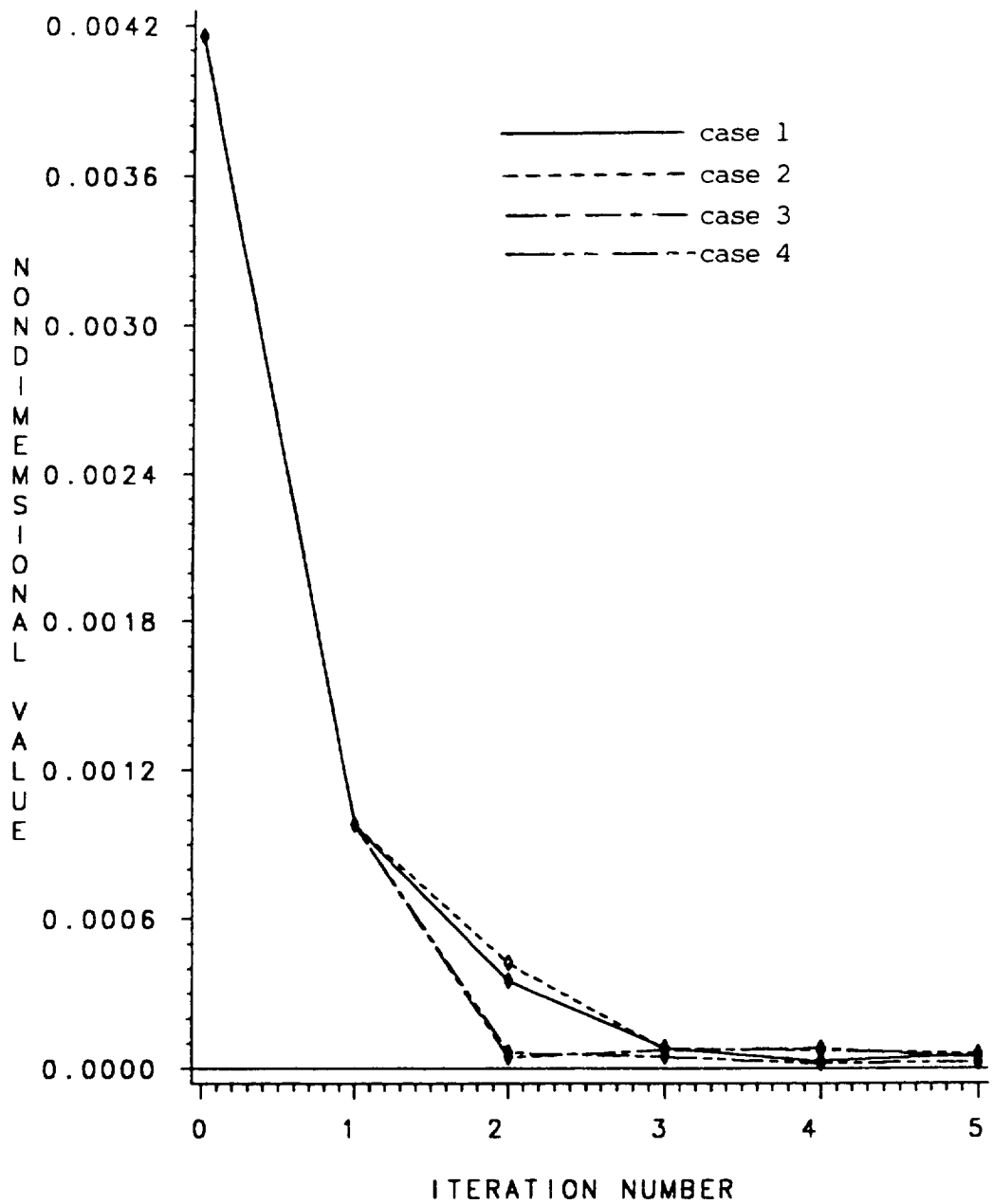

Figure 9.7: Iteration history of longitudinal shears, four different deterministic controllers, quasisteady aerodynamics, $\mu = 0.3$.

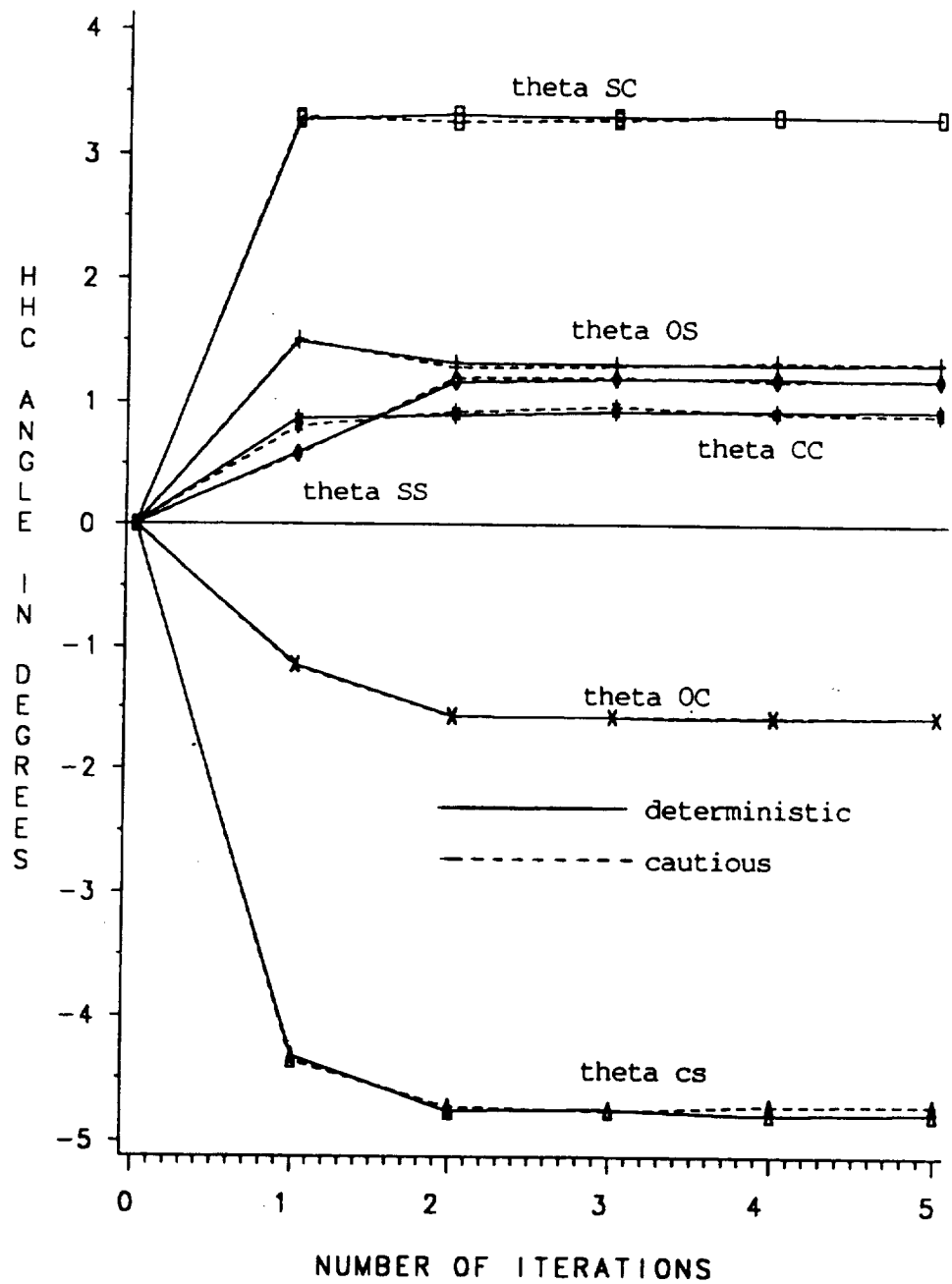

Figure 9.8: Iteration history of HHC input angles for deterministic versus cautious local control, quasisteady aerodynamics, $\mu = 0.3$.

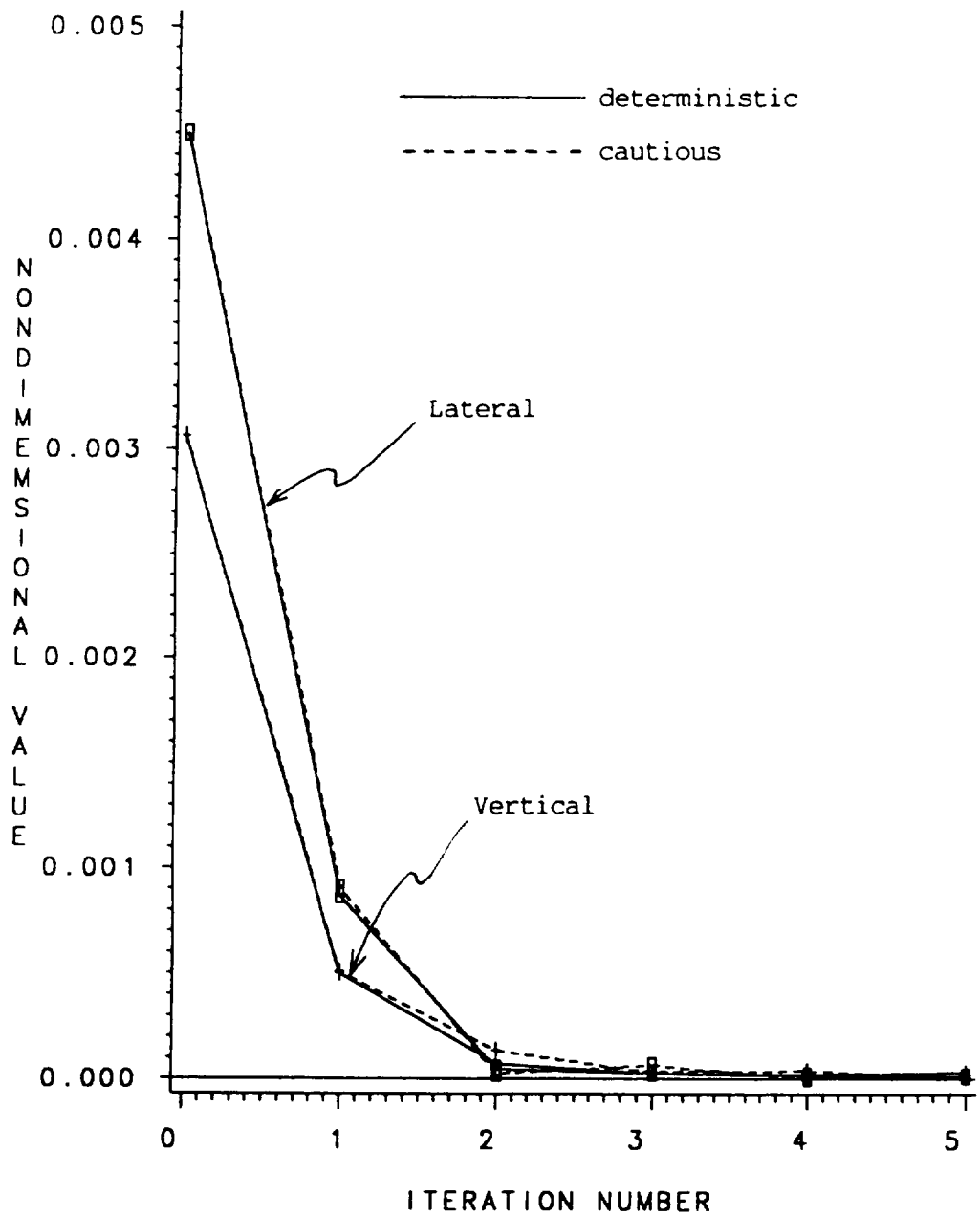

Figure 9.9: Iteration history of vertical and lateral hub shears for deterministic versus cautious local control, quasisteady aerodynamics, $\mu = 0.3$.

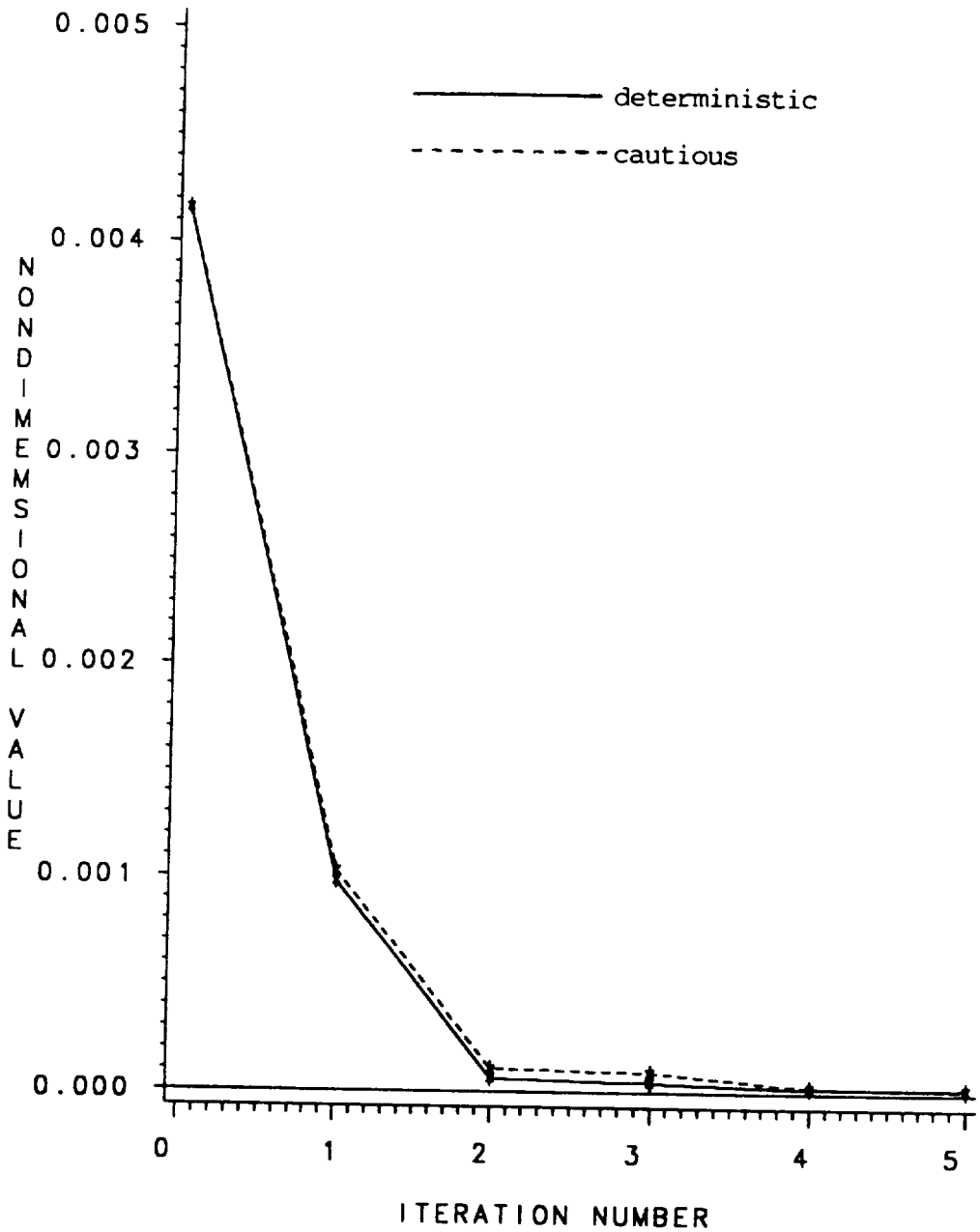

Figure 9.10: Iteration history of longitudinal hub shear for deterministic versus cautious local control, quasisteady aerodynamics, $\mu = 0.3$.

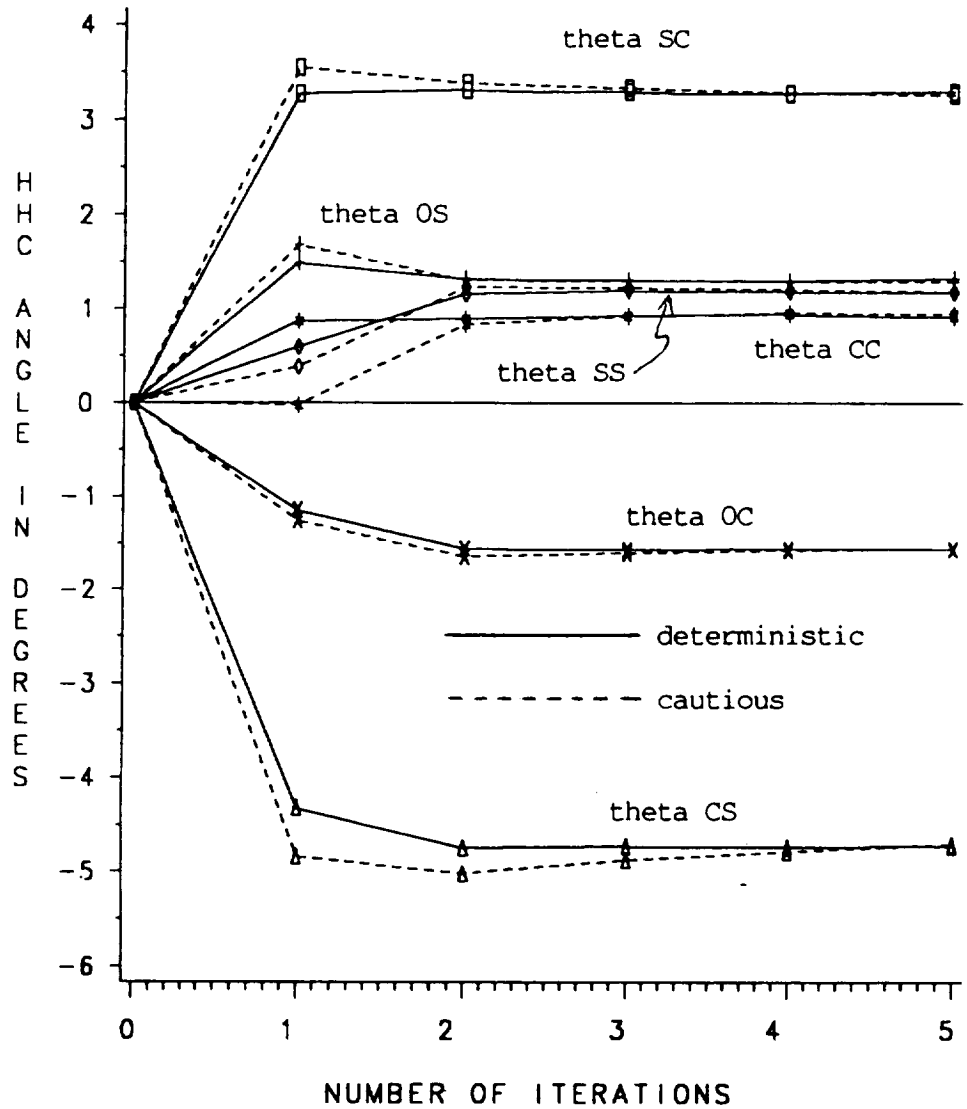

Figure 9.11: Iteration history of HHC input angles for deterministic versus cautious global control, quasisteady aerodynamics, $\mu = 0.3$.

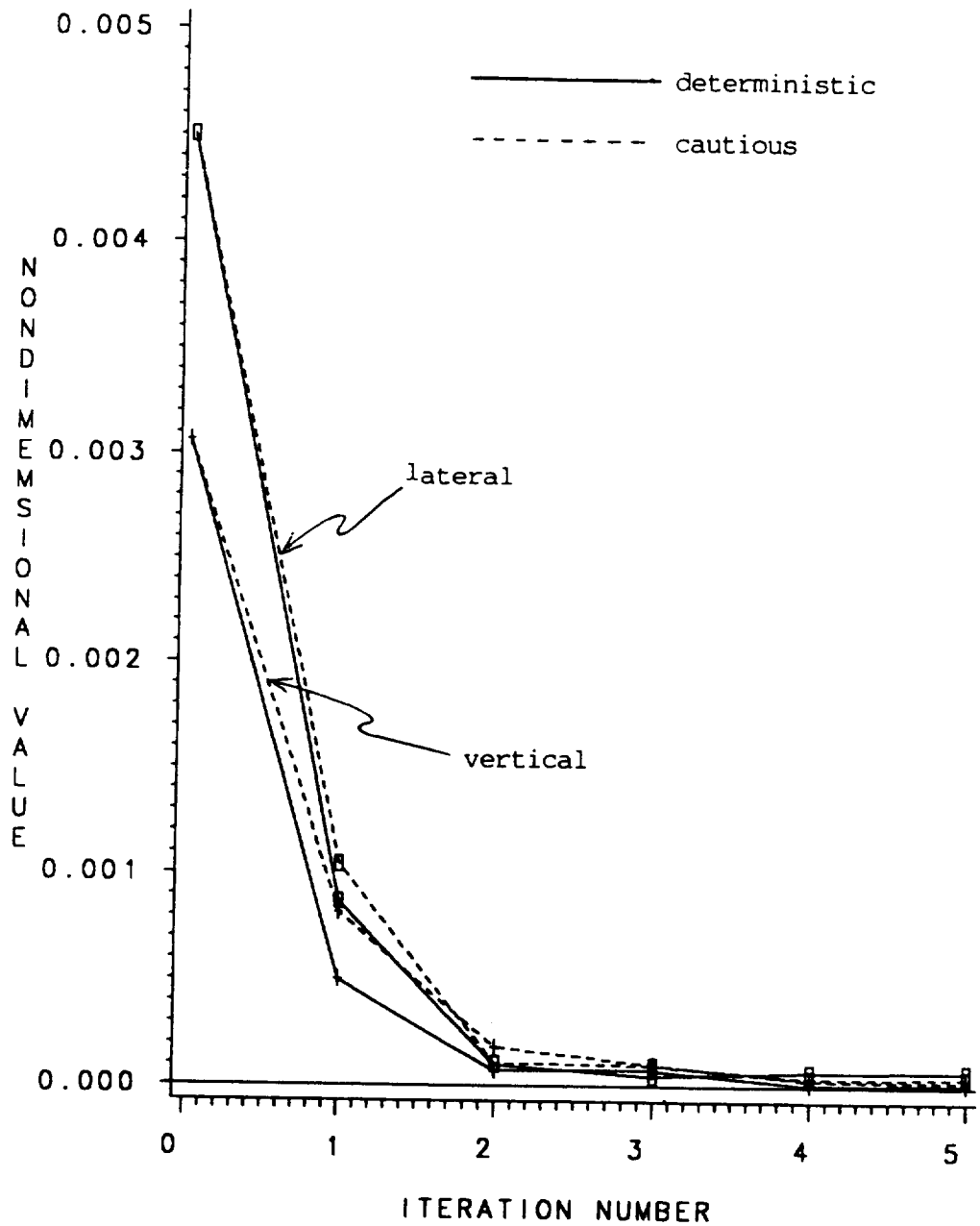

Figure 9.12: Iteration history of vertical and lateral hub shears for deterministic versus cautious global control, quasisteady aerodynamics, $\mu = 0.3$.

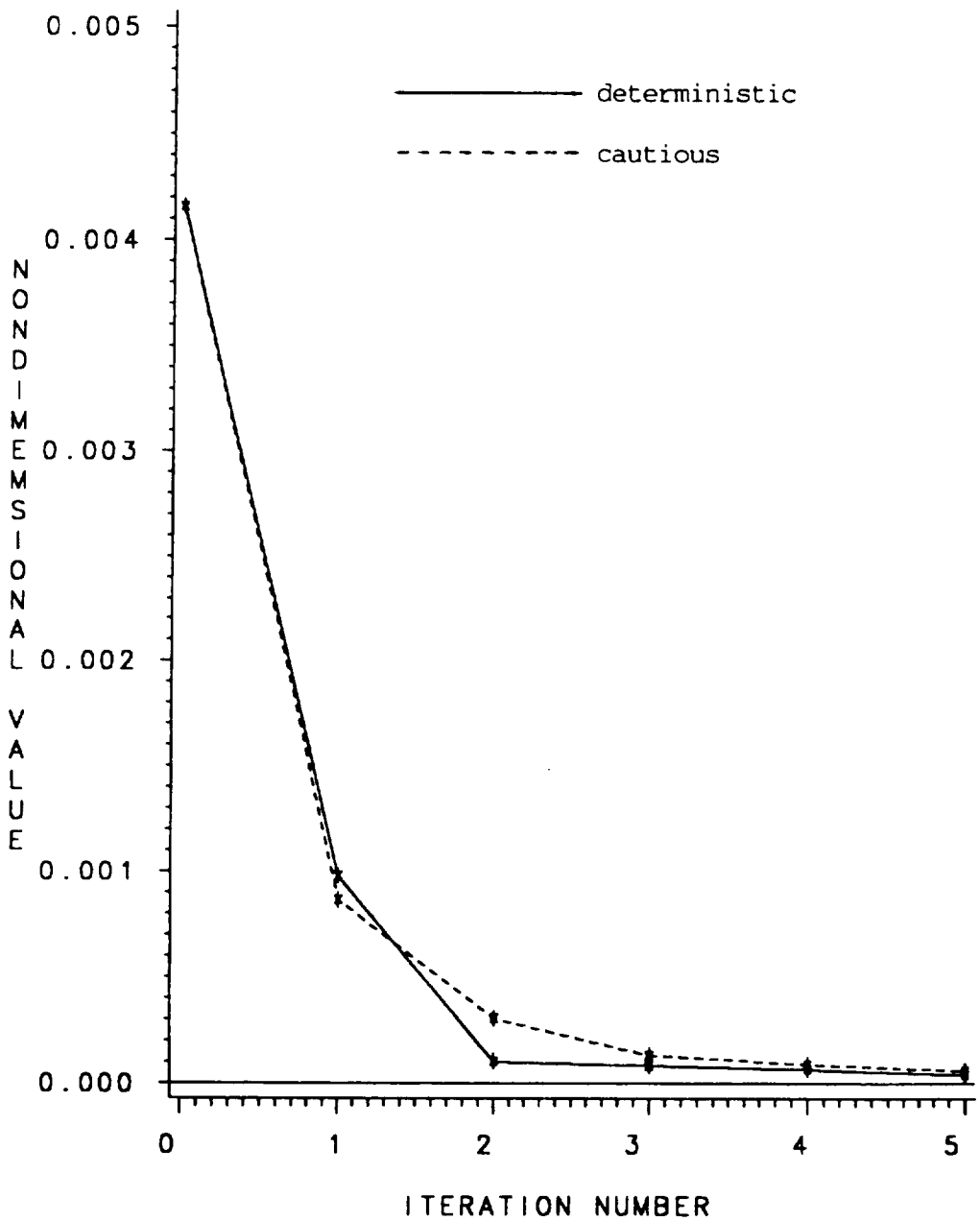

Figure 9.13: Iteration history of longitudinal hub shear for deterministic versus cautious global control, quasisteady aerodynamics, $\mu = 0.3$.

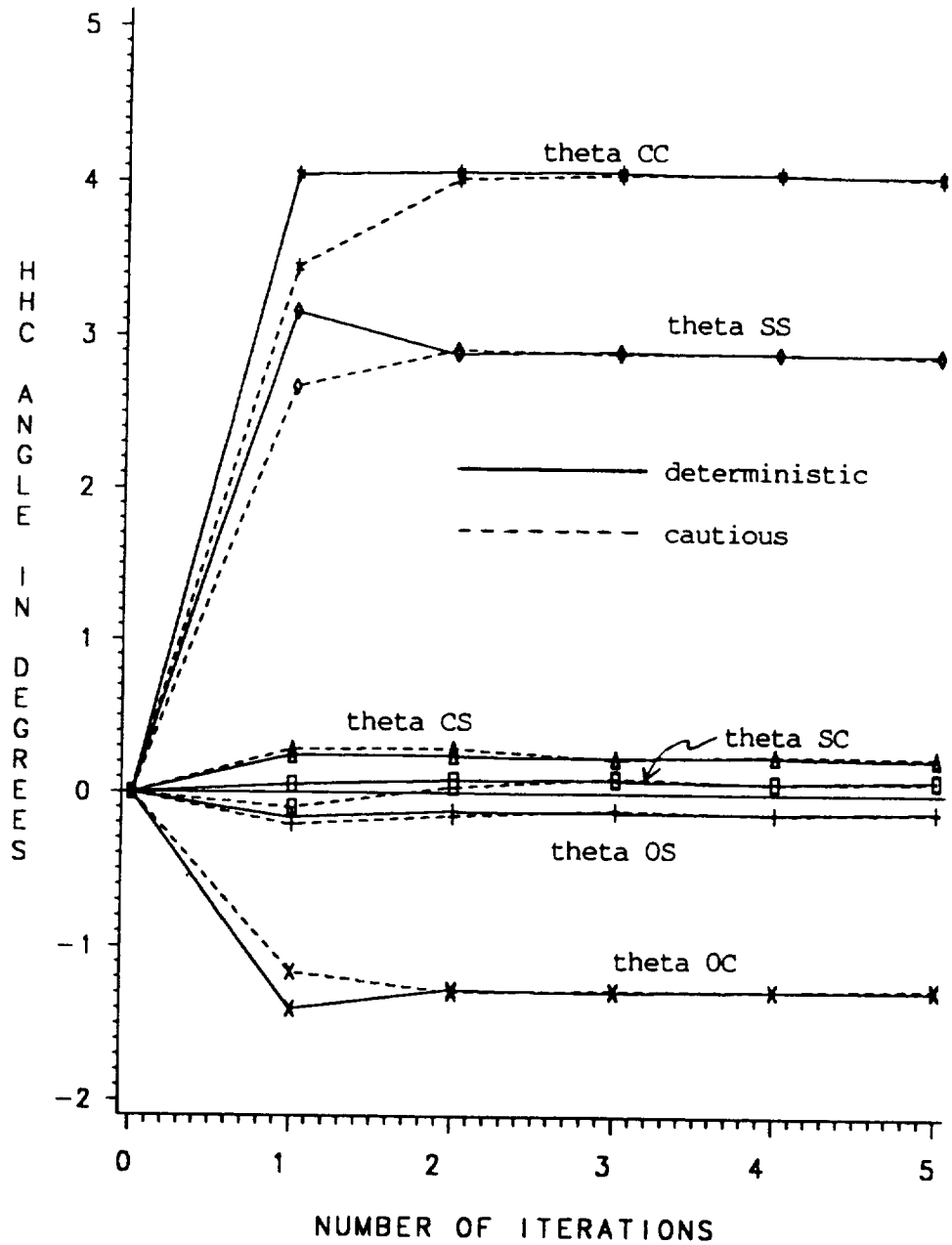

Figure 9.14: Iteration history of HHC input angles for deterministic versus cautious local control, unsteady aerodynamics, $\mu = 0.3$.

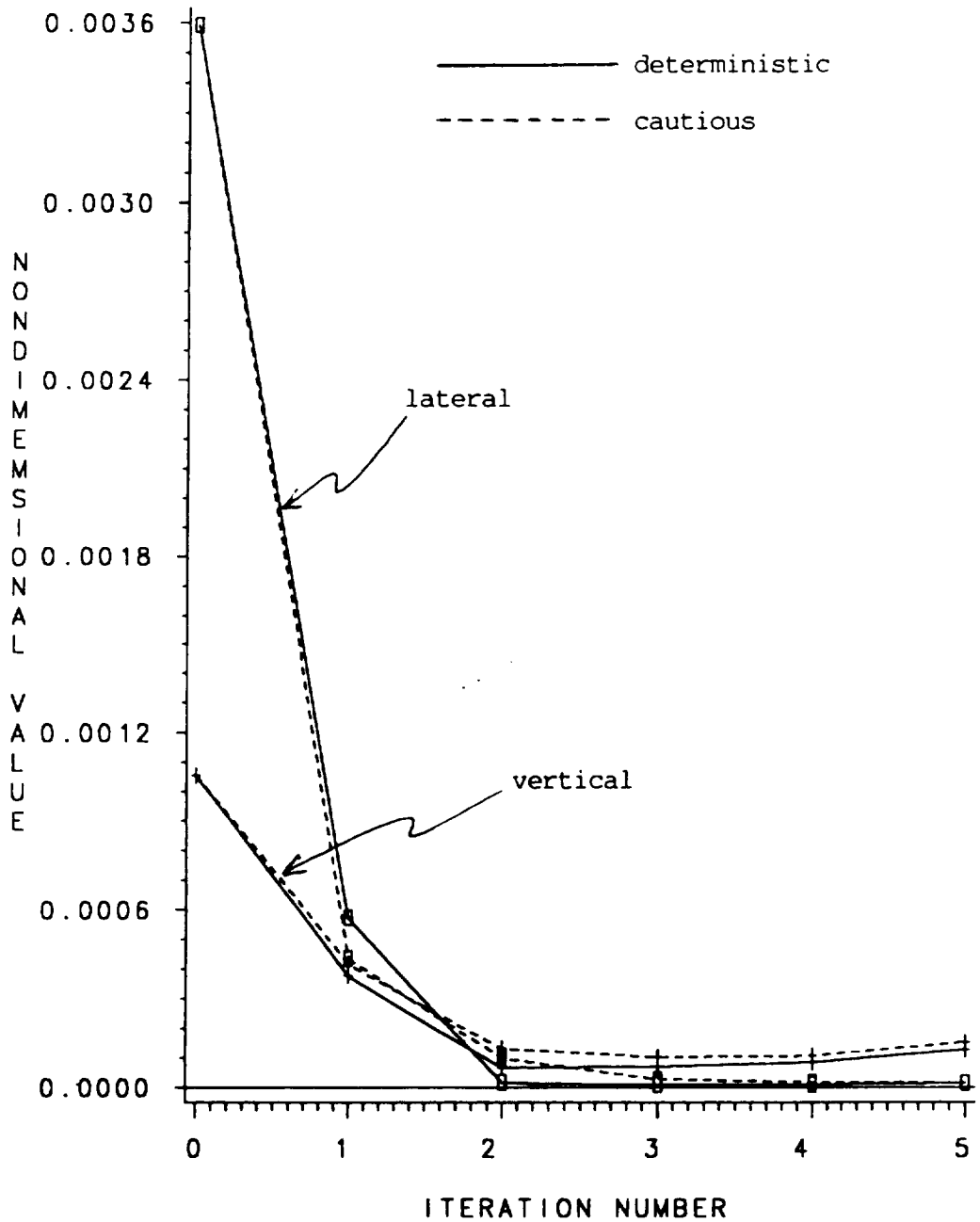

Figure 9.15: Iteration history of vertical and lateral hub shears for deterministic versus cautious local control, unsteady aerodynamics, $\mu = 0.3$.

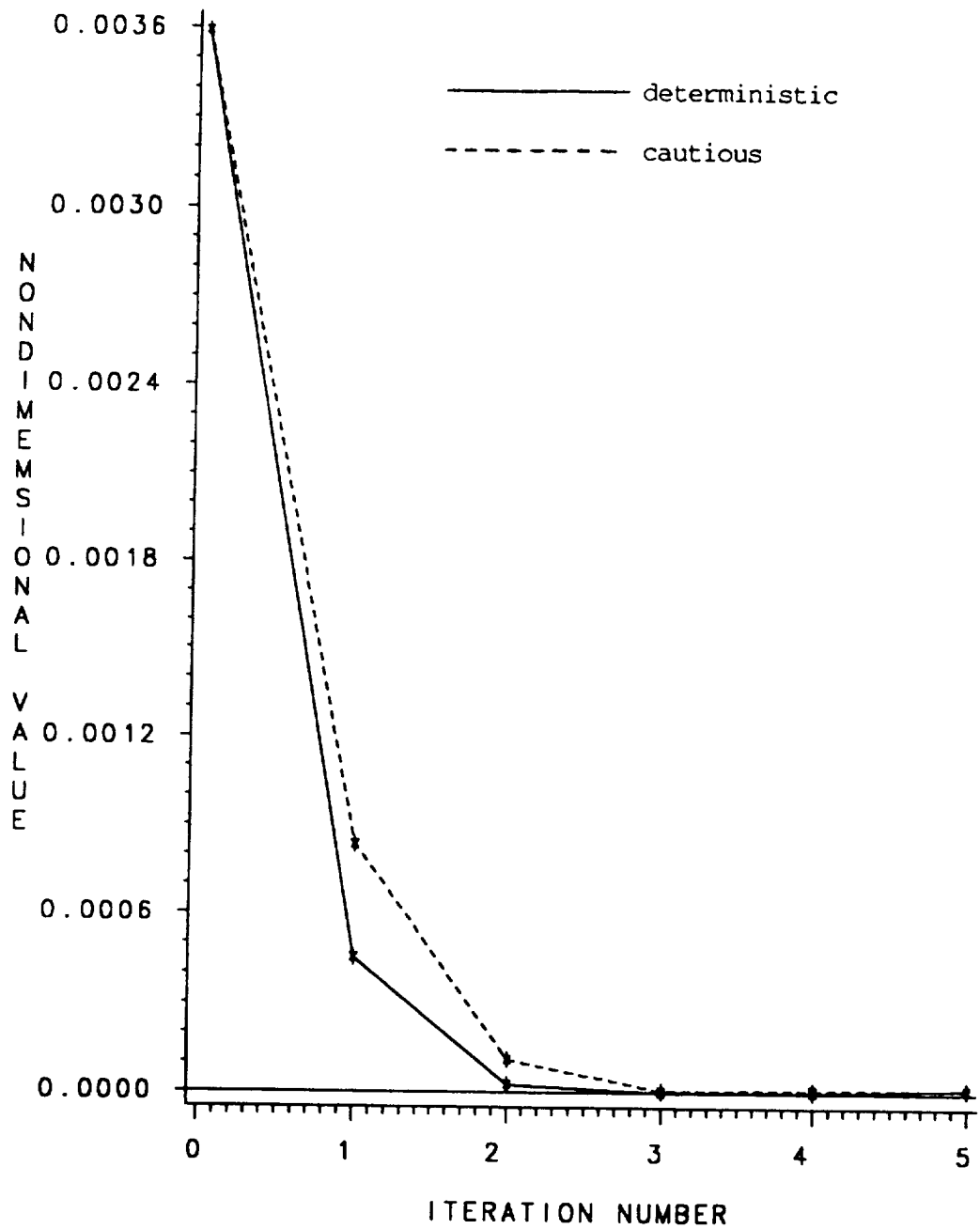

Figure 9.16: Iteration history of longitudinal hub shear for deterministic versus cautious local control, unsteady aerodynamics, $\mu = 0.3$.

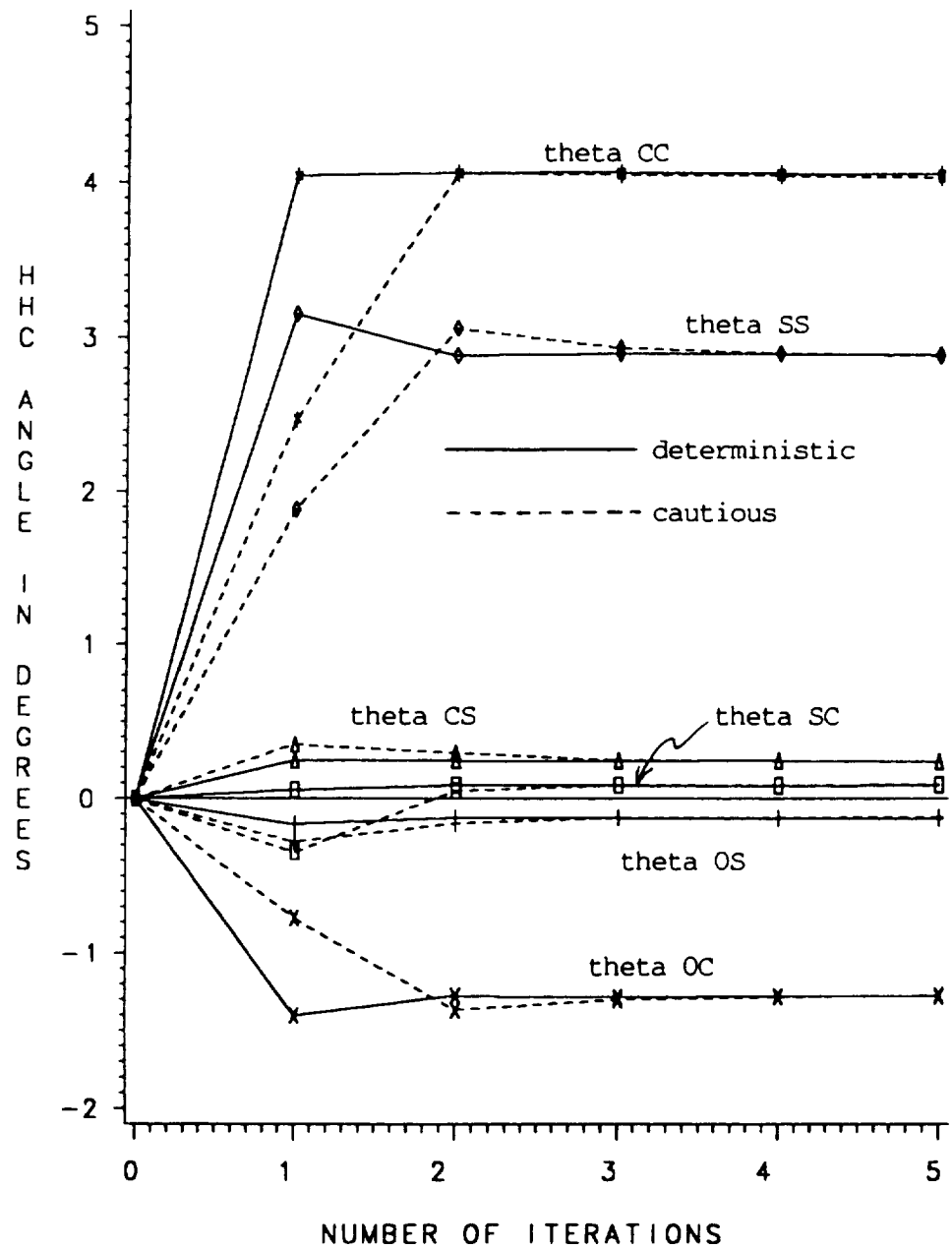

Figure 9.17: Iteration history of HHC input angles for deterministic versus cautious global control, unsteady aerodynamics, $\mu = 0.3$.

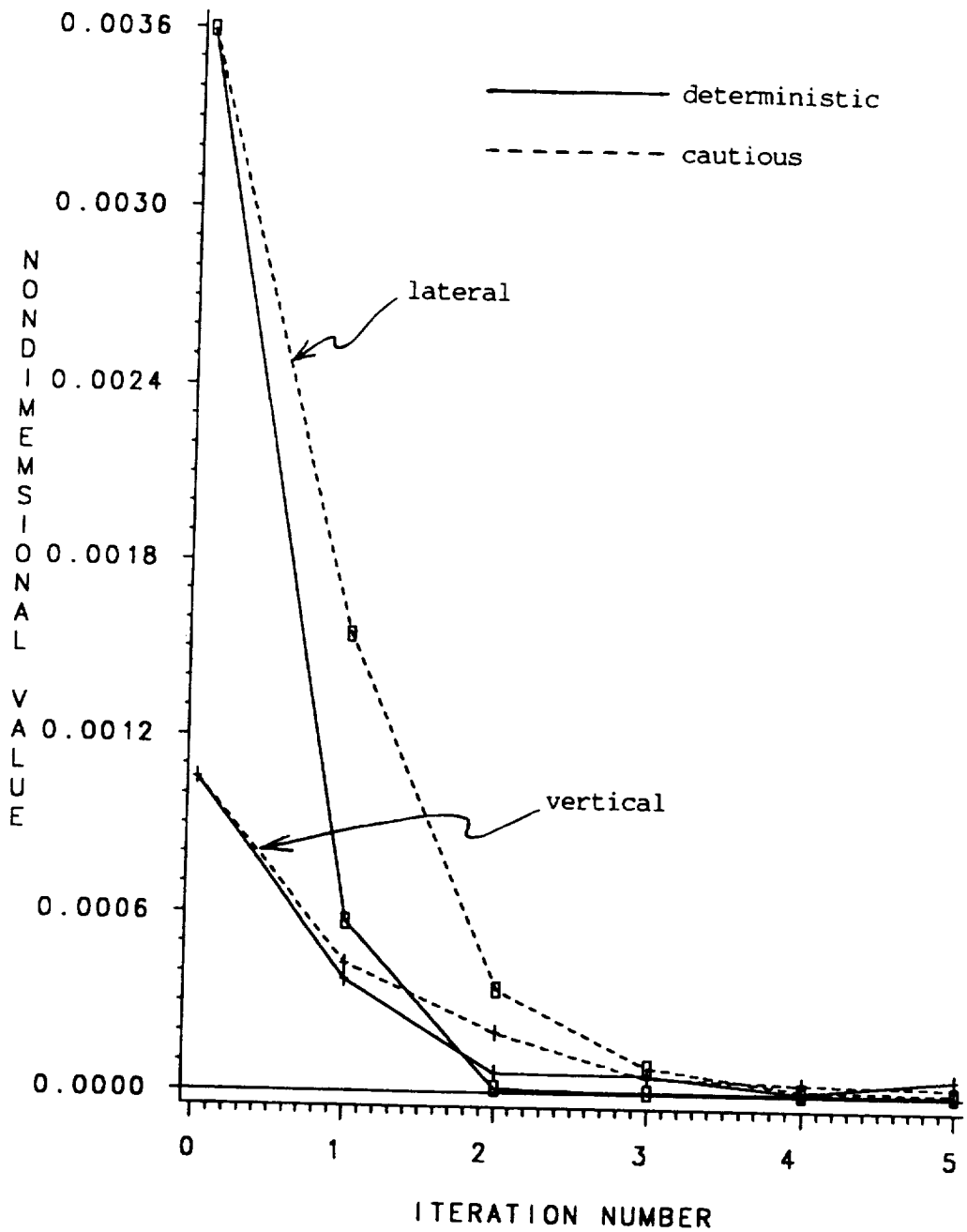

Figure 9.18: Iteration history of vertical and lateral hub shears for deterministic versus cautious global control, unsteady aerodynamics, $\mu = 0.3$.

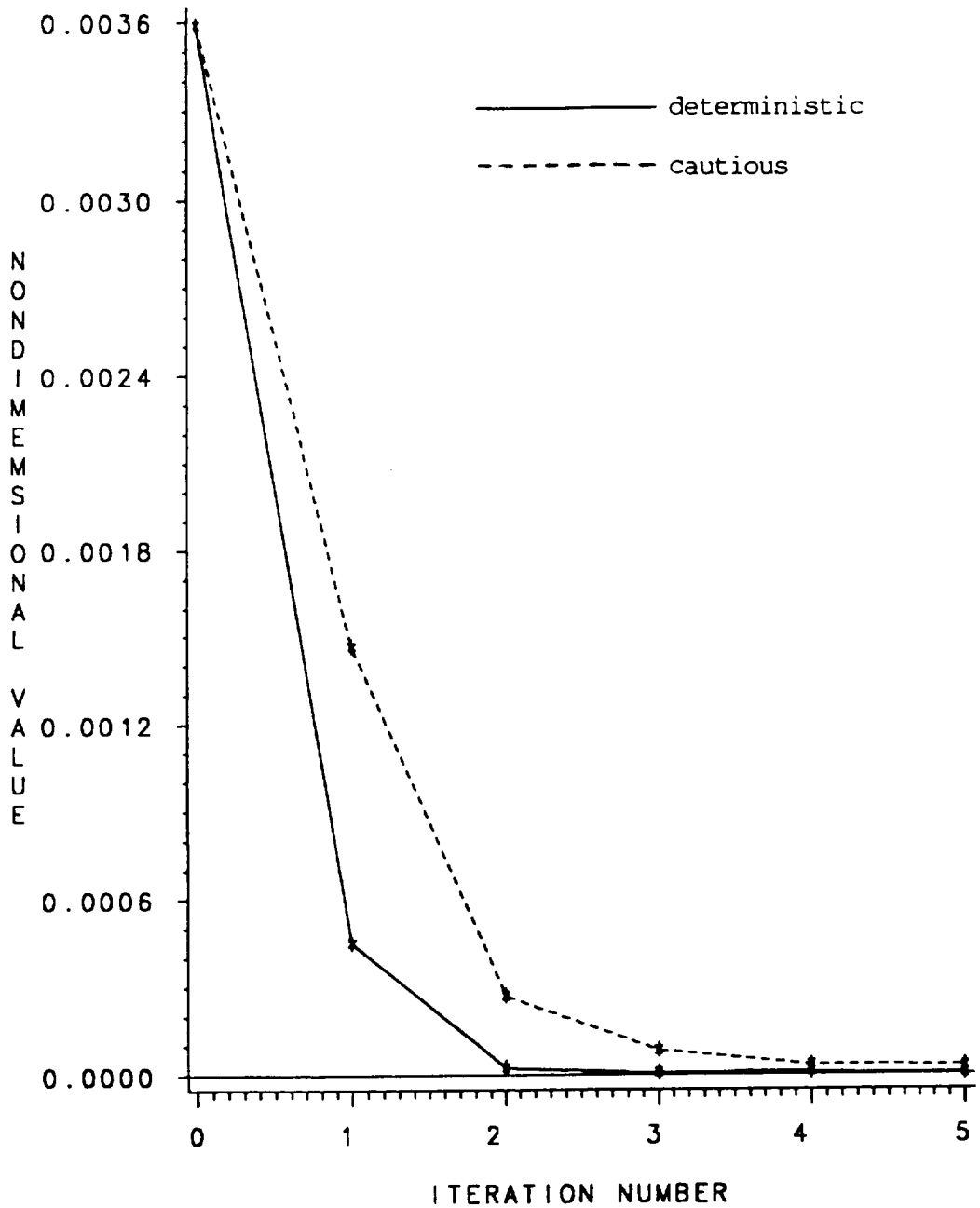

Figure 9.19: Iteration history of longitudinal hub shears for deterministic versus cautious global control, unsteady aerodynamics, $\mu = 0.3$.

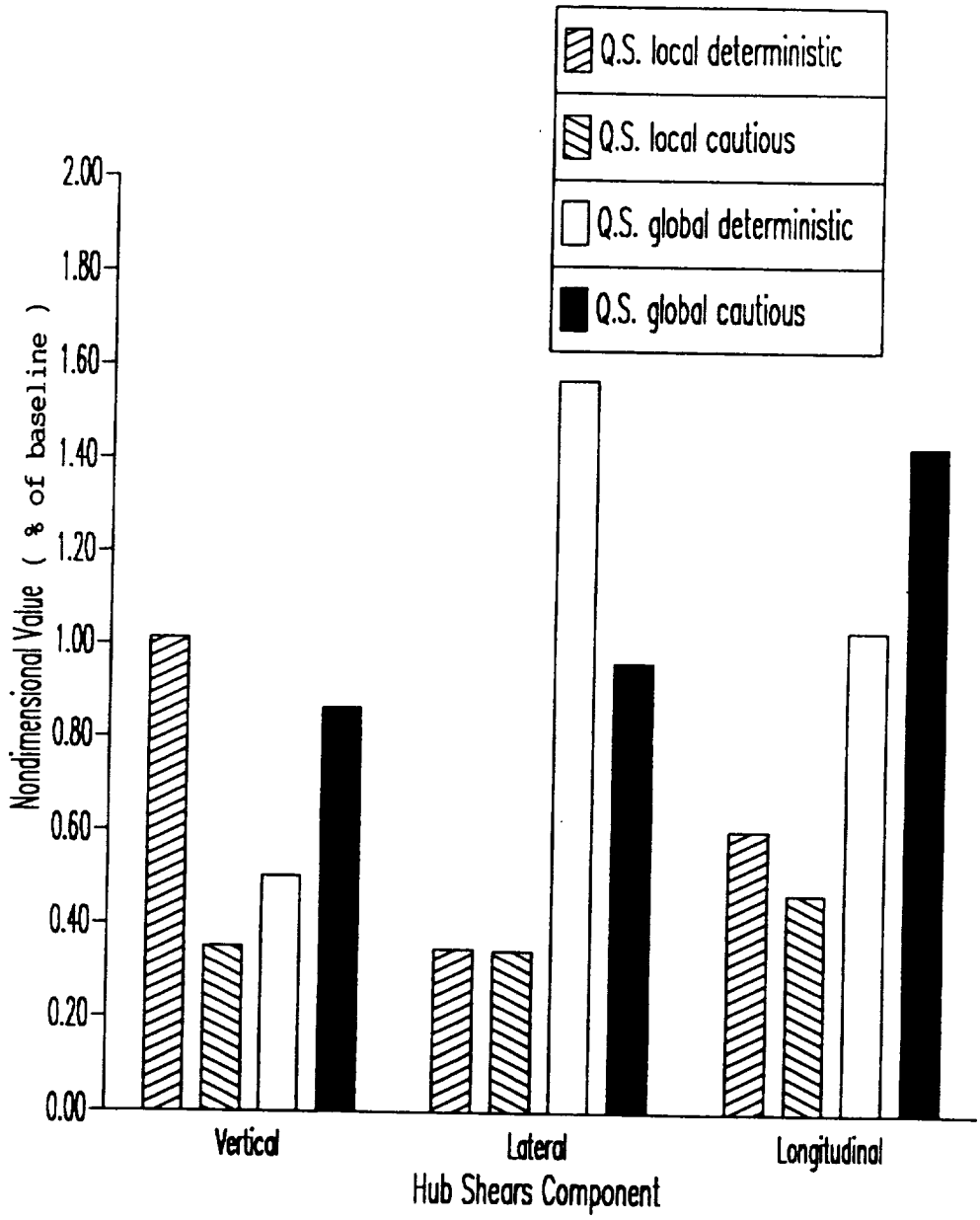

Figure 9.20: Optimal shears for deterministic and cautious versions of local and global controllers using quasisteady aerodynamics, $\mu = 0.3$.

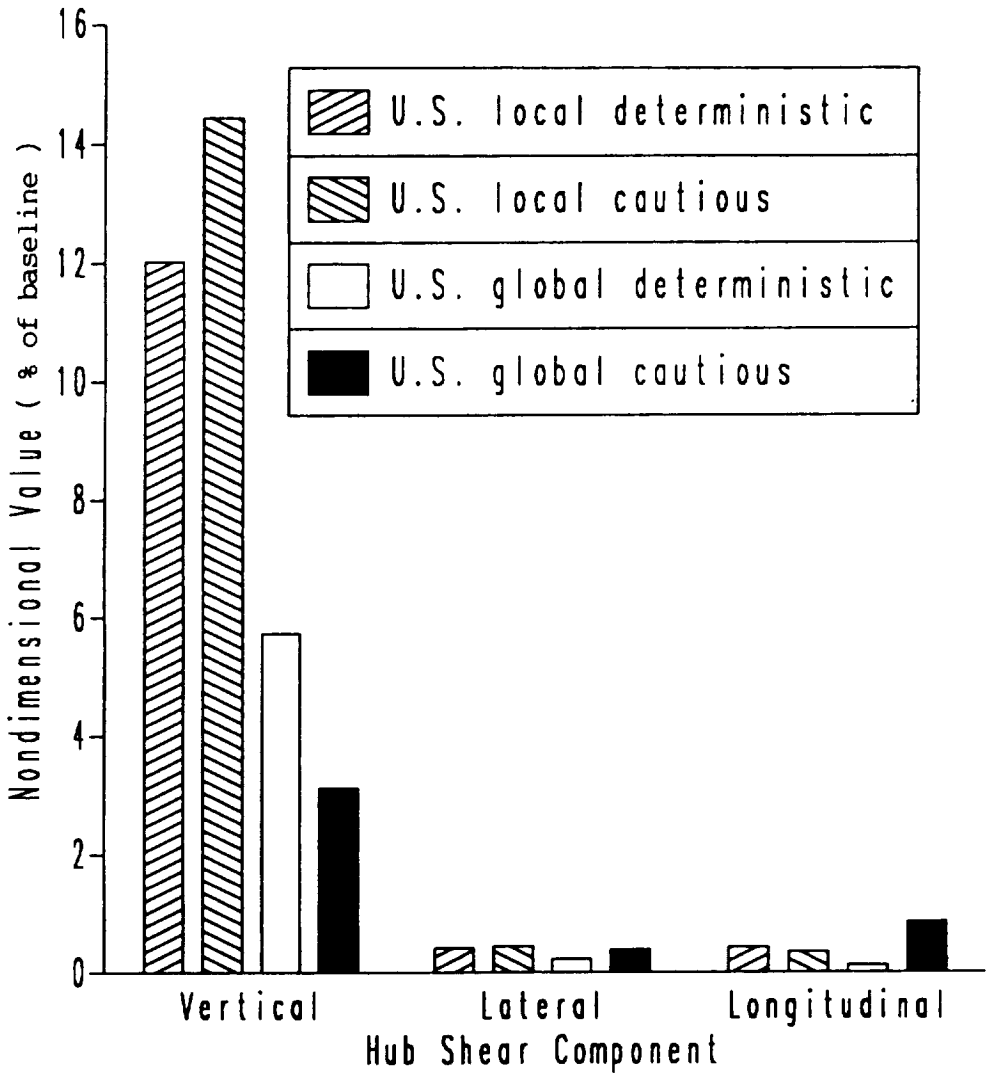

Figure 9.21: Optimal shears for deterministic and cautious versions of local and global controllers using unsteady aerodynamics, $\mu = 0.3$.

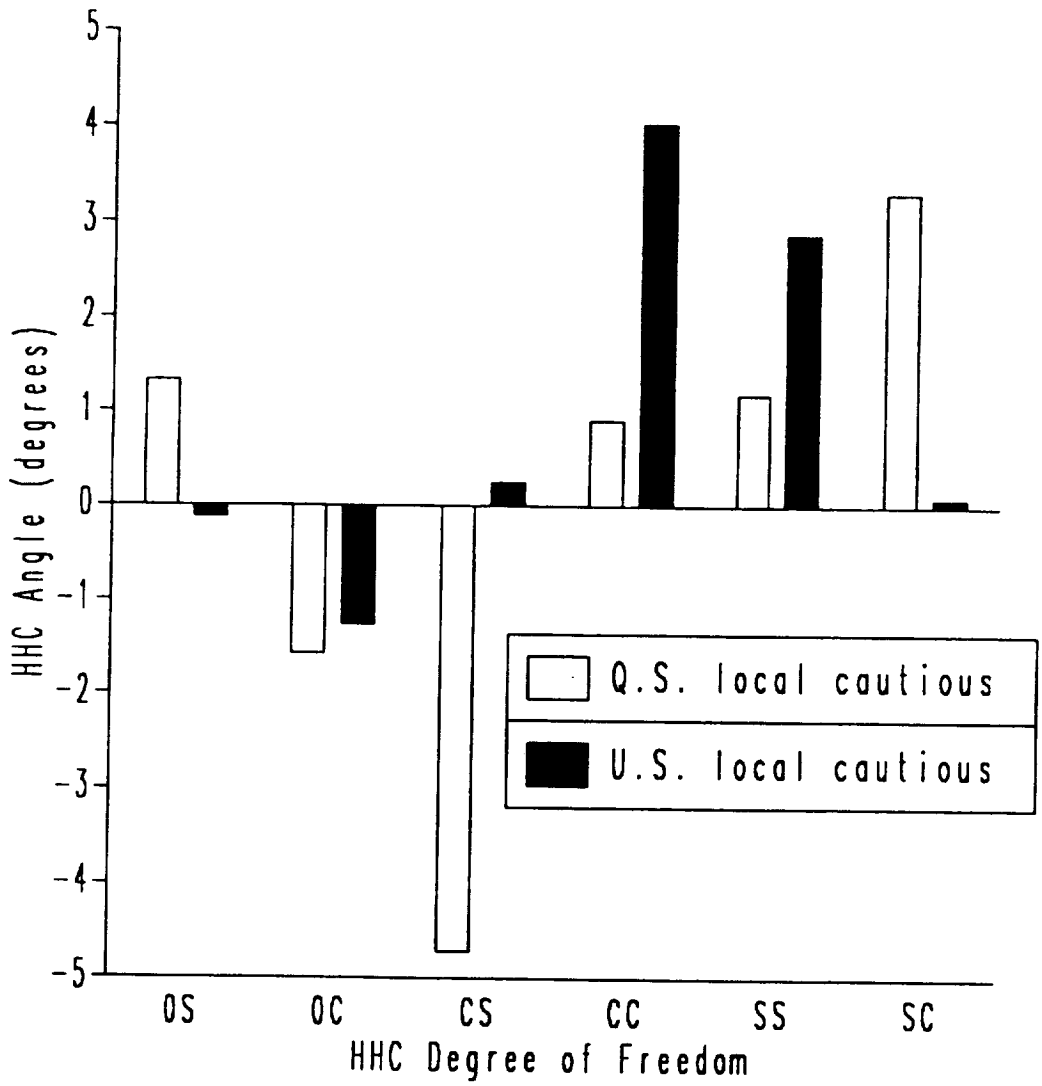

Figure 9.22: Comparison of optimal HHC inputs for the cautious version of the local controller using quasisteady versus unsteady aerodynamics, $\mu = 0.3$.

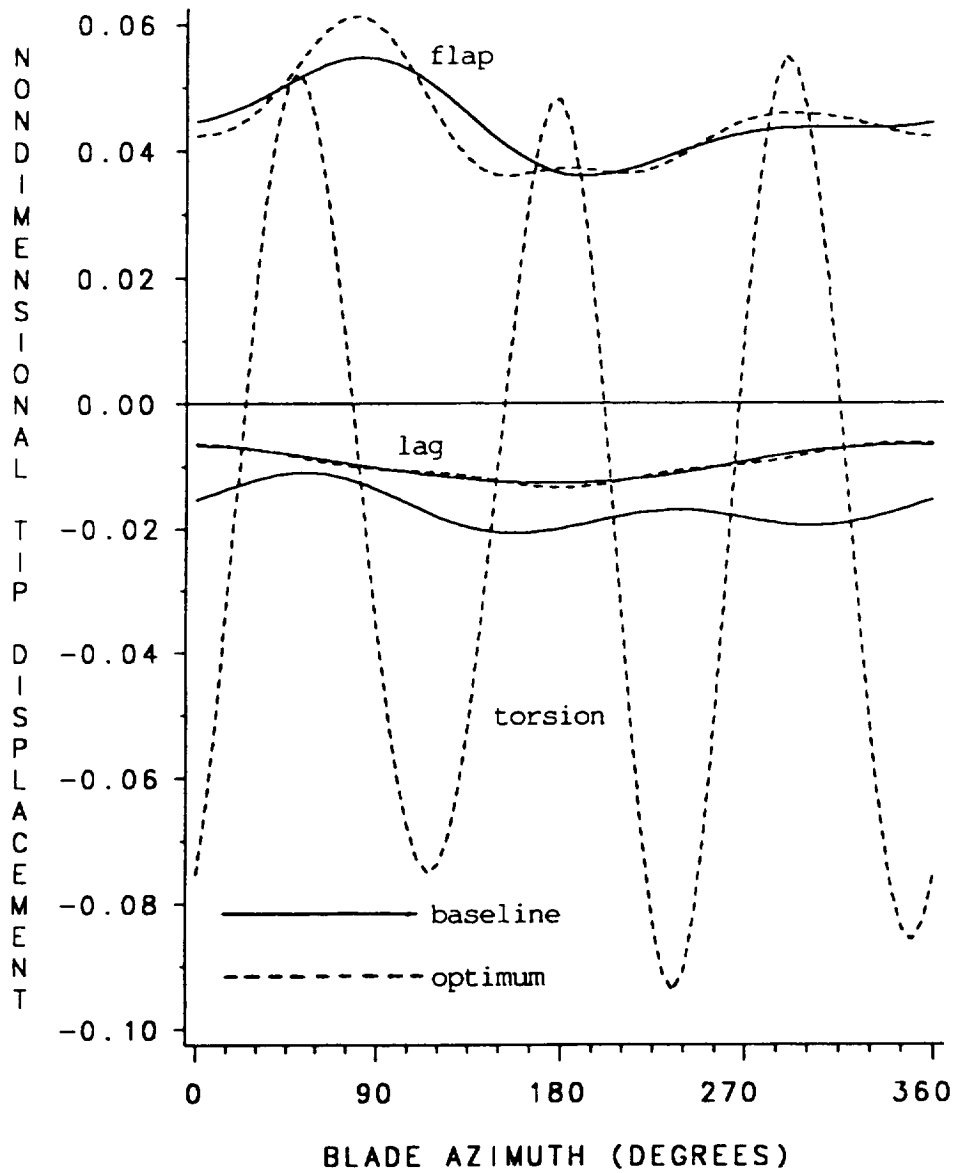

Figure 9.23: Flap, lag, and torsional elastic tip response, baseline response and optimal response due to cautious global HHC, unsteady aerodynamics, soft-in-plane blade, $\mu = 0.3$.

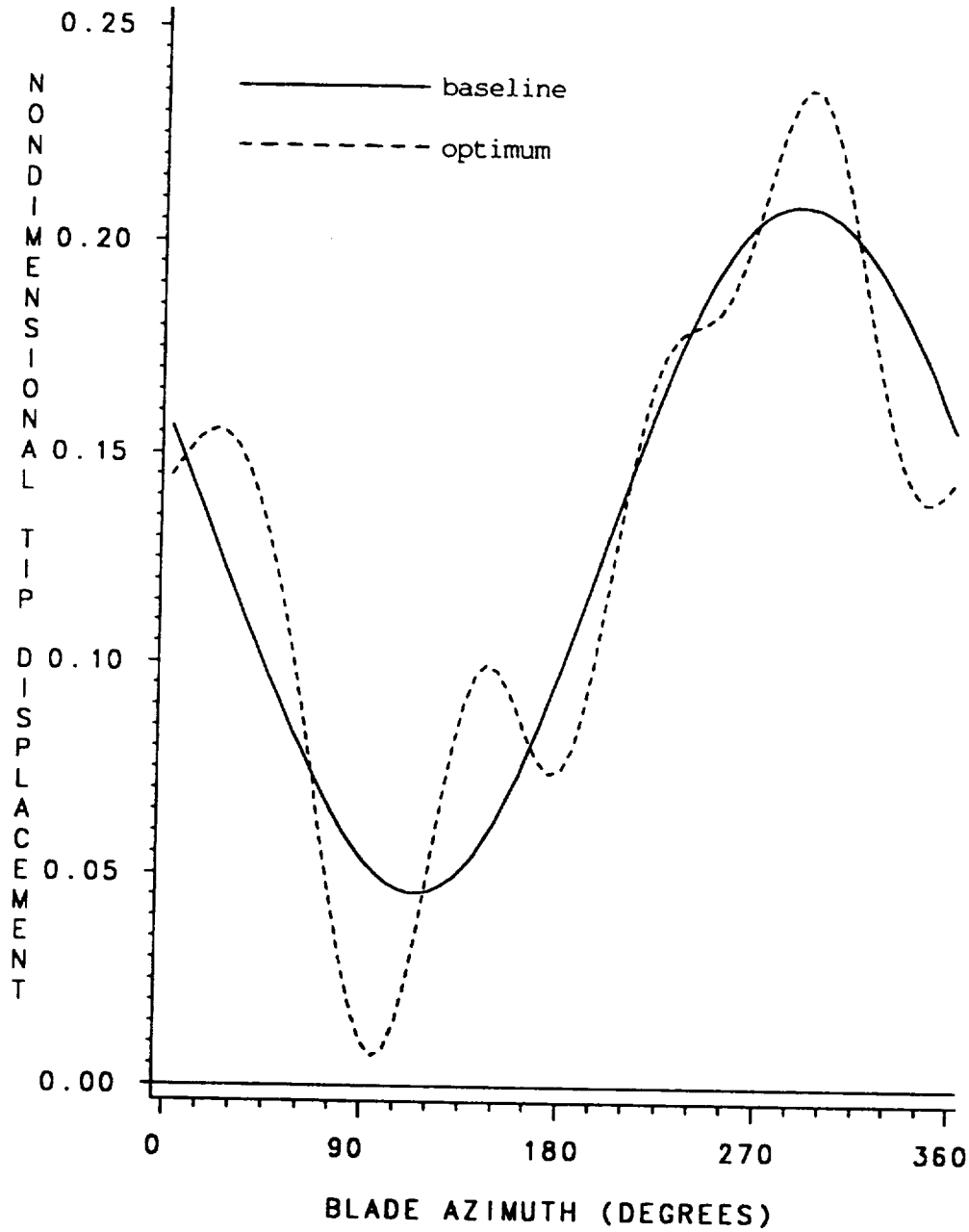

Figure 9.24: Total torsional geometric and elastic tip displacement, baseline response and optimal response due to cautious global HHC, unsteady aerodynamics, soft-in-plane blade, $\mu = 0.3$.

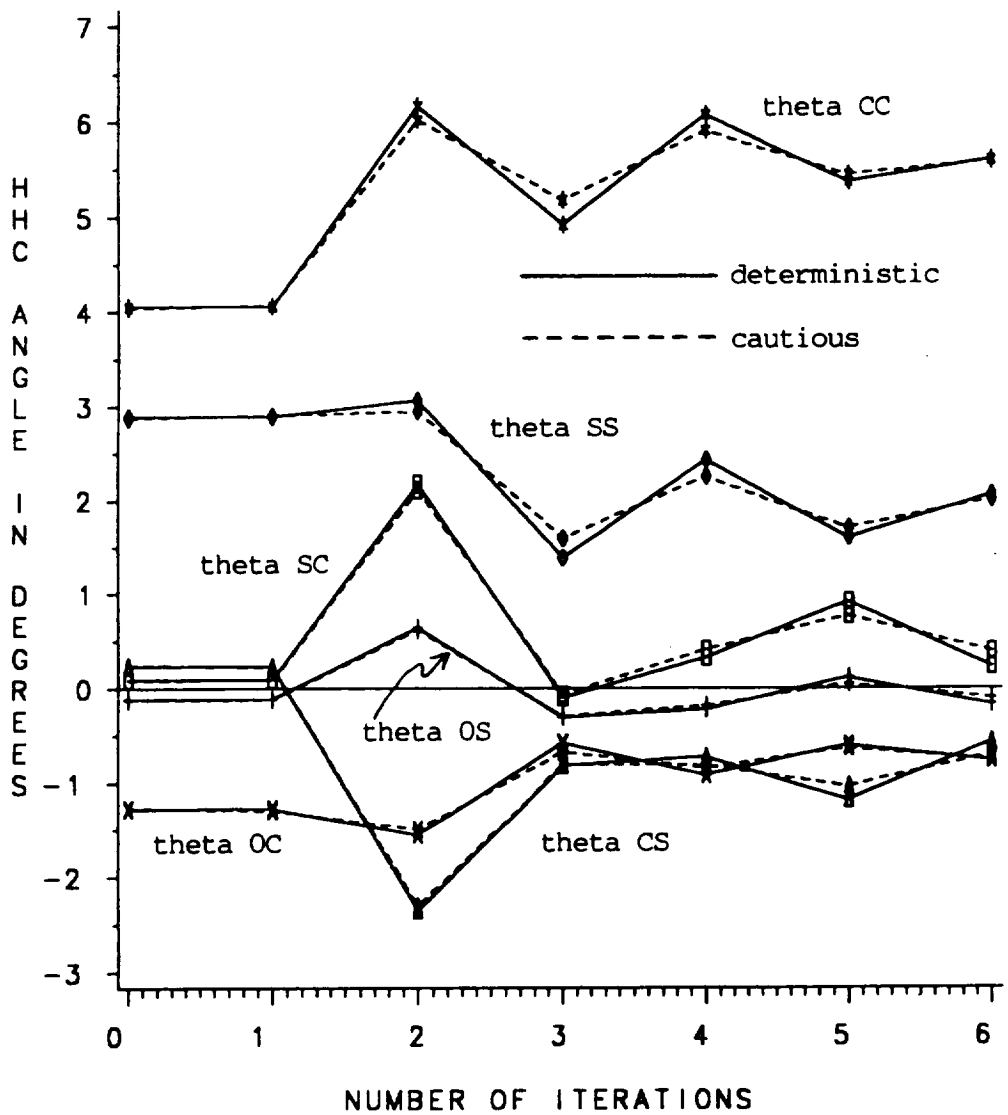

Figure 9.25: Iteration history of HHC input angles for deterministic versus cautious local control, unsteady aerodynamics, step change from $\mu = 0.3$ to $\mu = .35$.

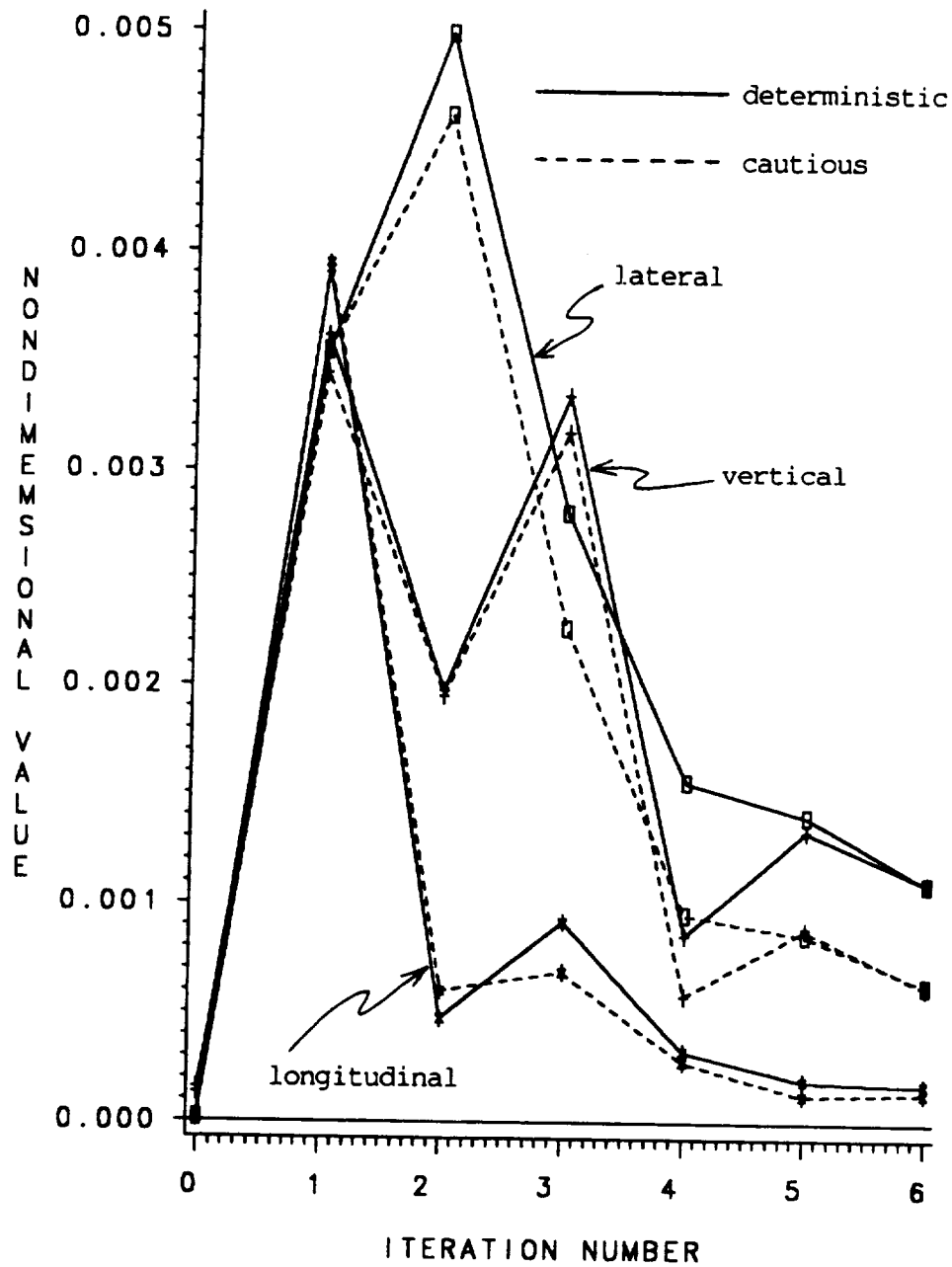

Figure 9.26: Iteration history of hub shears for deterministic versus cautious local control, unsteady aerodynamics, step change from $\mu = 0.3$ to $\mu = 0.35$.

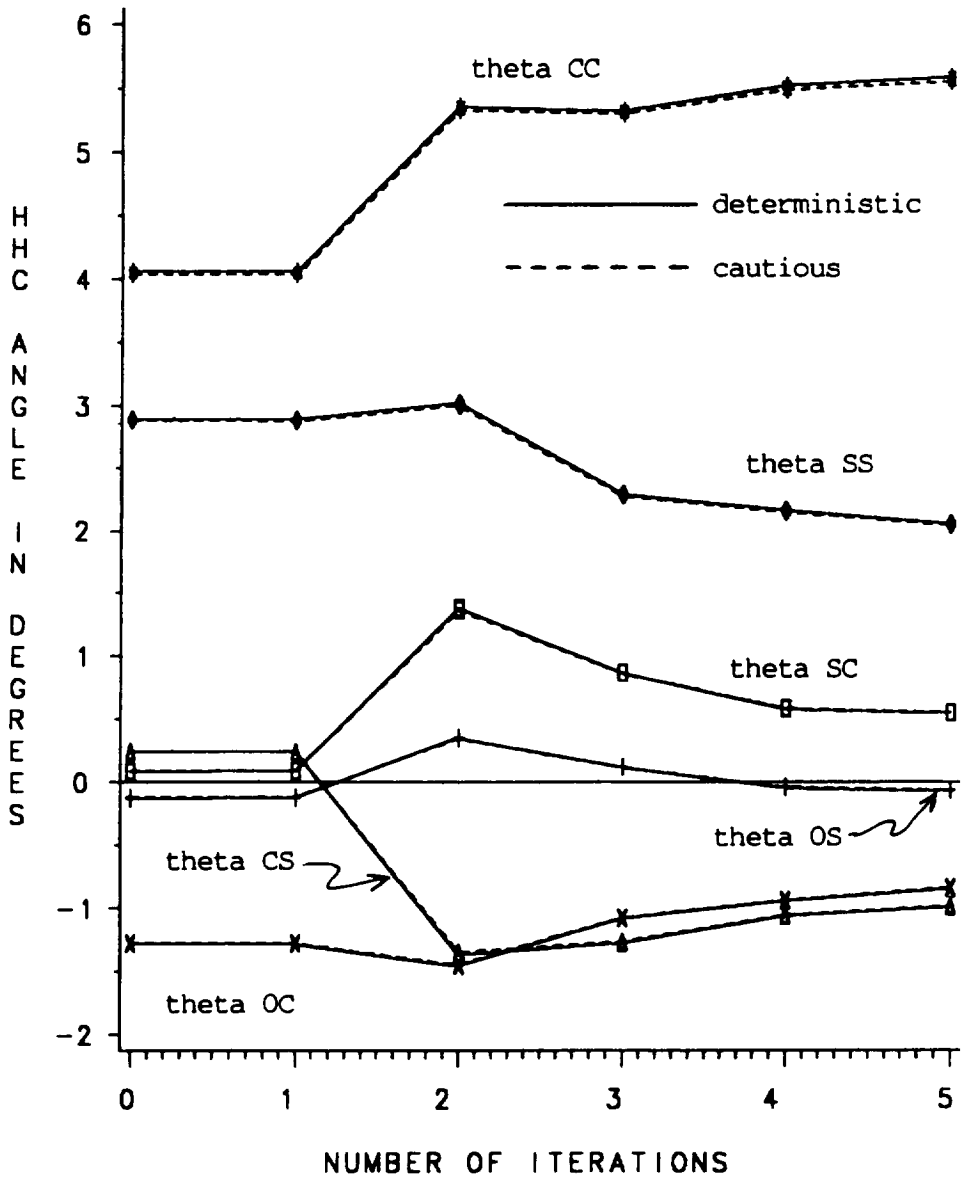

Figure 9.27: Iteration history of HHC input angles for deterministic versus cautious global control, unsteady aerodynamics, step change from $\mu = 0.3$ to $\mu = .35$.

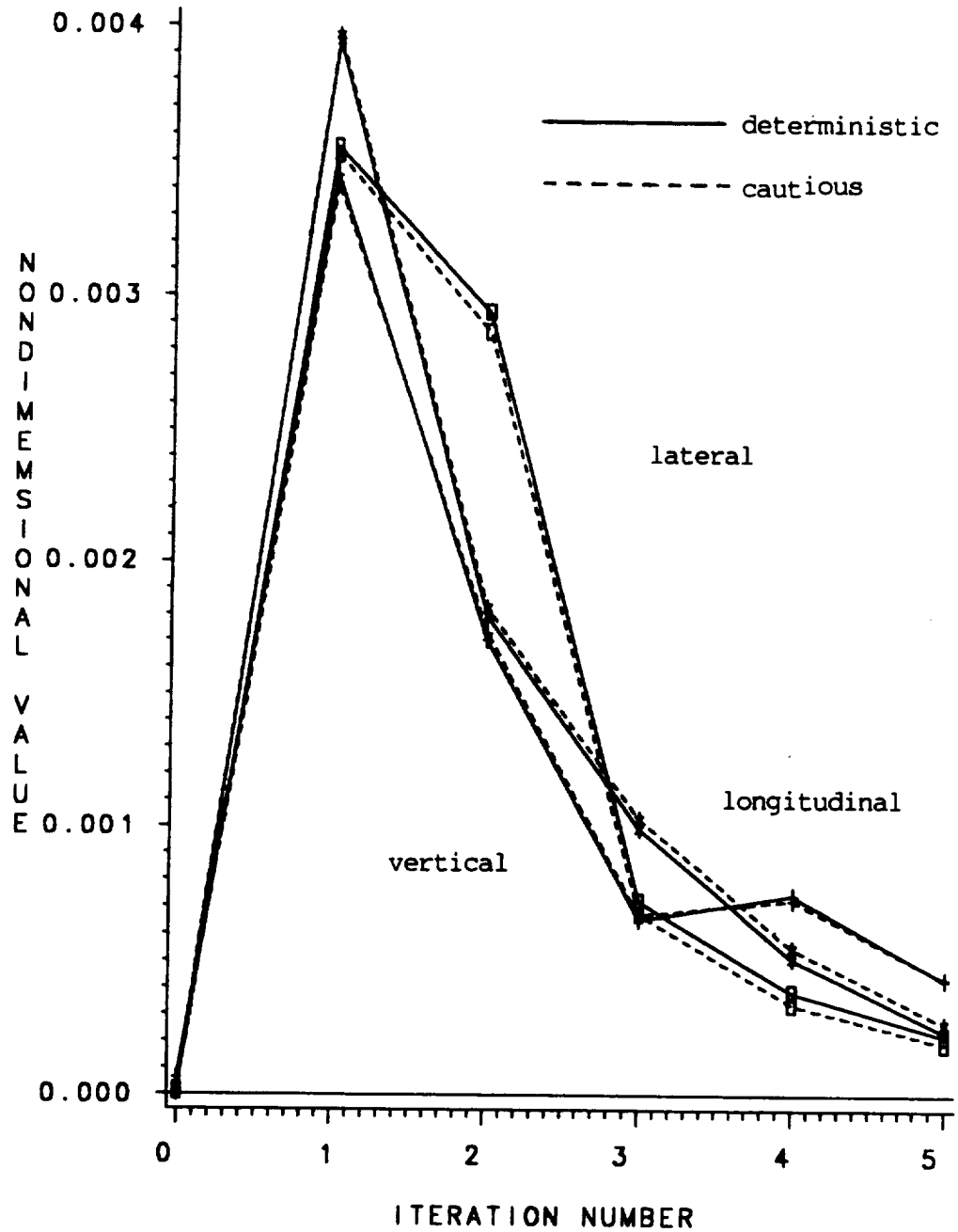

Figure 9.28: Iteration history of hub shears for deterministic versus cautious global control, unsteady aerodynamics, step change from $\mu = 0.3$ to $\mu = 0.35$.

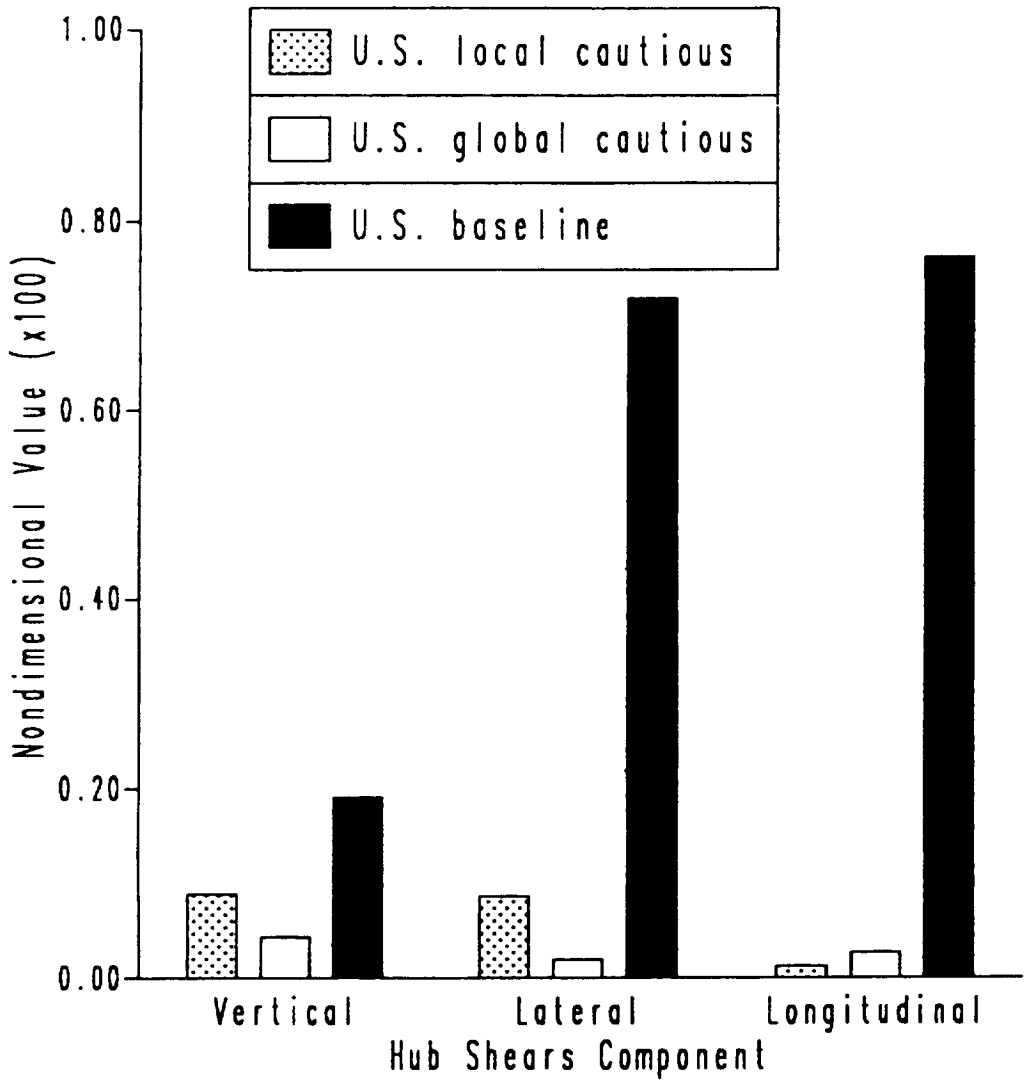

Figure 9.29: Baseline shears for $\mu = 0.35$, and shears five iterations after a step change from $\mu = 0.3$ to $\mu = 0.35$, local and global controllers, unsteady aerodynamics.

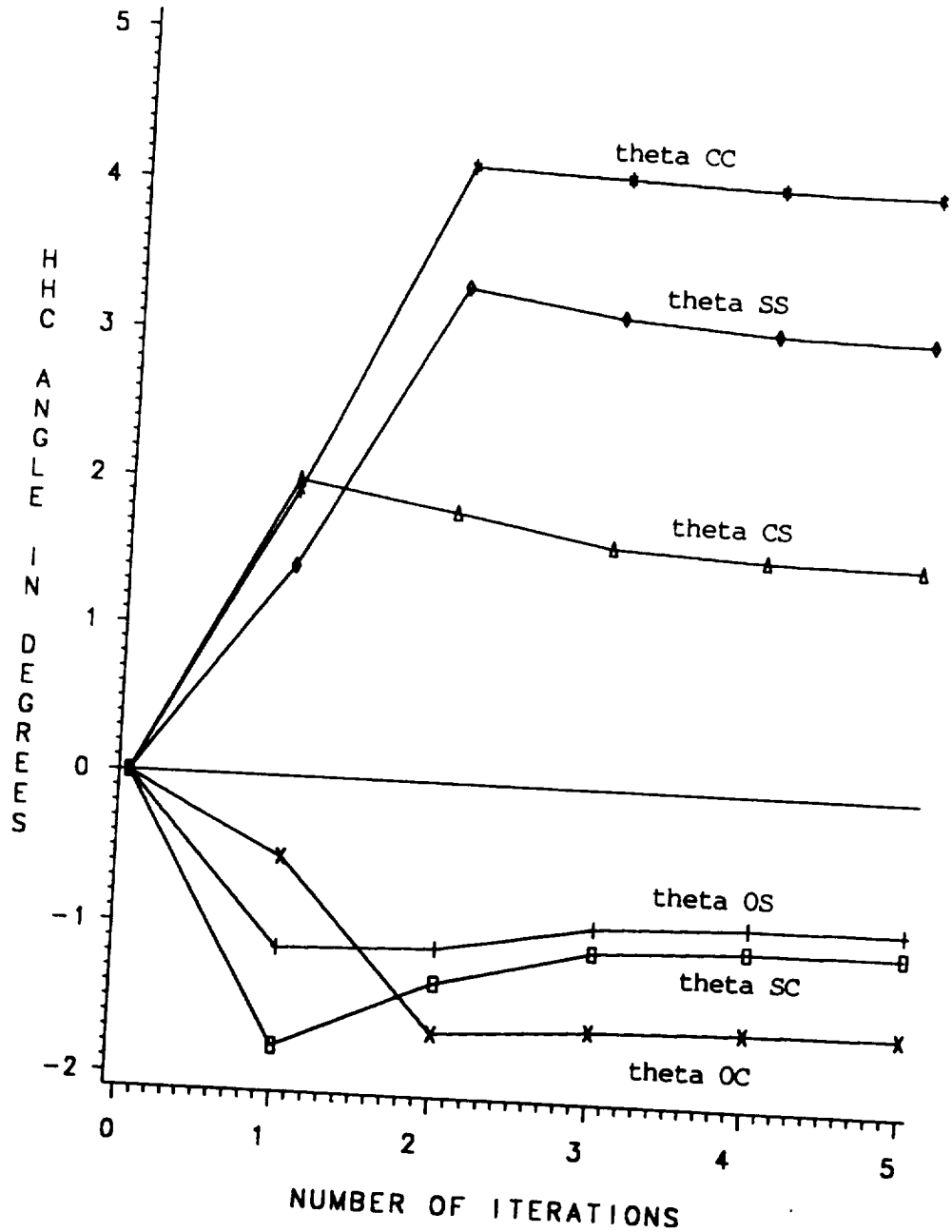

Figure 10.1: Iteration history of HHC input angles for hingeless blade, 5% blade root offset, cautious global control, $\mu = 0.3$.

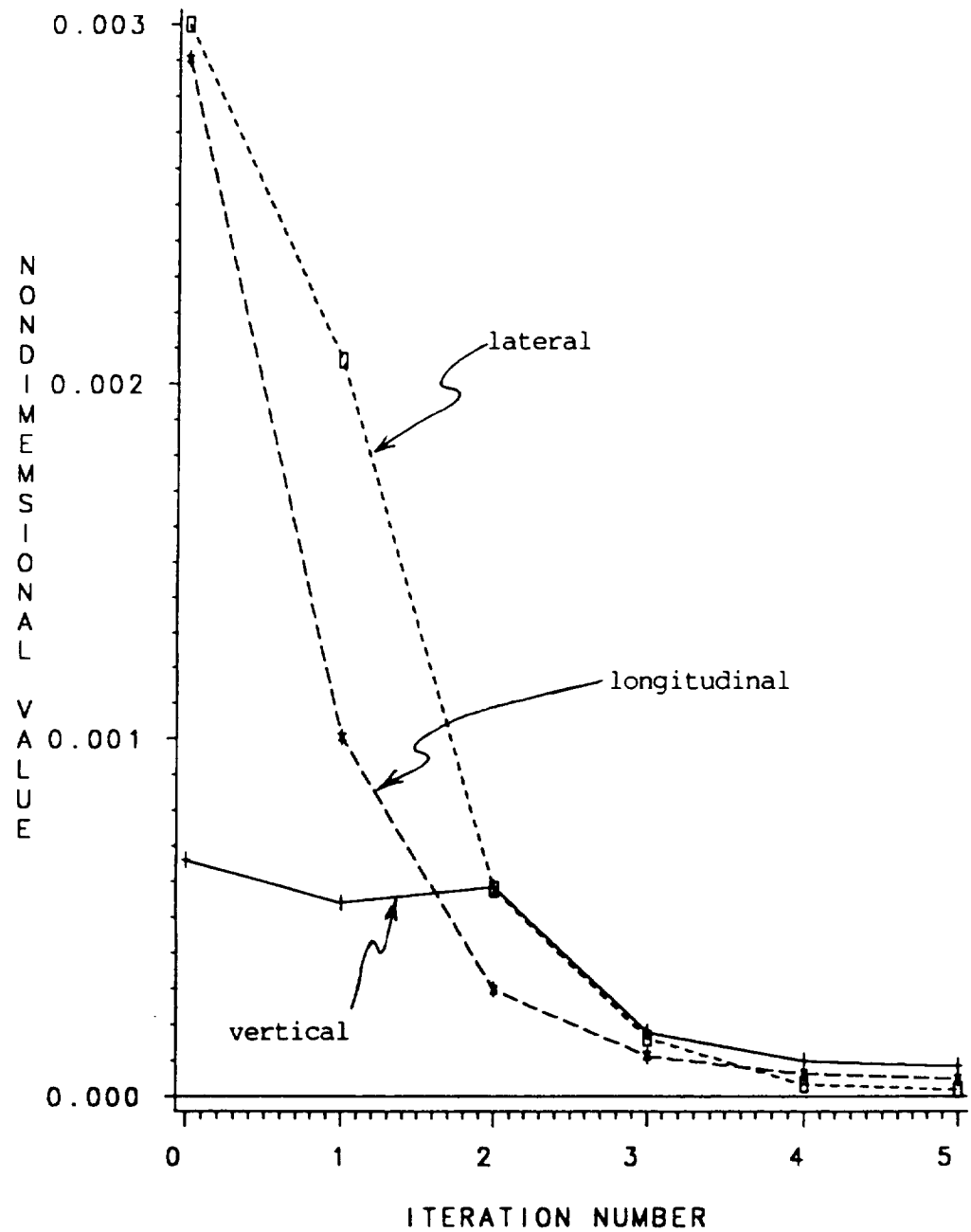

Figure 10.2: Iteration history of vertical, lateral and longitudinal peak-to-peak hub shears, hingeless blade, 5% blade root offset, cautious global control, $\mu = 0.3$.

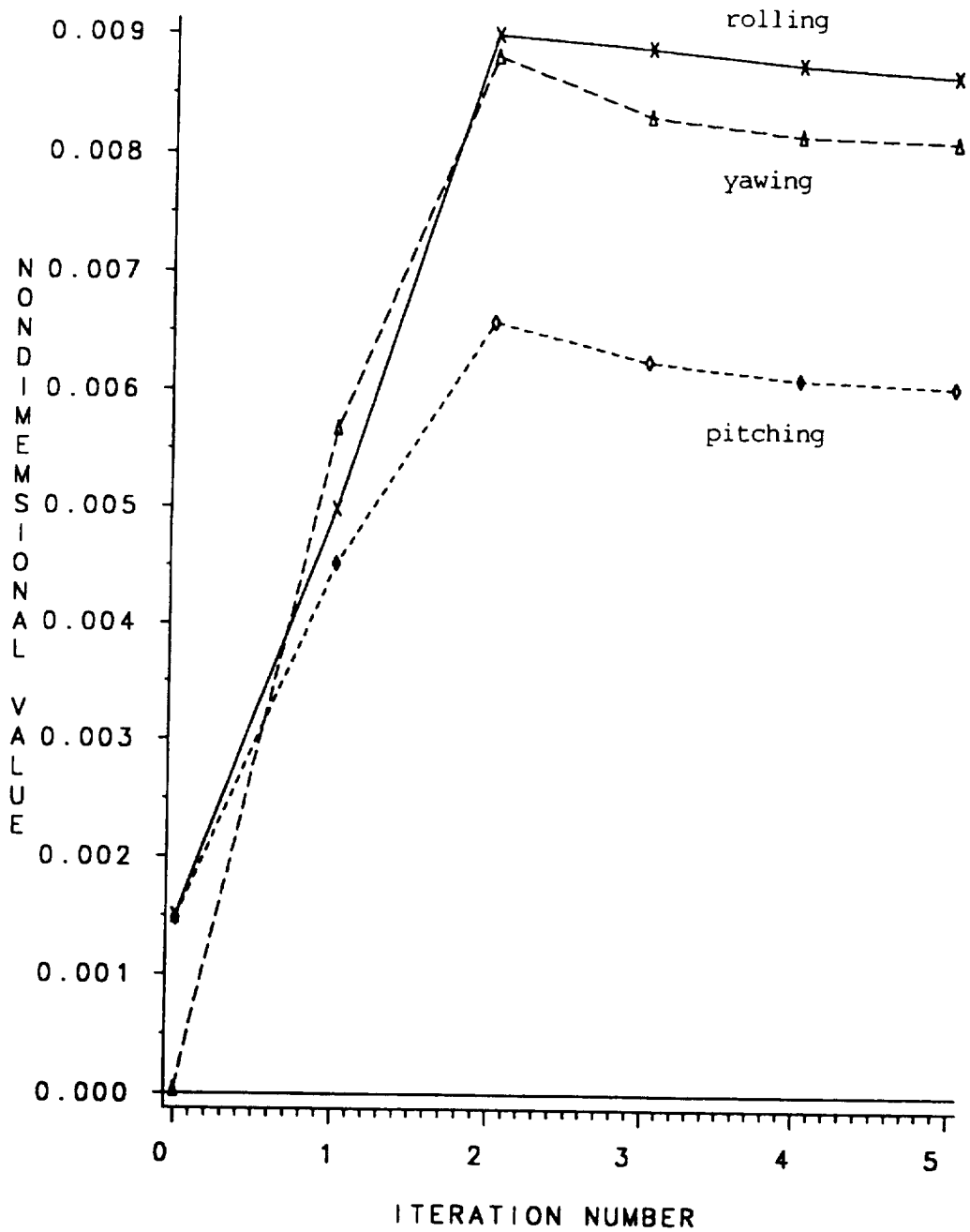

Figure 10.3: Iteration history of pitching, rolling and yawing peak-to-peak hub moments, hingeless blade, 5% blade root offset, cautious global control, $\mu = 0.3$.

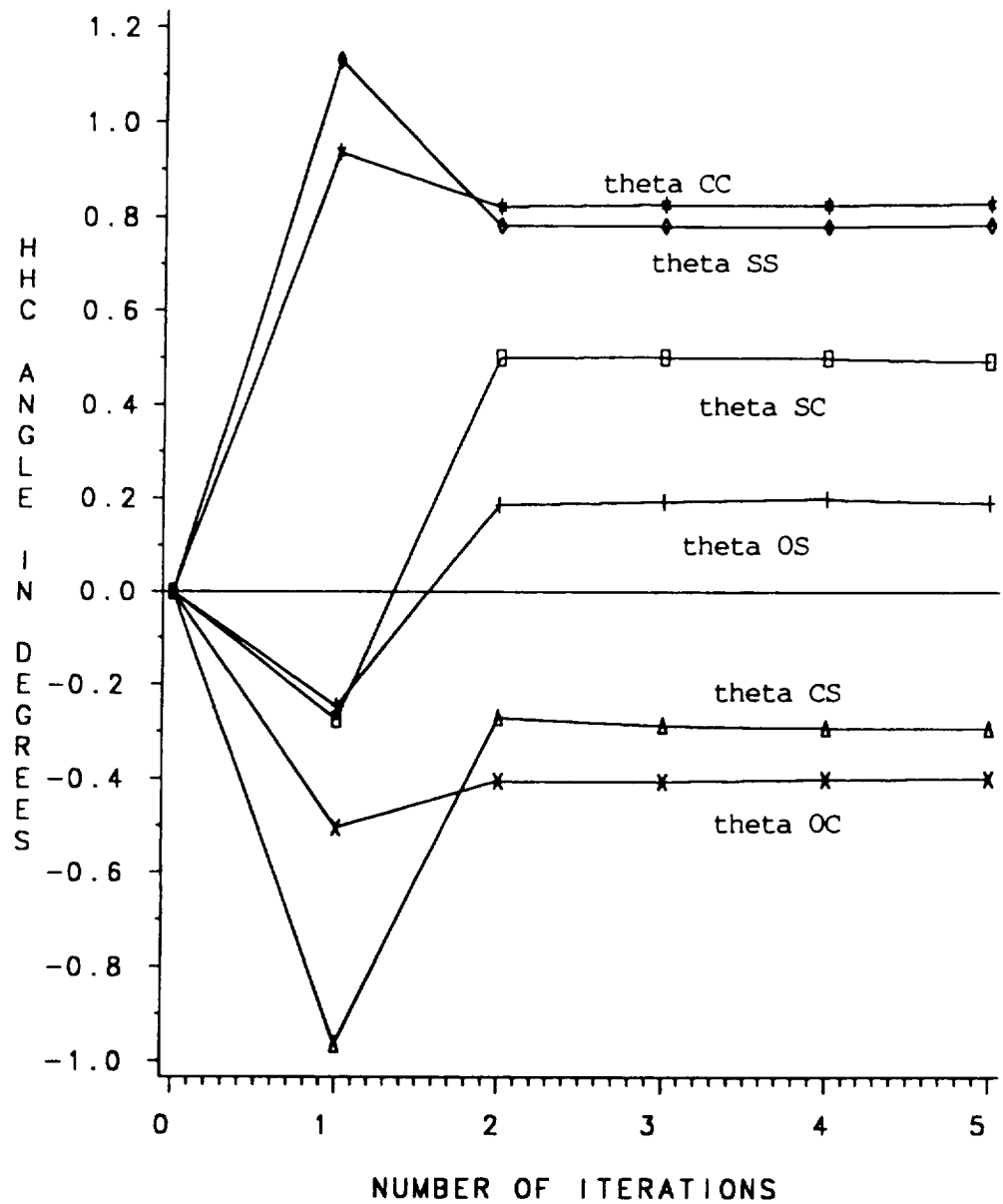

Figure 10.4: Iteration history of HHC input angles for articulated blade, 5% blade root offset, cautious global control, $\mu = 0.3$.

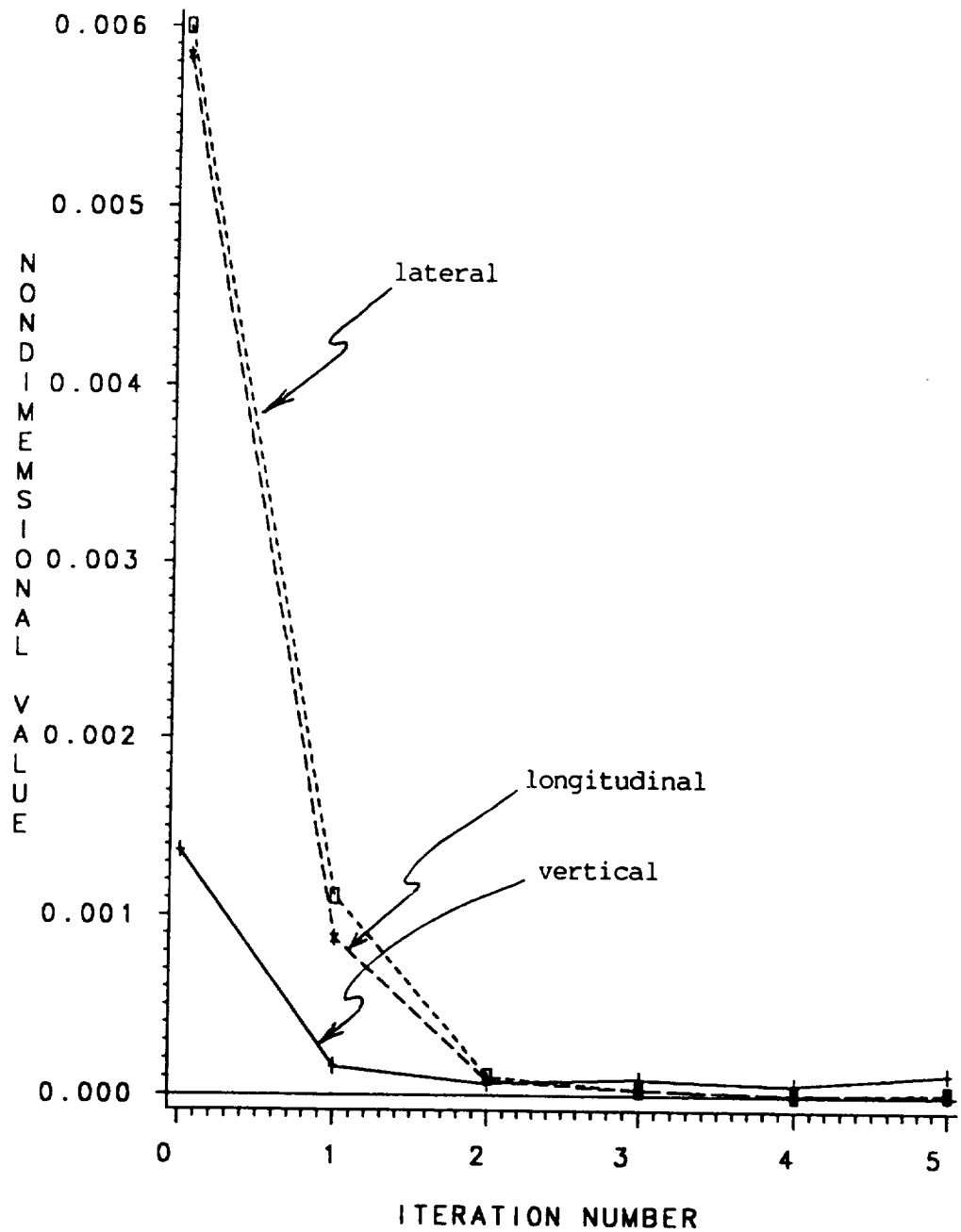

Figure 10.5: Iteration history of vertical, lateral and longitudinal peak-to-peak hub shears, articulated blade, 5% blade root offset, cautious global control, $\mu = 0.3$.

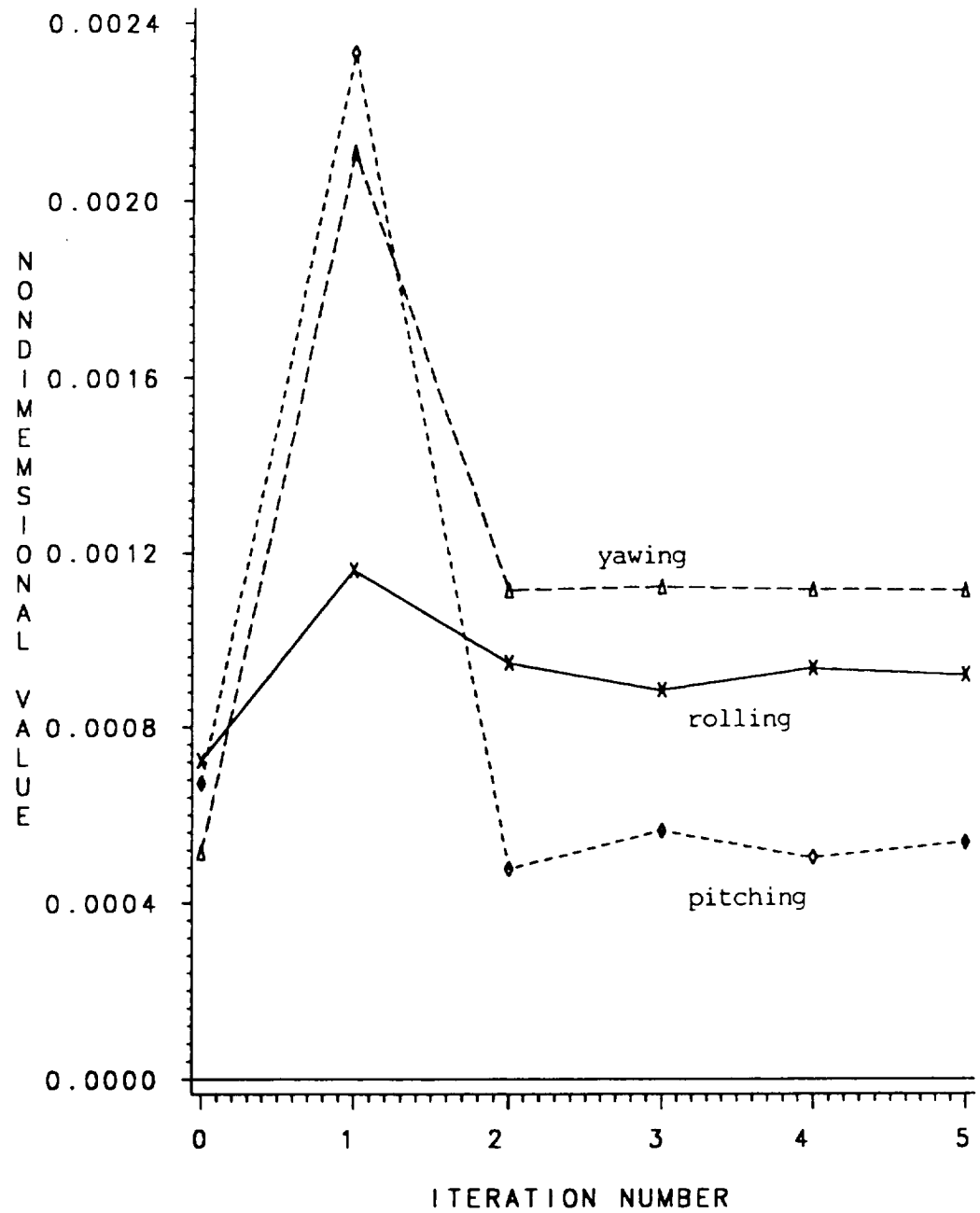

Figure 10.6: Iteration history of pitching, rolling and yawing peak-to-peak hub moments, articulated blade, 5% blade root offset, cautious global control, $\mu = 0.3$.

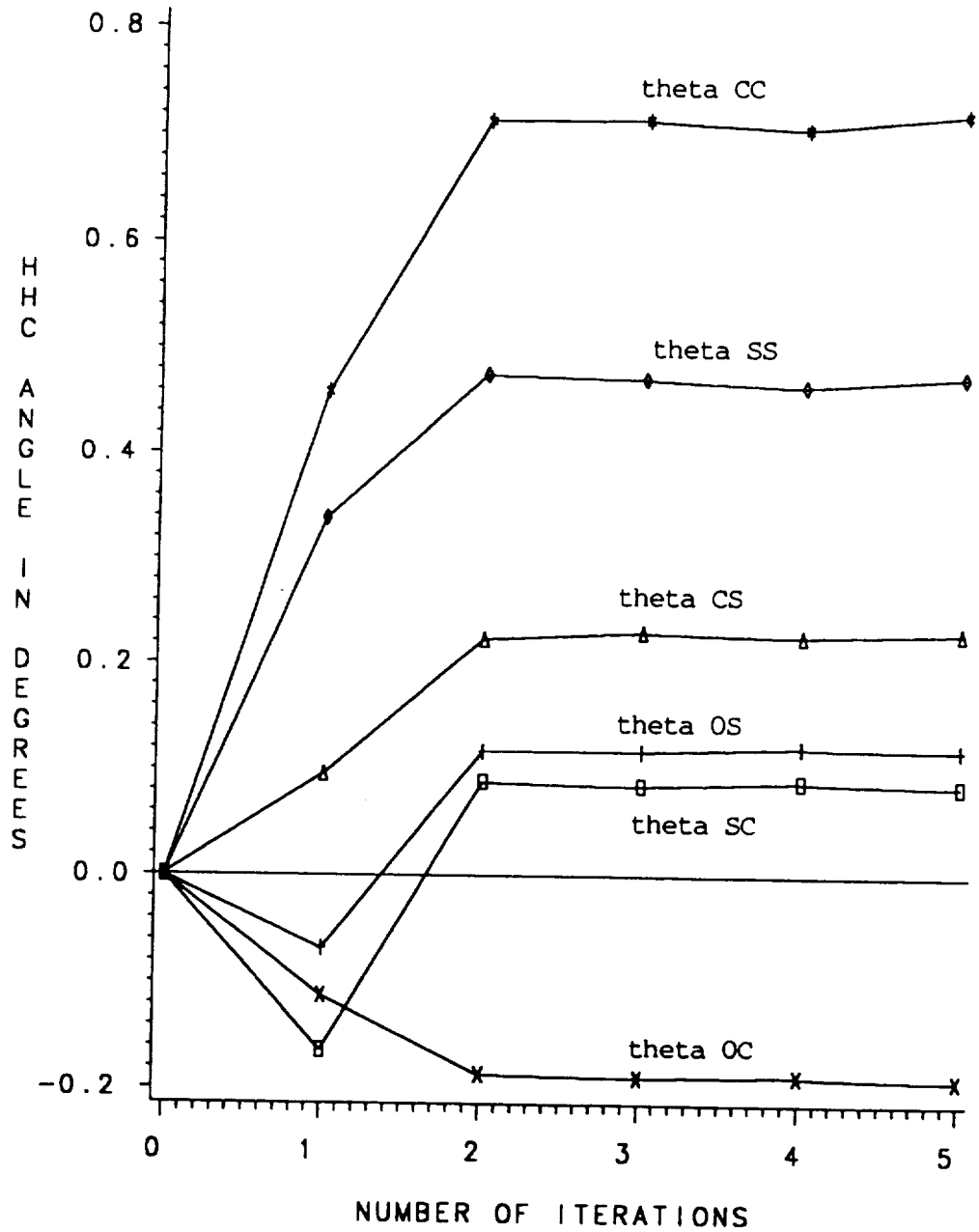

Figure 10.7: Iteration history of HHC input angles for hingeless blade, 5% blade root offset, 6×12 cautious global control, $\mu = 0.3$.

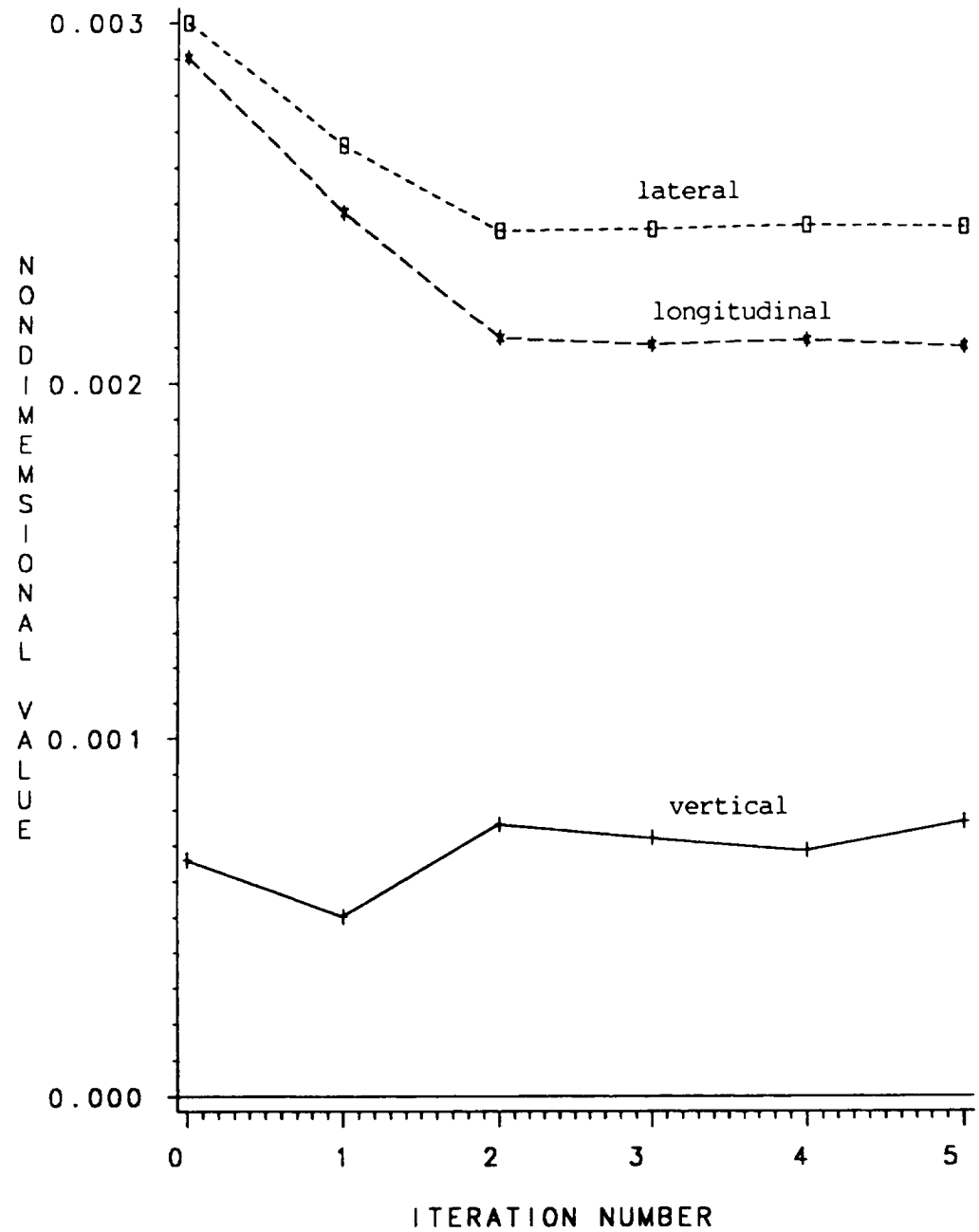

Figure 10.8: Iteration history of vertical, lateral and longitudinal peak-to-peak hub shears, hingeless blade, 5% blade root offset, 6×12 cautious global control, $\mu = 0.3$.

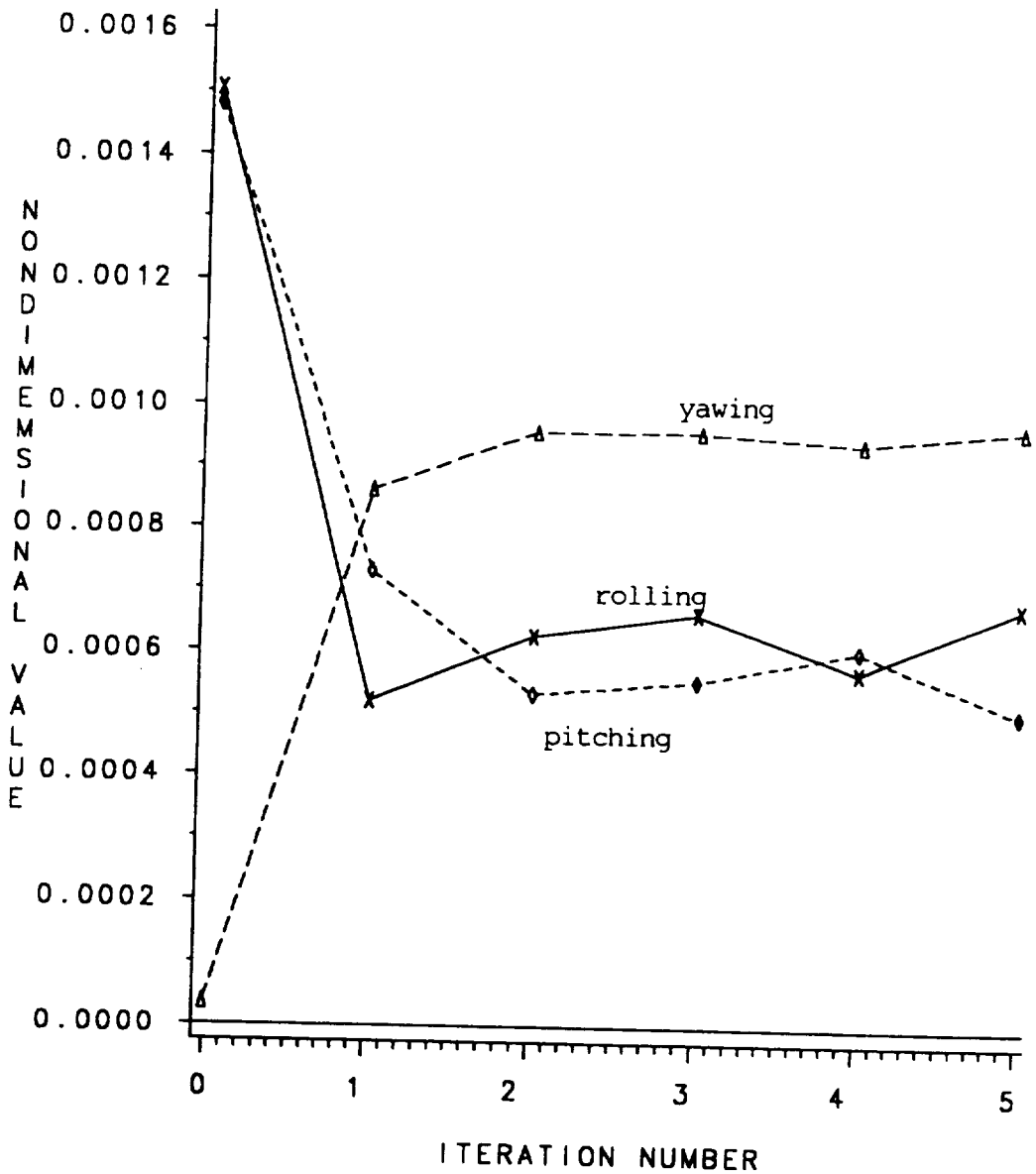

Figure 10.9: Iteration history of pitching, rolling and yawing peak-to-peak hub moments, hingeless blade, 5% blade root offset, 6×12 cautious global control, $\mu = 0.3$.

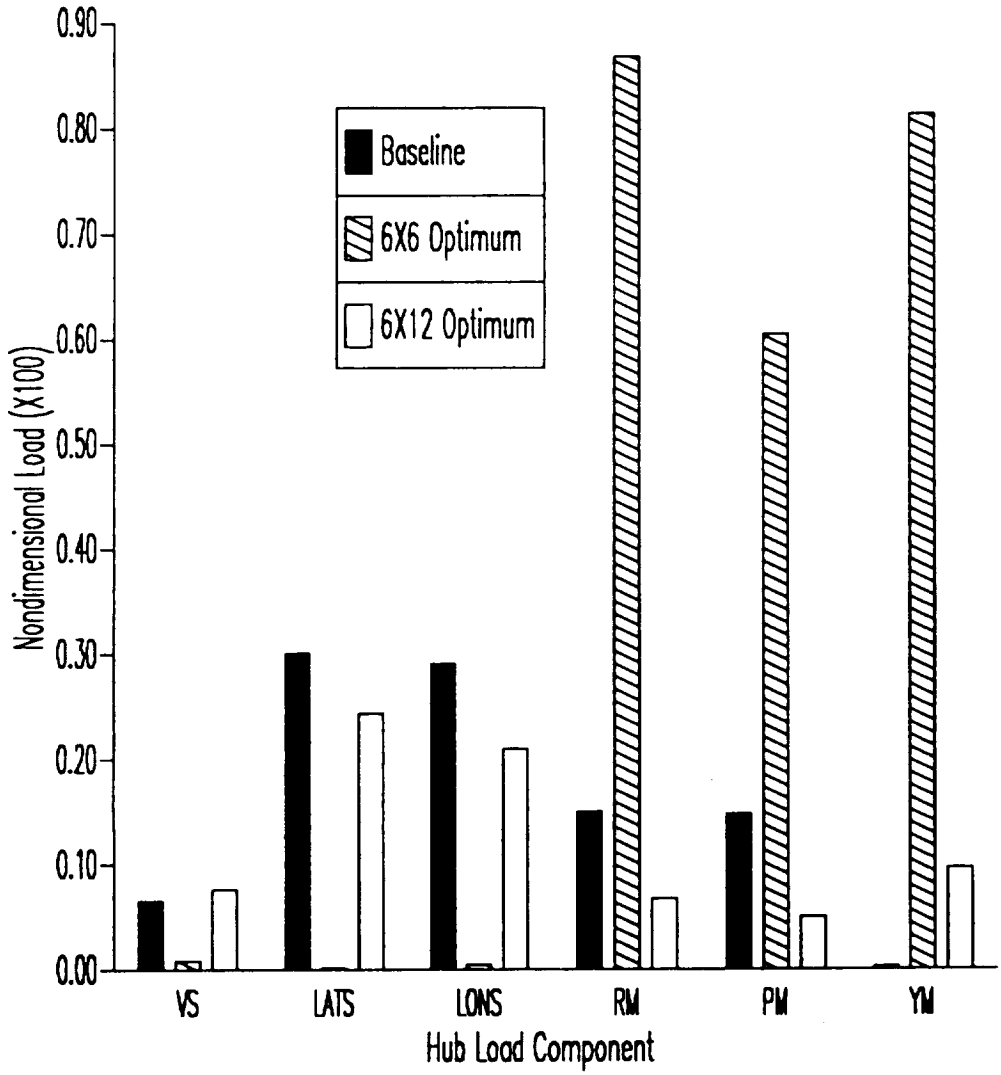

Figure 10.10: Comparison of peak-to-peak hub loads for baseline, 6×6 optimum, and 6×12 optimum, hingeless blade, 5% blade root offset, cautious global control, $\mu = 0.3$.

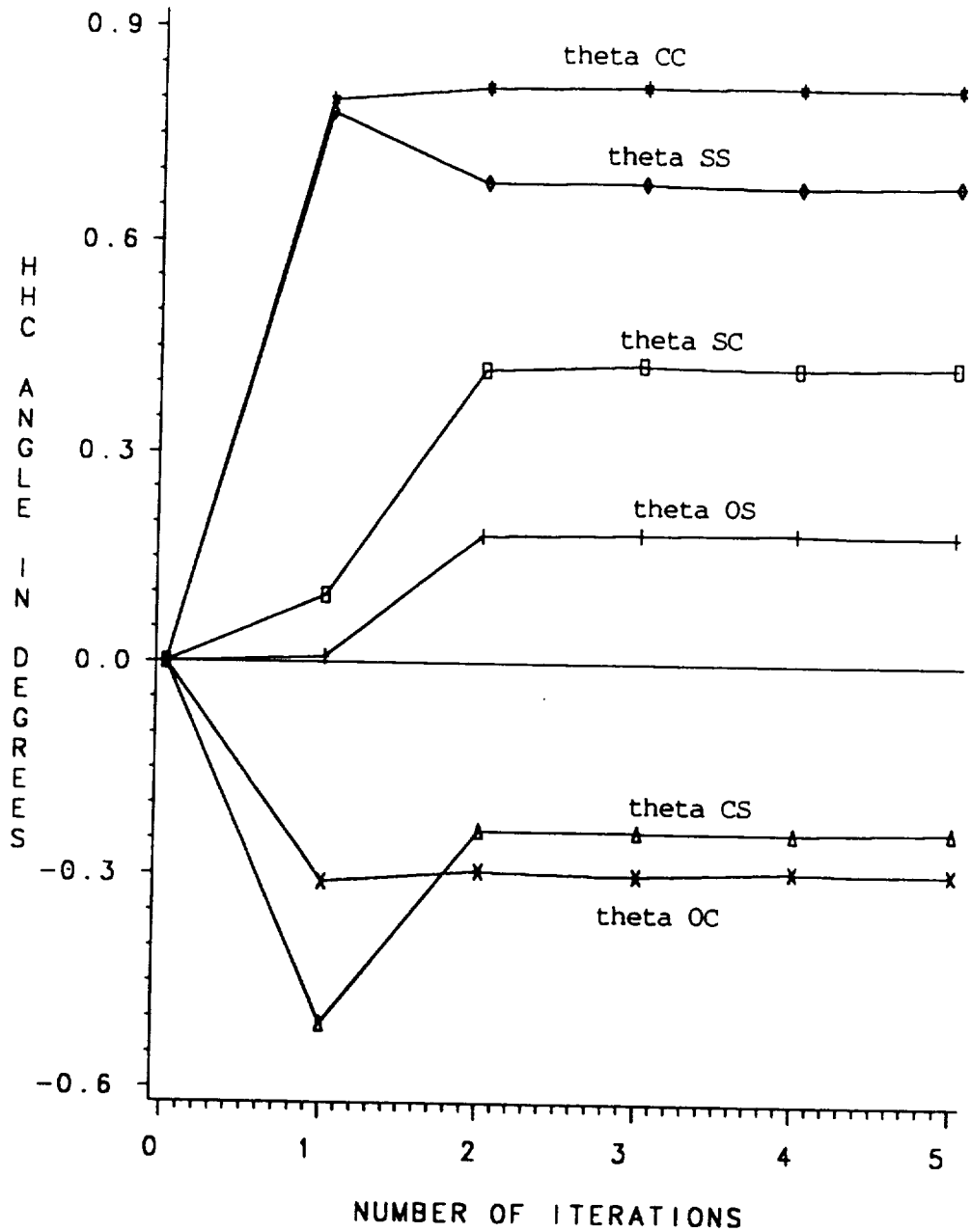

Figure 10.11: Iteration history of HHC input angles for articulated blade, 5% blade root offset, 6×12 cautious global control, $\mu = 0.3$.

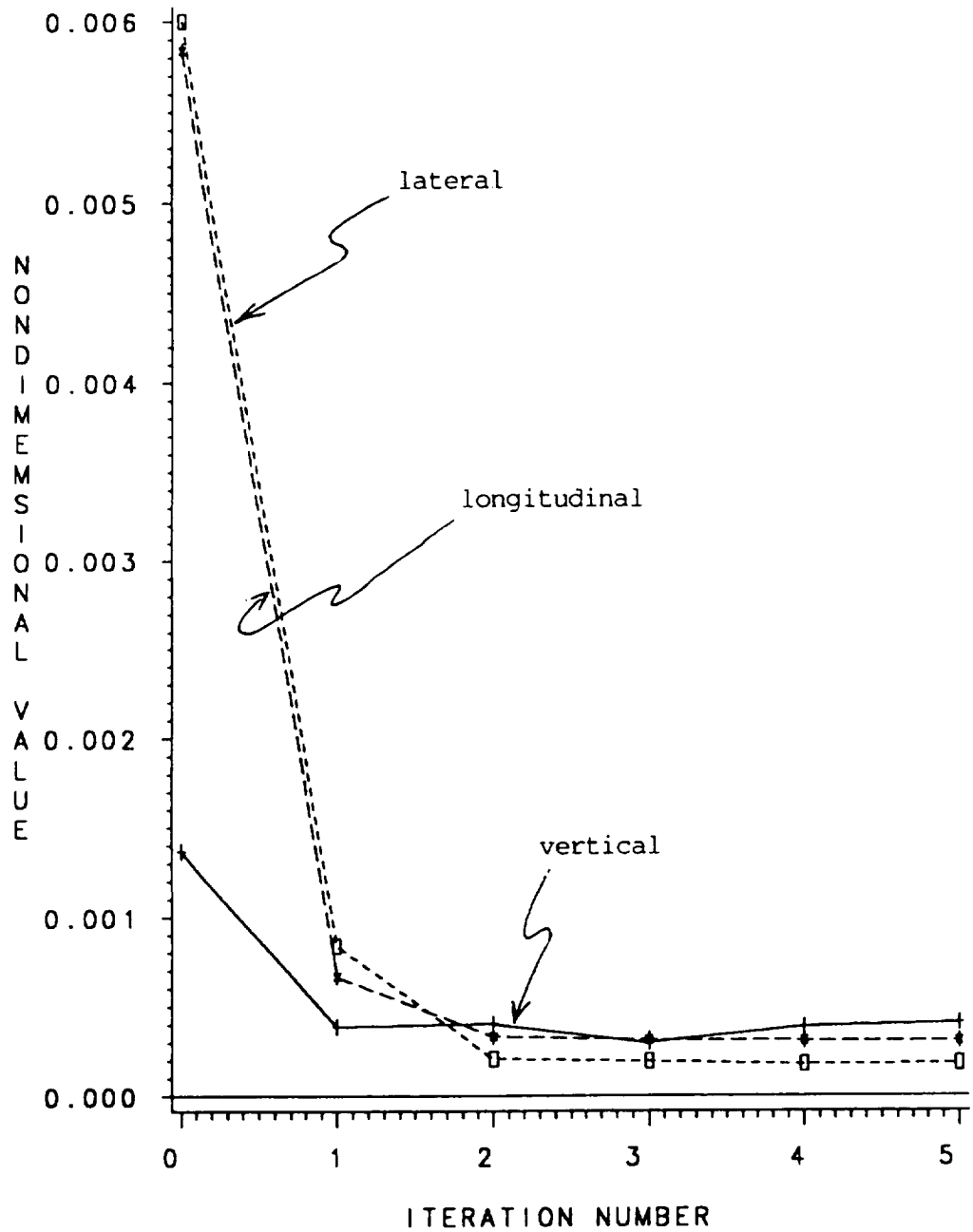

Figure 10.12: Iteration history of vertical, lateral and longitudinal peak-to-peak hub shears, articulated blade, 5% blade root offset, 6×12 cautious global control, $\mu = 0.3$.

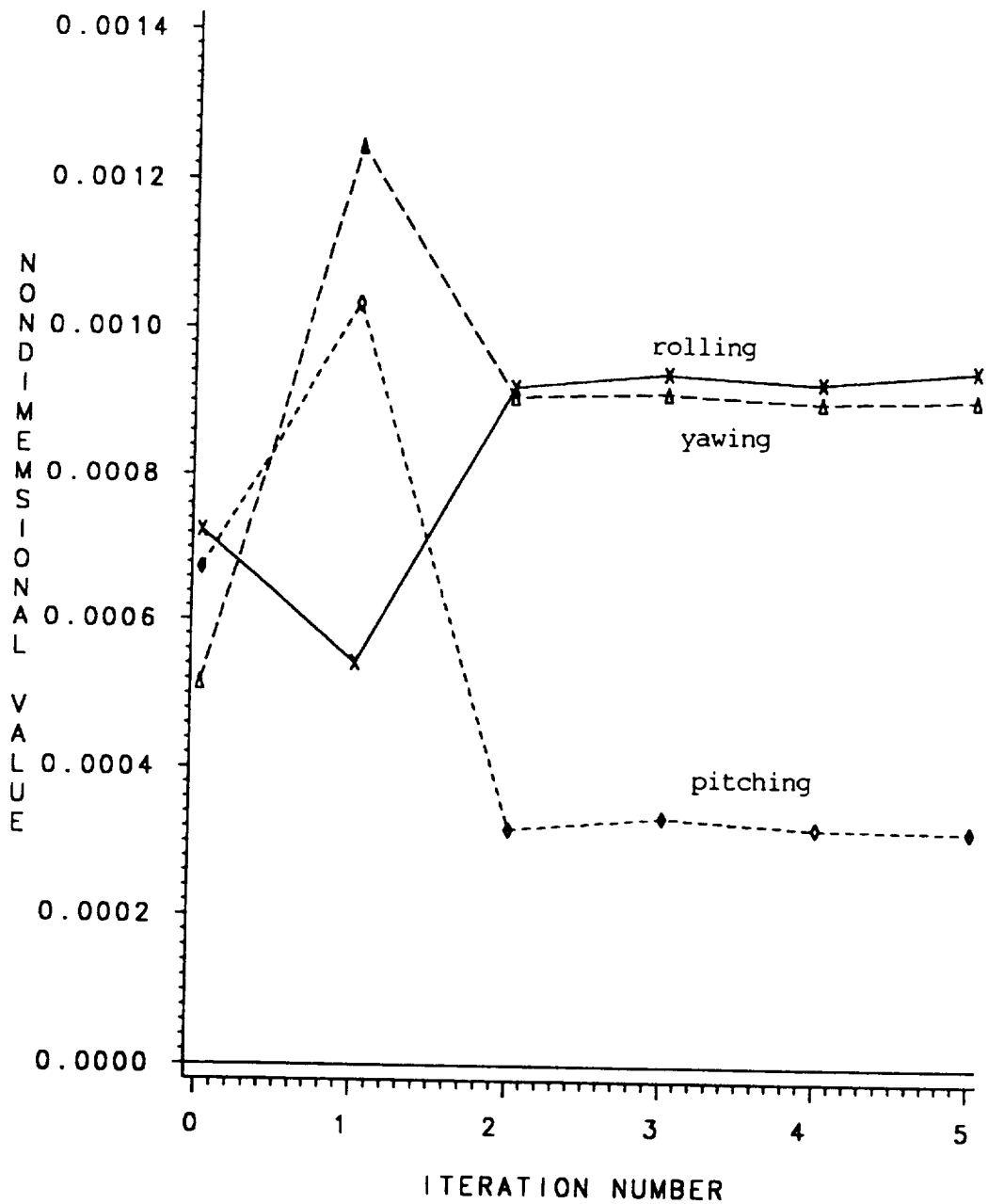

Figure 10.13: Iteration history of pitching, rolling and yawing peak-to-peak hub moments, articulated blade, 5% blade root offset, 6×12 cautious global control, $\mu = 0.3$.

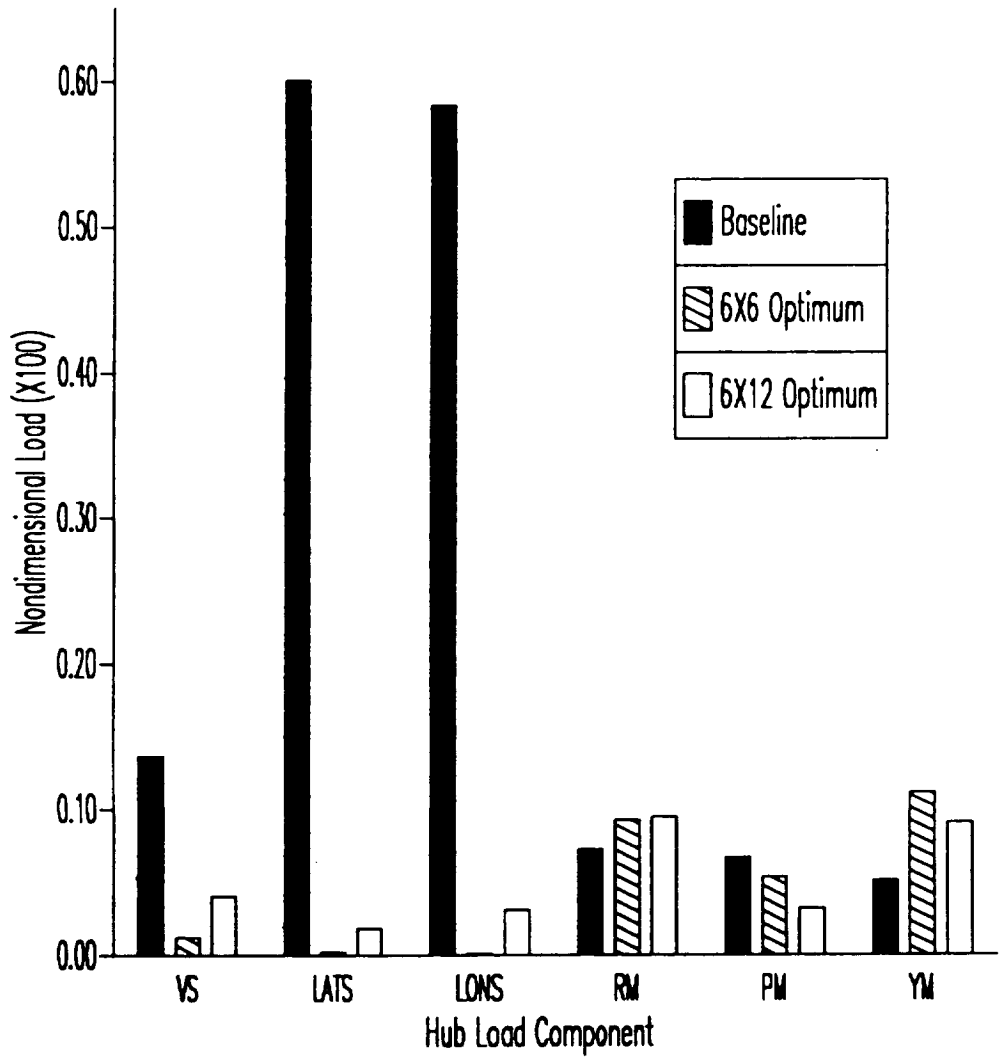

Figure 10.14: Comparison of peak-to-peak hub loads for baseline, 6×6 optimum, and 6×12 optimum, articulated blade, 5% blade root offset, cautious global control, $\mu = 0.3$.

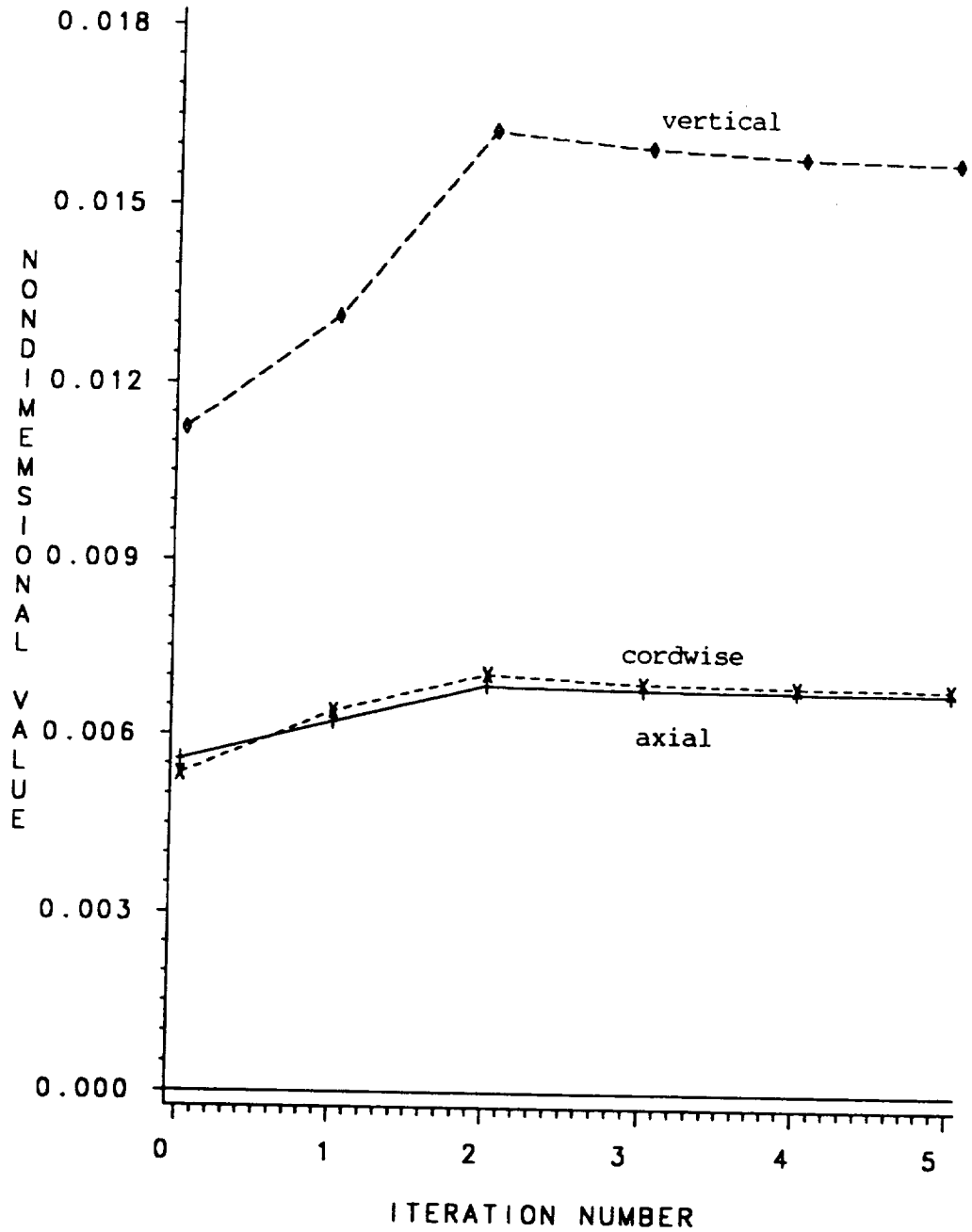

Figure 10.15: Iteration history of axial, cordwise, and vertical peak-to-peak rotating blade root shears, hingeless blade, 5% blade root offset, cautious global control, $\mu = 0.3$.

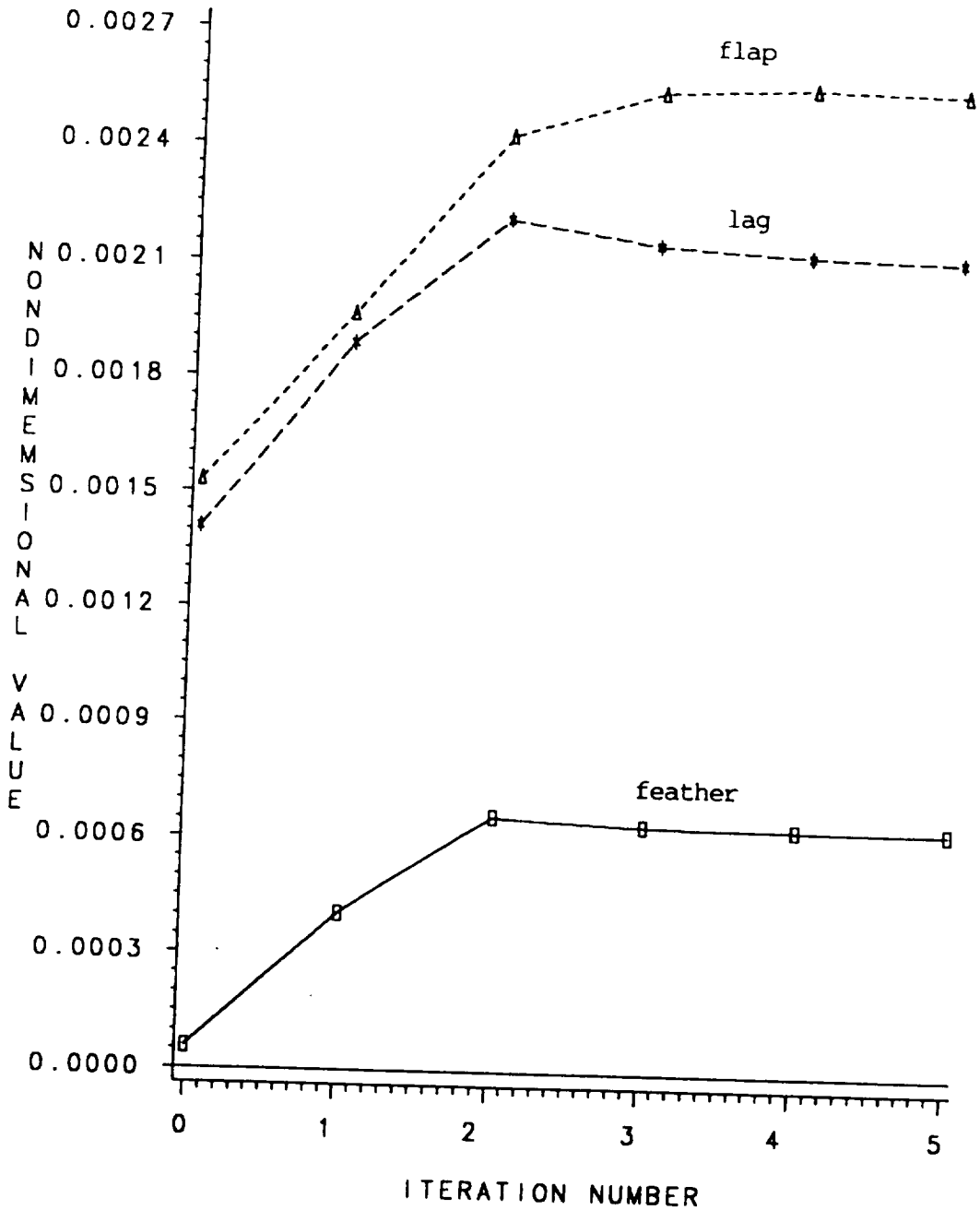

Figure 10.16: Iteration history of feathering, flapping, and lagging peak-to-peak rotating blade root moments, hingeless blade, 5% blade root offset, cautious global control, $\mu = 0.3$.

C-4.

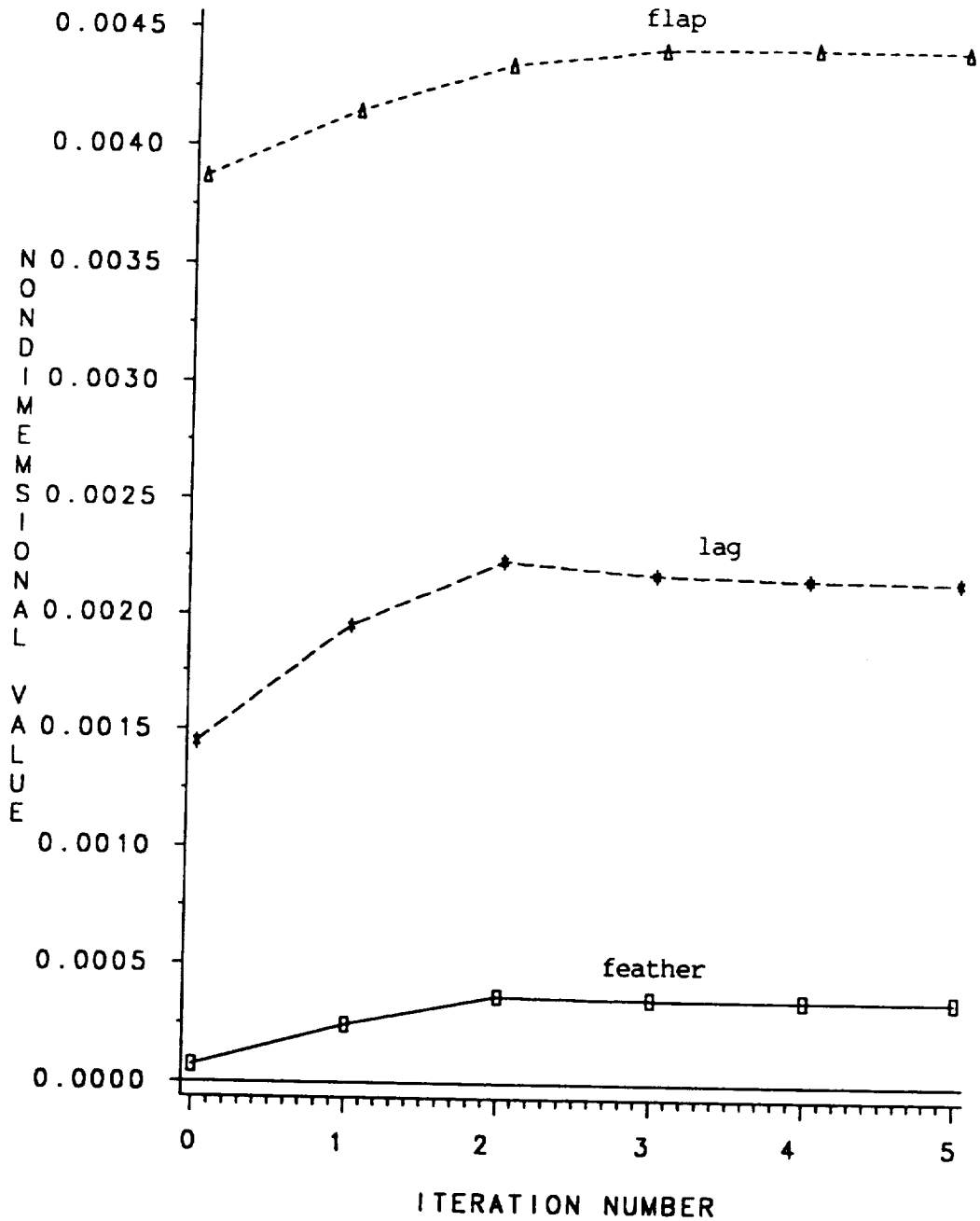

Figure 10.17: Iteration history of maximum values of feathering, flapping, and lagging rotating blade root moments, hingeless blade, 5% blade root offset, cautious global control, $\mu = 0.3$.

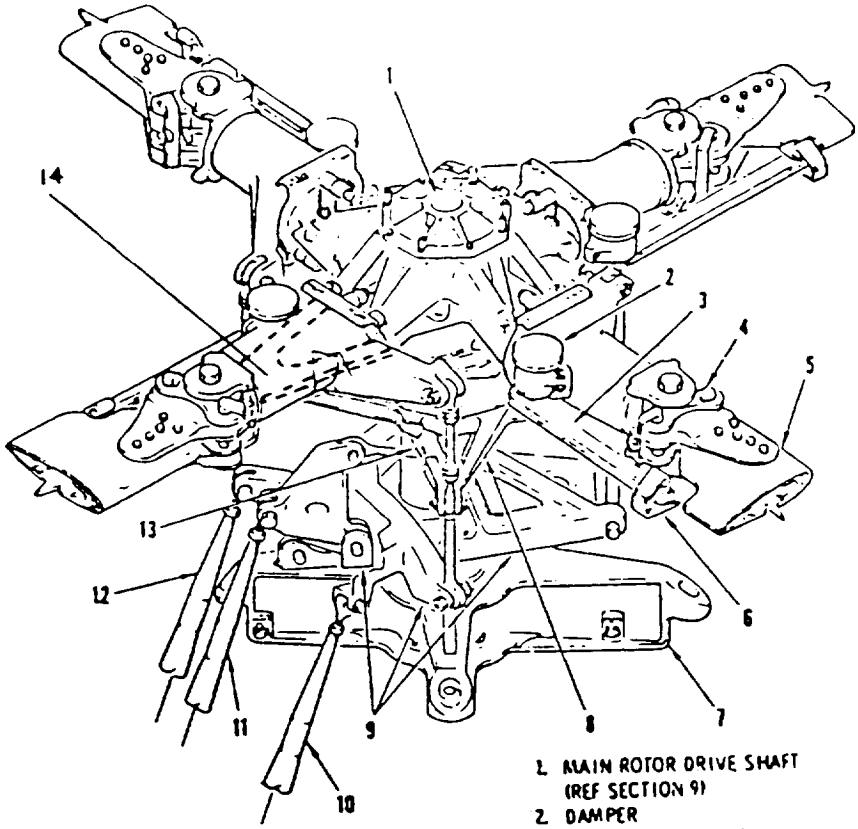

1. MAIN ROTOR DRIVE SHAFT (REF SECTION 9)
2. DAMPER
3. DAMPER ARM (LINK)
4. BLADE ATTACH PIN (TYP)
5. MAIN ROTOR BLADE
6. DAMPER LINK ATTACH PIN
7. MAIN ROTOR MAST BASE
8. ROTATING SWASHPLATE
9. MAIN ROTOR CONTROLS (MIXER, IDLER BELLCRANKS AND LINKS)
10. LATERAL MIXER CONTROL ROD (CYCLIC)
11. LONGITUDINAL MIXER CONTROL ROD (CYCLIC)
12. COLLECTIVE MIXER CONTROL ROD
13. STATIONARY SWASHPLATE
14. INSIDE THE PITCH CASE A STRAP PACK CARRIES THE TENSION LOADS FROM THE BLADE TO THE HUB

Figure 11.1: OH6A main rotor hub.

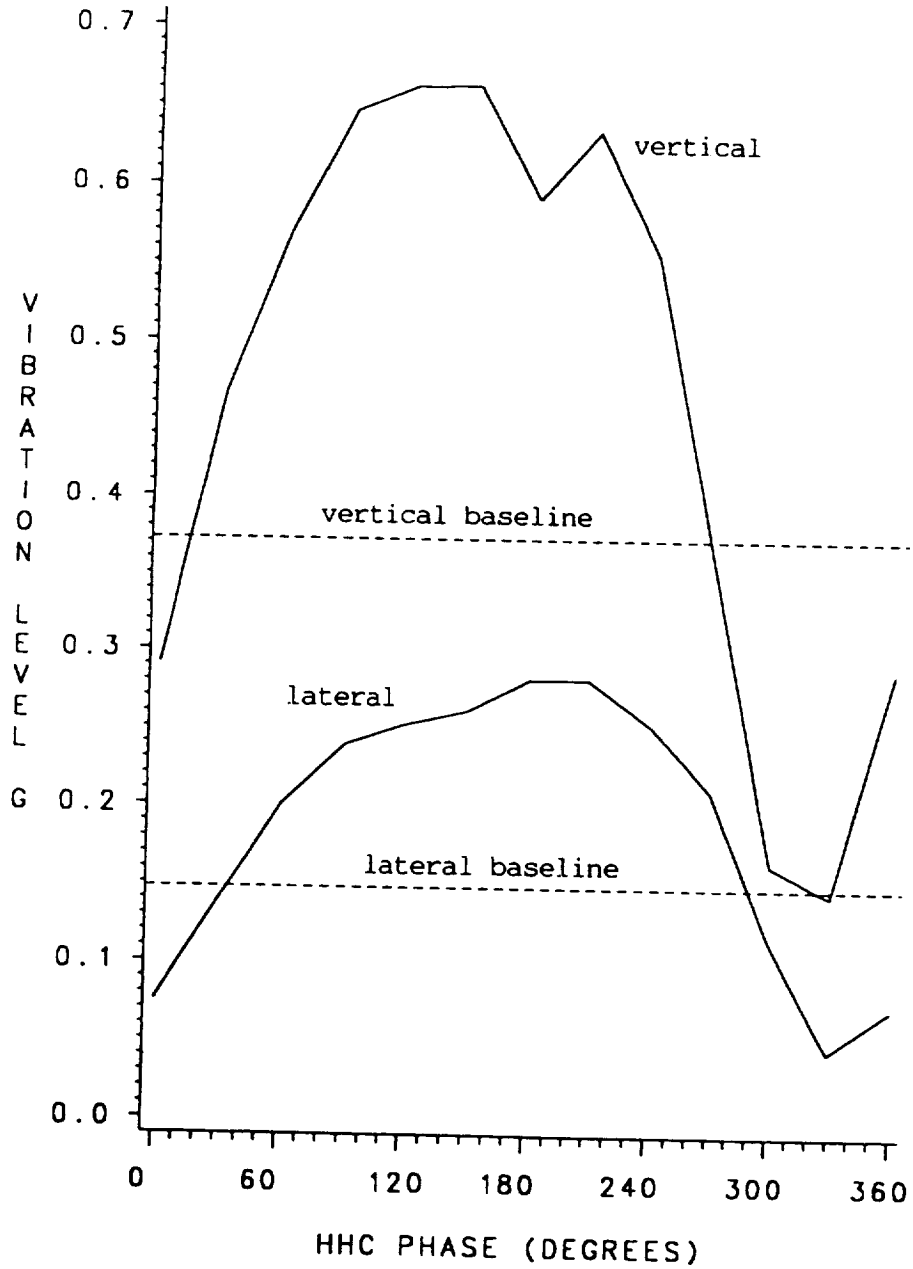

Figure 11.2: Variation of 4/rev. vertical and lateral pilot seat vibrations with phase of 1/3° lateral HHC input, flight test results of Ref. 67 for the OH6A helicopter, 100 knots.

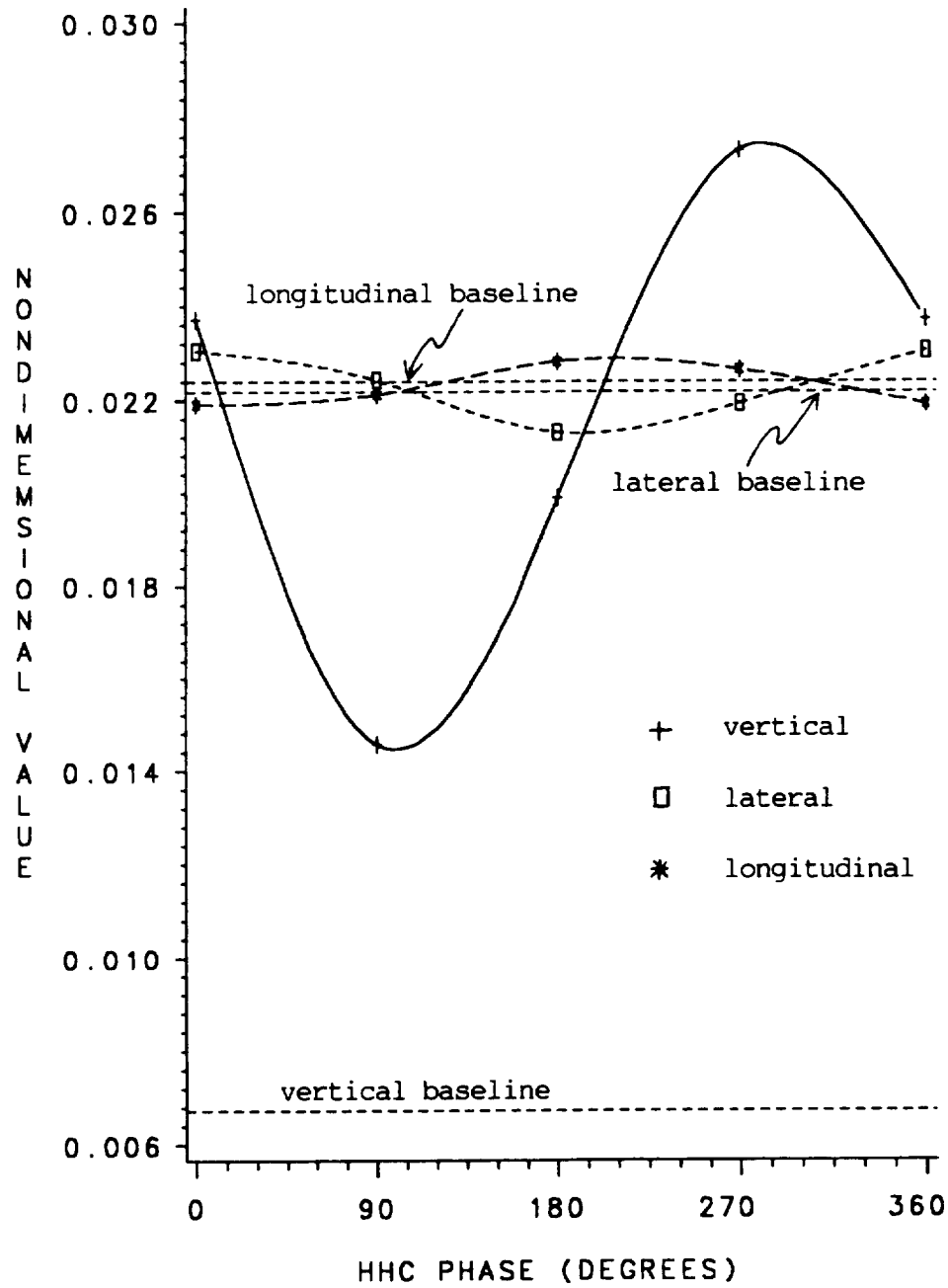

Figure 11.3: Variation of 4/rev. vertical, lateral, and longitudinal hub shears with HHC phase, 1/3° collective HHC input, OH6A rotor, unsteady aerodynamics, $\mu = 0.253$.

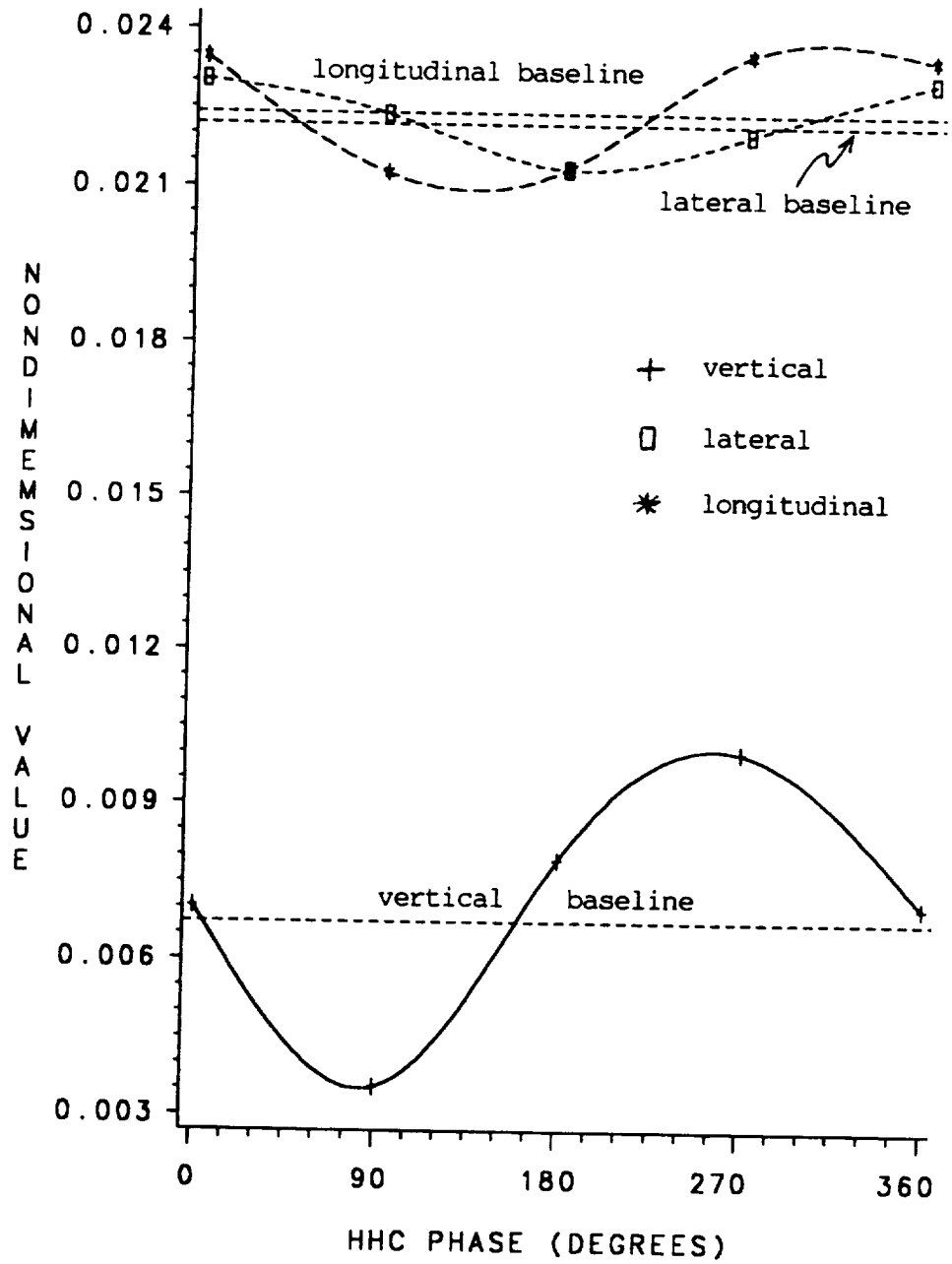

Figure 11.4: Variation of 4/rev. vertical, lateral, and longitudinal hub shears with HHC phase, 1/3° lateral HHC input, OH6A rotor, unsteady aerodynamics, $\mu = 0.253$.

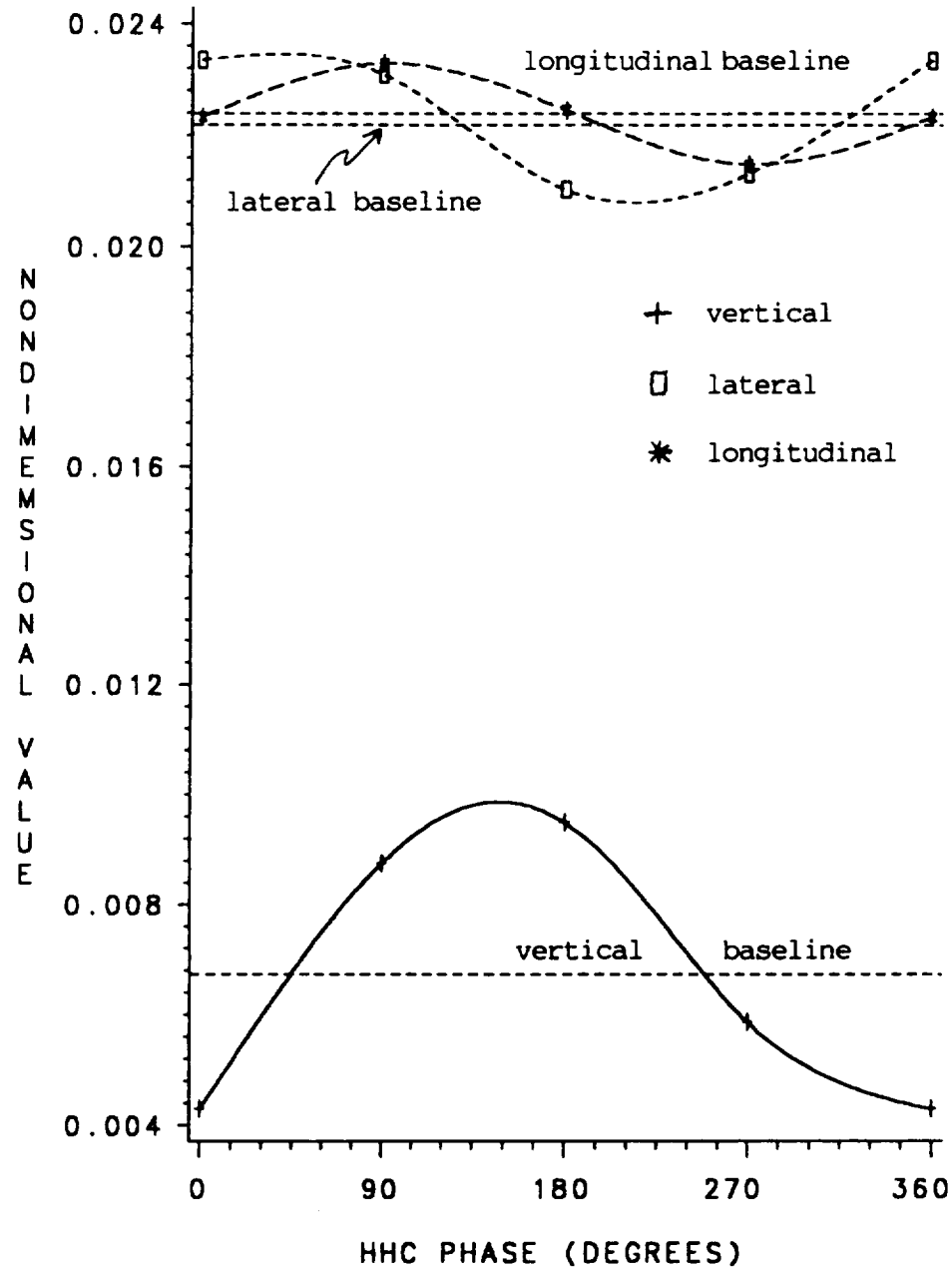

Figure 11.5: Variation of 4/rev. vertical, lateral, and longitudinal hub shears with HHC phase, 1/3° longitudinal HHC input, OH6A rotor, unsteady aerodynamics, $\mu = 0.253$.

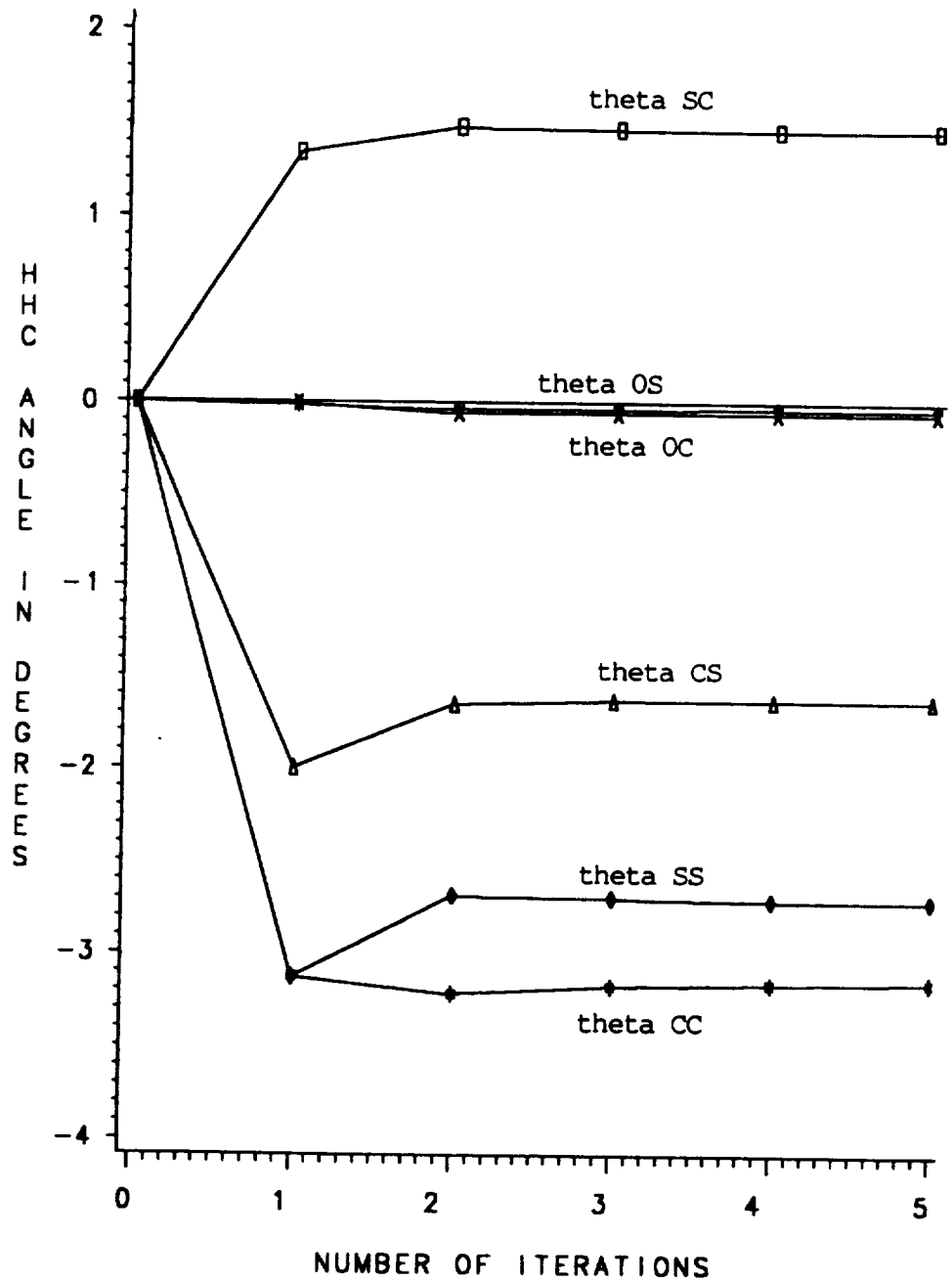

Figure 11.6: Iteration history of HHC input angles for OH6A rotor, cautious, global control, $\mu = 0.253$, unsteady aerodynamics.

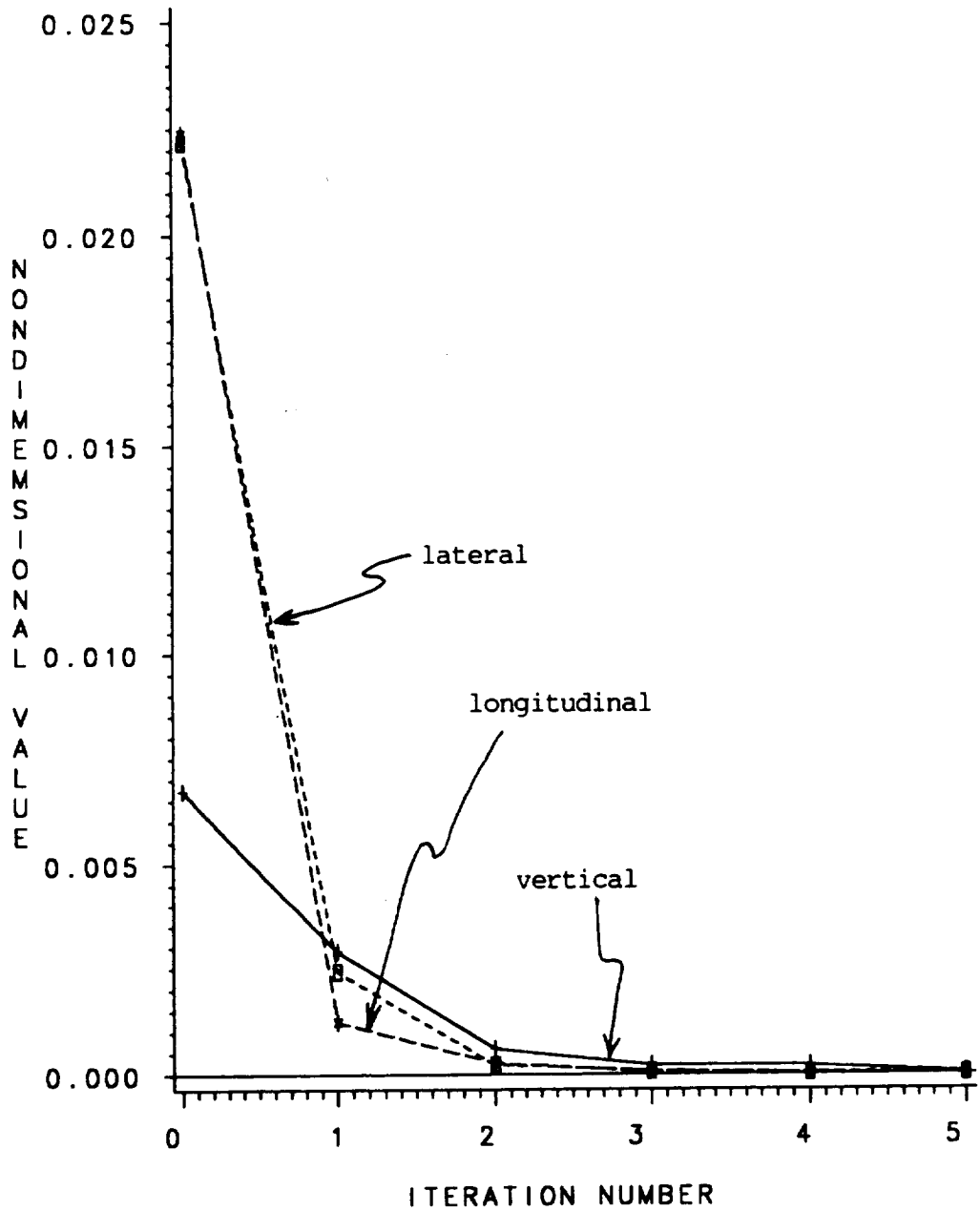

Figure 11.7: Iteration history of vertical, lateral, and longitudinal 4/rev. hub shears for OH6A rotor, cautious global controller, $\mu = 0.253$, unsteady aerodynamics.

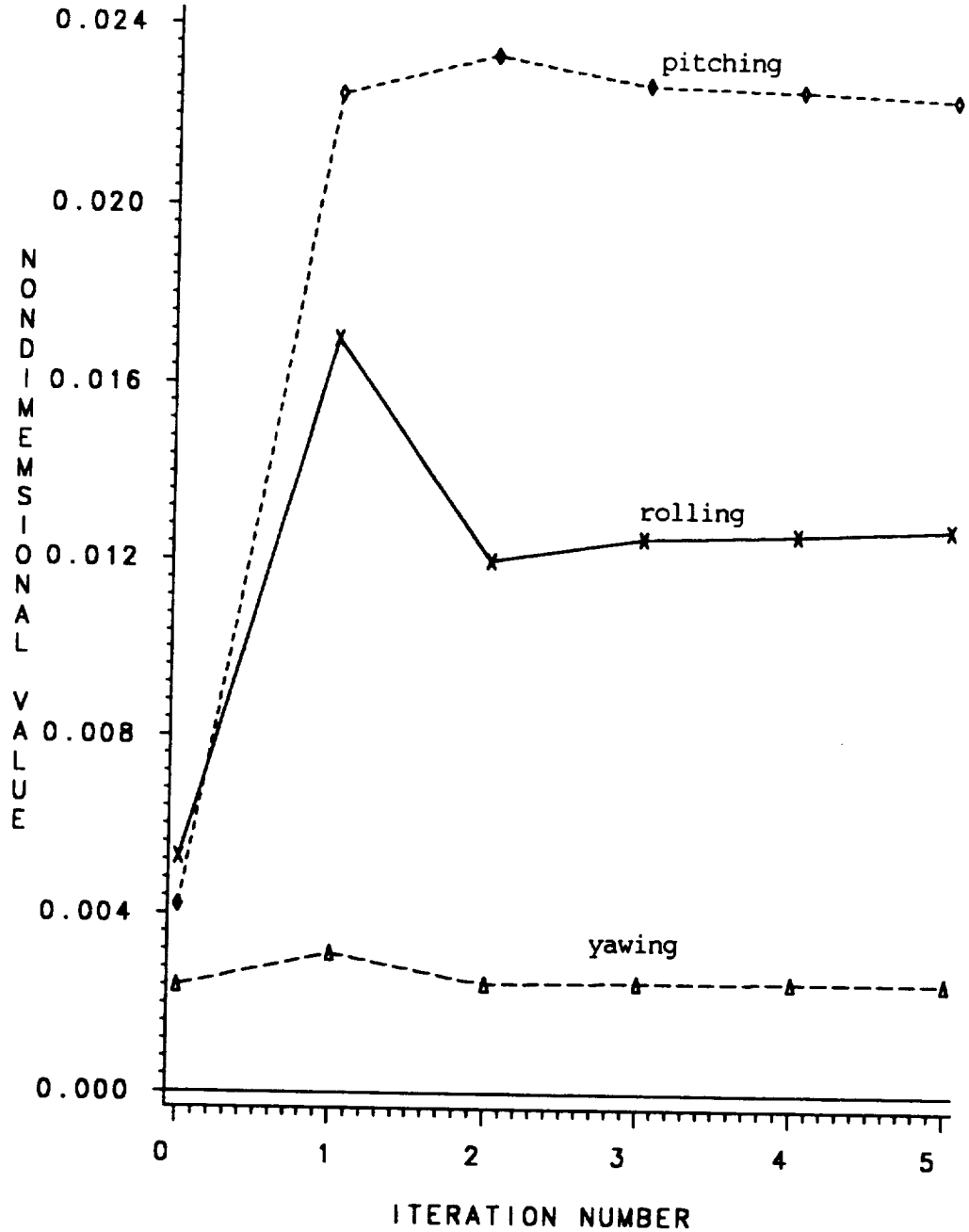

Figure 11.8: Iteration history of pitching, rolling, and yawing 4/rev. hub moments for OH6A rotor, cautious global controller, $\mu = 0.253$, unsteady aerodynamics.

REPORT DOCUMENTATION PAGE

Form Approved
OMB No. 0704-0188

Public reporting burden for this collection of information is estimated to average 1 hour per response, including the time for reviewing instructions, searching existing data sources, gathering and maintaining the data needed, and completing and reviewing the collection of information. Send comments regarding this burden estimate or any other aspect of this collection of information, including suggestions for reducing this burden, to Washington Headquarters Services, Directorate for information Operations and Reports, 1215 Jefferson Davis Highway, Suite 1204, Arlington, VA 22202-4302, and to the Office of Management and Budget, Paperwork Reduction Project (0704-0188), Washington, DC 20503.

1. AGENCY USE ONLY *(Leave blank)*

2. REPORT DATE
August 1994

3. REPORT TYPE AND DATES COVERED
Contractor Report

4. TITLE AND SUBTITLE
Aeroelastic Simulation of Higher Harmonic Control

5. FUNDING NUMBERS
NAG-477

6. AUTHOR(S)
Lawson H. Robinson and Peretz P. Friedmann

7. PERFORMING ORGANIZATION NAME(S) AND ADDRESS(ES)
Mechanical, Aerospace and Nuclear Engineering Department
School of Engineering and Applied Science
University of California, Los Angeles
405 Hilgard Avenue
Los Angeles, CA 90024-1597

8. PERFORMING ORGANIZATION REPORT NUMBER
A-94118

9. SPONSORING/MONITORING AGENCY NAME(S) AND ADDRESS(ES)
National Aeronautics and Space Administration
Washington, DC 20546-0001

10. SPONSORING/MONITORING AGENCY REPORT NUMBER
NASA CR-4623

11. SUPPLEMENTARY NOTES
Point of Contact: Steve Jacklin, Ames Research Center, MS T12-B, Moffett Field, CA 94035-1000; (415) 604-4567

12a. DISTRIBUTION/AVAILABILITY STATEMENT
Unclassified — Unlimited
Subject Category 02

12b. DISTRIBUTION CODE

13. ABSTRACT *(Maximum 200 words)*

This report describes the development of an aeroelastic analysis of a helicopter rotor and its application to the simulation of helicopter vibration reduction through higher harmonic control (HHC). An improved finite-state, time-domain model of unsteady aerodynamics is developed to capture high frequency aerodynamic effects. An improved trim procedure is implemented which accounts for flap, lead-lag and torsional deformations of the blade. The effect of unsteady aerodynamics is studied and it is found that its impact on blade aeroelastic stability and low frequency response is small, but it has a significant influence on rotor hub vibrations. Several different HHC algorithms are implemented on a hingeless rotor and their effectiveness in reducing hub vibratory shears is compared. All the controllers are found to be quite effective, but very differing HHC inputs are required depending on the aerodynamic model used. Effects of HHC on rotor stability and power requirements are found to be quite small. Simulations of roughly equivalent articulated and hingeless rotors are carried out, and it is found that hingeless rotors can require considerably larger HHC inputs to reduce vibratory shears. This implies that the practical implementation of HHC on hingeless rotors might be considerably more difficult than on articulated rotors.

14. SUBJECT TERMS
Rotary-wing aeroelasticity, Active control of vibrations, Helicopter higher harmonic control

15. NUMBER OF PAGES
277

16. PRICE CODE
A13

17. SECURITY CLASSIFICATION OF REPORT
Unclassified

18. SECURITY CLASSIFICATION OF THIS PAGE
Unclassified

19. SECURITY CLASSIFICATION OF ABSTRACT

20. LIMITATION OF ABSTRACT